

# NASA TECHNICAL MEMORANDUM

NASA TM X-64627

**CASE FILE  
COPY**

SPACE AND PLANETARY ENVIRONMENT  
CRITERIA GUIDELINES FOR USE IN  
SPACE VEHICLE DEVELOPMENT  
1971 Revision

Aero-Astrodynamics Laboratory

November 15, 1971

**NASA**

*George C. Marshall Space Flight Center  
Marshall Space Flight Center, Alabama*

1. REPORT NO. <b>TM X-64627</b>		2. GOVERNMENT ACCESSION NO.		3. RECIPIENT'S CATALOG NO.	
4. TITLE AND SUBTITLE <b>Space and Planetary Environment Criteria Guidelines for Use in Space Vehicle Development (1971 Revision)</b>				5. REPORT DATE <b>November 15, 1971</b>	
				6. PERFORMING ORGANIZATION CODE	
7. AUTHOR(S) <b>Robert E. Smith, editor</b>				8. PERFORMING ORGANIZATION REPORT #	
9. PERFORMING ORGANIZATION NAME AND ADDRESS  <b>George C. Marshall Space Flight Center Marshall Space Flight Center, Alabama 35812</b>				10. WORK UNIT NO.	
				11. CONTRACT OR GRANT NO.	
				13. TYPE OF REPORT & PERIOD COVERED  <b>Technical Memorandum</b>	
12. SPONSORING AGENCY NAME AND ADDRESS  <b>National Aeronautics and Space Administration Washington, D. C. 20546</b>				14. SPONSORING AGENCY CODE	
15. SUPPLEMENTARY NOTES <b>Prepared by Aero-Astroynamics Laboratory, Science and Engineering</b>					
16. ABSTRACT  <p>This document contains a consolidation of natural environment data for use as design criteria guidelines in space and planetary exploration vehicle development programs. In addition to information in the disciplinary areas of aeronomy, radiation, geomagnetism, astrodynamic constants, and meteoroids for the earth's environment above 90 kilometers, interplanetary space, and the planetary environments the upper atmosphere model currently recommended for use at MSFC is discussed in detail.</p> <p>This document supersedes all previous editions of NASA TM X-53957, entitled "Space Environment Criteria Guidelines for Use in Space Vehicle Development, 1969 Revision."</p>					
17. KEY WORDS			18. DISTRIBUTION STATEMENT  <i>www</i> <b>Unclassified-unlimited</b> <i>E. D. Geissler</i> <b>E. D. Geissler</b> <b>Director, Aero-Astroynamics Laboratory</b>		
19. SECURITY CLASSIF. (of this report)  <b>Unclassified</b>		20. SECURITY CLASSIF. (of this page)  <b>Unclassified</b>		21. NO. OF PAGES  <b>372</b>	
				22. PRICE  <b>\$6.00</b>	

# TABLE OF CONTENTS

	Page
SUMMARY .....	
INTRODUCTION.....	
SECTION I. INTERPLANETARY SPACE ENVIRONMENT.....	1-1
1.1 Definition .....	1-1
1.2 Gas Properties .....	1-1
1.2.1 Kinetic Gas Temperature .....	1-1
1.2.2 Gas Pressure .....	1-1
1.2.3 Density .....	1-1
1.2.4 Composition .....	1-1
1.3 Radiation Environment .....	1-1
1.3.1 Galactic Cosmic Radiation.....	1-2
1.3.2 Solar Cosmic Radiation.....	1-2
1.3.3 Radiation Properties of the Sun (Thermal)...	1-6
1.3.4 Solar Radio Noise.....	1-15
1.3.5 Additional Information.....	1-17
1.4 Meteoroids, Asteroids, and Comets .....	1-17
1.4.1 Cometary Meteoroids .....	1-17
1.4.2 Asteroidal Meteoroids.....	1-21
1.4.3 Additional Information.....	1-23
1.5 Geomagnetic Environment .....	1-23
1.5.1 Magnetic Field.....	1-23
1.6 Astrodynamic Constants .....	1-23
1.6.1 General Constants .....	1-23
1.6.2 Gravitational Constants and Mass Ratios ....	1-24
REFERENCES.....	1-25
SECTION II. TERRESTRIAL SPACE.....	2-1

## TABLE OF CONTENTS (Continued)

	Page
2.1 Definition . . . . .	2-1
2.2 Neutral Gas Properties . . . . .	2-1
2.2.1 Variations. . . . .	2-2
2.2.2 2500- to 65 000-km Altitude . . . . .	2-5
2.2.3 Additional Information. . . . .	2-5
2.3 Ionosphere . . . . .	2-5
2.3.1 Basic Concepts . . . . .	2-6
2.3.2 Ionospheric Parameters . . . . .	2-6
2.3.3 Spacecraft Interaction with the Ionosphere . . . . .	2-13
2.3.4 Communications. . . . .	2-17
2.4 Radiation Environment . . . . .	2-19
2.4.1 Galactic Cosmic Radiation . . . . .	2-19
2.4.2 Trapped Radiation . . . . .	2-20
2.4.3 Solar Particle Events . . . . .	2-27
2.4.4 Solar Cosmic Radiation . . . . .	2-29
2.4.5 Thermal and Albedo Radiation (Earth) . . . . .	2-30
2.4.6 Radiation Properties of the Sun (Thermal) . . . . .	2-33
2.4.7 Solar Cycle Predictions. . . . .	2-33
2.4.8 Dose Rate Calculation. . . . .	2-33
2.4.9 Additional Information. . . . .	2-33
2.5 Meteoroid Environment . . . . .	2-33
2.5.1 Average Total Meteoroid Environment . . . . .	2-34
2.5.2 Sporadic Meteoroids . . . . .	2-36
2.5.3 Stream Meteoroids . . . . .	2-37
2.5.4 Additional Information. . . . .	2-39
2.6 Geomagnetic Environment . . . . .	2-39
2.6.1 Magnetic Field. . . . .	2-39
2.6.2 Temporal Variations. . . . .	2-43



## TABLE OF CONTENTS (Continued)

	Page
2.6.3 Magnetic Field at Geosynchronous Altitudes . .	2-43
2.6.4 Models of the Earth's Magnetic Environment . . . . .	2-43
2.6.5 Additional Information. . . . .	2-43
2.7 Astrodynamics Constants. . . . .	2-44
2.7.1 Earth Constants (Epoch 1960.0) . . . . .	2-44
2.7.2 Gravitational Potential Function for the Earth . . . . .	2-44
2.7.3 Geodetic Models. . . . .	2-47
2.8 Winds . . . . .	2-47
2.8.1 Theoretical Models of the Wind Field. . . . .	2-47
2.8.2 Winds in the Lower Thermosphere — 90 to 150 km . . . . .	2-48
2.8.3 Winds Above 150 km . . . . .	2-55
2.8.4 Vertical Winds. . . . .	2-57
2.8.5 Anomalous Strong Winds . . . . .	2-57
2.8.6 Design Criteria . . . . .	2-57
REFERENCES . . . . .	2-60
BIBLIOGRAPHY. . . . .	2-63
SECTION III. CISELUNAR SPACE . . . . .	3-1
3.1 Definition . . . . .	3-1
3.2 Gas Properties . . . . .	3-1
3.3 Radiation Environment . . . . .	3-1
3.4 Meteoroid Environment. . . . .	3-1
3.4.1 Average Total Meteoroid Environment. . . . .	3-1
3.4.2 Sporadic Meteoroids . . . . .	3-1
3.4.3 Stream Meteoroids . . . . .	3-4
3.4.4 Additional Information. . . . .	3-5

## TABLE OF CONTENTS (Continued)

	Page
3.5 Geomagnetic Environment . . . . .	3-5
REFERENCES . . . . .	3-6
SECTION IV. MOON . . . . .	4-1
4.1 Atmospheric Environment . . . . .	4-1
4.1.1 Gas Properties . . . . .	4-1
4.1.2 Radiation Environment . . . . .	4-2
4.1.3 Meteoroid Environment . . . . .	4-3
4.1.4 Geomagnetic Environment . . . . .	4-9
4.1.5 Astrodynamic Constants . . . . .	4-9
4.2 Surface Environment . . . . .	4-11
4.2.1 Physical Properties . . . . .	4-12
4.2.2 Morphologic Subdivisions . . . . .	4-12
4.2.3 Topography . . . . .	4-13
4.2.4 Block and Crater Frequencies . . . . .	4-23
4.2.5 Soil Characteristics . . . . .	4-27
4.2.6 Thermal Properties . . . . .	4-31
4.2.7 Optical Properties . . . . .	4-40
4.2.8 Dielectric Constant . . . . .	4-45
4.2.9 Lunar Trafficability . . . . .	4-48
REFERENCES . . . . .	4-50
BIBLIOGRAPHY . . . . .	4-56
SECTION V. MERCURY . . . . .	5-1
5.1 Atmospheric Environment . . . . .	5-1
5.1.1 Definition . . . . .	5-1
5.1.2 Gas Properties (Surface to 1000 km Altitudes) . . . . .	5-1

## TABLE OF CONTENTS (Continued)

	Page
5.1.3 Gas Properties (1000 to 20 000 km Altitude) . . . . .	5-7
5.1.4 Ionosphere and Charged Particles . . . . .	5-10
5.1.5 Clouds . . . . .	5-10
5.1.6 Circulation . . . . .	5-10
5.1.7 Electromagnetic Radiation . . . . .	5-10
5.1.8 Meteoroid Environment . . . . .	5-19
5.1.9 Geomagnetic Environment . . . . .	5-20
5.1.10 Astrodynamic Constants (Epoch 1960.0) . . . .	5-21
 5.2 Surface Environment . . . . .	 5-22
5.2.1 Surface Features . . . . .	5-23
5.2.2 Physical Conditions . . . . .	5-23
5.2.3 Electromagnetic Properties . . . . .	5-31
5.2.4 Temperature and Thermal Properties . . . . .	5-31
 5.3 Satellites . . . . .	 5-36
 REFERENCES . . . . .	 5-37
 BIBLIOGRAPHY . . . . .	 5-44
 SECTION VI. VENUS . . . . .	 6-1
 6.1 Atmospheric Environment . . . . .	 6-1
6.1.1 Definition . . . . .	6-1
6.1.2 Gas Properties (Surface to 1000 km Altitude) . . . . .	6-1
6.1.3 Gas Properties (1000 to 20 000 km Altitude) . . . . .	6-4
6.1.4 Ionosphere . . . . .	6-8
6.1.5 Clouds . . . . .	6-8
6.1.6 Circulation . . . . .	6-9
6.1.7 Radiation Environment . . . . .	6-9

## TABLE OF CONTENTS (Continued)

	Page
6.1.8 Meteoroid Environment . . . . .	6-11
6.1.9 Geomagnetic Environment . . . . .	6-13
6.1.10 Astrodynamic Constants (Epoch 1960.0) . . . .	6-13
6.1.11 Additional Information. . . . .	6-13
6.2 Surface Environment. . . . .	6-14
6.2.1 Temperature . . . . .	6-14
6.2.2 Features. . . . .	6-14
6.2.3 Terrain and Composition. . . . .	6-14
6.2.4 Dielectric Constant. . . . .	6-14
6.3 Satellites . . . . .	6-14
REFERENCES . . . . .	6-15
SECTION VII. MARS . . . . .	7-1
7.1 Atmospheric Environment . . . . .	7-1
7.1.1 Definition . . . . .	7-1
7.1.2 Gas Properties (Surface to 1000 km Altitude). . . . .	7-1
7.1.3 Gas Properties (1000 to 20 000 km Altitude). . . . .	7-14
7.1.4 Ionosphere . . . . .	7-15
7.1.5 Clouds . . . . .	7-18
7.1.6 Winds. . . . .	7-20
7.1.7 Radiation Environment . . . . .	7-21
7.1.8 Meteoroid Environment. . . . .	7-24
7.1.9 Geomagnetic Environment . . . . .	7-26
7.1.10 Astrodynamic Constants . . . . .	7-26
7.1.11 Additional Information. . . . .	7-28
7.2 Surface Environment. . . . .	7-28

## TABLE OF CONTENTS (Continued)

	Page
7.2.1 Mechanical Properties . . . . .	7-28
7.2.2 Electrical Properties . . . . .	7-36
7.2.3 Thermal Properties . . . . .	7-36
7.2.4 Optical Thickness. . . . .	7-36
7.2.5 Surface Spectral Albedo. . . . .	7-37
7.2.6 Surface Photometric Function. . . . .	7-38
7.2.7 Surface Temperature . . . . .	7-38
7.2.8 Additional Information. . . . .	7-38
7.3 Satellites . . . . .	7-41
REFERENCES . . . . .	7-43
BIBLIOGRAPHY. . . . .	7-50
SECTION VIII. JUPITER . . . . .	8-1
8.1 Atmospheric Environment . . . . .	8-1
8.1.1 Definition . . . . .	8-1
8.1.2 Gas Properties . . . . .	8-1
8.1.3 Ionosphere . . . . .	8-12
8.1.4 Clouds . . . . .	8-13
8.1.5 Atmospheric Motions, Rotation Rate, and Winds . . . . .	8-14
8.1.6 Radiation Environment . . . . .	8-15
8.1.7 Meteoroid Environment. . . . .	8-25
8.1.8 Geomagnetic Environment . . . . .	8-27
8.1.9 Charged Particle Environment . . . . .	8-29
8.1.10 Astrodynamic Constants . . . . .	8-30
8.1.11 Additional Information. . . . .	8-32
8.2 Surface Environment. . . . .	8-32
8.3 Satellites . . . . .	8-33
REFERENCES . . . . .	8-34

## TABLE OF CONTENTS (Continued)

	Page
SECTION IX. SATURN .....	9-1
9.1 General .....	9-1
9.2 Composition of the Atmosphere .....	9-1
9.3 Radiation .....	9-1
9.4 Astrodynamic Constants (Epoch 1960.0) .....	9-2
9.5 Telescopic Appearance .....	9-2
9.6 Rings .....	9-3
9.7 Satellites .....	9-3
REFERENCES .....	9-5
SECTION X. URANUS .....	10-1
10.1 General .....	10-1
10.2 Astrodynamic Constants (Epoch 1960.0) .....	10-1
10.3 Satellites .....	10-2
REFERENCES .....	10-4
BIBLIOGRAPHY .....	10-4
SECTION XI. NEPTUNE .....	11-1
11.1 General .....	11-1
11.2 Astrodynamic Constants (Epoch 1960.0) .....	11-1
11.3 Satellites .....	11-1
REFERENCES .....	11-3
SECTION XII. PLUTO .....	12-1
12.1 General .....	12-1
12.2 Astrodynamic Constants (Epoch 1960.0) .....	12-1
REFERENCES .....	12-2

## TABLE OF CONTENTS (Concluded)

	Page
APPENDIX A. SOLAR CYCLE PREDICTION TECHNIQUE . . . . .	A-1
APPENDIX B. NEUTRAL ATMOSPHERE MODELS . . . . .	B-1
APPENDIX C. A PRELIMINARY SUMMARY OF THE MSFC PLANETARY ATMOSPHERE COMPUTER PROGRAM. . . . .	C-1

# LIST OF ILLUSTRATIONS

Figure	Title	Page
I-1.	Average relative velocity, cometary particles. . . . .	1-22
II-1.	Typical plot of temperature versus altitude and exospheric temperature . . . . .	2-3
II-2.	Typical daytime maximum and nighttime minimum atmospheric density profiles for high and low solar activity. . . . .	2-4
II-3.	Ionospheric electron concentration - nighttime . . . . .	2-9
II-4.	Ionospheric electron concentration - daytime . . . . .	2-9
II-5.	Daytime contours of equal electron density in the orbital plane of an Alouette Satellite. (Density units of $10^4$ electrons $\text{cm}^{-3}$ .) . . . . .	2-10
II-6.	Models of electron density profiles in the equatorial plane under solar sunspot extreme conditions. (The position of the knee or abrupt decrease in density is variable within the box as indicated.) . . . . .	2-10
II-7.	Ionic composition of solar minimum daytime winter ionosphere. . . . .	2-12
II-8.	Relative concentration of $\text{H}^+$ , $\text{O}^+$ , and $\text{He}^+$ and their average mass for solar minimum and a quiet summer time. (Nighttime summer profiles are also appropriate for winter daytime.) . . . . .	2-12
II-9.	Electron temperature, thermal velocity, and satellite/thermal velocity ratio . . . . .	2-14
II-10.	Ion temperature, thermal velocity, and satellite/thermal velocity ratio. . . . .	2-14
II-11.	Models of electron temperature profiles in $^{\circ}\text{K}$ or in $\text{eV}$ (viz., $\kappa T_e/e$ ) . . . . .	2-15



## LIST OF ILLUSTRATIONS (Continued)

Figure	Title	Page
II-12.	Thermal particle flux daytime . . . . .	2-18
II-13.	Thermal electron and ion particle fluxes . . . . .	2-18
II-14.	Cosmic-ray dose rate above the atmosphere as a function of geomagnetic latitude during solar maximum and minimum . . . . .	2-21
II-15.	Galactic radiation energy spectrum . . . . .	2-21
II-16.	Electron distribution in the earth's field (published by Vette in August 1964) . . . . .	2-22
II-17.	Proton distribution in the earth's field (published by Vette in September 1963) . . . . .	2-22
II-18.	South Atlantic Anomaly diagram . . . . .	2-23
II-19.	Proton flux densities at an altitude of 162 n.mi. . . . .	2-24
II-20.	Electron differential energy spectra . . . . .	2-25
II-21.	Proton differential energy spectra . . . . .	2-26
II-22.	Electron differential energy spectra . . . . .	2-28
II-23.	A typical spectral emissive power curve for the thermal radiation leaving the earth . . . . .	2-31
II-24.	Probability velocity distribution for sporadic meteoroids . . . . .	2-35
II-25.	Method for determining body shielding factor for randomly oriented spacecraft . . . . .	2-35
II-26a.	Activity ratio factor versus period of activity (Jan. - Aug.) for major streams based on photographic meteors (mass = 1 g, velocity = 20 km/s) . . . . .	2-40

## LIST OF ILLUSTRATIONS (Continued)

Figure	Title	Page
II-26b.	Activity ratio factor versus period of activity (Sept. - Dec.) for major streams based on photographic meteors (mass = 1 g, velocity = 20 km/s) . . . . .	2-41
II-27.	Contours of meridional wind speed at 45 degrees north latitude in units of $\text{ms}^{-1}$ , positive values directed toward the north. [Results are obtained with equinox transition times and the Jacchia and Slowey (1967) model.] . . . . .	2-49
II-28.	Wind vectors at the 300-km level are shown against a background of isobars at this level, the longest arrow representing a wind speed of about $225 \text{ ms}^{-1}$ . (The pressure and wind fields are symmetric about the equator.) . . . . .	2-49
II-29.	The atmospheric wind system in the northern hemisphere calculated for an altitude of 300 km when the peak electron density is $10^6 \text{ cm}^{-3}$ . . . . .	2-50
II-30.	The atmospheric wind system in the northern hemisphere calculated for an altitude of 300 km when the peak electron density is $3 \times 10^5 \text{ cm}^{-3}$ . . . . .	2-50
II-31.	The variation with height of the horizontal velocity components at 15.00 L.M.T. at a latitude of 45 degrees. . . . .	2-51
II-32.	Resultant components of the wind near latitude 38 degrees N. (The upper part is based on 25 sodium cloud experiments from Wallops Island. Arrows indicate the resultant wind.) . . . . .	2-52
II-33.	Averages of the absolute value of wind velocity regardless of direction (i.e. the mean scalar speed), based on the same data as Figure II-32. (Inset: frequency of occurrence of speeds over 80, 100, and 120 m/s.) . . . . .	2-53

## LIST OF ILLUSTRATIONS (Continued)

Figure	Title	Page
II-34.	Magnitude of vertical wind shears based on sodium cloud data from Wallops Island. (The shears were computed for $\Delta Z = 1$ km and plotted for each km of elevation. N is the number of observations.) . . . . .	2-53
II-35.	Results of rocket soundings by sodium clouds in Sardinia 1961-1963, east-west. (Numerical indications give speed in m/s.) . . . . .	2-54
II-36.	Result of rocket soundings by sodium clouds in Sardinia 1961-1963, north-south. (Numerical indications give speed in m/s.) . . . . .	2-54
II-37.	Mean upper-atmosphere rotation rate, derived from analysis of 29 satellite orbits . . . . .	2-56
III-1.	Probability velocity distribution for sporadic meteoroids . . . . .	3-2
IV-1.	Method for determining body shielding factor for randomly oriented spacecraft . . . . .	4-5
IV-2.	Probability velocity distribution for sporadic meteoroids . . . . .	4-5
IV-3.	Smooth Mare cumulative slope frequency distribution for three base lengths . . . . .	4-15
IV-4.	Rough Mare cumulative slope frequency distributions for three base lengths . . . . .	4-15
IV-5.	Hummocky Uplands cumulative slope frequency distributions for three base lengths . . . . .	4-16
IV-6.	Rough Uplands cumulative slope frequency distributions for three base lengths . . . . .	4-17

## LIST OF ILLUSTRATIONS (Continued)

Figure	Title	Page
IV-7.	Smooth Mare power spectral density versus frequency . .	4-18
IV-8.	Rough Mare power spectral density versus frequency . . .	4-19
IV-9.	Hummocky Upland power spectral density versus frequency . . . . .	4-20
IV-10.	Rough Upland power spectral density versus frequency . .	4-21
IV-11.	Cumulative frequency and relief of craters for various age groups that occur on the smooth Mare, rough Mare, and Upland terrains . . . . .	4-25
IV-12.	Cumulative crater distribution for smooth Mare, rough Mare, and Upland terrains. . . . .	4-26
IV-13.	Cumulative number of blocks in intercrater region of smooth Mare, rough Mare, and Upland terrains . . . . .	4-28
IV-14.	Percent of intercrater area of smooth Mare, rough Mare, and Upland terrains which are covered by blocks . . . . .	4-29
IV-15.	Cumulative distribution of blocks between crater rim and two crater radii as seen around craters in smooth Mare, rough Mare, and Upland terrains. . . . .	4-30
IV-16.	Percent of area covered by blocks between crater rim and two crater radii as seen around craters in smooth Mare, rough Mare, and Upland terrains. . . . .	4-30
IV-17.	Temperatures nearest surface for different thermal parameter values . . . . .	4-35
IV-18.	Angles used in directionality analysis . . . . .	4-36

## LIST OF ILLUSTRATIONS (Continued)

Figure	Title	Page
IV-19.	Brightness temperature versus observer's elevation angle to the surface with the sun at different elevation angles . . . . .	4-37
IV-20.	Photometric model geometry; (a) geometry, (b) positive and negative $\alpha$ . . . . .	4-43
IV-21.	Variation of photometric function with phase angle $g$ and angle $\alpha$ . . . . .	4-44
IV-22.	Variation of photometric function with angle $\alpha$ and phase angle $g$ . . . . .	4-44
IV-23.	Polarization of lunar surface as a function of phase angle $g$ . . . . .	4-46
V-1.	Range of temperatures between dark and sunlit profiles versus altitude for the Mercury upper density limit model. . . . .	5-3
V-2.	Dark and sunlit model profiles of density and pressure versus altitude for upper density limit atmospheres . . . .	5-9
V-3.	The range of brightness temperature $T_B$ for Mercury. . .	5-16
V-4.	Map of the surface features of Mercury from Carmichel and Dollfus . . . . .	5-24
V-5.	Roughness of Mercury's surface, given by the power spectral density of the elevation as a function of the wave number . . . . .	5-28
V-6.	Variation of mean slope of Mercury's surface with horizontal base length . . . . .	5-29
V-7.	Relative distribution of slopes on Mercury's surface for use with Figure 8. . . . .	5-30

## LIST OF ILLUSTRATIONS (Continued)

Figure	Title	Page
V-8.	Number per unit area of blocks, particles, and craters larger than specified characteristic size for the surface of Mercury . . . . .	5-32
V-9.	Fraction of surface area covered by blocks and particles larger than specified characteristic size for the surface of Mercury . . . . .	5-33
VI-1.	Altitude versus temperature for Venus atmosphere . . . .	6-2
VI-2.	Altitude versus molecular weight for Venus atmosphere . . . . .	6-3
VI-3.	A model for the Venus ionosphere . . . . .	6-8
VII-1.	Altitude versus temperature for Mars atmosphere . . . .	7-4
VII-2.	Altitude versus molecular weight for Mars atmosphere . . . . .	7-11
VII-3.	Electron number-density distributions measured by Mariners 4, 6, and 7 . . . . .	7-17
VII-4.	Calculated mean zonal (east-west) component of wind near surface (at top of boundary layer) . . . . .	7-21
VII-5.	Power spectral density function band for Martian surface. . . . .	7-29
VII-6.	Mars topographical variation from radar measurements centered about four latitudes . . . . .	7-31
VII-7.	Comparisons of Martian and Lunar size distributions: (a) comparison of large craters on Mars with those on the Lunar Uplands, and (b) comparison of small craters on Mars with those on the Lunar Maria . . . . .	7-32

## LIST OF ILLUSTRATIONS (Continued)

Figure	Title	Page
VII-8.	Size-frequency distribution on the undisturbed surface . .	7-33
VII-9.	Seasonal mean surface temperatures on Mars . . . . .	7-39
VII-10.	Daily temperature variation of surface of Mars at the equator . . . . .	7-40
VIII-1.	Pressure versus temperature for the Jupiter model atmospheres . . . . .	8-8
VIII-2.	Pressure versus density and cloud masses at cloud bases for the Jupiter model atmospheres . . . . .	8-8
VIII-3.	Pressure versus altitude for the Jupiter model atmospheres . . . . .	8-9
VIII-4.	Temperature versus altitude for the Jupiter model atmospheres . . . . .	8-10
VIII-5.	Density versus altitude and cloud masses at cloud bases for the Jupiter model atmospheres . . . . .	8-11
VIII-6.	Ranges of geometric albedo and disk brightness temperature as functions of wavelength . . . . .	8-18
VIII-7.	Schematic volume for the calculation of the brightness temperature, $T_{BS}$ , of Jupiter's synchrotron emission source . . . . .	8-19
VIII-8.	Typical values of geometric albedo $p$ and disk brightness temperature $T_{BD}$ , taken from Table VIII-8. . . . .	8-24
A-1.	Prediction of sunspot numbers (using data available in October 1971) . . . . .	A-7
B-1.	Four temperature profiles from the present models . . . .	B-2

## LIST OF ILLUSTRATIONS (Concluded)

Figure	Title	Page
B-2.	Atmospheric composition for three values of the exospheric temperature. . . . .	B-3
B-3.	Density profiles for seven values of the exospheric temperature . . . . .	B-4
B-4.	Ten-day means of the densities obtained from the drag of the Explorer 1 satellite compared with variations in the 10.7-cm solar flux. . . . .	B-5
B-5.	Densities obtained from the drag of the Explorer 1 satellite compared with variations in the 10.7-cm solar flux . . . . .	B-6
B-6.	Exospheric isotherms ( $^{\circ}$ K) above the globe, for the case when the minimum temperature is $1000^{\circ}$ K. . . . .	B-7
B-7.	Atmospheric temperatures obtained on November 30, 1967, by Carru and Waldteufel by use of Thomson-scatter techniques, compared with temperatures predicted by the present models for a height of 3000 km (solid line) . . . . .	B-8
B-8.	The semiannual density variation as derived from drag analysis on Satellite 1966 44 A (Explorer 32) . . . . .	B-9
B-9.	The geomagnetic effect as derived from the drag of six satellites in May and June 1967. . . . .	B-10
B-10.	Observed and computed density variations caused by the helium migration, as derived from the drag on Satellite 1963 53A (Explorer 10). . . . .	B-11



# LIST OF TABLES

Table	Title	Page
I-1.	Total Estimated Solar Flare Doses by Event for 10 Shielding Configurations . . . . .	1- 5
I-2.	Solar Spectral Irradiance at 1 AU (Solar Constant of $135.30 \text{ mWcm}^{-2}$ ) . . . . .	1- 6
I-3.	Orbital Elements for Major Meteor Streams . . . . .	1-18
I-4.	Orbital Elements for Some Asteroids . . . . .	1-19
I-5.	Comets . . . . .	1-20
II-1.	Major Meteoroid Streams . . . . .	2-38
IV-1.	Large-Scale Slopes and Other Data For Lunar Features . . . . .	4-22
IV-2.	Idealized Crater Shapes in Relation to Their Morphology . . . . .	4-24
IV-3.	Soil Parameters . . . . .	4-32
IV-4.	Fourier Series Coefficients . . . . .	4-34
IV-5.	Lunar Surface Thermal Properties . . . . .	4-39
IV-6.	Normal Albedo Values of Front and Back Faces of the Moon . . . . .	4-41
IV-7.	Normal Albedo for Selected Lunar Features . . . . .	4-42
V-1.	Summary of Spectroscopic Results for Mercury . . . . .	5- 5
V-2.	Mercury Upper Density Limit Atmospheric Models . . . . .	5- 8
V-3.	Photometric Parameters for the Sun, Moon, and Planets . . . . .	5-12
V-4.	Infrared Observations of Mercury Interpreted as Surface Temperatures . . . . .	5-14

## LIST OF TABLES (Continued)

Table	Title	Page
V- 5.	Electromagnetic Radiation Near Mercury . . . . .	5-15
V- 6.	Summary of Mercury's Radio Brightness Temperature Measurements . . . . .	5-18
V- 7.	Radar Investigations of Mercury . . . . .	5-25
V- 8.	Soil Mechanics Properties for Mercury . . . . .	5-27
V- 9.	Electromagnetic Properties of Mercury's Surface Layers . . . .	5-34
V-10.	Thermal Parameter Ranges for Mercury Cited in Literature . .	5-36
VI- 1.	Mean Venus Model Atmosphere . . . . .	6- 5
VI- 2.	Minimum Venus Model Atmosphere . . . . .	6- 6
VI- 3.	Maximum Venus Model Atmosphere . . . . .	6- 7
VII-1.	Mean Mars Model Atmosphere . . . . .	7- 6
VII-2.	Minimum Mars Model Atmosphere . . . . .	7- 7
VII-3.	Maximum Mars Model Atmosphere . . . . .	7- 8
VII-4.	Observed and Assumed Constituents of the Martian Atmosphere . . . . .	7-10
VII-5.	Martian Clouds . . . . .	7-19
VII-6.	Mechanical Properties of Martian Surface . . . . .	7-35
VII-7.	Data Summary for Satellites of Mars . . . . .	7-42
VIII-1.	Compositions and Other Parameters for Model Atmospheres of Jupiter . . . . .	8- 2

## LIST OF TABLES (Concluded)

Table	Title	Page
VIII- 2.	Values at Selected Pressures for Nominal Model Atmosphere of Jupiter . . . . .	8- 5
VIII- 3.	Values of Physical Quantities at Selected Pressures for Cool, Dense Model Atmosphere of Jupiter . . . . .	8- 6
VIII- 4.	Values at Selected Pressures for Warm, Extended Model Atmosphere of Jupiter . . . . .	8- 7
VIII- 5.	Electromagnetic Radiation Parameters Near Jupiter With Maximum Illumination . . . . .	8-17
VIII- 6.	Magnitudes and Colors for Satellites of Jupiter and Planets . . . . .	8-20
VIII- 7.	Thermal Radiation Parameters Below the Tropopause in Jupiter's Atmosphere . . . . .	8-21
VIII- 8.	Observed Geometric Albedos for Jupiter . . . . .	8-23
VIII- 9.	Properties of Jupiter's Satellites . . . . .	8-26
IX- 1.	Data Summary for Satellites of Saturn . . . . .	9- 4
X- 1.	Data Summary for Satellites of Uranus . . . . .	10- 3
XI- 1.	Data Summary for Satellites of Neptune . . . . .	11- 2
A- 1.	Prediction of Sunspot Numbers, Solar Flux and Geomagnetic Index (Using Data Available in December 1971) . . . . .	A- 2
A- 2.	Mean and Standard Deviation of Sunspot Numbers and 10.7-cm Solar Flux . . . . .	A- 8

## FOREWORD

This document provides information relative to the natural environment for altitudes greater than 90 km above the surface of the earth. NASA Technical Memorandum TM X-64589, entitled, "Terrestrial Environment (Climatic) Criteria Guidelines for Use in Space Vehicle Development, 1971 Revision," dated May 10, 1971, provides natural environment information for altitudes below 90 km.

Contractural work that was begun before the distribution of this document should not be altered on the basis of revised data contained herein without prior approval of the responsible NASA contracting officer's representative. If the data in this document and TM X-64589 are not sufficient for application to a design or operational planning problem, then the user should submit a request to the appropriate NASA organization for the required information. Users under contract to the Marshall Space Flight Center should submit a request through appropriate MSFC contracting office channels to the Aerospace Environment Division of the Aero-Astroynamics Laboratory.

This document, which supersedes all editions of TMX-53957, entitled "Space Environment Criteria Guidelines for Use in Space Vehicle Development, 1969 Revision," is recommended for use in the development of space vehicles and associated equipment, unless otherwise stated in contract specifications.

## SUMMARY

This document provides a consolidated presentation of natural environment data for use as design criteria guidelines in space vehicle development programs.

Specifically, information is provided in the disciplinary areas of atmospheric and ionospheric properties, radiation, solar cycle predictions, geomagnetic field, astrodynamic constants, and meteoroids for the earth's atmosphere above 90 km, interplanetary space, and the atmospheres and surfaces (when available) of the moon and the planets (other than earth) of this solar system. The current MSFC upper atmosphere model and solar cycle prediction routines are described in detail.

In compiling this document, extensive use has been made of the technical contributions and review comments furnished by personnel at the Marshall Space Flight Center, the Manned Spacecraft Center, other NASA centers, and other government agencies.

## INTRODUCTION

Much of the space and planetary environmental data available today are speculative, and will remain so until additional satellites, planetary probes, and manned space flights provide more information. Considerable care must therefore be used in the interpretation and use of available space environment data for a specific design decision. Although the data in this document provide valuable guides for preliminary design studies and analyses, their use for final program decisions depends upon the specific design problem involved. When a design problem area requiring specific space environment data is identified, the contractor should contact the appropriate government agency for concurrence on the specific environmental criteria to be employed. This report was prepared primarily for use in NASA space vehicle development and advanced study projects. The data contained in this document are reviewed on a continuing basis, and revisions or amendments will be published as necessary. The numbers given in brackets refer to references given at the end of each section.

Based on known and projected user requirements, it was decided that it is more advantageous to present the natural environment parameters grouped according to spatial regions rather than scientific disciplinary areas. These spatial areas are interplanetary space and the spheres of influence surrounding the individual planets and the earth's moon. The outer limit of these spheres of influence depends upon the component of the environment being discussed. For clarity in discussion, limits for these spheres have been arbitrarily taken to be 10 radii above the surface of the planet or moon. In the discussion of the meteoroid environment, however, the spheres of influence extend to a point where the gravitational attraction of the planet or moon becomes negligible.

MSFC personnel responsible for the development and/or coordination of the data contained herein are listed by disciplinary area below:

Scientific Area	MSFC
Earth Upper Atmospheric Gas Properties ( > 90 km)	R. E. Smith G. Swenson
Ionosphere	R. E. Smith
Radiation (earth)	M. Burrell J. Wright
Thermal Radiation	P. Craven A. Gary
Meteoroids	S. Clifton
Geomagnetic and Geopotential Fields	H. Euler
Solar Cycle Predictions	H. Euler J. Scissum
Astrodynamic Constants	H. Euler
Planetary Atmospheres	G. West O. H. Vaughan
Lunar and Planetary Surface Environment	O. H. Vaughan N. Costes B. Jones

# SPACE AND PLANETARY ENVIRONMENT CRITERIA GUIDELINES FOR USE IN SPACE VEHICLE DEVELOPMENT (1971 REVISION)

## SECTION I. INTERPLANETARY SPACE ENVIRONMENT

### 1.1 Definition

Interplanetary space is defined as the region from the sun to the outer limits of the solar system, exclusive of those spheres under the influence of the individual planetary systems.

### 1.2 Gas Properties

The sun is coupled to the environments of the planets through the interplanetary medium. The sun's varying input to this medium and its impact on solar wind particle radiation and plasma flow is of primary concern. For design purposes, the following gas properties should be employed.

#### 1.2.1 Kinetic Gas Temperature

Approximately  $2 \times 10^5$  °K.

#### 1.2.2 Gas Pressure

Approximately  $10^{-10}$  dynes/cm<sup>2</sup>.

#### 1.2.3 Density

Approximately  $10^{-23}$  gm/cm<sup>3</sup>.

#### 1.2.4 Composition

The composition of interplanetary space is primarily hydrogen, protons, helium, and alpha particles.

### 1.3 Radiation Environment

A spacecraft on an interplanetary trajectory is constantly exposed to charged and uncharged particles and to photons. When an encounter occurs,

a charge transfer to or from the body will occur. This mechanism of charge transfer can be classified as either charge collection or charge emission. The latter consists of processes such as photoemission, secondary emission (caused by impingement of energetic particles on the body), thermal emission, and field emission. The most important processes for the regions of space are the collection of environmental electrons and ions, photoemission, and secondary emission. There are other, less important charging mechanisms, such as cosmic rays, collisions with dust grains, and the thermal and field emissions.

A distinction should be made in the charge buildup process between highly energetic particles and lower energy, thermal particles in that the latter are influenced by the spacecraft charge present whereas the former are essentially unaffected by spacecraft charge. It is also noted that the production of electrons by photoemission and secondary emission is dependent on the target material and perhaps even the cleanliness of the material (presence of oxides).

#### 1.3.1 Galactic Cosmic Radiation

Composition:

~ 85 percent proton ( $H^+$ )

~ 13 percent alpha particles ( $He^{++}$ )

~ 2 percent nuclei of elements  $Li \rightarrow Fe$

(in approximate cosmic abundance) .

Flux at sunspot minimum:  $\sim 4$  protons/cm<sup>2</sup>-s (isotropic) .

Integrated yearly rate:  $\sim 1.3 \times 10^8$  protons/cm<sup>2</sup> .

Flux at sunspot maximum:  $\sim 2.0$  protons/cm<sup>2</sup>-s (isotropic) .

Integrated yearly rate:  $\sim 7 \times 10^7$  protons/cm<sup>2</sup> .

Energy range: 40 MeV to  $10^{13}$  MeV .

Integrated dose (without shielding):  $\sim 4$  to 10 rad/year.

#### 1.3.2 Solar Cosmic Radiation



### 1.3.2.1 Solar High Energy Particle Radiation

Composition: Predominantly of protons ( $H^+$ ) and alpha particles ( $He^{++}$ ) .

Integrated yearly flux at 1 AU:

Energy  $> 30$  MeV,  $N \approx 8 \times 10^9$  protons/cm<sup>2</sup> near solar maximum.

$N \approx 5 \times 10^5$  protons/cm<sup>2</sup> near solar minimum.

Energy  $> 100$  MeV,  $N \approx 6 \times 10^8$  protons/cm<sup>2</sup> near solar maximum.

$N \approx 5 \times 10^4$  protons/cm<sup>2</sup> near solar minimum.

Maximum dosage with shielding of 5 g/cm<sup>2</sup> (equivalent thickness):

$\sim 200$  rad per week ( 3 flares), skin dose at a point detector.

This radiation environment applies for a solar distance of 1.0 AU. Since the dispersion processes acting upon this environmental parameter have not yet been defined, an accurate description of the radiation environment for solar distances of 0.5 and 1.75 AU cannot be provided. A rough estimate may be to scale by  $R^{-2}$  for implied spatial continuity.

#### 1.3.2.1.1 Solar Flare Particle Events

A solar flare is a bright eruption of the sun's chromosphere associated with the release of large amounts of energy into the interplanetary medium.

#### 1.3.2.1.2 Particle Flux Spectrum

The time-integrated spectrum describing the particle flux for a given solar flare particle event is given by

$$J(>P) = N_0 \exp (-P/P_0) ,$$

where

$J(>P)$  = particles/cm<sup>2</sup>-flare having rigidity greater than  $P$ .

$N_0$  = constant determined from  $P_0$  and  $J(>P)$  .

$P_0$  = characteristic rigidity in units of MV.

$P$  = magnetic rigidity in MV, which is related to the particle kinetic energy ( $E$ ) in MeV by

$$P(E) = \frac{\sqrt{E^2 + 2ME}}{q}$$

$q$  = total electron charge ( 1 for protons, 2 for alpha particles)

$M$  = particle rest mass energy (MeV) .

For protons and alpha particles,

$$P \approx \frac{\sqrt{2ME}}{q} = 43.5 \sqrt{E}$$

when

$$E \leq 100 \text{ MeV},$$

and

$$P \approx \frac{E}{q}$$

when

$$E \geq 10^5 \text{ MeV} .$$

#### 1.3.2.1.3 Free Space Dose Rates

The free space dose rates associated with 20 of the more energetic solar flare particle events that have occurred in the past are given in Table I-1 [I-1].

TABLE I-1. TOTAL ESTIMATED SOLAR FLARE DOSES BY EVENT  
FOR 10 SHIELDING CONFIGURATIONS

Date	Shielding Configuration									
	1/0 <sup>a</sup>	2/0	5/0	10/0	20/0	1/5	2/5	5/5	10/5	20/5
2/23/56	280.00	181.00	91.80	50.20	24.80	64.78	58.00	43.75	30.40	17.90
8/3/56	8.50	5.00	2.20	1.00	0.40	1.39	1.21	0.85	0.53	0.27
1/20/57	122.00	43.50	8.30	1.80	0.30	3.42	2.57	1.23	0.46	0.11
8/29/57	77.00	25.10	4.20	0.80	0.10	1.63	1.20	0.54	0.19	0.04
10/20/57	18.50	10.30	4.10	1.80	0.70	2.53	2.17	1.46	0.88	0.41
3/23/58	148.00	53.60	10.90	2.50	0.40	4.67	3.55	1.75	0.69	0.17
7/7/58	150.00	53.70	10.50	2.30	0.40	4.38	3.30	1.60	0.61	0.15
8/16/58	23.70	8.60	1.80	0.40	0.10	0.75	0.57	0.28	0.11	0.03
8/22/58	45.00	14.90	2.50	0.50	0.10	0.96	0.71	0.32	0.11	0.02
8/26/58	75.00	23.10	3.40	0.50	0.10	1.19	0.85	0.36	0.11	0.02
5/10/59	470.00	211.10	59.30	18.30	4.40	30.18	24.28	13.60	6.70	2.10
7/10/59	420.00	214.00	73.20	27.40	8.40	41.56	34.65	21.76	11.84	4.80
7/14/59	650.00	284.50	75.90	22.30	5.00	37.56	30.00	16.75	7.80	2.50
7/16/59	382.00	194.80	67.20	25.30	7.80	38.30	31.98	20.16	11.03	4.50
9/3/60	13.00	7.20	2.90	1.20	0.50	1.77	1.52	0.10	0.06	0.03
11/12/60	484.00	269.60	105.50	44.90	16.20	64.53	55.12	36.87	21.83	10.05
11/15/60	288.00	151.90	55.90	22.40	7.50	30.04	7.91	18.14	10.33	4.49
11/20/60	17.30	9.50	3.60	1.50	0.05	2.14	1.82	1.20	0.69	0.31
7/12/61	25.70	8.40	1.40	0.30	0.03	0.54	0.40	0.18	0.06	0.01
7/18/61	128.00	64.20	21.60	8.00	2.40	12.16	10.11	6.30	3.39	1.35

a. Shielding configurations are given as X/Y where x is the shielding thickness in g/cm<sup>2</sup> of aluminum and Y is the shielding thickness in g/cm<sup>2</sup> of tissue.

### 1.3.3 Radiation Properties of the Sun (Thermal)

#### 1.3.3.1 Solar Radiation [I-2]

The solar constant refers to the rate at which energy is received upon a unit surface, oriented perpendicular to the sun's direction, in free space at some mean distance from the sun. The magnitude of the solar constant is determined by integrating the measured spectral irradiance over all wavelengths (see Table I-2 [I-3] for solar spectral irradiance data).

TABLE I-2. SOLAR SPECTRAL IRRADIANCE AT 1 AU  
(SOLAR CONSTANT OF 135.30mWcm<sup>-2</sup>)

Wavelength, $\lambda$ ( $\mu\text{m}$ )	Average Irradiance, $P_\lambda$ (W cm <sup>-2</sup> $\mu\text{m}^{-1}$ ) <sup>a</sup>	Area Under Curve, 0 to $\lambda$ , $A_\lambda$ (mW cm <sup>-2</sup> )	Portion of Solar Constant with Wavelength < $\lambda$ , $D_\lambda$ (%)
0.120	0.000010	0.00059993	0.00044
0.140	0.000003	0.00073000	0.00054
0.150	0.000007	0.00072000	0.00058
0.160	0.000023	0.00093000	0.00069
0.170	0.000063	0.00135000	0.00101
0.180	0.000125	0.00230000	0.00170
0.190	0.000271	0.00428000	0.00316
0.200	0.00107	0.010985	0.0081
0.210	0.00229	0.027785	0.0205
0.220	0.00575	0.067985	0.0502
0.225	0.00649	0.098585	0.0729
0.230	0.00667	0.131485	0.0972
0.235	0.00593	0.162985	0.1205
0.240	0.00630	0.193560	0.1430
0.245	0.00723	0.227385	0.1681
0.250	0.00704	0.263060	0.1944
0.255	0.0104	0.306660	0.2267
0.260	0.0130	0.365160	0.270
0.265	0.0185	0.443910	0.328
0.270	0.0232	0.548160	0.405

TABLE I-2. (Continued)

Wavelength, $\lambda$ ( $\mu\text{m}$ )	Average Irradiance, $P_\lambda$ ( $\text{W cm}^{-2} \mu\text{m}^{-1}$ ) <sup>a</sup>	Area Under Curve, 0 to $\lambda$ , $A_\lambda$ ( $\text{mW cm}^{-2}$ )	Portion of Solar Constant With Wavelength < $\lambda$ , $D_\lambda$ (%)
0.275	0.0204	0.657160	0.486
0.280	0.0222	0.763660	0.564
0.285	0.0315	0.897910	0.644
0.290	0.0482	0.09716	0.811
0.295	0.0584	1.36366	1.008
0.300	0.0514	1.63816	1.211
0.305	0.0603	1.91741	1.417
0.310	0.0689	2.24041	1.656
0.315	0.0764	2.60366	1.924
0.320	0.0830	3.00216	2.219
0.325	0.0975	3.45341	2.552
0.330	0.1059	3.96191	2.928
0.335	0.1081	4.49691	3.324
0.340	0.1074	5.03566	3.722
0.345	0.1069	5.57141	4.118
0.350	0.1093	6.11191	4.517
0.355	0.1083	6.65591	4.919
0.360	0.1068	7.19366	5.317
0.365	0.1132	7.74366	5.723
0.370	0.1181	8.32191	6.151
0.375	0.1157	8.90641	6.583
0.380	0.1120	9.47566	7.003
0.385	0.1098	10.0302	7.413
0.390	0.1098	10.5792	7.819
0.395	0.1189	11.1509	8.242
0.400	0.1429	11.8054	8.725
0.405	0.1644	12.5737	9.293
0.410	0.1751	13.4224	9.920
0.415	0.1774	14.3037	10.572
0.420	0.1747	15.1839	11.222
0.425	0.1693	16.0439	11.858
0.430	0.1639	16.8769	12.474
0.435	0.1663	17.7024	13.084
0.440	0.1810	18.5707	13.726
0.445	0.1922	19.5037	14.415

TABLE I-2. (Continued)

Wavelength, $\lambda$ ( $\mu\text{m}$ )	Average Irradiance, $P_\lambda$ ( $\text{W cm}^{-2} \mu\text{m}^{-1}$ ) <sup>a</sup>	Area Under Curve, 0 to $\lambda$ , $A_\lambda$ ( $\text{mW cm}^{-2}$ )	Portion of Solar Constant With Wavelength $< \lambda$ , $D_\lambda$ (%)
0.450	0.2006	20.4857	15.141
0.455	0.2057	21.5014	15.892
0.460	0.2066	22.5322	16.653
0.465	0.2048	23.5607	17.414
0.470	0.2033	24.5809	18.168
0.475	0.2044	25.6002	18.921
0.480	0.2074	26.6297	19.682
0.485	0.1976	27.6422	20.430
0.490	0.1950	28.6237	21.156
0.495	0.1960	29.6012	21.878
0.500	0.1942	30.5767	22.599
0.505	0.1920	31.5422	23.313
0.510	0.1882	32.4927	24.015
0.515	0.1833	33.4214	24.702
0.520	0.1833	34.3379	25.379
0.525	0.1852	35.2592	26.060
0.530	0.1842	36.1827	26.743
0.535	0.1818	37.0977	27.419
0.540	0.1783	37.9979	28.084
0.545	0.1754	38.8822	28.738
0.550	0.1725	39.7519	29.381
0.555	0.1720	40.6132	30.017
0.560	0.1695	41.4669	30.648
0.565	0.1705	42.3169	31.276
0.570	0.1712	43.1712	31.908
0.575	0.1719	44.0289	32.542
0.580	0.1715	44.8874	33.176
0.585	0.1712	45.7442	33.809
0.590	0.1700	46.5972	34.440
0.595	0.1682	47.4427	35.065
0.600	0.1666	48.2797	35.683
0.605	0.1647	49.1079	36.296
0.610	0.1635	49.9284	36.902

TABLE I-2. (Continued)

Wavelength, $\lambda$ ( $\mu\text{m}$ )	Average Irradiance, $P_\lambda$ ( $\text{W cm}^{-2} \mu\text{m}^{-1}$ ) <sup>a</sup>	Area Under Curve, 0 to $\lambda$ , $A_\lambda$ ( $\text{mW cm}^{-2}$ )	Portion of Solar Constant with Wavelength < $\lambda$ , $D_\lambda$ (%)
0.620	0.1602	51.5469	38.098
0.630	0.1570	53.1329	39.270
0.640	0.1544	54.6899	40.421
0.650	0.1511	56.2174	41.550
0.660	0.1486	57.7159	42.658
0.670	0.1456	59.1869	43.745
0.680	0.1427	60.6284	44.810
0.690	0.1402	62.0429	45.856
0.700	0.1369	63.4284	46.880
0.710	0.1344	64.7849	47.882
0.720	0.1314	66.1139	48.865
0.730	0.1290	67.4159	49.827
0.740	0.1260	68.6909	50.769
0.750	0.1235	69.9384	51.691
0.800	0.1107	75.7934	56.019
0.850	0.0988	81.0309	59.890
0.900	0.0889	85.7234	63.358
0.950	0.0835	90.0334	66.544
1.000	0.0746	93.9859	69.465
1.100	0.0592	100.676	74.409
1.200	0.0484	106.056	78.386
1.300	0.0396	110.456	81.638
1.400	0.0336	114.116	84.343
1.500	0.0287	117.231	86.645
1.600	0.0244	119.886	88.607
1.700	0.0202	122.116	90.256
1.800	0.0159	123.921	91.590
1.900	0.0126	125.346	92.643
2.000	0.0103	126.491	93.489
2.100	0.0090	127.456	94.202
2.200	0.0079	128.301	94.827
2.300	0.0068	129.036	95.370

TABLE I-2. (Continued)

Wavelength, $\lambda$ ( $\mu\text{m}$ )	Average Irradiance, $P_\lambda$ ( $\text{W cm}^{-2} \mu\text{m}^{-1}$ ) <sup>a</sup>	Area Under Curve, 0 to $\lambda$ , $A_\lambda$ ( $\text{mW cm}^{-2}$ )	Portion of Solar Constant with Wavelength $< \lambda$ , $D_\lambda$ (%)
2.400	0.0064	129.696	95.858
2.500	0.0054	130.286	96.294
2.600	0.0048	130.796	96.671
2.700	0.0043	131.251	97.007
2.800	0.00390	131.661	97.3104
2.900	0.00350	132.031	97.5838
3.000	0.00310	132.361	97.8277
3.100	0.00260	132.646	98.0384
3.200	0.00226	132.889	98.2180
3.300	0.00192	133.098	98.3724
3.400	0.00166	133.277	98.5047
3.500	0.00146	133.433	98.6200
3.600	0.00135	133.573	98.7239
3.700	0.00123	133.702	98.8192
3.800	0.00111	133.819	98.9057
3.900	0.00103	133.926	98.9848
4.000	0.00095	134.025	99.0580
4.100	0.00087	134.116	99.1252
4.200	0.00078	134.199	99.1862
4.300	0.00071	134.273	99.2412
4.400	0.00065	134.341	99.2915
4.500	0.00059	134.403	99.3373
4.600	0.00053	134.459	99.3787
4.700	0.00048	134.510	99.4160
4.800	0.00045	134.556	99.4504
4.900	0.00041	134.559	99.482195
5.000	0.0003830	134.63906	99.511500
6.000	0.0001750	134.91806	99.717709
7.000	0.0000990	135.05506	99.818965
8.000	0.0000600	135.13456	99.877724
9.000	0.0000380	135.18356	99.913939
10.000	0.0000250	135.21506	99.937221
11.000	0.0000170	135.23606	99.952742
12.000	0.0000120	135.25056	99.963459



TABLE I-2. (Concluded)

Wavelength, $\lambda$ ( $\mu\text{m}$ )	Average Irradiance, $P_\lambda$ ( $\text{W cm}^{-2}\mu\text{m}^{-1}$ ) <sup>a</sup>	Area Under Curve, 0 to $\lambda$ , $A_\lambda$ ( $\text{mW cm}^{-2}$ )	Portion of Solar Constant with Wavelength < $\lambda$ , $D_\lambda$ (%)
13.000	0.0000087	135.26091	99.971109
14.000	0.0000055	135.26801	99.976356
15.000	0.0000049	135.27321	99.980200
16.000	0.0000038	135.27756	99.983415
17.000	0.0000031	135.28101	99.985965
18.000	0.0000024	135.28376	99.987997
19.000	0.0000020	135.28596	99.989623
20.000	0.0000016	135.28776	99.990953
25.000	0.000000610	135.29328	99.995037
30.000	0.000000300	135.29556	99.996718
35.000	0.000000160	135.29671	99.997568
40.000	0.000000094	135.29735	99.998038
50.000	0.000000038	135.29801	99.998525
60.000	0.000000019	135.29829	99.998736
80.000	0.000000007	135.29855	99.998928
100.000	0.000000003	135.29865	99.999002
1000.000	0.000000000	135.30000	100.000000

a. Spectral irradiance averaged over small bandwidth centered at  $\lambda$ : 0.3 to 0.75  $\mu\text{m}$  (bandwidth, 100  $\text{\AA}$ ); 0.75 to 1.0  $\mu\text{m}$  (bandwidth, 500  $\text{\AA}$ ); and 1.0 to 5.0  $\mu\text{m}$  (bandwidth, 1000  $\text{\AA}$ ).

Solar constant at 1.0 AU:  $1353 \pm 13.5 \text{ W/m}^2$ ;  $1.94 \pm 0.02 \text{ cal/cm}^2/\text{min}$ ; and variation with distance from sun follows  $R^{-2}$  relation.

Perihelion to aphelion variation of the solar constant is 3.43 to -3.26 percent. For example, solar constant in space equals solar constant at 1 AU/ $R^2$  where  $R$  is the distance from the sun in AUs.

### Solar Irradiance at the Distance of Semi-major Axis for the Nine Planets

Planet	Solar Constant	W-m <sup>-2</sup>
Mercury	6.6735	9029
Venus	1.9113	2586
Earth	1.000	1353
Mars	0.4307	582.8
Jupiter	0.03695	49.9
Saturn	0.01099	14.87
Uranus	0.002718	3.678
Neptune	0.001106	1.496
Pluto	0.000643	0.870

The mean brightness of solar disk outside the atmosphere is  $6.33 \times 10^5$  Lamberts or  $2.015 \times 10^9$  candles/m<sup>2</sup>. Solar illumination is  $(1.37 \times 10^5) R^{-2}$  lumens/m<sup>2</sup> where R is the distance from the sun (AU).

#### 1.3.3.1.1 Visible and Infrared Radiation [I-2, I-4]

Radiant energy distribution:

Approximated by that from a 5800 °K blackbody.

Fraction of solar radiation:

Above 7000 Å = 53.12 percent.

Above 4000 Å ~ 91.28 percent.

3000 Å - 30 000 Å = 96.62 percent.

### 1.3.3.1.2 Ultraviolet and X-Ray Radiation [I-2]

Fraction of solar radiation:

Below 4000 Å = 8.72 percent.

Below 3000 Å = 1.21 percent.

Below 2000 Å = 0.008 percent (variable).

Below 1000 Å =  $10^{-4}$  percent (variable).

Principle line emission fluxes at 1.0 AU:

Lyman Alpha HI (1215.67Å):  $51.0 \times 10^{-4} \text{ W/m}^2$

HE II (303.8Å):  $2.5 \times 10^{-4} \text{ W/m}^2$

HI (1025.72Å):  $0.60 \times 10^{-4} \text{ W/m}^2$

C III (977Å):  $0.50 \times 10^{-4} \text{ W/m}^2$ .

X-ray flux:

	2 to 8 Å	8 to 20 Å	20 to 200 Å
Sunspot min (quiet sun)	$3 \times 10^{-9} \text{ W/m}^2$	$4 \times 10^{-7} \text{ W/m}^2$	$1.3 \times 10^{-4} \text{ W/m}^2$
Sunspot max (quiet sun)	$2 \times 10^{-6} \text{ W/m}^2$	$2.3 \times 10^{-5} \text{ W/m}^2$	$1.0 \times 10^{-3} \text{ W/m}^2$
Upper limit during flare activity	$2.2 \times 10^{-4} \text{ W/m}^2$	$4.5 \times 10^{-4} \text{ W/m}^2$	$92 \times 10^{-4} \text{ W/m}^2$

Strength of line emission flux varies as  $R^{-2}$ ; e.g., flux in space is flux at 1.0 AU/ $R^2$  where  $R$  is the solar distance (AU).

#### 1.3.3.1.3 Solar Radiation Pressure

Pressure on a flat plate at 1.0 AU:

For 100 percent reflecting body =  $9.02 \times 10^{-6} \text{ N/m}^2$ .

For blackbody =  $4.51 \times 10^{-6} \text{ N/m}^2$ .

Radiation pressure on a flat plate variation with solar distance follows the relation:

$P = S/c$  for blackbody

$P = 2 S/c$  for 100 percent reflecting body

where

$P$  = radiation pressure,

$S$  = solar constant at specified solar distance,

and

$c$  = speed of light.

#### 1.3.3.1.4 Solar Wind

Mean Density:

0.5 AU =  $\sim 20$  hydrogen atoms/cm<sup>3</sup>

1.0 AU =  $\sim 5$  hydrogen atoms/cm<sup>3</sup>

1.75 AU =  $\sim 2$  hydrogen atoms/cm<sup>3</sup>

Mean Flux:

0.5 AU =  $\sim 8 \times 10^8$  hydrogen atoms/cm<sup>2</sup>/s

1.0 AU =  $\sim 2 \times 10^8$  hydrogen atoms/cm<sup>2</sup>/s

1.75 AU =  $\sim 10^8$  hydrogen atoms/cm<sup>2</sup>/s.

Mean velocity of solar wind from 0.5 to 1.75 AU is 450 to 500 km/s.

#### 1.3.4 Solar Radio Noise

Noise power flux =  $\frac{(4.5 \times 10^{-31}) (f)^{1.1}}{R^2}$  W/m<sup>2</sup>/Hz, where f is frequency (Hz) and R is astronomical units distance from sun.

Approximate noise power at 1.0 AU, quiet sun: 10<sup>-19</sup> W/m<sup>2</sup>/Hz at 1.0 cm wavelength to 10<sup>-22</sup> W/m<sup>2</sup>/Hz at 400 cm wavelength.

During solar storms, noise power may increase from 1 to 8 orders of magnitude. The variation with sunspots is greatest between 6- to 200-cm wavelengths, with the spectral power showing a range of variation of 4 orders of magnitude.

##### 1.3.4.1 Characteristics of Solar Radio Noise [III-5]

Type	Identifying Characteristics	Source Characteristics	Frequency Characteristics
I	Noise storms usually lasting from hours to days; or bursts of ~ 1 s duration.	Assumed to be of a nonthermal origin, associated with sunspots, "R centers," and sometimes flares.	Less than ~ 250 MHz with bandwidth 1 to 10 MHz/s for bursts and 10 to 100 MHz/s for continuum. The intensity at 100 MHz/s, 10 <sup>-21</sup> to 10 <sup>-19</sup> W/m <sup>2</sup> (Hz/s).
II	Bursts with slow drift of ~ 0.3 MHz/s <sup>2</sup> lasting from 5 to 10 min.	Source is due to plasma oscillations associated with flares. Occurrence begins about 7 min after flare. The source moves outward at ~ 1000 km/s.	Mainly less than 150 MHz/s with the bandwidth of about 2 × 10 <sup>-1</sup> of the observed frequency. Intensity usually at 100 MHz/s, 10 <sup>-20</sup> to 10 <sup>-19</sup> W/m <sup>2</sup> (Hz/s).

Type	Identifying Characteristics	Source Characteristics	Frequency Characteristics
III	Bursts with fast drift of $\sim 0.3 \text{ MHz/s}^2$ lasting singly 3-10 s or in groups of 1 to 5 min.	Assumed to be associated with plasma oscillation associated 50-60% of the time with flares. The source has an outward velocity of $\sim 10^5 \text{ km/s}$ .	Ranges from $< 4000 \text{ MHz/s}$ to $> 10 \text{ MHz/s}$ with a bandwidth almost equal to the frequency. The intensity usually is less than $10^{-20} \text{ W/m}^2 (\text{Hz/s})$ .
IV	Smooth continuum lasting from minutes to hours.	Source is due to synchrotron radiation. Occurring 70 to 80% of the time with flares at $\sim 15 \text{ min}$ after start. Initial source velocity ranges from $1 \text{ to } 5 \times 10^3 \text{ km/s}$ for about 10 min and then source becomes stationary.	Cover the complete radio band but vary from burst to burst. The bandwidth is frequently several octaves with intensities from $10^{-20}$ to $10^{-19} \text{ W/m}^2 (\text{Hz/s})$ .
V	Smooth continuum lasting from 1 to 2 min.	Synchrotron radiation occurring before the maximum of solar flares. The velocity of the source is $\sim 5 \times 10^3 \text{ km/s}$ .	Frequencies less than $200 \text{ MHz/s}$ with a bandwidth of several MHz/s at $50 \text{ to } 100 \text{ MHz/s}$ . Intensities, $10^{-20}$ to $10^{-19} \text{ W/m}^2 (\text{Hz/s})$ .
Micro-wave	Continuum and bursts lasting 0.5 to 20 min.	Assumed to be of synchrotron and possibly thermal origin associated about 80% of the time with flares.	The frequency range is $\sim 1000 \text{ to } 20\,000 \text{ MHz/s}$ with a bandwidth of several octaves. The intensity is usually $\sim 5 \times 10^{-22}$ to $5 \times 10^{-20} \text{ W/m}^2 (\text{Hz/s})$ at $3000 \text{ MHz/s}$ .

### 1.3.5 Additional Information

Additional information relative to the interplanetary radiation environment is given in References I-1, I-3, I-6, I-7, and I-8.

## 1.4 Meteoroids, Asteroids, and Comets

Major meteor streams, asteroids, and comets are listed in Tables I-3, I-4, and I-5.

### 1.4.1 Cometary Meteoroids

#### 1.4.1.1 Spatial Density

The spatial density of cometary meteoroids is expressed mathematically as follows: For  $10^{-6} \leq m \leq 10^2$ ,

$$\log S_c = -18.173 - 1.213 \log m - 1.5 \log R - 0.869 |\sin \beta| ,$$

and for  $10^{-12} \leq m \leq 10^{-6}$ ,

$$\begin{aligned} \log S_c = & -18.142 - 1.584 \log m - 0.063 (\log m)^2 \\ & - 1.5 \log R - 0.869 \sin \beta . \end{aligned}$$

Spatial density is related to flux on a randomly tumbling surface by

$$F_c = \frac{1}{4} S_c V_c$$

where

$S_c$  = number of cometary meteoroids of mass  $m$  or greater per  $m^3$ .

$m$  = mass of the meteoroid in grams.

$F_c$  = number of cometary meteoroids of mass  $m$  or greater per  $m^2/s$ .

$R$  = distance from the sun in AUs.

TABLE I-3. ORBITAL ELEMENTS FOR MAJOR METEOR STREAMS [I-9]

Name	Period of Activity	Date Max.	F <sub>max</sub>	$\Omega$ (deg)	$\pi$ (deg)	$\omega$ (deg)	i (deg)	$\epsilon$	q (AU)	a (AU)	Velocity		Period (Years)
											Geocentric (km/s)	Heliocentric (km/s)	
Quadrantids <sup>a</sup>	Jan. 2-4	Jan 3	8.0	282	92	166	67	0.46	0.97	1.7	42	39	13
Lyrid	April 19-22	April 21	0.85	30.5	--	210	81	0.88	0.90	---	48	40	19.8
$\eta$ - Aquarid	May 1-8	May 4-6	2.2	45	152	108	162	0.96	0.66	17.95	64	41	11
$\theta$ - Cetid	May 14-23	May 14-23	2.0	238	89	211	34	0.91	0.11	1.3	37	33	1.5
Arietid	May 29-June 19	June 6	4.5	77	106	29	21	0.94	0.09	1.6	38	34	1.8
$\zeta$ - Perseid	June 1-16	June 6	3.0	78	--	59	$4 \pm 2$	0.79	0.35	1.6	29	35	2.2
$\beta$ - Taurids	June 24-July 5	June 28	2.0	276	$162 \pm 4$	$246 \pm 4$	$9 \pm 4$	0.86	0.36	2.5	31	37	3.3
$\delta$ - Aquarid	July 26-Aug. 5	July 28	1.5	305	$101 \pm 2$	$156 \pm 2$	$24 \pm 5$	0.96	0.08	1.8	40	35	3.6
Perseid	July 15-Aug. 18	Aug. 10-14	5.0	142	--	155	114	0.96	0.97	23.0	60	42	109.5
Giacobinid <sup>a</sup>	Oct. 9-10	Oct. 10	20.0	196	--	172	30.8	0.72	0.99	3.5	23	41	6.57
Orionid	Oct. 15-25	Oct. 20-23	1.2	29.3	103	87.8	163	0.92	0.54	6.32	66	41.5	--
Arietid, Southern	Oct. - Nov.	Nov. 5	1.1	27	150	122	6	0.85	0.30	1.91	28	36	2.64
Taurids, Northern	Oct. 26-Nov. 22	Nov. 10	0.4	221	160	308	2.5	0.86	0.31	2.16	29	37	3.2
Taurids, Night	Nov.		1.0	220	160	300	3	0.86	0.3	2.1	37	37	3.3
Taurids, Southern	Oct. 26-Nov. 22	Nov. 5	0.9	45	157	112	5.1	0.85	0.36	2.39	28	38	3.69
Leonid <sup>a</sup>	Nov. 15-20	Nov. 16-17	0.9	234	49	179	162	0.92	0.99	12.8	72	41	33.25
Bielids <sup>a</sup>	Nov. 15-Dec. 6		2.5	250	109	223	13	0.76	0.88	3.6	16	39.5	6.6
Geminid	Nov. 25-Dec. 17	Dec. 12-13	4.0	261	--	324	24	0.90	0.14	1.4	35	35	1.7
Ursids	Dec. 20-24	Dec. 22	2.5	270	--	210	$5 \pm 3$	1.0	0.92	--	37	42	--

a. Periodic streams



TABLE I-4. ORBITAL ELEMENTS FOR SOME ASTEROIDS [I-9]

Cat. No.	Name	Year of Discovery	Diameter (miles) Diameter (miles)	Opposition Magnitude	Semi-Major Axis of Orbit (AU)	Orbital Period (years)	Eccentricity	Inclination of Orbit (deg)
1	Ceres	1801	478.5	7.4	2.767	4.6	0.0802	10.60
2	Pallas	1802	304.5	8.0	2.770	4.61	0.2394	34.82
3	Juno	1804	118	8.7	2.670	4.36	0.2574	13.02
4	Vesta	1807	236	6.5	2.361	3.63	0.0889	7.14
5	Astraea	1845	49.7	9.9	2.577	4.13	0.1862	5.33
6	Hebe	1847	69.6	7.0	2.42	3.77	0.2019	11.65
7	Iris	1847	77.7	6.7	2.386	3.69	0.2309	5.47
8	Flora	1847	56	7.8	2.201	3.27	0.1567	5.88
9	Metis	1848	77.7	8.1	2.387	3.69	0.1233	5.60
12	Victoria	1850	37.3	8.1	2.334	3.57	0.2190	8.38
15	Eunomia	1851	?	7.4	2.644	4.30	0.1870	11.76
18	Melpomene	1852	59	7.7	2.296	3.48	0.2176	10.15
20	Massalia	1852	65.9	8.2	2.409	3.74	0.1426	0.68
192	Nausicaa	1879	46.6	7.5	2.403	3.72	0.2445	6.87
324	Bambergia	1892	59	7.3	2.68	4.39	0.3346	11.30
387	Aquitania	1894	66.5	8.2	2.74	4.53	0.2383	17.97
433	Eros	1898	15.5	7.2	1.458	1.76	0.2230	10.83
719	Albert	1911	2.5	12.0	2.58	4.16	0.54	10.82
851	Wladilena	1920	?	12.7	2.362	3.63	0.274	23.0
944	Hidalgo	1920	21.7	11.0	5.71	13.7	0.65	43.06
1036	Ganymede	1924	?	12.5	2.665	4.35	0.54	26.2
1221	Amor	1932	1.6	16.0	1.973	2.77	0.45	----
----	Apollo	1932	1.2	17.0	1.486	1.81	0.566	6.4
----	Adonis	1936	0.6	19.0	1.969	2.76	0.78	1.5
----	Hermes	1937	0.9	18.0	1.290	1.47	0.474	4.7
1566	Icarus	1949	0.9	12.6	1.078	1.12	0.827	23.0

TABLE I-5. COMETS [I-4]

Comet <sup>a</sup>	Recent Perihelion Date, and Return Number		Mean Orbital Elements <sup>b</sup>						
			P (year)	$\omega$	$\Omega$	i	e	q (AU)	a (AU)
Encke	1961. 10	46	3. 30	185	335	12. 4	0. 847	0. 339	2. 21
Grigg-Skjellerup	1957. 09	9	4. 90	356	215	17. 6	0. 704	0. 855	2. 89
Temple	1957. 10	12	5. 28	191	119	12. 5	0. 545	1. 38	3. 0
Kopff	1958. 05	8	6. 3	160	120	5	0. 556	1. 51	3. 4
Giacobini-Zenner	1959. 82	7	6. 5	172	196	30. 8	0. 72	0. 94	3. 5
Schwass. -W. <sup>c</sup>	1961. 68	6	6. 53	358	126	3. 7	0. 384	2. 155	3. 50
Wirtanen	1961. 29	3	6. 67	343	86	13. 4	0. 543	1. 62	3. 55
Reinmuth	1960. 90	3	6. 7	45	296	7. 0	0. 46	1. 93	3. 6
Brooks	1960. 46	10	6. 75	197	177	5. 6	0. 50	1. 76	3. 6
Finlay	1960. 67	7	6. 85	321	42	3. 5	0. 705	1. 07	3. 6
Borrelly	1960. 45	7	7. 01	351	76	31. 1	0. 604	1. 450	3. 67
Faye	1955. 17	14	7. 42	201	206	10. 6	0. 565	1. 655	3. 80
Whipple	1955. 91	4	7. 42	190	189	10. 2	0. 356	2. 450	3. 80
Reinmuth	1958. 23	4	7. 67	13	124	8. 4	0. 478	2. 03	3. 90
Oterma	1958. 44	Annual	7. 89	355	155	4. 0	0. 144	3. 39	3. 96
Schaumasse	1960. 29	6	8. 18	52	86	12. 0	0. 705	1. 195	4. 05
Wolf	1959. 22	10	8. 42	161	204	27. 3	0. 396	2. 505	4. 15
Comas Sola	1961. 26	5	8. 57	40	63	13. 5	0. 577	1. 775	4. 19
Vaisala	1960. 35	3	10. 5	44	135	11. 3	0. 635	1. 745	4. 79
Schwass. -W.	1957. 36	Annual	16. 1	356	322	9. 5	0. 132	5. 53	6. 4
Neujmin	1948. 96	3	17. 9	347	347	15. 0	0. 774	1. 54	6. 8
Crommelin	1956. 80	6	27. 9	196	250	28. 9	0. 919	0. 744	9. 2
Olbers	1956. 45	3	69. 6	65	85	44. 6	0. 930	1. 18	16. 8
Pons-Brooks	1954. 39	3	70. 9	199	255	74. 1	0. 955	0. 775	17. 2
Halley	1910. 30	29	76. 2	112	57	162. 3	0. 967	0. 587	17. 8

a. These comets have appeared at least three times and are expected to reappear as predicted.

b. Orbital elements equinox 1950.

c. Schwassmann-Wachmann.

Note: This table is used with the permission of Oxford University Press (C. W. Allen's, Astrophysical Quantities).

$V_c$  = average cometary velocity relative to the spacecraft  
(paragraph 1.4.1.2), m/s.

$\beta$  = heliocentric latitude.

#### 1.4.1.2 Cometary Meteoroid Velocity

The average velocity (m/s) of cometary meteoroids relative to the spacecraft,  $V_c$ , is expressed as follows:

$$V_c (R, \sigma, \theta) = R^{-1/2} U_c (\sigma, \theta)$$

where

$R$  = distance from the sun in AUs.

$U_c$  = cometary velocity parameter (Fig. I-1) as a function of  $\sigma$  and  $\theta$ ,  
km (AU)<sup>1/2</sup>/s.

$\sigma$  = ratio of the spacecraft's heliocentric speed at  $R$  to the speed of  
a circular orbit of radius  $R$ .

$\theta$  = angle between the spacecraft velocity vector and the surface of  
an imaginary sphere of radius  $R$  (deg).

#### 1.4.2 Asteroidal Meteoroids

Asteroidal meteoroids need not be considered inside the orbit of Mars.

##### 1.4.2.1 Asteroidal Flux-Mass Model

The model given here is an approximation of that given in Reference  
I-10. For  $10^{-9} \leq m \leq 10^0$ ,  $1.5 \leq R \leq 2.2$ ,

$$\log F_a = -15.89 - 0.84 \log m + 2.92 (R - 1),$$

where

$F_a$  = number of asteroidal impacts/m<sup>2</sup>/s of mass  $m$  or greater.

$m$  = mass in grams.

$R$  = distance from the sun in AUs.

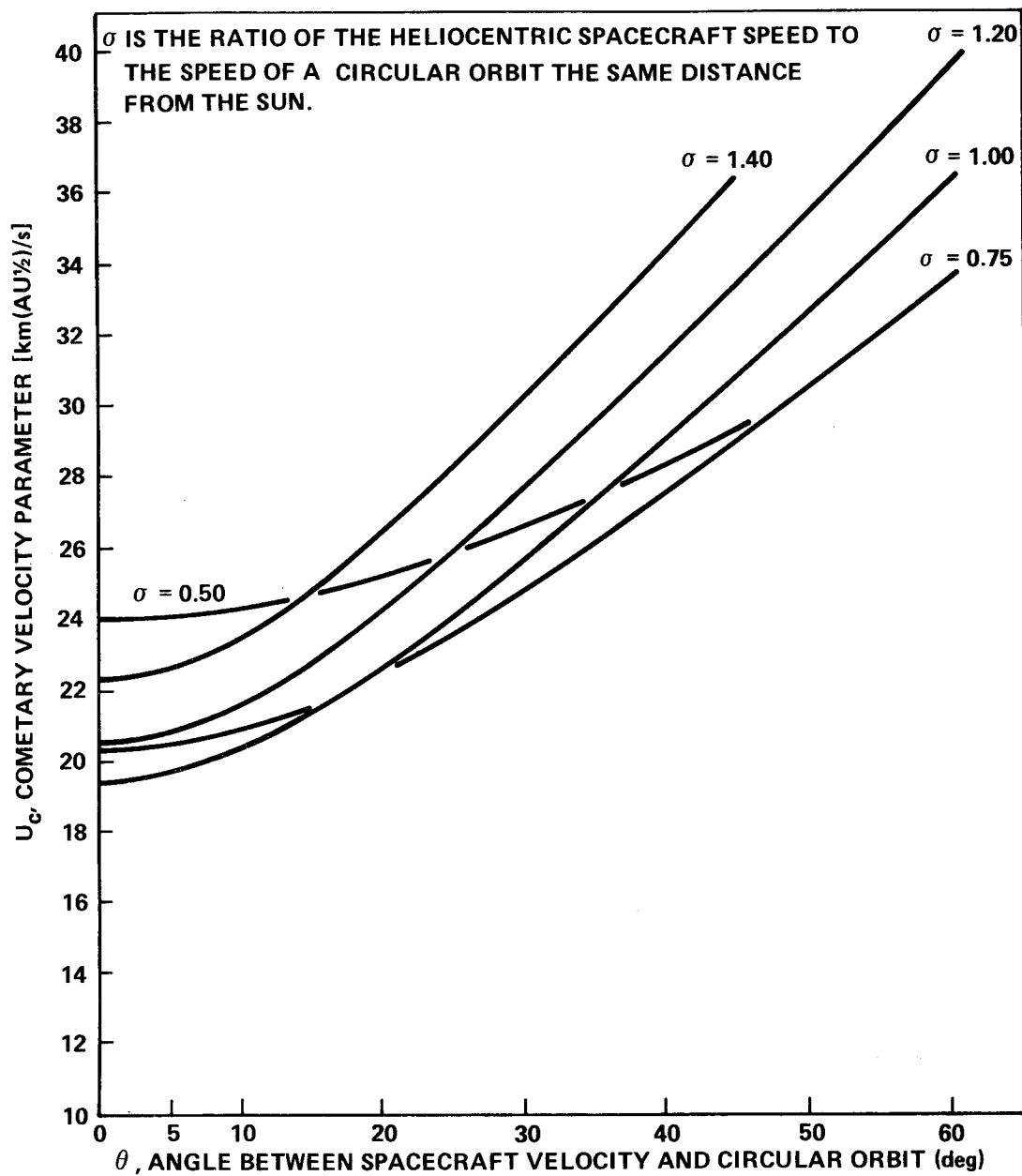


Figure I-1. Average relative velocity, cometary particles.

#### 1.4.2.2 Asteroidal Meteoroid Velocity

The average asteroidal velocity in this region of space is approximately 10 km/s.

#### 1.4.2.3 Asteroidal Mass Density

The average asteroidal mass density is approximately  $3.5 \text{ g/cm}^3$ .

#### 1.4.3 Additional Information

Detailed information relative to asteroidal meteoroids and the interplanetary meteoroid environment is given in References I-10, I-11, and I-12.

### 1.5 Geomagnetic Environment

#### 1.5.1 Magnetic Field

The principal magnetic field in space from 1.0 to 1.5 AU solar distance is that of the sun as carried by the solar plasma. The strength of the solar interplanetary magnetic field at 1.0 AU is about  $5 \gamma$ . The strength of the field depends upon solar activity, with maximum field strength at maximum solar activity. Fluctuations of one or two orders of magnitude may occur depending upon solar activity.

The interplanetary field appears to be directed along the classical Archimedean spiral from the sun as described by Parker, but the remote possibility of a distorted solar dipole field should not be excluded.

### 1.6 Astrodynamic Constants

#### 1.6.1 General Constants

Astronomical Unit [I-13]:  $\text{AU} = 1.495978930 \times 10^8 \text{ km}$ .

Ephemeris-Universal Time reduction: The relationship between Ephemeris Time and Universal Time is given in "The American Ephemeris and Nautical Almanac," U. S. Government Printing Office. For 1972, the difference is

$$\Delta T = ET - UT = 42.43 \text{ s.}$$

Velocity of light in a vacuum [I-13]:  $c = 299792.5 (\pm 0.3) \text{ km/s}$ .

1.6.2 Gravitational Constants and Mass Ratios [I-13]

Body	Mass Ratio $M_{\text{sun}}/M_{\text{planet}}$	Gravitational Constant ( $\text{km}^3/\text{s}^2$ )
Sun	1	$1.32712499 \times 10^{11}$
Mercury	$5\,987\,000 \pm 32\,000$	$2.218159 \times 10^4$
Venus	$408\,522 \pm 3$	$3.24860 \times 10^5$
Earth and Moon	$328\,900.1 \pm 0.3$	$4.035040 \times 10^5$
Mars	$3\,098\,700 \pm 100$	$4.28284 \times 10^4$
Jupiter	$1047.39 \pm 0.04$	$1.267076 \times 10^8$
Saturn	$3499.3 \pm 1.5$	$(3.7925 \pm 0.0016) \times 10^7$
Uranus	$22\,930 \pm 6$	$5.787722 \times 10^6$
Neptune	$19\,260 \pm 100$	$6.890574 \times 10^6$
Pluto	$1\,812\,000 \pm 40\,000$	$7.324088 \times 10^5$
Earth	$332\,945.6$	$3.986012 \times 10^5$
Moon		$4.90278 \times 10^3$

## REFERENCES

- I - 1. Burrell, M. O., Wright, J. J., and Watts, J. W.: An Analysis of Energetic Space Radiation and Dose Rates. NASA TN D-4404, February 1968.
- I - 2. Johnson, F. S.: Satellite Environment Handbook. Second Edition, Stanford University Press, Stanford, California, 1965.
- I - 3. Solar Electromagnetic Radiation. NASA SP-8005, May 1971.
- I - 4. Allen, C. W.: Astrophysical Quantities. Athlone Press, University of London, 1963.
- I - 5. Roberts, W. T.: Space Radiations: A Compilation and Discussion. NASA TM X-53018, George C. Marshall Space Flight Center, March 5, 1964.
- I - 6. Webber, W. R.: An Evaluation of the Radiation Hazard Due to Solar-Particle Events. Technical Report D2-90496, The Boeing Company, Seattle, Washington, December 1963.
- I - 7. Brandli, H. W.: The Natural Environment of a Satellite in a Synchronous Circular Orbit. Technical Report 192, Air Weather Service, USAF, June 1967.
- I - 8. Thekaekara, M. P., Editor: The Solar Constant and the Solar Spectrum Measured from a Research Aircraft. NASA TR R-351, Washington, D. C., October 1970.
- I - 9. Burbank, P. B., Cour-Palais, B. G., and McAllum, W. E.: A Meteoroid Environment for Near-Earth Cislunar and Near Lunar Operations. NASA TN D-2747, Manned Spacecraft Center, Houston, Texas, April 1965.
- I -10. Meteoroid Environment Model - 1970. NASA SP-8038, Interplanetary and Planetary, October 1970.
- I -11. Kessler, D. J.: Spatial Density of the Known Asteroids in the Ecliptic Plane. NASA TM X-538026, Manned Spacecraft Center, March 1969.

## REFERENCES (Concluded)

- I -12. Kessler, D. J.: Average Relative Velocity of Sporadic Meteoroids in Interplanetary Space. AIAA Journal, vol. 7, no. 12, December 1969.
- I -13. Melbourne, W. G., Mulholland, J. D., Sjogren, W. L., and Sturms, F. M., Jr.: Constants and Related Information for Astrodynamic Calculations, 1968. Jet Propulsion Lab., Technical Report 32-1306, July 15, 1968.



## SECTION II. TERRESTRIAL SPACE

### 2.1 Definition

"Terrestrial space" is defined in this document as the region between 90 and 65 000 km above the surface of the earth for all environment components except meteoroids, where the outer limit of the earth's sphere of influence extends into space until the gravitational attraction becomes negligible.

### 2.2 Neutral Gas Properties<sup>1</sup>

Atmospheric conditions encountered by a spacecraft in orbit about the earth are important factors in space vehicle design, mission planning, and mission operations. Density is the primary atmospheric property that affects the spacecraft's orbital altitude, lifetime, and motion in the altitude range of 90 to 1000 km. Near the lower limit of this range where density is greatest, a spacecraft will generally remain in orbit for a very short time; near the upper limit, the density effect on orbital lifetime is almost negligible. Density directly affects the torques which result from aerodynamic interaction between the space vehicle and the atmosphere; such torques must be considered in design of spacecraft attitude control systems. Density scale height is required in heating calculations for space vehicles re-entering the earth's upper atmosphere. Density, as well as chemical composition and temperature, is needed in calculating a spacecraft's drag coefficient. Chemical composition and temperature are also required in the design of experiment sensors to be flown in this altitude range.

Because of variability of atmospheric conditions with spatial location and solar condition, invariant models of the earth's atmosphere (90 to 2500 km) are not useful for most engineering applications. Therefore, a computerized version of a prediction method to provide models of the earth's atmosphere which vary with solar condition and location is required. The resulting atmospheric models, which are predicted for particular times and locations, provide atmospheric density, chemical composition, temperature, molecular mass, and density scale height between 90 and 2500 km altitude.

Most of the density values for the atmosphere between 90 and 2500 km have been derived from the analysis of changes in the periods of orbiting satel-

---

1. Appendix B contains a complete discussion.

lites. Temperature and chemical composition may be inferred from the drag determined densities under the assumption of static diffusion. Since mass density, temperature, and chemical composition at these altitudes vary with solar and geomagnetic activity, the level of such activity must be considered to estimate these parameters for a given time.

### 2.2.1 Variations

#### 2.2.1.1 Chemical Composition

In the earth's homosphere, extending from the surface to an altitude of near 90 to 100 km, the atmospheric gases mix thoroughly so the constituent gas distribution (chemical composition) does not vary. However, above 90 km and primarily near 105 km, extreme ultraviolet (EUV) solar radiation causes molecular oxygen to dissociate. The resulting atomic oxygen is then transported up and down, changing constituent distribution. Accordingly, the chemical composition above the 90- to 100-km altitude level is a function of the variable amounts of EUV radiation received from the sun.

#### 2.2.1.2 Temperature

The temperature lapse rate is influenced by solar radiation. In the lower thermosphere (100 to 300 km), solar radiation in the EUV band (40 to 1000 Å) is absorbed and causes the temperature to increase steadily with altitude. Above 300 km, where little or no solar radiation is absorbed, the temperature increases very little with altitude and becomes isothermal as shown in Figure II-1. The isothermal temperature, which is designated as the "exospheric temperature," varies diurnally, seasonally, and with solar and geomagnetic activity from about 650° to 2100°K.

#### 2.2.1.3 Density

Variation in density has been found to be related closely to the amount of EUV received from the sun. Although EUV cannot be measured at the earth's surface, early investigators assumed that there was correlation between EUV and radiation at about 10-cm wavelength which can be measured at the earth's surface. Data from the first Orbiting Solar Observatory (OSO-1) confirmed this assumption, showing close correlation between EUV and radiation at 10.7 cm [II-1]. Therefore, the mean daily solar flux at 10.7 cm which is measured by the National Research Council, Ottawa, Canada, has been accepted as an indicator of the amount of EUV radiation that reaches the atmosphere.

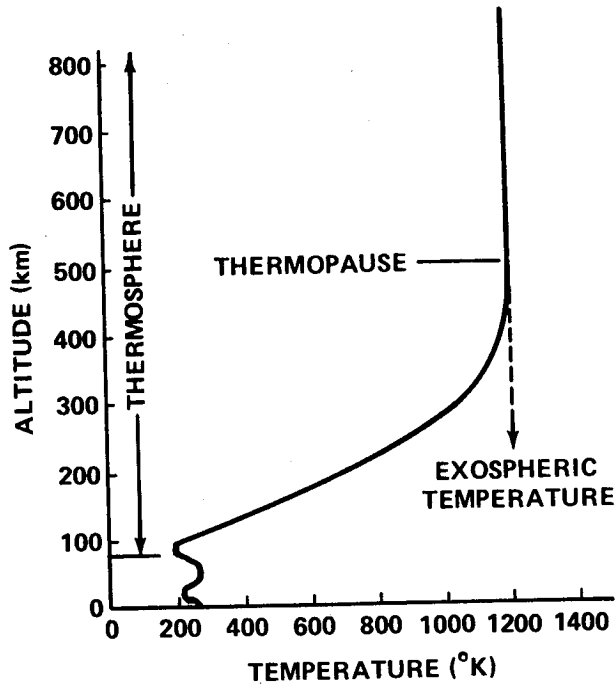


Figure II-1. Typical plot of temperature versus altitude and exospheric temperature.

The principal periodic variability found in the solar flux at 10.7 cm occurs at a cycle of 27 days, corresponding to the 27-day solar rotation. The same periodicity is reflected in atmospheric density. Semiannual, diurnal, and 11-year or solar cycle variations have also been identified (Fig. II-2).

Density variation also can be related to fluctuations in the three-hourly geomagnetic index of magnetic activity at the earth's surface. Although the physical relationship between geomagnetic activity and density variation is not known, the correlation between changes in geomagnetic activity and density variation is useful in density prediction.

Density also varies between the winter and summer hemispheres in the 60- to 80-deg latitude range. Some investigators attribute the higher density in the winter hemisphere to increased concentration of helium.

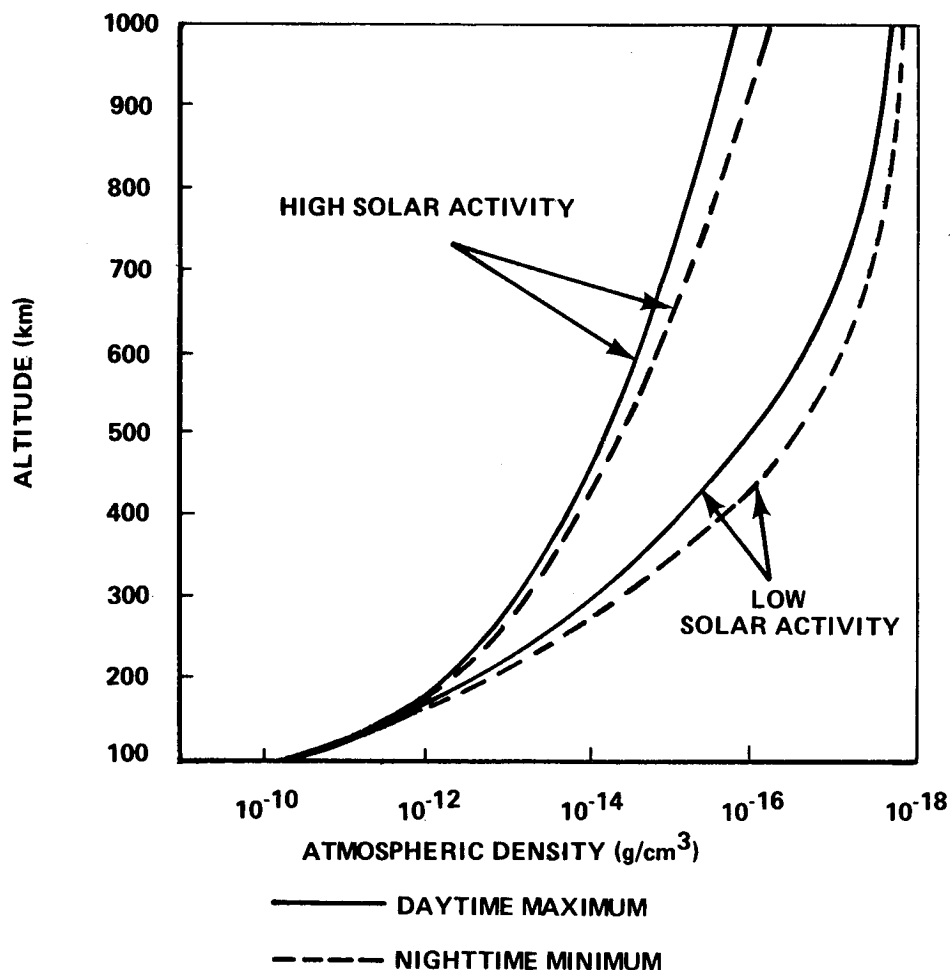


Figure II-2. Typical daytime maximum and nighttime minimum atmospheric density profiles for high and low solar activity.

#### 2.2.1.4 Criteria

The upper atmosphere model used by MSFC is described in Appendix B and should be used to predict the neutral gas properties of the atmosphere between 90 and 2500 km altitude for orbital dynamics, lifetime, and control and guidance analyses. The model should be used for reentry and analyses from orbital altitudes down to 25 km above the earth's surface. This model provides only nominal atmospheric density data below ~ 90 km. Solar activity data required for input to this model are described in Section 2.4.7 and Appendix A.

### 2.2.2 2500- to 65 000-km Altitude

Gas pressure decreases exponentially with increasing altitude above 2500 km until it reaches the interplanetary value of  $10^{-10}$  dynes/cm<sup>2</sup> near 20 000 km. It then remains relatively constant with increasing altitude.

Gas density decreases exponentially above 2500 km altitude to a value of  $10^{-23}$  g/cm<sup>3</sup> near 20 000 km and then remains relatively constant to 65 000 km altitude.

Kinetic temperature increases linearly above 2500 km to about  $2 \times 10^5$  °K at 20 000 km and then remains relatively constant with increasing altitude.

### 2.2.3 Additional Information

Additional information relative to the structure and variability of the atmosphere is given in References II-1 through II-3.

## 2.3 Ionosphere<sup>2</sup>

The ionosphere is that region of the upper atmosphere where an appreciable amount of ionization exists. This region extends outward from altitudes of approximately 60 km until it merges with the plasma of interplanetary space.

The ionosphere is of concern to space vehicle designers because of the effects of spacecraft interaction with the electrically active medium and because of the influence of the ionosphere on mission communications, guidance, and tracking. Specifically, the ionosphere may affect frequency selection and design of receivers, transmitters, and antennas. In addition, the flow of charge between the plasma and the spacecraft represents a leakage current to exposed conductors which may lead to electrical breakdown of normally nonconducting paths.

The interaction of the spacecraft and medium must be considered in the design of experiments having the purpose of taking measurements within the ionosphere. These interactions include formation of wakes by passage of the spacecraft through the medium, generation of large electrical potentials by long antennas and booms, and formation of plasma sheaths around the

---

2. These data were extracted from NASA SP-8049 [II-4] which contains additional information.

spacecraft which can isolate it from the ambient medium. Sheaths can affect results of direct measurement experiments such as Langmuir probes and experiments mounted on booms. In addition, the electric potential acquired by the spacecraft usually serves as a reference for onboard experiments of this type.

### 2.3.1 Basic Concepts

The ionization of the upper atmosphere is the result of solar radiation and cosmic rays interacting with the atmosphere to produce a plasma consisting of (usually) equal concentrations of positively and negatively charged particles. The plasma remains in a state of dynamic equilibrium because the loss of charged particles through recombination is balanced by the creation of new particles. Because the prime source of energy for the ionosphere is the sun, the parameters defining the ionosphere vary diurnally, seasonally, and with the solar cycle. Geographical variations from anomalies in the earth's magnetic field also exist.

At equatorial and middle latitudes, the terrestrial magnetic field tends to "hold" ionospheric particles within a magnetic shell at an average geocentric distance  $\rho$ , given approximately by  $\rho = 4 R_E \cos^2 \lambda$  where  $R_E$  is the earth's radius and  $\lambda$  is the geographic latitude. Electron densities at this "boundary" (plasmopause) are of the order of  $100 \text{ electrons cm}^{-3}$ . Beyond the plasmopause, the ionosphere has electron densities of at least one order of magnitude smaller and is linked with the outer magnetosphere. In the polar regions, the ionospheric particles are not held by the terrestrial magnetic field but escape via the polar wind mechanism. Consequently, electron densities are typical of those beyond the plasmopause and the ionosphere is linked with the outer magnetosphere.

### 2.3.2 Ionospheric Parameters

#### 2.3.2.1 The Ionosphere Below 1000 km

Three regions have been identified as prominent features of the structure of the lower ionosphere during the daytime. In order of increasing altitude and increasing ion concentration they are the D, E, and F regions. Large diurnal effects exist which occur in this part of the ionosphere. At

nighttime, the D region virtually disappears and a depression in electron concentration occurs between the E and F regions.

The D region is the lowest ionospheric region and has an approximate altitude range from 60 to 85 km. The predominant ionizing agent is Lyman alpha radiation with cosmic rays contributing in the lower altitudes. Nitric oxide ( $\text{NO}^+$ ) and oxygen ( $\text{O}_2^+$ ) are the principal ionic constituents together with heavy ion complexes involving water vapor. The D region has the lowest electron density concentration of the three regions with a maximum of  $10^3$  electrons/cm<sup>3</sup> near 80 km.

The approximate altitude range of the E region is from 85 to 140 km. Ultraviolet and soft x-radiation are the principal ionizing agents in this region. The predominant ionic constituents are  $\text{NO}^+$  and  $\text{O}_2^+$ . The electron concentration in the E region ranges from approximately  $10^5$  electrons/cm<sup>3</sup> during solar minimum to a value 50 percent larger during solar maximum.

The F region has an approximate altitude range from 140 to 1000 km and in daytime has two divisions:  $F_1$  and  $F_2$ . The solar spectrum in the wavelength range from 200 to 900 Å is the principal ionizing agent in this region. The two divisions or density peaks occur because the degree of ionization and recombination falls off with decreasing altitude at different rates. The  $F_1$  region is associated with the ion production peak occurring in the vicinity of 150 km. The  $F_1$  region disappears at night as the concentration of electrons decreases above the E region. The  $F_2$  region is associated with the peak in the electron density distribution which varies with time of day, season, solar cycle, and latitude. It usually lies within the region from 200 to 400 km. The predominant ions near the low altitude boundary are mainly  $\text{NO}^+$  and  $\text{O}_2^+$ ; with increasing altitude, a gradual transition occurs until at the upper boundary  $\text{O}^+$  becomes the principal ion.

The section of ionosphere above the peak of the  $F_2$  region commonly is referred to as the topside ionosphere. Information on the topside ionosphere is obtained mainly through satellite measurements and the incoherent backscatter radar technique.

#### 2.3.2.2 The Ionosphere Above 1000 km

The ionosphere above 1000 km includes the upper portion of the topside ionosphere and the region of the near-earth plasma (or outer ionosphere) extending to altitudes of the order of 3 to 4.5 earth's radii ( $R_0$ ).

From this altitude to about  $10 R_0$  is the region of transition to the interplanetary medium.

Most information on the outer ionosphere has come through experimental research with the aid of whistlers (RF electromagnetic signals generated by some lightning discharges) although in situ measurements by satellites also have provided useful results. The data indicate a steady decrease in electron concentration with increasing altitude until a rapid and abrupt decrease occurs at altitudes of 15 000 to 25 000 km above the magnetic equator. This decrease in electron concentration is called the "knee" or plasmapause.

The predominant ions in the outer ionosphere vary with altitude. In the lowest part of the region, atomic oxygen ( $O^+$ ) predominates, whereas atomic hydrogen ( $H^+$ ) is the main constituent above 2000 km (protonosphere).

#### 2.3.2.3 Electron Densities

The density of electrons in the ionosphere varies geographically, diurnally, seasonally, and with solar activity. It is not yet possible, however, to produce models of the electron density distribution which show all these variations because of the limited number of observations. Available information is provided mainly by vertical incidence sounders and rockets and by satellites.

Below the peak of the  $F_2$  region, the electron density increases with altitude. Above this region, measurements (made primarily with topside sounders and incoherent backscatter radars) indicate a rather smooth and slow decrease in electron concentration with increasing altitude. In the region of the knee (where measurements have been made by whistlers and satellites), a rapid decrease in electron concentration occurs. This decrease occurs even during the periods of relatively weak magnetic disturbances.

Typical mid-latitude electron density profiles for the ionosphere below 1000 km are presented in Figures II-3 and II-4. Variations with latitude are shown in Figure II-5. If greater accuracy is required, the tabulated values of electron density in References II-5 and II-6 should be consulted; these references cover both the mid-latitude and polar ionosphere. Profiles for the ionosphere above 1000 km are presented in Figure II-6. The solar maximum curve is an average daytime profile; the solar minimum profile up to the knee region is derived from incoherent scatter data.



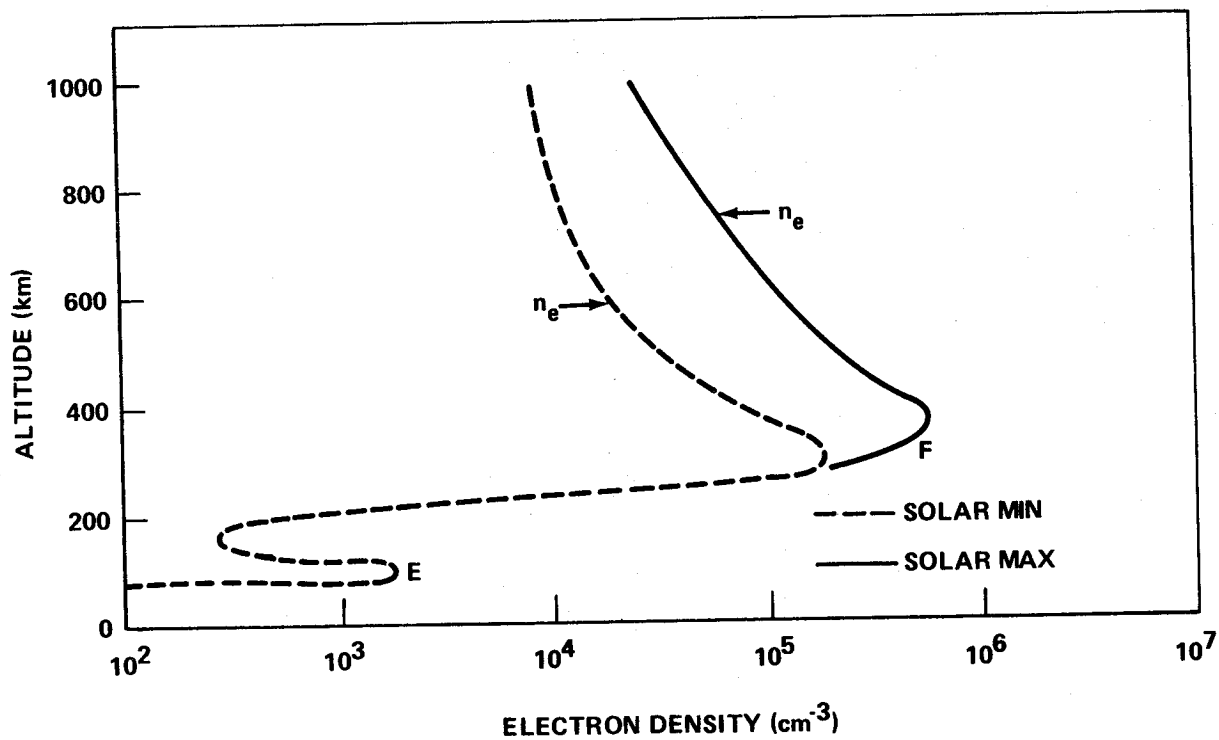


Figure II-3. Ionospheric electron concentration - nighttime.

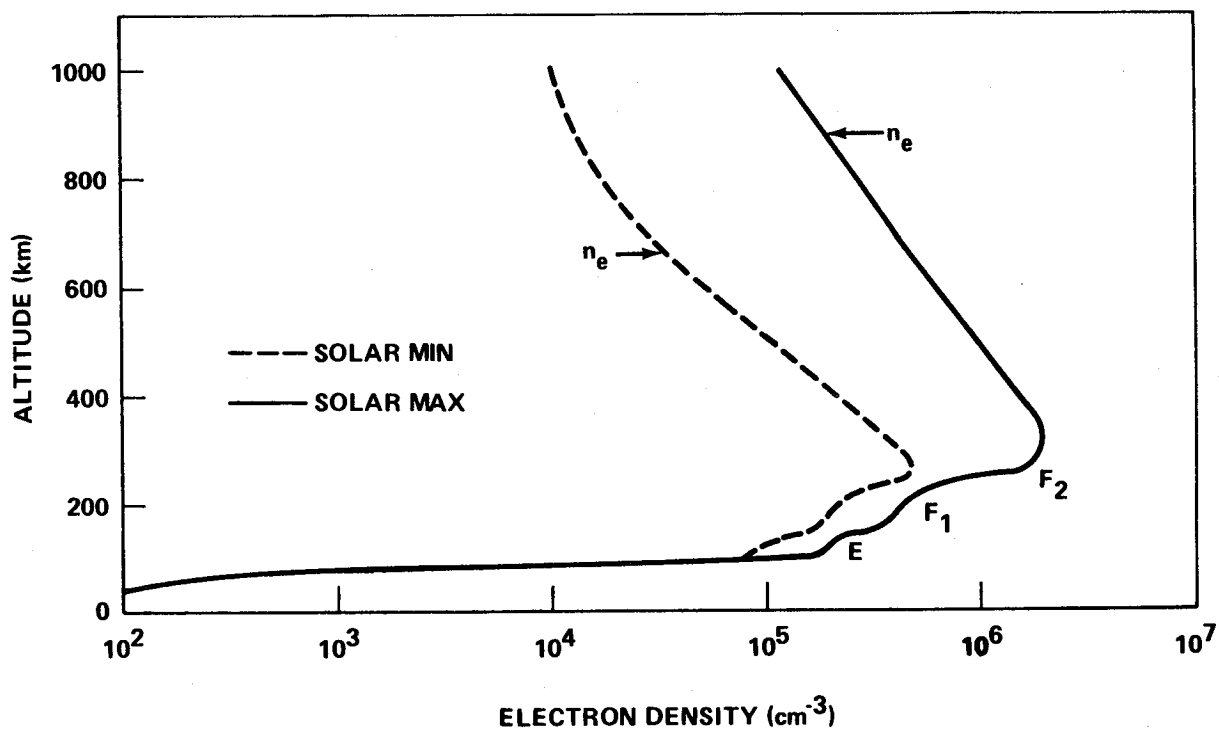


Figure II-4. Ionospheric electron concentration - daytime.

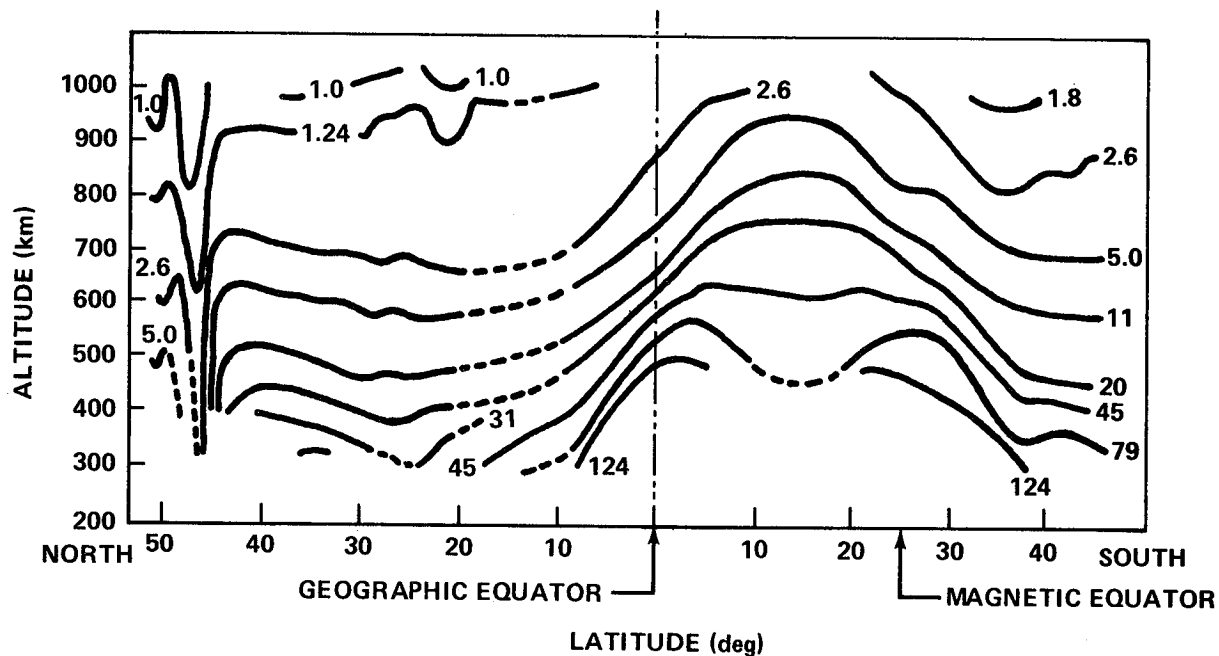


Figure II-5. Daytime contours of equal electron density in the orbital plane of an Alouette Satellite. (Density units of  $10^4$  electrons  $\text{cm}^{-3}$ .)

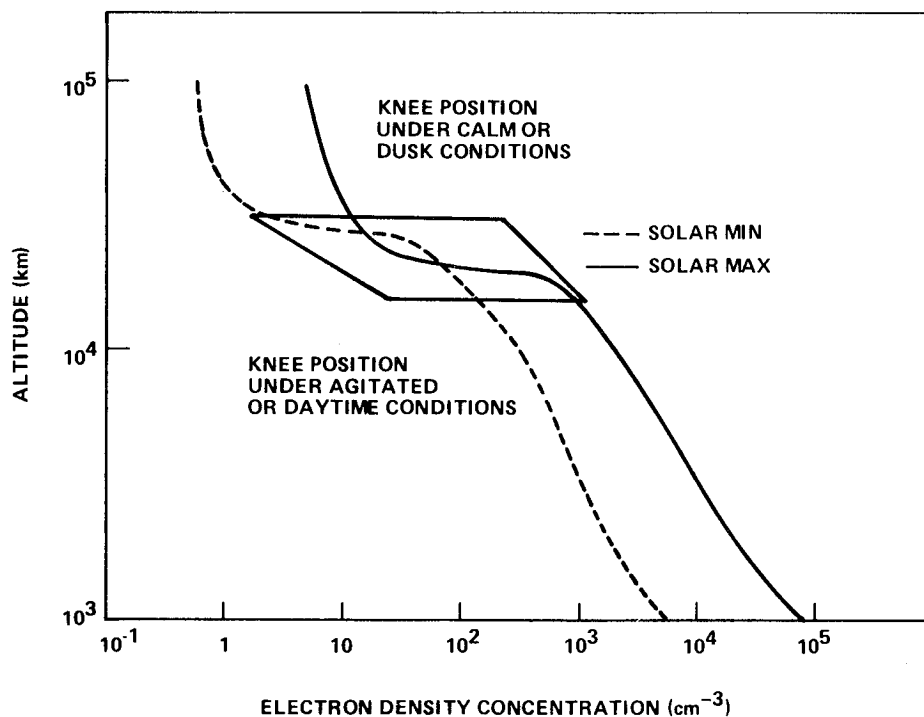


Figure II-6. Models of electron density profiles in the equatorial plane under solar sunspot extreme conditions. (The position of the knee or abrupt decrease in density is variable within the box as indicated.)

#### 2.3.2.4 Ionic Composition

In the lower regions of the ionosphere,  $\text{NO}^+$  and  $\text{O}_2^+$  predominate with  $\text{O}^+$  becoming the main ionic constituent in the higher part of the F region. A transition between a predominantly  $\text{O}^+$  ionosphere to one predominantly of  $\text{H}^+$  occurs in moving upward in the topside ionosphere. Helium is never a predominant ion species. It is, however, a minor constituent at all times; its maximum density is 15 percent of the total at about 450 km.

Above 1000 km, the ionic composition is predominantly  $\text{H}^+$ ; it becomes almost exclusively  $\text{H}^+$  above 2800 km. The only other component of interest is  $\text{He}^+$  with a concentration of about 1 to 4 percent of the hydrogen concentration. The concentration of hydrogen ions is deduced from proton whistler observations by the Alouette 1 and Injun 3 satellites. Concentrations of ions other than hydrogen are derived from incoherent backscatter data. Observations indicate that the concentration of hydrogen ions increases in winter and that the nighttime summer results may be applied to daytime winter conditions. The values then merge with those below 1000 km.

The number variation of ionic composition in the lower ionosphere in daytime is presented in Figure II-7. The percentage variation of ionic composition is presented in Figure II-8. This information was deduced from proton whistler observations on the Alouette 1 and Injun 3 satellites and from incoherent backscatter data. Averaging the various percentage concentrations with respect to mass yields night and day profiles of average ion mass.

#### 2.3.2.5 Ionospheric Temperature

The temperature profile of the ionosphere above the E region has been obtained with measurements by sounding rockets and satellites and backscatter sounders. The temperature of the ionosphere depends on the balance between the various heating and cooling processes in the ionosphere and the diurnal and seasonal variation of this balance. The daytime temperature of the ionospheric electrons in the  $F_1$  region is generally larger than the ambient gas temperature by a factor of two. This results from the relative efficiency of the ambient electrons in removing the excess kinetic energy from the continually released energetic photoelectrons and the relatively small number of electrons to share such energy. The resulting hot electron gas is cooled mainly by collisions with neutral particles at altitudes below about 250 km and by collision with ions at higher altitudes. The temperature of the ions approaches that of the electrons above 600 km with both exceeding the neutral gas temperature.

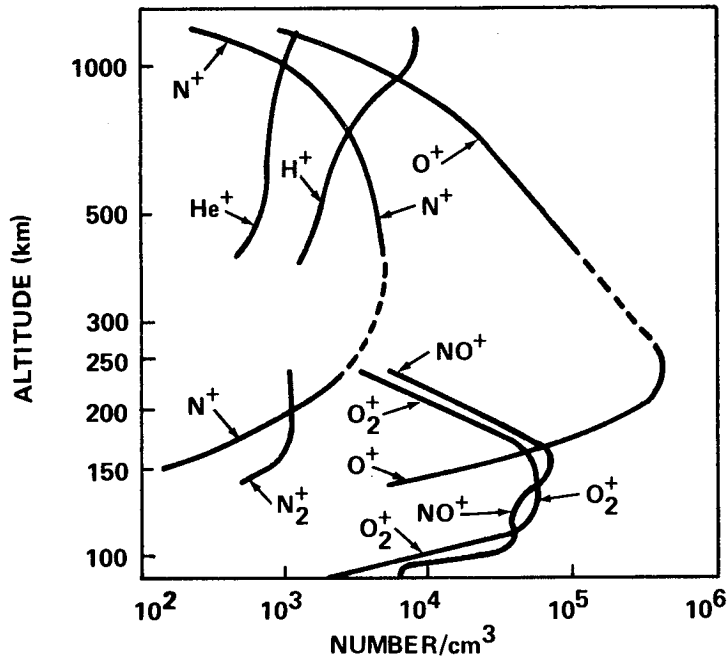


Figure II-7. Ionic composition of solar minimum daytime winter ionosphere.

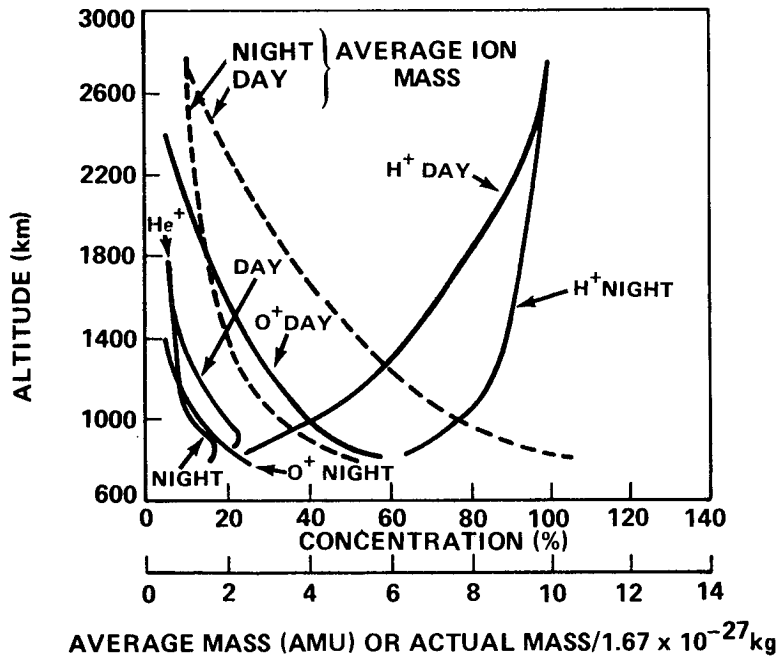


Figure II-8. Relative concentration of  $H^+$ ,  $O^+$ , and  $He^+$  and their average mass for solar minimum and a quiet summer time. (Night-time summer profiles are also appropriate for winter daytime.)

The model presented herein is based on experimental results for altitudes below 1000 km.

Temperature measurements made by the IMP 1 spacecraft in the region from 2 to 5  $R_E$  show that the electron temperature,  $T_e$ , is approximately proportional to the square of the radial distance,  $L$ , from the earth. Here, the value of 2.4 for the power of  $L$  is used to join lower altitude daytime temperature to data obtained from the OGO-1 satellite. The value of 1.9 was used as the power of  $L$  to match nighttime values of  $T_e$  with the low temperature readings.

The electron temperature profiles for daytime summer solar minimum conditions at altitudes below 1000 km are presented in Figure II-9; the ion temperature profiles are presented in Figure II-10.

Above 1000 km, the ion temperature is taken as equal to the electron temperature because the ion temperatures theoretically approach the electron temperature values. Figure II-11 gives the electron temperature profiles during periods of minimum and maximum solar activity.

### 2.3.3 Spacecraft Interaction with the Ionosphere

#### 2.3.3.1 Spacecraft Potential

A spacecraft moving through the ionospheric plasma will gather charge as a result of its contact with both positive and negative charges. In a state of equilibrium, the spacecraft will assume a potential sufficiently negative to equalize the flow of ions and electrons. This potential depends upon the temperature of the ambient plasma, the relative spacecraft motion, the electron density, the electrostatic fields surrounding electrically active surfaces, the incident flux of ultraviolet radiation and energetic particles, and the intentional ejection of charge by onboard equipment.

The spacecraft potential is important because it generally is used as a potential reference for onboard experiments. In this case, the spacecraft vehicle potential is assumed to be constant, and any variation in its value appears as an inaccuracy in the final experimental result.

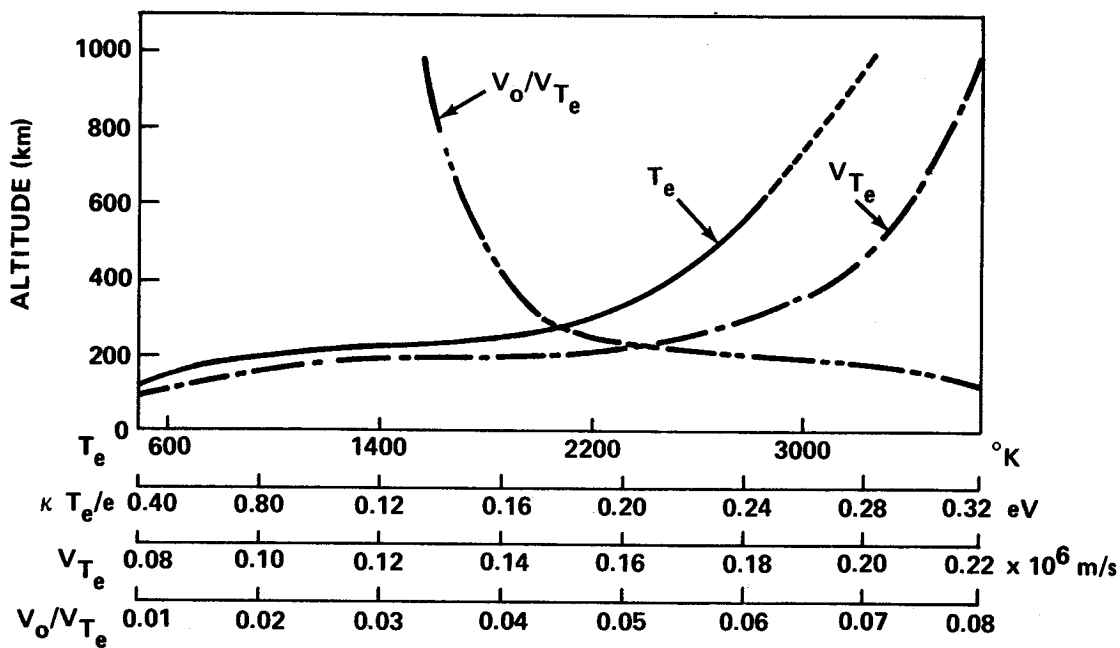


Figure II-9. Electron temperature, thermal velocity, and satellite/thermal velocity ratio.

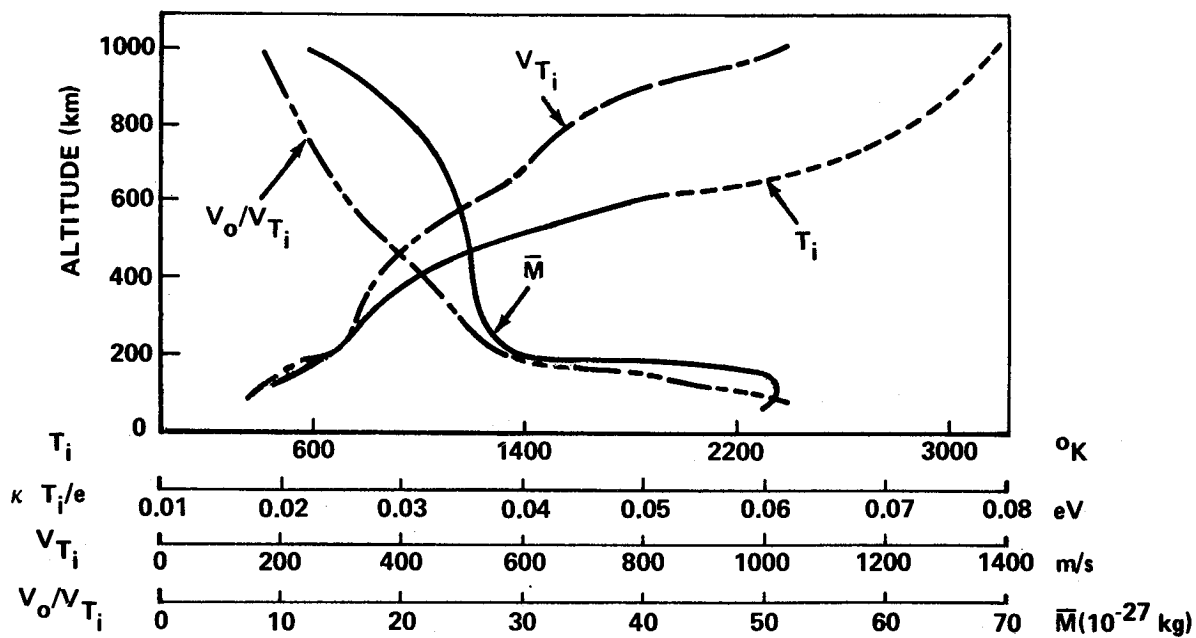


Figure II-10. Ion temperature, thermal velocity, and satellite/thermal velocity ratio.

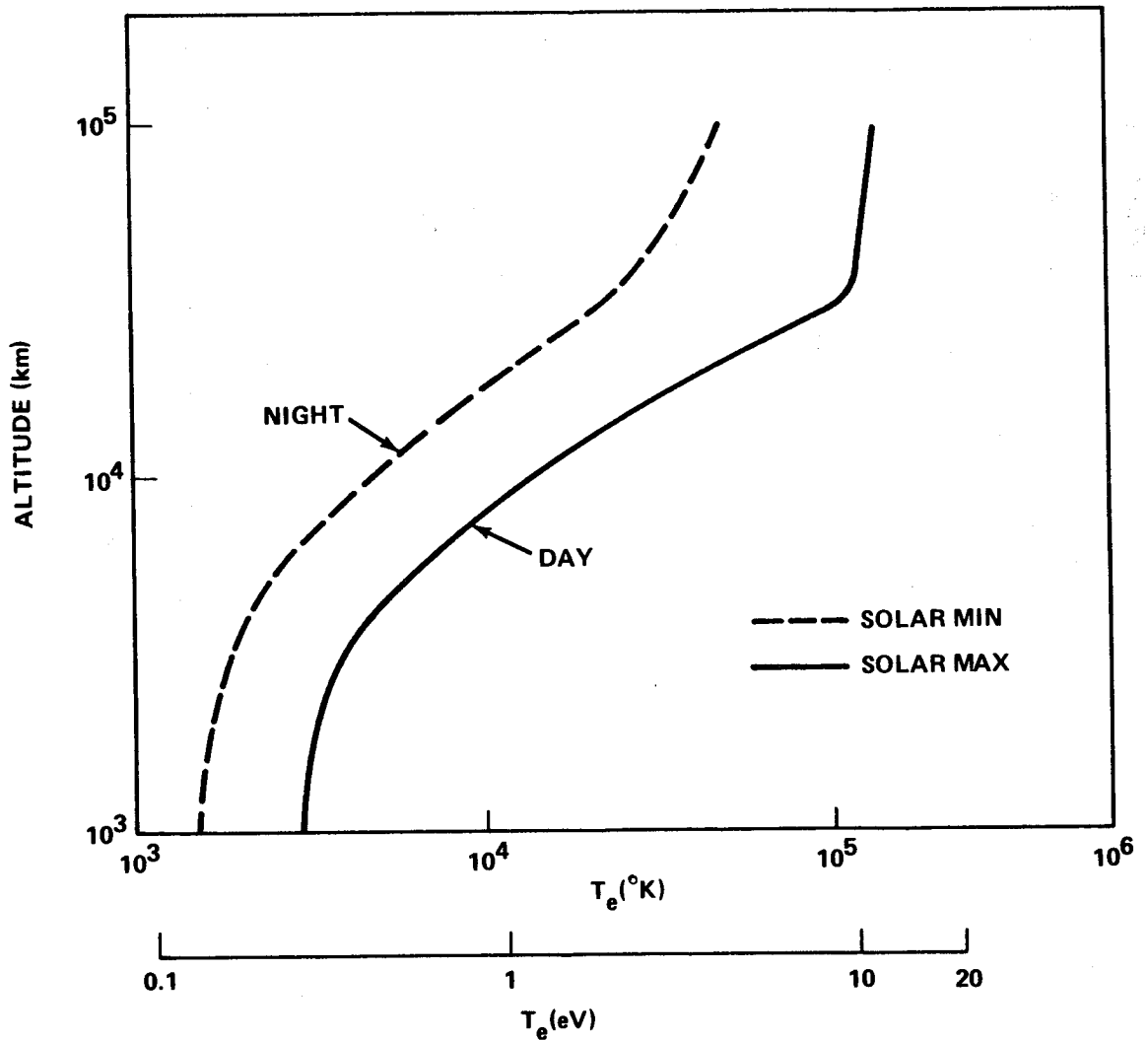


Figure II-11. Models of electron temperature profiles in °K or in eV (viz.,  $\kappa T_e/e$ ).

#### 2.3.3.2 Plasma Sheaths

The potential of the spacecraft is usually different from that of the ambient plasma and, as a result, the spacecraft tends to be surrounded by a plasma sheath. Three different classes of plasma sheaths exist: (a) the stationary sheath, (b) the wake, and (c) the specialized sheaths formed by exposure to direct voltages induced by RF or  $\vec{V} \times \vec{B}$ . It should be noted, however, that the spacecraft plasma sheath usually is a compound of all three forms unless special measures have been taken to eliminate certain of them.

The stationary sheath is formed around a body placed in a plasma. Theoretical analyses usually assume that the body is spherical and the sheath is of the dimension considerably larger than the plasma Debye length,  $\lambda_D$  (defined as  $6.9 [T_e/N_e]^{1/2}$  where  $T_e$  is the electron temperature in °K and  $N_e$  the electron density in  $\text{cm}^{-3}$ ). However, the sheath is considered smaller than the mean free path of the particles. These conditions permit collisionless treatment of the plasma in such analyses.

The sheath effects associated with the presence of an RF signal on an antenna strongly depend on the relationship between its frequency and the local plasma frequency. In general, an RF signal can cause the formation of quite extensive sheaths around an antenna which may disturb direct measurement experiments.

#### 2.3.3.3 $\overline{\mathbf{V}} \times \overline{\mathbf{B}}$ Effects

When a conductor moves through a magnetic field, an electric field is developed across the conductor according to the relationship,

$$\overline{\mathbf{E}} = \overline{\mathbf{V}} \times \overline{\mathbf{B}}$$

where

$\overline{\mathbf{E}}$  = the electric field produced

$\overline{\mathbf{V}}$  = the velocity vector of the conductor

$\overline{\mathbf{B}}$  = the magnetic field.

In the case of the spacecraft's interaction with the environment, the magnetic field is that of the earth, and the conductor is the metallic skin or appendages of the spacecraft.

If good coupling exists between the spacecraft and the plasma, an appreciable current will flow under the influence of the induced field. The energy of the spacecraft can be radiated away by resistive heating, and the net effect is equivalent to a loss of energy by a drag mechanism. This drag effect of the  $\overline{\mathbf{V}} \times \overline{\mathbf{B}}$  mechanism is treated in Reference II-7. It concludes that the drag is proportional to the cube of the spacecraft's characteristic dimension and may exceed the mass drag for spacecraft larger than 50 m in diameter above an altitude of 1200 km. However, Reference II-8 treats only spherical



spacecraft, whereas small spacecraft may have very large booms or antennas so that the total potential difference induced may be considerable (this potential is  $(\vec{V} \times \vec{B}) \cdot \vec{L}$  where  $\vec{L}$  is the vector length of a boom or antenna).

Another  $\vec{V} \times \vec{B}$  effect is the formation of an induced plasma sheath associated with a large potential of perhaps tens of volts. This sheath varies as the spacecraft spins and thus changes orientation with respect to the magnetic field. Therefore, it can have unfortunate effects on experiments mounted on the spacecraft such as Langmuir probes measuring ambient densities and temperatures.

#### 2.3.3.4 The Spacecraft Wake

The wake, which is a distorted sheath formed by the relative motion between the spacecraft and the plasma, extends many spacecraft diameters downstream. Immediately behind the spacecraft there is a region of high negative potential followed by an ion-focusing or concentration. Indications are that from this concentration an ion density enhancement extends downstream as a V wave analogous to a Mach cone. This enhancement is not attached to the spacecraft but commences at a number of body radii downstream equal to the Mach number.

#### 2.3.3.5 Thermal Particle Flux to a Spacecraft at Plasma Potential

Particle fluxes for electrons and ions at altitudes below 1000 km are presented in Figure II-12 and fluxes above 1000 km are presented in Figure II-13. For electrons, the number of particles flowing through unit area is based on the electron thermal velocity,  $V_{T_e}$ ; for ions, the

number is based on the satellite orbital velocity,  $V_o$  (circular orbit). The orbital velocity is used as a basis for the ion flux because it is generally greater than the ion thermal velocity,  $V_{T_i}$ .

#### 2.3.4 Communications

Attenuation of radio waves is a function of the refractive index,  $\mu$ , which in turn is a function of electron density  $N_e$ , where

$$\mu^2 = 1 - \frac{4\pi N_e e^2}{\epsilon_o m_e \omega^2}$$

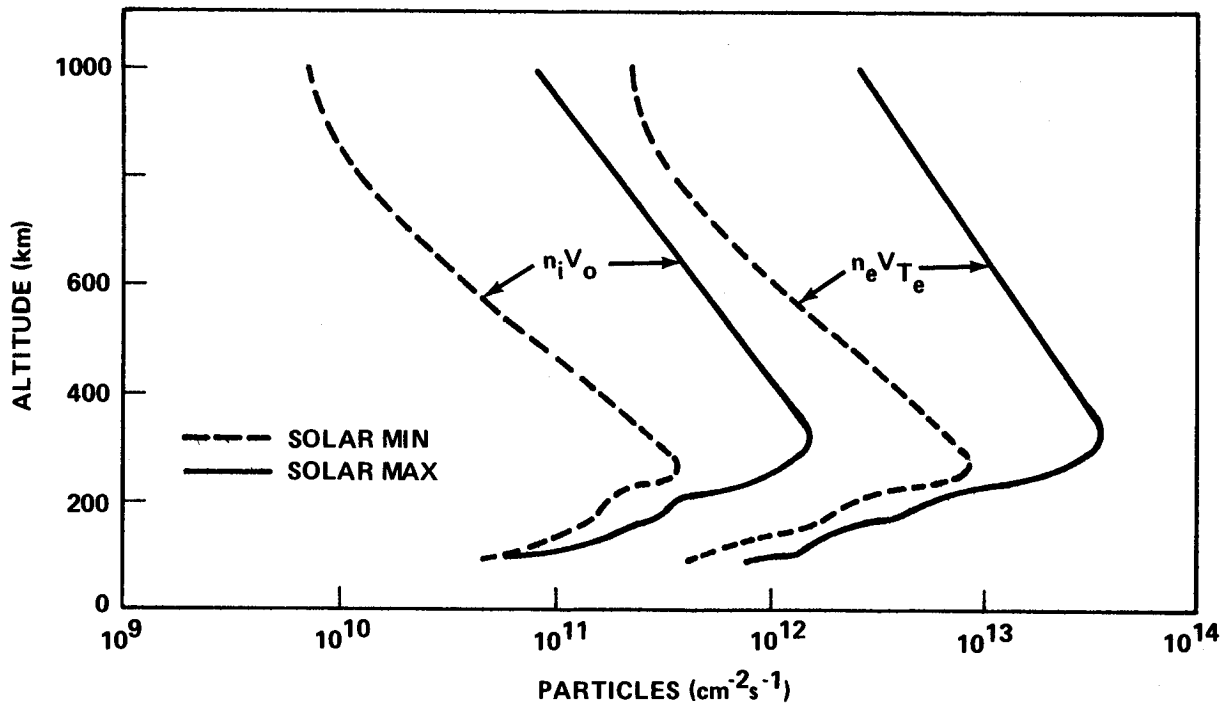


Figure II-12. Thermal particle flux daytime.

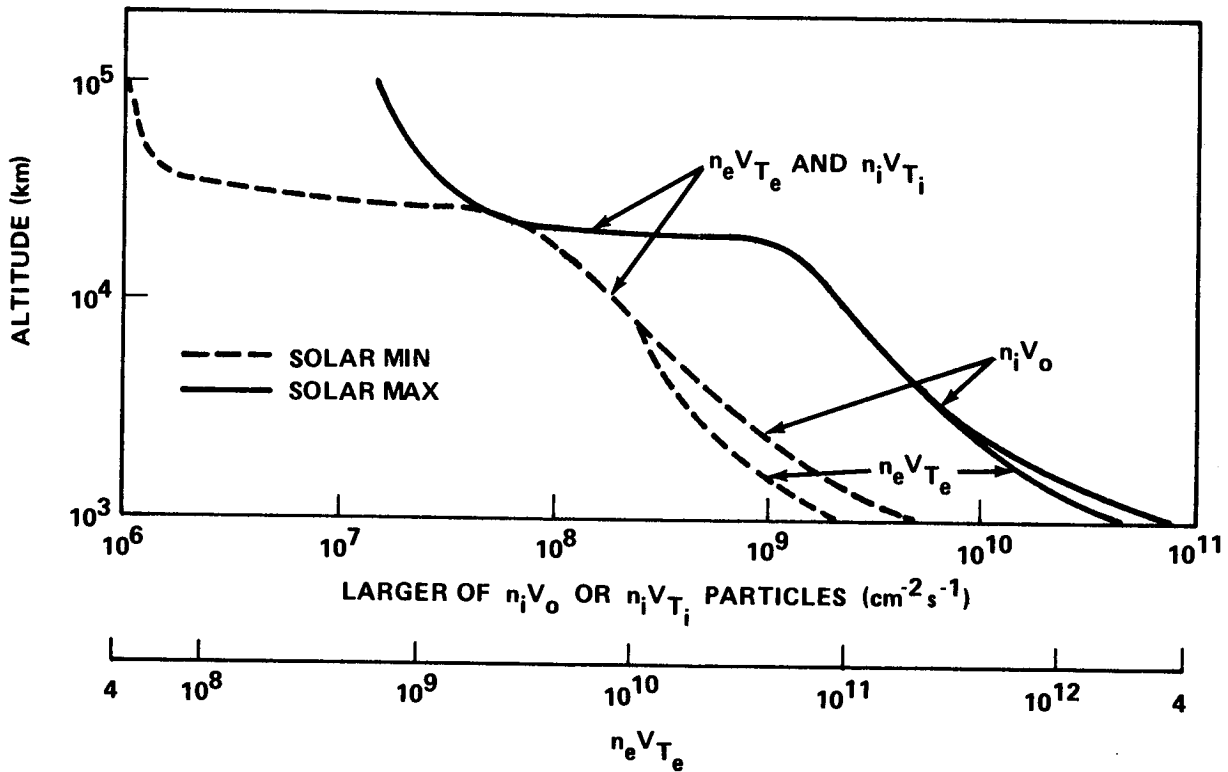


Figure II-13. Thermal electron and ion particle fluxes.

and

$e_e$  = electron charge (coulombs)

$m_e$  = electron mass (kg)

$\omega$  = angular frequency of the wave (rads/s)

$\epsilon_o$  = permittivity of free space (assuming the effects of ions are negligible).

At the  $F_2$  peak (point of maximum electron density) of the ionosphere, the frequency of the radio wave which will penetrate is called the critical frequency,  $f_c$ . For satellite communications, a frequency higher than  $f_c$  must be selected, and for the best signal strength possible, frequencies considerably higher than  $f_c$  (max) should be chosen. However, some investigations have indicated that the ionosphere may have resonance modes which could interfere significantly with even much higher frequency signals.

## 2.4 Radiation Environment

The natural radiation environment in terrestrial space consists of galactic cosmic radiation, geomagnetically trapped radiation, and solar flare particle events. This environment may be defined by establishing a description of the particle flux as a function of energy, species, and location (time and space).

Radiation dose rates should be calculated as specified in Paragraph 2.4.8.

### 2.4.1 Galactic Cosmic Radiation

Galactic cosmic radiation consists of low intensity, extremely high-energy particles. These particles, about 85 percent protons, 13 percent alphas, and the remainder heavier nuclei, bombard the solar system from all directions. They have energies from  $10^8$  to  $10^{19}$  eV per particle and are encountered essentially everywhere in space. The intensity of this environment in "free-space" (e.g., outside the influence of the earth's

magnetic field) is relatively constant (0.2 to 0.4 particles/cm<sup>2</sup>/steradian/s) except during periods of enhanced solar activity when the fluxes of cosmic rays have been observed to decrease. This decrease is caused by an increase in the strength of the interplanetary magnetic field which acts as a shield to incoming particles. Near the earth, cosmic rays are similarly influenced by the earth's magnetic field resulting in a spatial variation in their intensity (Fig. II-14).

Composition: ~ 85 percent protons (H<sup>+</sup>)

~ 13 percent alpha particles (He<sup>++</sup>)

~ 2 percent nuclei of elements Li → Fe in approximate cosmic abundance.

Flux at sunspot minimum: ~ 4 protons/cm<sup>2</sup>-s (isotropic)

Integrated yearly rates: ~  $1.3 \times 10^8$  protons/cm<sup>2</sup>

Flux at sunspot maximum: ~  $2.0 \pm 0.3$  protons/cm<sup>2</sup>

Integrated yearly rates: ~  $7 \times 10^7$  protons/cm<sup>2</sup>

Energy range: 10 to 10<sup>13</sup> MeV; predominant energy  $10^3 \times 10^7$  MeV.

Integrated dose: ~ 4 to 10 rads/year.

Energy spectrum - illustrated in Figure II-15 [II-9]:

$$1 \text{ BeV} = 10^9 \text{ eV}$$

$$1 \text{ MeV} = 10^6 \text{ eV}$$

$$1 \text{ KeV} = 10^3 \text{ eV}.$$

#### 2.4.2 Trapped Radiation

The earth's magnetic field provides the mechanism which traps charged particles in belts about the earth. Electrons and protons are trapped in a region about the equator extending in geomagnetic latitude to about ±50 deg and in altitude from the top of the atmosphere to the outer limits of the magnetosphere. Figures II-16 and II-17 show the spatial distribution of electrons and protons, respectively.

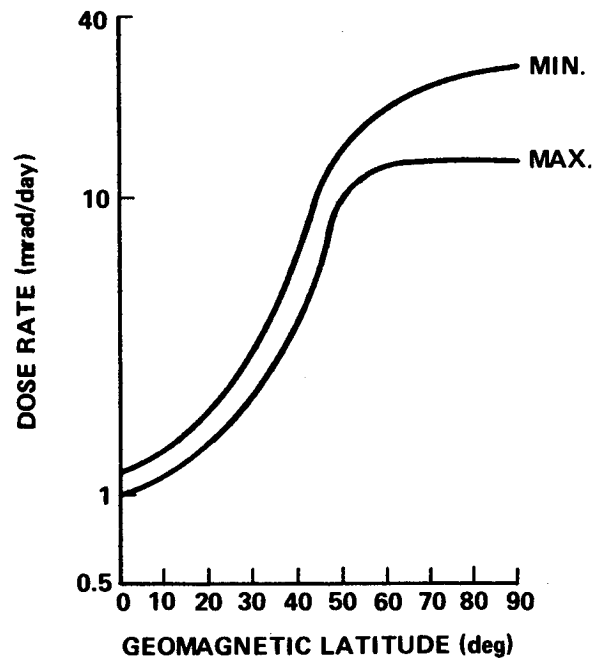


Figure II-14. Cosmic-ray dose rate above the atmosphere as a function of geomagnetic latitude during solar maximum and minimum.

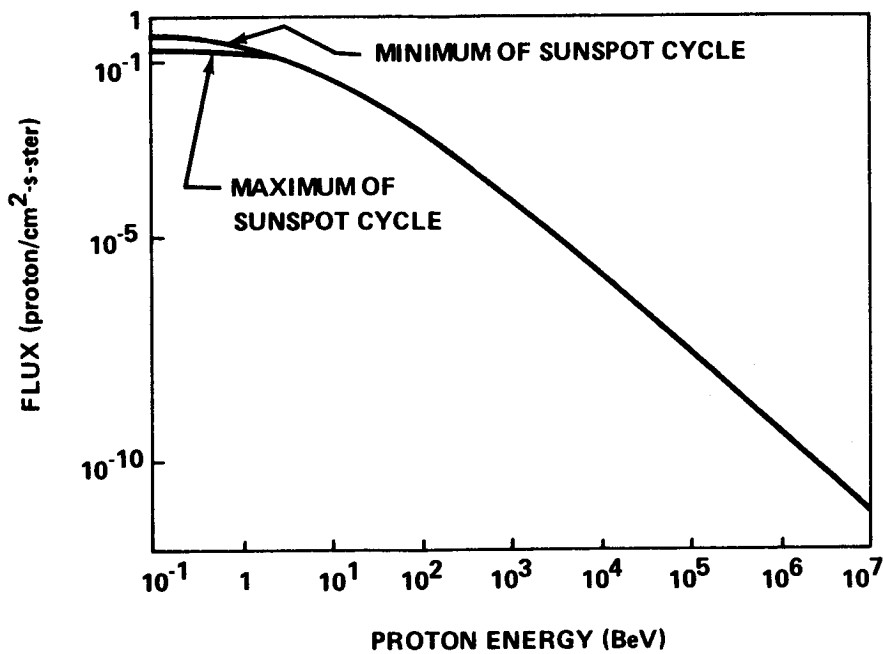


Figure II-15. Galactic radiation energy spectrum.

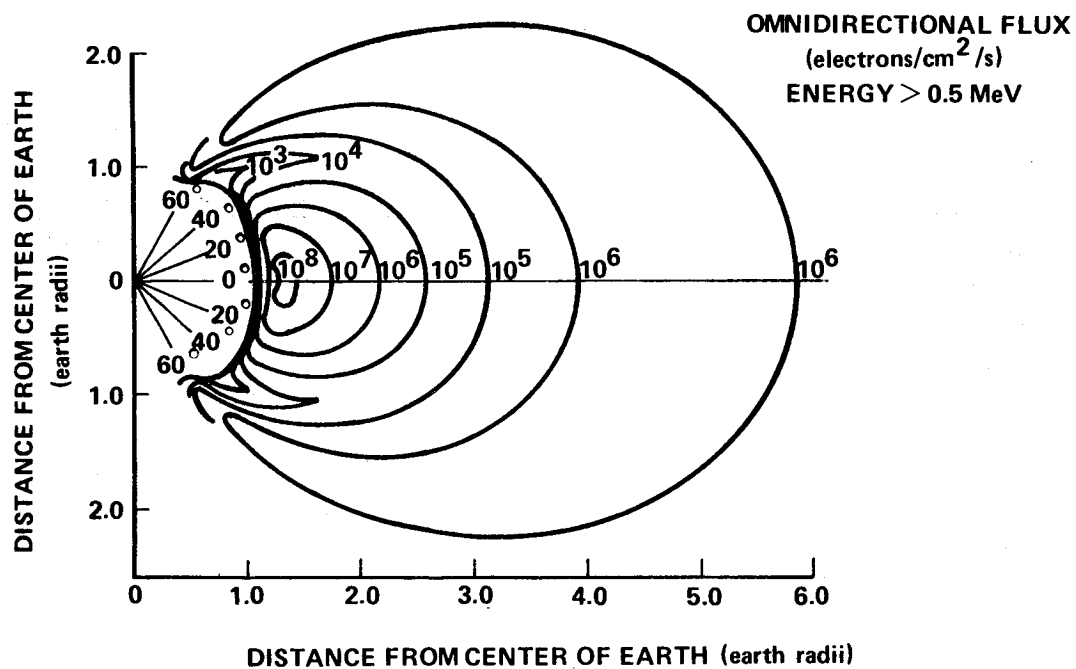


Figure II-16. Electron distribution in the earth's field  
(published by Vette in August 1964).

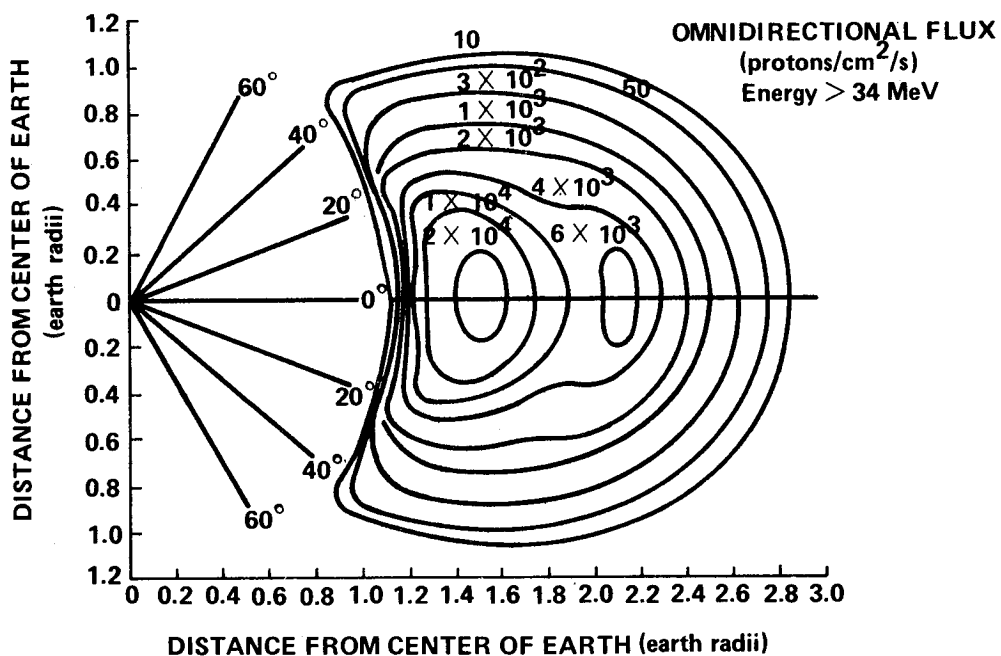


Figure II-17. Proton distribution in the earth's field  
(published by Vette in September 1963).

#### 2.4.2.1 Near-Earth Environment

The radiation belts trapped near the earth are approximately azimuthally symmetric, with the exception of the South Atlantic Anomaly. The earth's magnetic field can be approximated by a magnetic dipole whose axis is displaced 450 km from the center of the earth and tilted 10 deg with respect to the spin axis of the earth. In addition, the magnetic field is anomalously low in the region over the South Atlantic, which allows the radiation belts to reach their lowest altitude (Fig. II-18). Figure II-19 reflects the presence of the anomaly in the area where proton fluxes are encountered at an altitude of 160 n. mi. The natural occurring trapped radiation environment in the anomaly region remains fairly constant with time although it fluctuates with solar activity. In addition to the electrons in the anomaly region at low altitudes, electrons will also be encountered in the auroral zones.

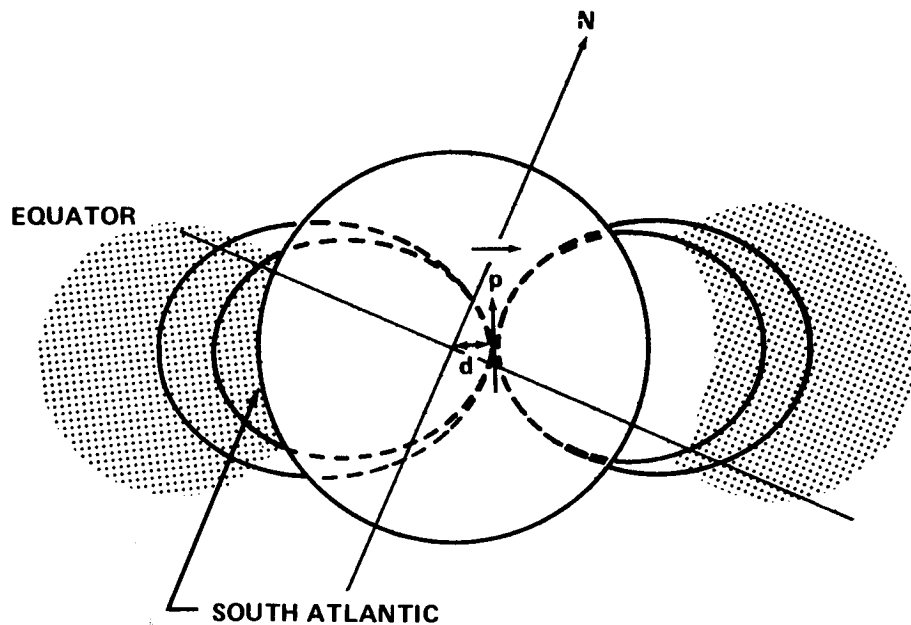


Figure II-18. South Atlantic Anomaly diagram.

The trapped radiation to be encountered in a 200 n. mi. polar orbit and in a 255-n. mi., 55-deg inclination orbit has been determined. The electron and proton energy spectra design values are shown in Figures II-20 and II-21, respectively.

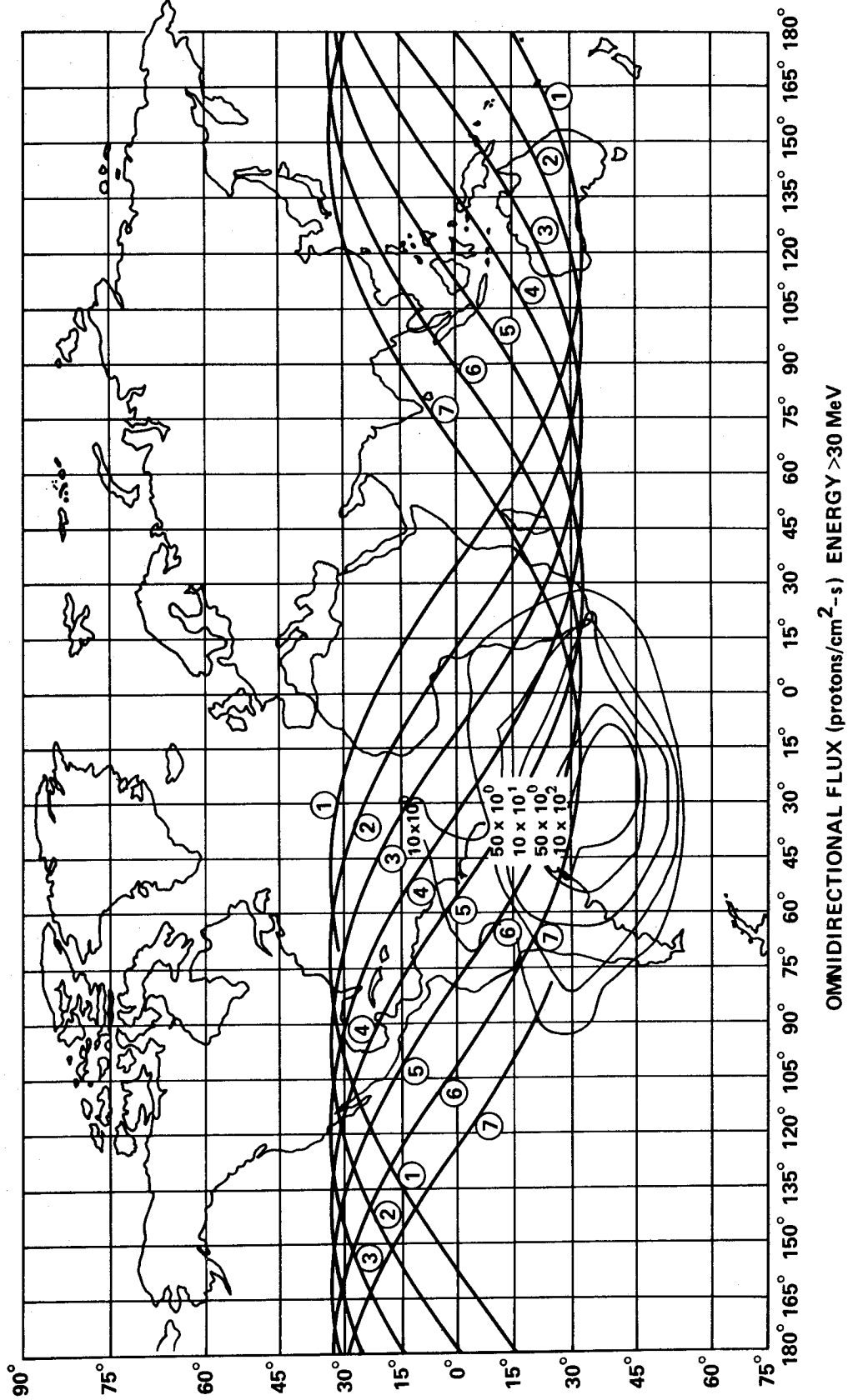


Figure II-19. Proton flux densities at an altitude of 162 n.mi.



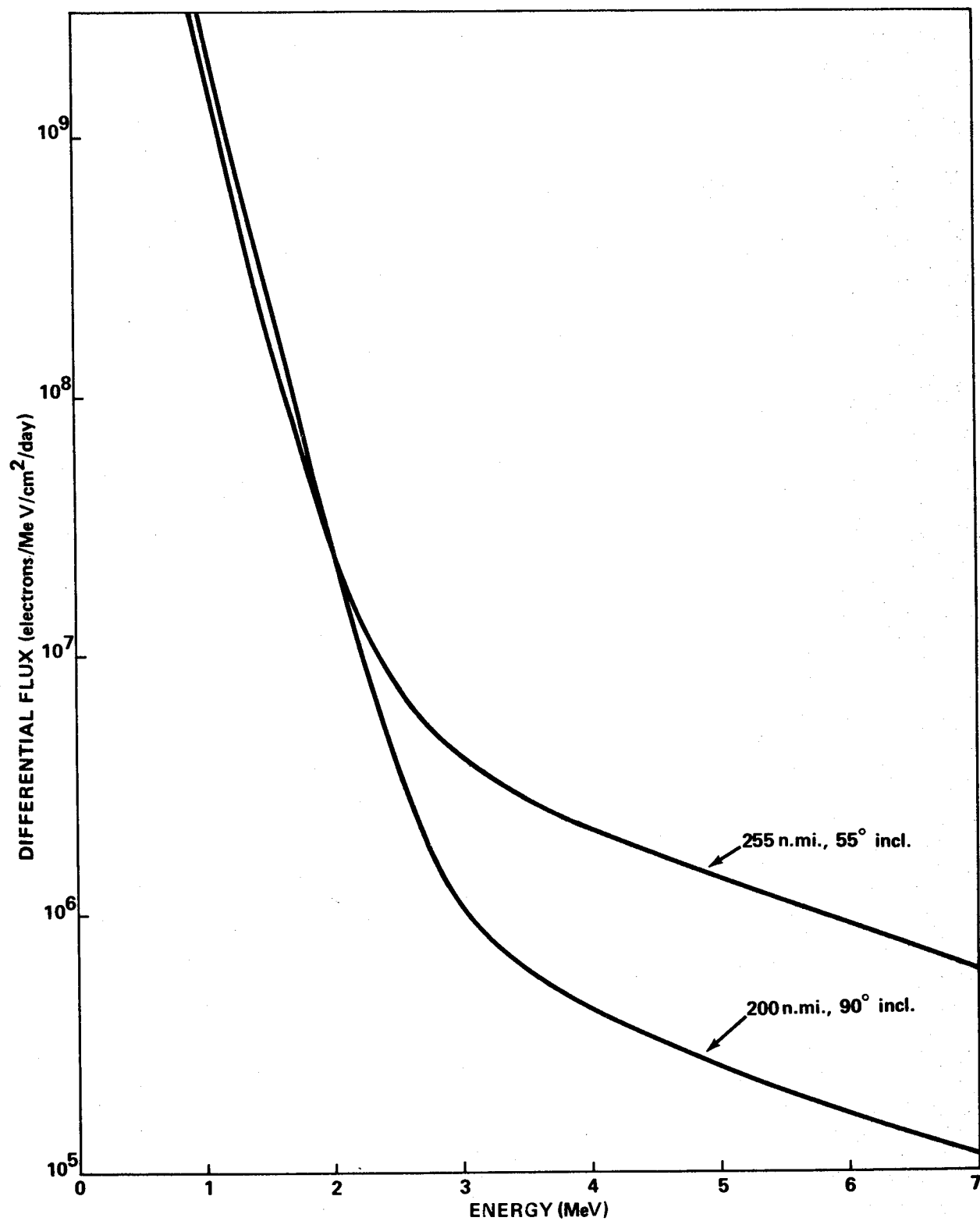


Figure II-20. Electron differential energy spectra.

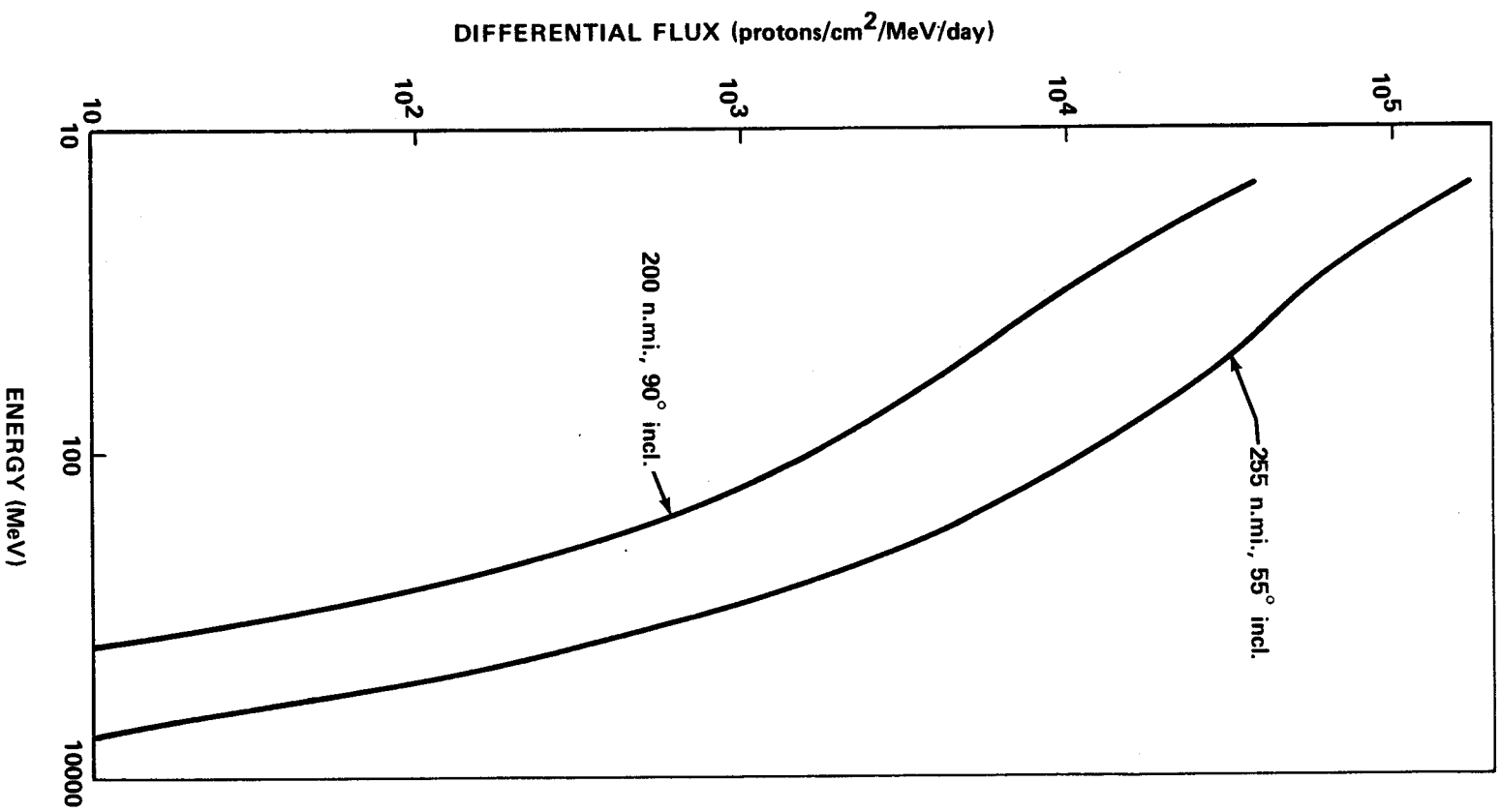


Figure II-21. Proton differential energy spectra.

#### 2.4.2.2 Synchronous Orbit Altitude Environment

The trapped proton environment at synchronous orbit altitude is of no direct biological significance, but may cause deterioration of material surfaces over long exposure times. The proton flux at this altitude is composed of only low energy protons (less than 4 MeV) and is on the order of  $10^5$  protons/cm<sup>2</sup>-s. A detailed description of this environment is given in Reference II-10.

The trapped electron environment at synchronous altitude is characterized by variations in particle intensity of several orders of magnitude over periods as short as a few hours. However, for extended synchronous altitude missions, a local time-averaged environment can be used. The local time-averaged electron energy spectrum for an equatorial synchronous orbit is shown in Figure II-22. The environment encountered by synchronous orbit missions having different inclinations will be less than the equatorial environment [II-11, II-12].

#### 2.4.3 Solar Particle Events

Solar particle events are the emission of charged particles from disturbed regions on the sun during solar flares. They are composed of energetic protons and alpha particles that occur sporadically and last for several days.

##### 2.4.3.1 Particle Event Model

The free-space particle event model which should be used for spacecraft studies is given below.

$$\text{Protons: } N_p(>T) = \begin{cases} 7.25 \times 10^{11} T^{-1.2}; & 1 \text{ MeV} \leq T \leq 10 \text{ MeV} \\ 3.54 \times 10^{11} e^{-P(T)/67}; & 10 \text{ MeV} \leq T \leq 30 \text{ MeV} \\ 2.64 \times 10^{11} e^{-P(T)/73}; & T \geq 30 \text{ MeV}. \end{cases}$$

$$\text{Alphas: } N_\alpha(>T) = \begin{cases} N_p(>T); & T < 30 \text{ MeV} \\ 7.07 \times 10^{12} T^{-2.14}; & T \geq 30 \text{ MeV}. \end{cases}$$

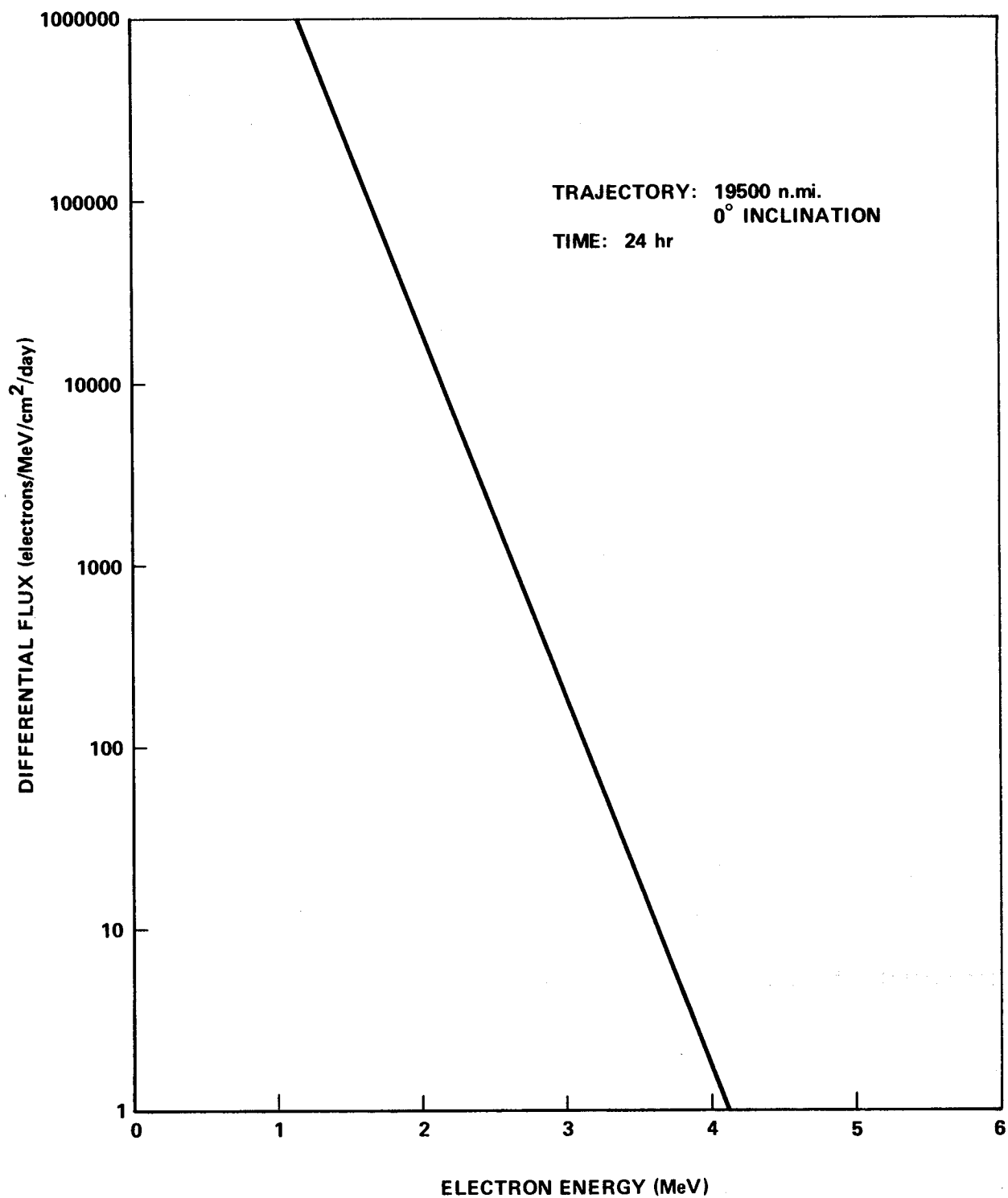


Figure II-22. Electron differential energy spectra.

The terms  $N_p(>T)$  and  $N_\alpha(>T)$  are the integral fluxes in units of protons/cm<sup>2</sup> and alphas/cm<sup>2</sup>, respectively.  $T$  is the particle's kinetic energy in units MeV and  $P(T)$  is the particle's magnetic rigidity in units mV given by

$$P(T) = \frac{1}{Ze} \sqrt{T(T + 2m_0 C^2)} \quad ,$$

where the quantity  $Ze$  is the magnitude of the particle's charge in units of electron charge; i.e.,  $Ze = 1$  for protons and  $Ze = 2$  alphas. The rest mass energy for the particle is given by  $m_0 C^2$ ; i.e.,  $m_0 C^2 = 938$  MeV for protons and 3728 MeV for alpha particles.

For synchronous orbit altitudes, the free-space solar particle event model described above should be used. For near-earth orbital altitudes, however, the free-space event model must be modified to account for the fact that the earth's magnetic field deflects some of the low-energy particles that would enter the atmosphere at low latitudes to the poles.

Solar particle events are more likely to occur at times of the solar maximum than at solar minimum.

#### 2.4.4 Solar Cosmic Radiation

##### 2.4.4.1 Particle Flux Spectrum

The particle flux spectrum is the same as interplanetary space (see Paragraph 1.3.2.1.2).

##### 2.4.4.2 Cutoff Rigidity

The magnetic field alters the penetration of charged particles in the vicinity of the earth. The minimum rigidity (cutoff rigidity) necessary to reach some geomagnetic latitude ( $L$ ) and geocentric radius ( $R$ ), in units of earth radii, is given by

$$P_c = \frac{60 \cos^4 L}{R^2 (1 + \sqrt{1 - \cos^3 L \cos \gamma})^2} \quad ,$$

where  $P_c$  is the cutoff rigidity in mV units and  $\gamma$  is the half angle of the allowed cone about the normal to the meridian plane.

For vertical arrival,  $\gamma = 90$  deg,

$$P_c = \frac{15 \cos^4 L}{R^2}.$$

#### 2.4.4.3 Additional Information

Additional information relative to the terrestrial radiation environment is given in References II-6, II-7, II-8, and II-10.

#### 2.4.5 Thermal and Albedo Radiation (Earth)

The radiation of the earth consists of the sum of the earth-emitted thermal radiation and the reflected (albedo) radiation. The visual earth radiation, for the purpose of this section, consists entirely of visual albedo.

##### 2.4.5.1 Earth Radiation [II-13, II-14, II-15, II-16, II-17]

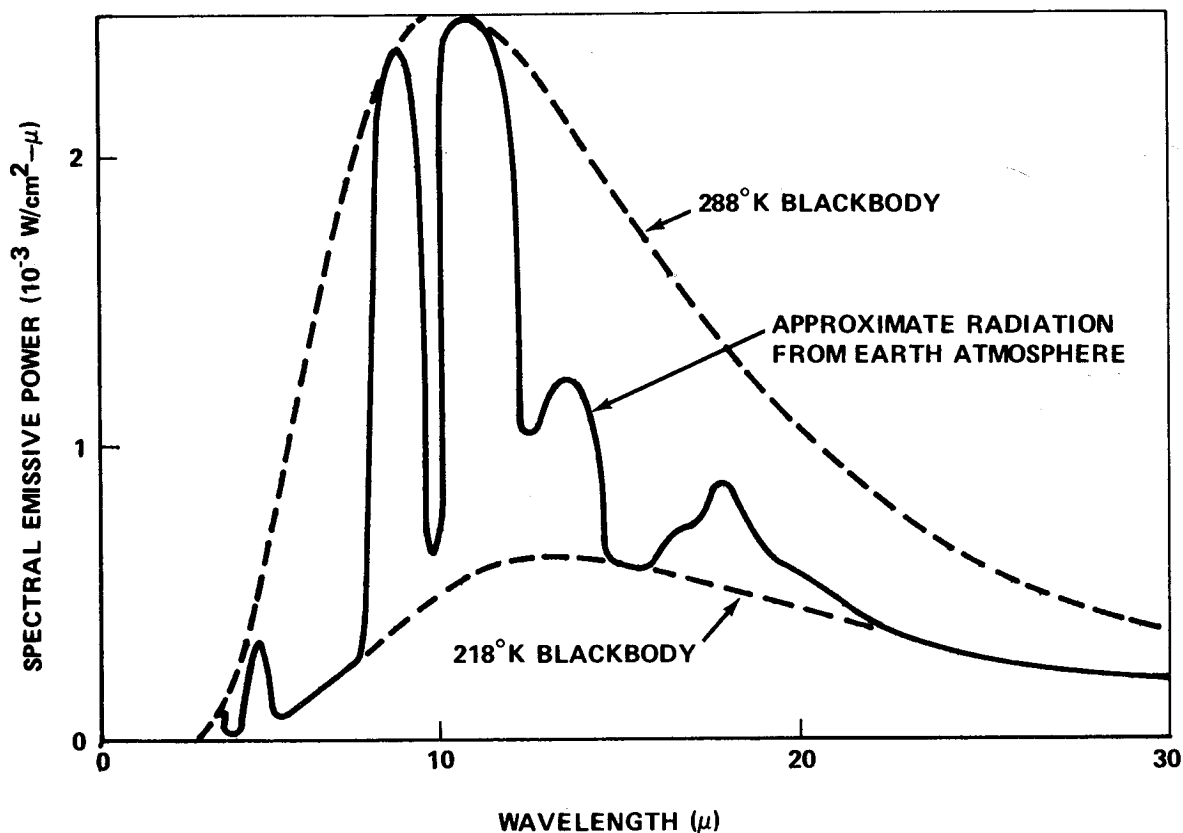
The average blackbody temperature of the earth-atmosphere system when in near-radiative equilibrium and having a global albedo of 30 percent is 254°K. The thermal radiation flux (5- to 30- $\mu$ ) from this system is 237 W/m<sup>2</sup> (0.34 cal cm<sup>-2</sup> min<sup>-1</sup> or 75 Btu ft<sup>-2</sup> hr<sup>-1</sup>).

Between 8 and 12 $\mu$ , the thermal spectral radiation emitted by the earth's atmosphere system is approximately the same as that emitted from a blackbody at 288°K. For longer wavelengths, it is approximated by a blackbody at 218 °K (Fig. II-23).

The emitted thermal radiation is not a constant over the globe. It is principally influenced by the temperature of the earth's surface, the amount of cloud cover, the temperature of the air and the moisture content of the air.

##### 2.4.5.2 Earth Albedo Radiation [II-13, II-16, II-17]

The global earth albedo is the ratio of the total radiation reflected from the earth to the solar radiation incident on the earth. The spectral



NOTE: THE 288°K BLACKBODY CURVE APPROXIMATES THE RADIATION FROM THE EARTH'S SURFACE, AND THE 218°K BLACKBODY CURVE APPROXIMATES THE RADIATION FROM THE ATMOSPHERE IN THOSE SPECTRAL REGIONS WHERE THE ATMOSPHERE IS OPAQUE (FROM REF. II-19).

Figure II-23. A typical spectral emissive power curve for the thermal radiation leaving the earth.

distribution can be approximated by a blackbody at 5760 °K. Total ( $\sim 0.2$  to  $4.0 \mu$ ) global is 0.30. Visual albedo ( $0.4$  to  $0.7 \mu$ ) is approximately 0.40. Visual albedo is somewhat higher than total albedo since less solar radiation in the visual wavelengths is absorbed in the earth's atmosphere system.

Local albedo for a wavelength region is defined by

$$\frac{\int_0^{2\pi} \int_0^{\pi/2} I(\theta, \phi) \cos \theta \sin \theta \, d\theta \, d\phi}{F \cos z}$$

where  $I$  is the emergent intensity,  $F$  is the incident flux and  $z$  the solar zenith angle.  $\theta$  and  $\phi$  are the geocentric latitude and longitude, respectively. Local albedo is highly variable, depending on the spatial position of the observer and the time of the observation.

Local albedo values range from 0.10 to 0.80 for clouds, 0.05 to 0.45 for land, and 0.03 to 0.20 for water. To date, there is no precise theoretical or empirical model for the albedo which includes:

- a. The geometrical-physical aspects of the surface, scattering by the clear atmosphere and clouds.
- b. The geographical-meteorological aspects as a function of time and position.

#### 2.4.5.3 Thermal Environment Parameters [II-16, II-17]

Variation of the Time Average Effective Values about Their Global Values

Time Increment	Albedo Variation	Earth Emitted Thermal Radiation Variation $W/m^2$
$\Delta t < 0.3$ hr	+0.30	+28
	+0.30	237
	-0.15	-97
$0.3 < \Delta t < 3$ hr		+24
	$0.30 \pm 0.10$	237
		-48
$\Delta t > 3$ hr	$0.30 \pm 0.05$	$237 \pm 21$

The time average effective value is defined to be the average value of the albedo (or earth thermal radiation), taken over a time increment  $\Delta t$ , to which a satellite in near-earth orbit (period  $\lesssim 3$  hr) is exposed. The range of the time average effective value decreases with increasing  $\Delta t$  and for large  $\Delta t$  (i.e.,  $\approx 3$  hr) approaches the range because of the seasonal variation.

See Paragraph 1.3.1.1 for the value of the solar constant.



#### 2.4.5.4 Mean Visual Illumination of Earth by Sun (Day Outside Atmosphere)

$$1.37 \times 10^5 \text{ lumens/m}^2.$$

#### 2.4.5.5 Mean Brightness of Full Earth at Subsolar Point [II-17]

$$1.7 \times 10^4 \text{ candles/m}^2.$$

#### 2.4.6 Radiation Properties of the Sun (Thermal)

See Paragraph 1.3.3.

#### 2.4.7 Solar Cycle Predictions

A complete description of the MSFC Solar Cycle Prediction Program is given in Appendix A.

#### 2.4.8 Dose Rate Calculation

The radiation dose contributed by electrons and protons trapped in the earth's magnetic field should be determined for a given shielding configuration and trajectory by the MSC Orbital Dose Code which uses the MSC Radiation and Fields Branch dose calculation programs. The geomagnetic coordinates corresponding to each spacecraft position should be obtained from the McIlwain field-fit code [II-18] and Jensen and Cain coefficients [II-19]. The electron energy spectra should be obtained from the Vette 1968 [II-11, II-12] projected electron environment. The proton energy spectra should be determined from the Air Force Weapons Laboratory proton flux data [II-20] by fitting the flux data to a power spectrum for proton energies less than 30 MeV and an exponential spectrum for proton energies greater than 30 MeV. A more complete description of this dose rate calculation technique is given in Reference II-21.

#### 2.4.9 Additional Information

Additional information relative to radiation and thermal properties is given in References II-22, II-23, and II-24.

## 2.5 Meteoroid Environment [II-25]

The meteoroid environment model encompasses particles of only cometary origin and is composed of sporadic meteoroids in the mass range between 1 and  $10^{-12}$  g and stream meteoroids in the mass range from 1 to  $10^{-6}$ g.

### 2.5.1 Average Total Meteoroid Environment

The average total meteoroid (average sporadic plus a derived average stream) environment is to be used for preliminary design and for mission periods that cannot be rigidly specified. When the mission launch date and duration are specified later in the design, the probability of stream damage should be evaluated.

#### 2.5.1.1 Particle Density

The mass density is  $0.5 \text{ g/cm}^3$  for all meteoroid particle sizes.

#### 2.5.1.2 Particle Velocity

The average meteoroid particle velocity is  $20 \text{ km/s}$  with the distribution as given in Figure II-24.

#### 2.5.1.3 Flux-Mass Model

The average annual cumulative meteoroid flux-mass model in logarithmic plot is described mathematically as follows:

$$10^{-6} \leq m \leq 10^0, \log N_t = -14.37 \text{ to } 1.213 \log m$$

$$10^{-12} \leq m \leq 10^{-6}, \log N_t = -14.339 \text{ to } 1.584 \log m \\ - 0.063 (\log m)^2$$

where  $N_t$  is the number of particles/ $\text{m}^2/\text{s}$  of mass  $m$  or greater and  $m$  is the mass in g.

The gravitationally focused, unshielded flux,  $N_t$ , must be multiplied by an appropriate defocusing factor for earth,  $G_e$ , and, if applicable, by the shielding factor. The  $G_e$  factor applies to all missions and is to be obtained from the equation given below. The body shielding factor for randomly oriented spacecraft,  $\zeta$ , is calculated by the method given in Figure II-25 and applies to all missions. For oriented spacecraft, the effects of body shielding on the number of impacts as seen by parts of the spacecraft must be determined on a unique basis. The defocusing factor ( $G_e$ ) may be calculated by

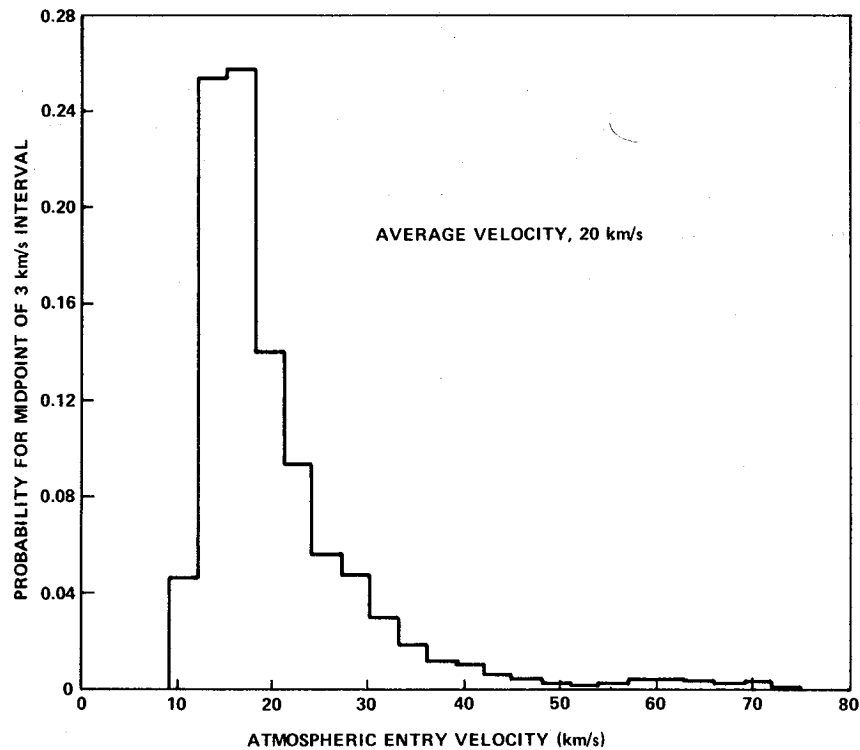
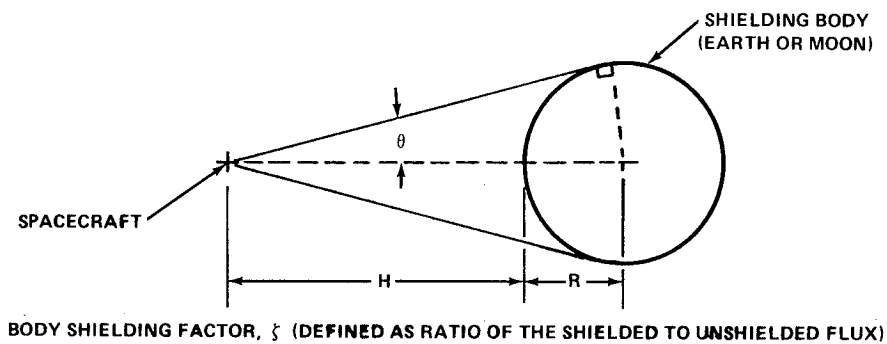


Figure II-24. Probability velocity distribution for sporadic meteoroids.



$$\zeta = \frac{1 + \cos \theta}{2}$$

WHERE:  $\sin \theta = \frac{R}{R + H}$

R = RADIUS OF SHIELDING BODY

H = ALTITUDE ABOVE SURFACE

SUBSCRIPTS:

e = EARTH

m = MOON

Figure II-25. Method for determining body shielding factor for randomly oriented spacecraft.

$$G_e = 0.568 + \frac{0.432}{r}$$

where  $r$  is the distance from the center of the earth in units of the earth's radius.

## 2.5.2 Sporadic Meteoroids

The average sporadic meteoroid environment is to be used in conjunction with the specific stream meteoroid environment for the design of a vehicle with a specified mission period (launch date and duration).

### 2.5.2.1 Particle Density

The mass density is  $0.5 \text{ g/cm}^3$  for all sporadic particle sizes.

### 2.5.2.2 Particle Velocity

The average sporadic particle velocity is  $20 \text{ km/s}$  with the distribution as given in Figure II-24.

### 2.5.2.3 Flux-Mass Model

The flux-mass model for sporadic meteoroids is described mathematically as follows: For  $10^{-6} \leq m \leq 10^0$ ,

$$\begin{aligned} \log N_{sp} = & -14.41 - 1.22 \log m + \log G_e \\ & + \log \frac{1 + \sqrt{1 - 1/r^2}}{2} + \log F_{\text{seasonal}}, \end{aligned}$$

for  $10^{-12} \leq m \leq 10^{-6}$ ,

$$\begin{aligned} \log N_{sp} = & -14.339 - 1.584 \log m - 0.063 (\log m)^2 \\ & + \log G_e + \log \frac{1 + \sqrt{1 - 1/r^2}}{2} + \log F_{\text{seasonal}}, \end{aligned}$$

where

$N_{sp}$  = number of particles/ $\text{m}^2/\text{s}$  of mass  $m$  or greater encountered by a randomly oriented surface

$m$  = mass in g

$G_e$  = the defocusing factor for the earth, which is applicable to all missions and is equal to  $0.568 + 0.432/r$

$r$  = the distance from the center of the earth in units of the earth's radius

$F_{\text{seasonal}}$  = a seasonal factor obtained from the table below. (The factor is obtained by taking the average of monthly factors listed for the months of the mission duration.)

Monthly Factors

January	0.6
February	0.4
March	0.5
April	0.6
May	1.1
June	1.6
July	1.8
August	1.6
September	1.1
October	1.1
November	0.9
December	0.7

2.5.3 Stream Meteoroids

The specific stream environment is to be used in conjunction with the sporadic meteoroid environment in the design of a vehicle with a specified mission period (launch date and duration).

2.5.3.1 Particle Density

The mass density is  $0.5 \text{ g/cm}^3$  for all stream particle sizes.

2.5.3.2 Particle Velocity

The particle velocity of each stream is that given in Table II-1.

TABLE II-1. MAJOR METEOROID STREAMS

Name	Period of Activity	Date of Maximum	$F_{\max}^a$	Geocentric Velocity (km/s)
Quadrantids	Jan. 2 to 4	Jan. 3	8.0	42
Lyrids	Apr. 19 to 22	Apr. 21	0.85	48
$\eta$ -Aquarids	May 1 to 8	May 4 to 6	2.2	64
O-Cetids	May 14 to 23	May 14 to 23	2.0	37
Arietids	May 29 to June 19	June 6	4.5	38
$\zeta$ -Perseids	June 1 to 16	June 6	3.0	29
$\beta$ -Taurids	June 24 to July 5	June 28	2.0	31
$\delta$ -Aquarids	July 26 to Aug. 5	July 8	1.5	40
Perseids	July 15 to Aug. 18	Aug. 10 to 14	5.0	60
Orionids	Oct. 15 to 25	Oct. 20 to 23	1.2	66
Arietids, southern	Oct. through Nov.	Nov. 5	1.1	28
Taurids, northern	Oct. 26 to Nov. 22	Nov. 10	0.4	29
Taurids, night	Nov.		1.0	37
Taurids, southern	Oct. 26 to Nov. 22	Nov. 5	0.9	28
Leonids, southern	Nov. 15 to 20	Nov. 16 to 17	0.9	72
Bielids	Nov. 12 to 16	Nov. 14	0.4	16
Geminids	Nov. 25 to Dec. 17	Dec. 12 to 13	4.0	35
Ursids	Dec. 20 to 24	Dec. 22	2.5	37

a.  $F_{\max}$  is the ratio of average maximum cumulative stream to average sporadic flux for a mass of 1 g and a velocity of 20 km/s.

### 2.5.3.3 Flux-Mass Model

The cumulative flux-mass model applicable to each individual stream is described mathematically as follows: For  $10^{-6} \leq m \leq 10^0$ ,

$$\log N_{st} = -14.41 - \log m - 4.0 \log (V_{st}/20) + \log F$$

where

$N_{st}$  = number of particles/m<sup>2</sup>/s of mass  $m$  or greater

$m$  = mass in g

$V_{st}$  = geocentric velocity of each stream in km/s

$F$  = ratio of cumulative flux of stream to the average cumulative sporadic flux as calculated from Figures II-26a and II-26b for the portion of the stream's duration within the mission period.

No gravitational factor is to be applied to the flux of a specific stream. Similarly, no shielding effect exists unless a shielding body eclipses the spacecraft relative to the radiant of a stream. When an eclipse occurs, the flux of that specific stream is zero.

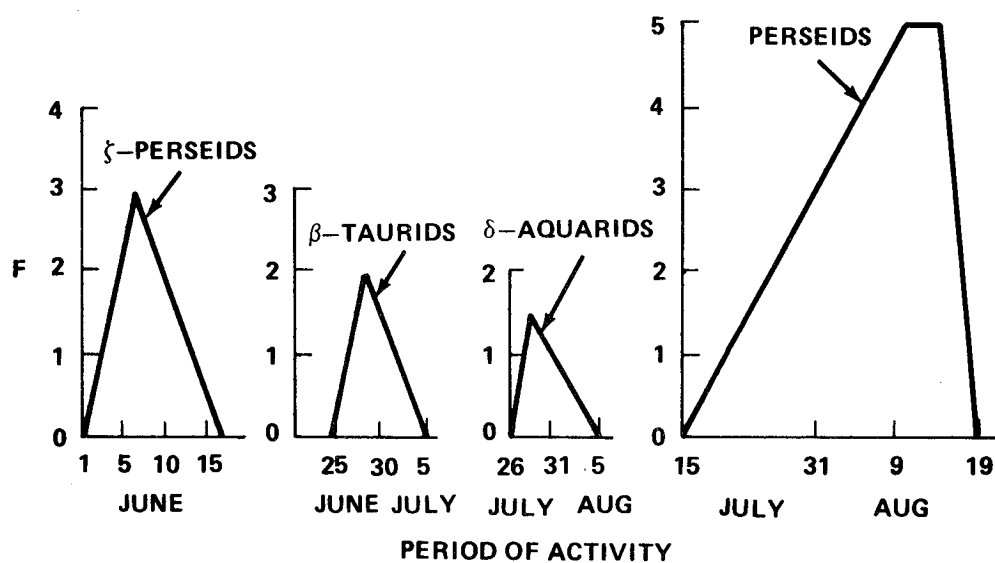
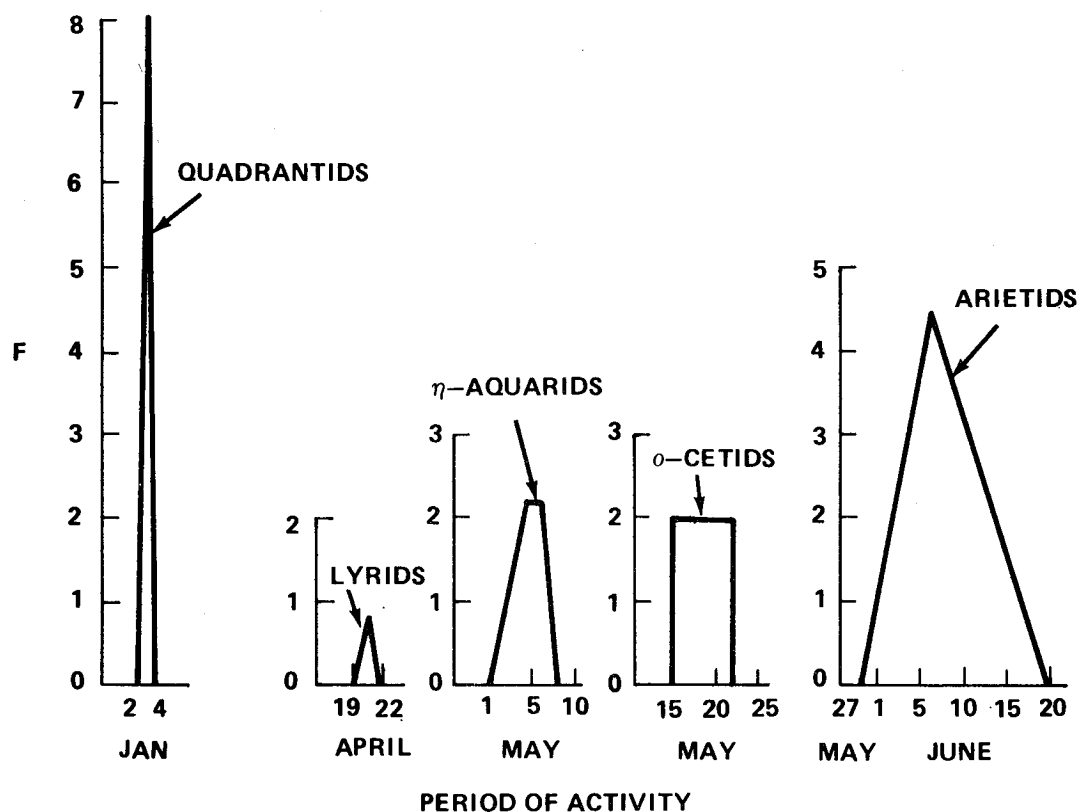
### 2.5.4 Additional Information

Additional information relative to the meteoroid environment is given in Reference II-25.

## 2.6 Geomagnetic Environment

### 2.6.1 Magnetic Field

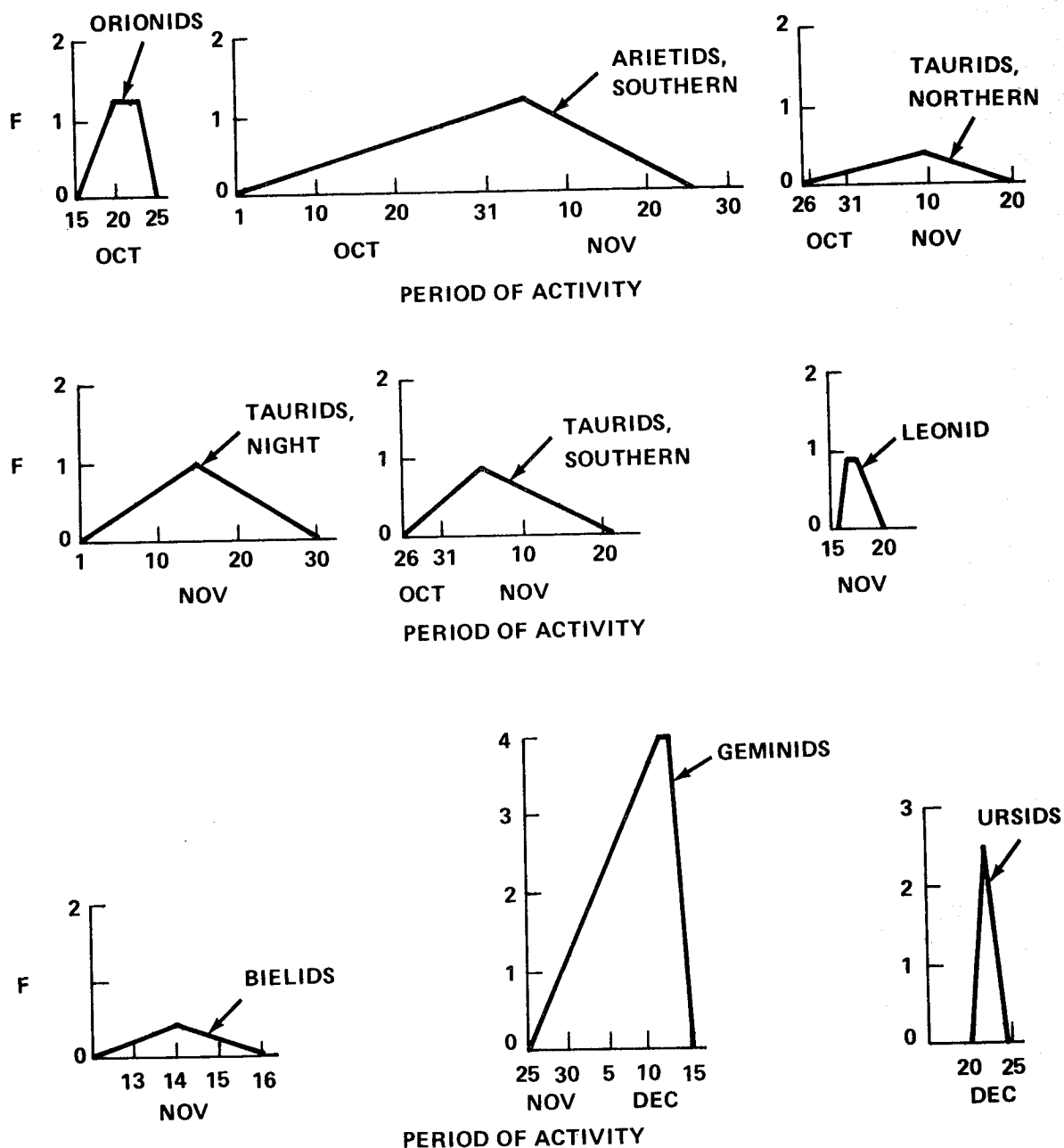
The earth is surrounded by a magnetic field, often called the geomagnetic or terrestrial magnetic field, originating in its interior. The axis of the hypothetical magnet does not coincide with the north-south poles, and is displaced from the center by a distance of about 450 km. Consequently, the geomagnetic field is not exactly symmetrical to the earth's surface.



$$F = \frac{\text{CUMULATIVE FLUX OF STREAM}}{\text{AVERAGE CUMULATIVE SPORADIC FLUX}}$$

Figure II-26a. Activity ratio factor versus period of activity (Jan. - Aug.) for major streams based on photographic meteors (mass = 1 g, velocity = 20 km/s).





$$F = \frac{\text{CUMULATIVE FLUX OF STREAM}}{\text{AVERAGE CUMULATIVE SPORADIC FLUX}}$$

Figure II-26b. Activity ratio factor versus period of activity (Sept. - Dec.) for major streams based on photographic meteors (mass = 1 g, velocity = 20 km/s).

The magnetic poles on the surface are the locations that, for all practical purposes, have the lines of force perpendicular to the surface.

The geomagnetic axis is a line joining the two magnetic poles. At the magnetic equator the lines of force are parallel everywhere to the earth's surface; i.e., horizontal. From about 170 deg W eastward to about 30 deg E, the geomagnetic equator is south, but at other longitudes it is north of the geographic equator.

The total strength of the earth's magnetic field varies over the surface of the earth from 0.65 to 0.70 gauss near the magnetic poles; it is weakest toward the equatorial region where its value is 0.30 to 0.35 gauss. Its variation with latitude is by no means uniform — an exceptionally low value of 0.25 gauss has been recorded in southeast Brazil.

At some distance from the earth, the intensity variation may be taken to be inversely proportional to the cube of the distance from the center of the dipole. The average total magnetic field is given in the following tabulation.

Average Total Magnetic Field in Gauss

Altitude (km)	Geodetic Colatitude (deg)			
	0	30	60	90
200	0.52243	0.50782	0.40338	0.31406
400	0.48121	0.46403	0.36670	0.28630
1000	0.37978	0.35841	0.28088	0.21778
2000	0.26428	0.24682	0.18904	0.14629
3000	0.19052	0.17608	0.13343	0.10330
4000	0.14158	0.12988	0.09773	0.07571
6371.2	0.07693	0.07001	0.05217	0.04044

From measurements of the strength of the geomagnetic field, it is clear that the field is not steady, but has secular and transient variations. It takes many years for the effect of the secular variations to become significant. The transient variation, however, occur within days or less and are caused by external factors, some of which are of solar origin.

### 2.6.2 Temporal Variations

Temporal variations are short-duration disturbances in the geomagnetic field resulting from solar activity and changing relative positions of the sun and earth. These variations typically have durations ranging from a few seconds to several days and amplitudes from a few hundredths to several hundred gammas.

The sun's emission of a solar plasma (i.e., the solar wind) influences the earth's magnetic field. When the solar plasma enters the earth's magnetic field, the interaction produces a sheath of current in the plasma which opposes, by Lenz's law, the earth's field. The earth's field is compressed until its magnetic pressure (i.e., its magnetic energy density) balances the kinetic pressure of the solar plasma. This balance is reached at about 10 earth radii, and therefore the earth's magnetic field is to be limited to such a finite distance in a direction toward the sun. In directions that make an appreciable angle with the sun, the influence of the earth's magnetic field will be extended considerably.

### 2.6.3 Magnetic Field at Geosynchronous Altitudes

At synchronous altitude, an average magnetic field of about 138  $\gamma$  (138 nT) is to be expected. Approximations to the magnetic field in this region may be obtained from the spherical harmonic expansion model [II-26], but expansion beyond the first 8 terms in this model is not warranted because contributions from external sources are not included.

### 2.6.4 Models of the Earth's Magnetic Environment

For design studies requiring a detailed description of the earth's magnetic field, Reference 26 should be used.

### 2.6.5 Additional Information

More detailed information relative to the geomagnetic environment is given in the two design criteria monographs [II-27, II-28].

## 2.7 Astrodynamics Constants

### 2.7.1 Earth Constants (Epoch 1960.0) [29]

Distance from sun (average)	$1.495978930 \times 10^8$ km
Eccentricity of orbit	0.0167295
Orbital period (sidereal) <sup>3</sup>	365.25636 days
Radius (equatorial)	6378.160 km
Mass ratio (sun/planet)	332945.6
Flattening (dynamic)	1:298.25
Average density <sup>3</sup>	5.517 g/m <sup>3</sup>
Rotational period <sup>3</sup>	23 hr, 56 min, 4.099 s
Gravitational parameter	$3.986012 \times 10^5$ km <sup>3</sup> /s <sup>2</sup>

### 2.7.2 Gravitational Potential Function for the Earth [II-29]

One of the environmental forces which exerts a torque on a large spacecraft in earth orbit is the gravity gradient. This force acts in a direction tangent to a contour line of the geopotential surface. When a spacecraft attitude is locked into a particular coordinate system (e.g., solar-fixed), the gravity gradient forces vary with time as the spacecraft's main moments of inertia axes have varying inclinations to the geopotential contour lines. Stable equilibrium may be reached by producing correcting forces of the proper magnitude and direction. The energy required for the main spacecraft attitude hold control over a period of months against gravity gradient torques can be quite large for certain spacecraft configurations.

$$U = \frac{GE}{r} \left[ 1 - \sum_{n=2}^{\infty} (a_e/r)^n J_n P_n(\sin \phi') + \sum_{n=2}^{\infty} \sum_{m=1}^{\infty} (a_e/r)^n P_{nm}(\sin \phi') (C_{nm} \cos m \lambda + S_{nm} \sin m \lambda) \right]$$

---

3. Unpublished report entitled "Astronomical Constants of the Solar System," by H. G. L. Krause, 1965, MSFC, Huntsville, Alabama.

where

$r$  = radius from center of the earth

$\phi'$  = geocentric latitude

$\lambda$  = geographic longitude

$P_{nm}$  = associated Legendre functions

$GE$  = geocentric gravitational constant

$a_e$  = equatorial radius of the earth.

Values for the zonal harmonics ( $J_n$ ) are as follows:

$$J_2 = (1082.7 \pm 0.1) \times 10^{-6}$$

$$J_3 = (-2.56 \pm 0.1) \times 10^{-6}$$

$$J_4 = (-1.58 \pm 0.2) \times 10^{-6}$$

$$J_5 = (-0.15 \pm 0.2) \times 10^{-6}$$

$$J_6 = (0.59 \pm 0.2) \times 10^{-6}$$

$$J_7 = (-0.44 \pm 0.2) \times 10^{-6}.$$

Values for the tesseral harmonics ( $C_{nm}$ ,  $S_{nm}$ ) are given in the following tabulation:

n	m	$C_{nm}$	$S_{nm}$
2	1	$0 \times 10^{-6}$	$0 \times 10^{-6}$
2	2	$1.57 \times 10^{-6}$	$-0.897 \times 10^{-6}$
3	1	$2.10 \times 10^{-6}$	$0.16 \times 10^{-6}$

n	m	C <sub>nm</sub>	S <sub>nm</sub>
3	2	0.25 × 10 <sup>-6</sup>	-0.27 × 10 <sup>-6</sup>
3	3	0.077 × 10 <sup>-6</sup>	0.173 × 10 <sup>-6</sup>
4	1	-0.58 × 10 <sup>-6</sup>	-0.46 × 10 <sup>-6</sup>
4	2	0.074 × 10 <sup>-6</sup>	0.16 × 10 <sup>-6</sup>
4	3	0.053 × 10 <sup>-6</sup>	0.004 × 10 <sup>-6</sup>
4	4	-0.0065 × 10 <sup>-6</sup>	0.0023 × 10 <sup>-6</sup>

The zonal harmonics ( $J_2, J_3, J_4 \dots$ ) have a greater effect on the orbit of a satellite than the tesseral harmonics. The tesseral harmonics cause oscillatory disturbances that change sign rapidly, but the zonal harmonic effect is cumulative. The even coefficients,  $J_2, J_4, \dots$ , can well be determined from the regression of the node, and the rotation of perigee. Reliable gravitational coefficients have been obtained from low altitude artificial satellites. Perhaps the most significant result obtained from artificial satellites is the reliable determination of  $J_2$ , and hence the flattening  $f$ . Presently accepted values of  $1/f$  range from 298.2 to 298.3. This flattening of the earth's surface causes the largest but not the only deviation of the gravitational field of the earth from that of a homogeneous sphere. Numerous higher-order spherical harmonic expansions derived from analysis of artificial satellite motions present different sets of coefficients with each analysis. Since the data still yield divergent results, only the first few terms have been used for these approximation calculations since they make the largest contribution with additional terms giving diminishing returns.

For most applications, the gravitational function may be approximated using the first three zonal harmonic coefficients ( $J_2, J_3$ , and  $J_4$ ) and the main tesseral harmonic coefficients ( $C_{22}$  and  $S_{22}$ ). The following expressions for the gravitational potential function of the earth [II-30] is therefore recommended for space vehicle design studies:

$$U = \frac{GE}{r} \left[ 1 - \frac{J_2}{2} \left( \frac{a_e}{r} \right)^2 (3 \sin^2 \phi' - 1) - \frac{J_3}{2} \left( \frac{a_e}{r} \right)^3 (5 \sin^3 \phi' - 3 \sin \phi') \right]$$

$$\begin{aligned}
& - \frac{J_4}{8} (a_e/r)^4 (35 \sin^4 \phi' - 30 \sin^2 \phi' + 3) \\
& + 3(C_{22} \cos 2\lambda + S_{22} \sin 2\lambda) (a_e/r)^2 \cos^2 \phi' \Big]
\end{aligned}$$

where

$r$  = radial distance from center of the earth

$\phi'$  = geocentric latitude

$$J_2 = 1082.7 (\pm 0.1) \times 10^{-6}$$

$$J_3 = -2.56 (\pm 0.1) \times 10^{-6}$$

$$J_4 = -1.58 (\pm 0.2) \times 10^{-6}$$

$$C_{22} = 1.57 (\pm 0.01) \times 10^{-6}$$

$$S_{22} = -0.897 (\pm 0.01) \times 10^{-6}$$

$a_e$  = equatorial radius of the earth

$\lambda$  = geographic longitude.

### 2.7.3 Geodetic Models

If accurate geodetic positions are required, the geodetic model given in Reference II-31 should be used.

## 2.8 Winds

### 2.8.1 Theoretical Models of the Wind Field

Geisler [II-32] and Kohl and King [II-33] have computed wind fields from Jacchia's [II-34, II-35] static diffusion model, J64, of the thermosphere, and Geisler [II-36] has computed winds using Jacchia and Slowey's [II-37]

modifications to J64. In these studies, the temperature, density, and mean molecular weight fields are used to derive pressure gradients which then are combined with ion drag forces in the form of models of the electron density distribution and simple vertical profiles of the kinematic viscosity to generate wind fields. Figures II-27 and II-28 [II-36] depict the distribution of winds as a function of time and latitude, respectively. The meridional winds become large at night, approaching 225 m/s above 300 km at 0200 LT, and then decrease to about 100 m/s above 300 km at 1400 LT because of the increase in ion drag (electron number density). Figures II-29 and II-30 [II-35] show that the change in electron number density changes both the wind speed and the direction. Figure II-31 shows the height distribution of the meridional and zonal wind components for the low electron number density case [II-35]. These models provide an estimate of the distribution of both the direction and speed of the winds on a global basis. They are useful first approximations; however, they should not be expected to be quantitatively accurate.

#### 2.8.2 Winds in the Lower Thermosphere — 90 to 150 km

Winds in the lower thermosphere are principally deduced from direct measurements of motions of chemiluminescent clouds, although measurements of meteor drifts, distortions of the geomagnetic currents, and measurements of charged particle drifts have contributed. Tidal and gravity waves contribute significantly to motions observed below 200 km. Kochanski [II-38] indicates that internal gravity waves contribute to all observed wind profiles between 80 and 120 km. The energy of the internal gravity waves decreases exponentially [II-39] from 80 to 180 km so that at approximately 180 km only about 20 percent of the wind data include a wave portion.

Figure II-32 shows the resultant components of the wind (the internal gravity wave motions have been removed) obtained from 25 sodium cloud experiments. Figure II-33 shows the annual, summer, and winter mean wind velocities and the frequency of occurrence of wind speeds above specific values. One of the principal features is the persistently high speeds observed between 100 and 105 km. Figure II-34 shows that intense wind shears are also observed in the region just above 100 km.

Figures II-35 and II-36 show the meridional and zonal components of winds measured at Sardinia from nine sodium cloud experiments [II-39]. These figures show the autumn to spring variations in the vertical wind profile. The zone of strong vertical shear found above 100 km by Kochanski [II-38] and shown in Figure II-34 is easily recognizable.



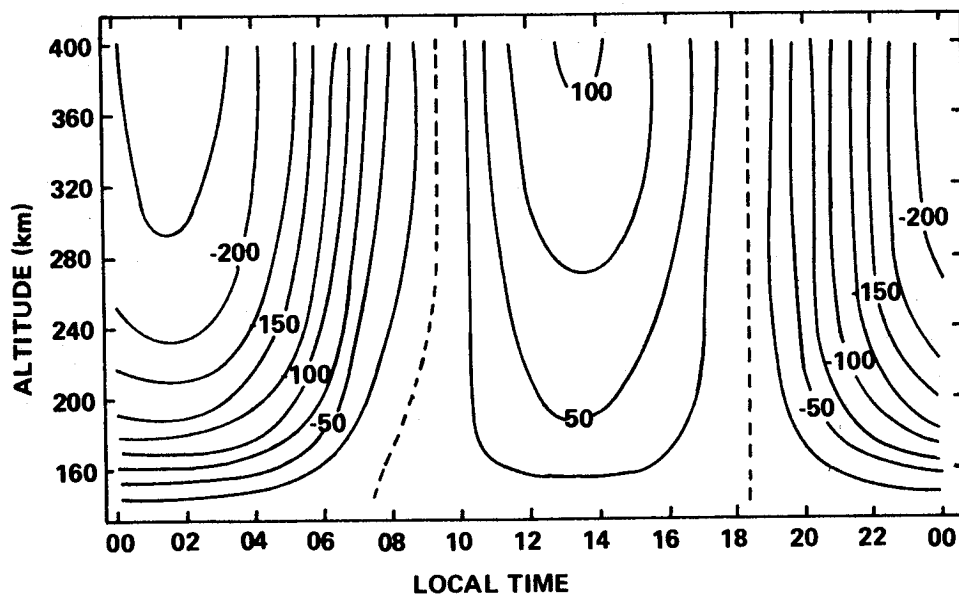


Figure II-27. Contours of meridional wind speed at 45 degrees north latitude in units of  $\text{ms}^{-1}$ , positive values directed toward the north. [Results are obtained with equinox transition times and the Jacchia and Slowey (1967) model.]

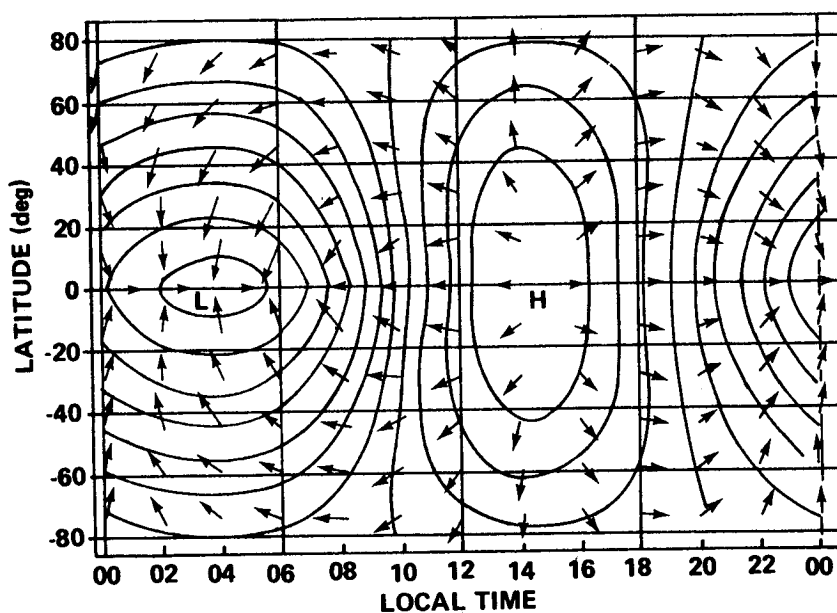


Figure II-28. Wind vectors at the 300-km level are shown against a background of isobars at this level, the longest arrow representing a wind speed of about  $225 \text{ ms}^{-1}$ . (The pressure and wind fields are symmetric about the equator.)

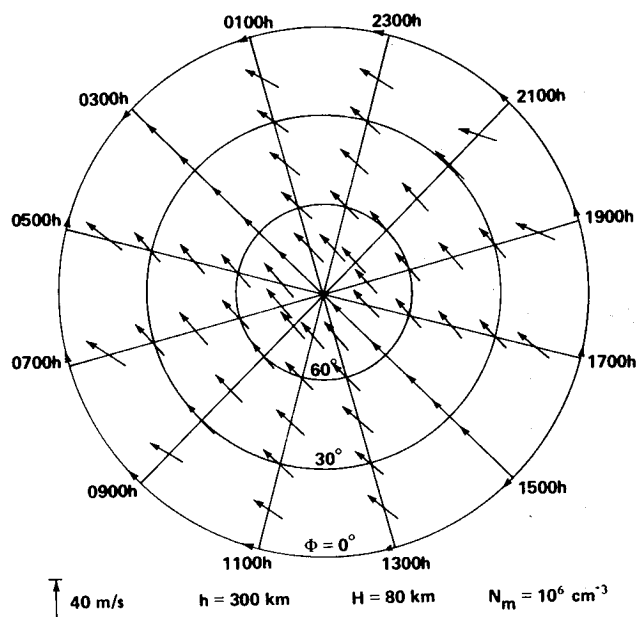


Figure II-29. The atmospheric wind system in the northern hemisphere calculated for an altitude of 300 km when the peak electron density is  $10^6 \text{ cm}^{-3}$ .

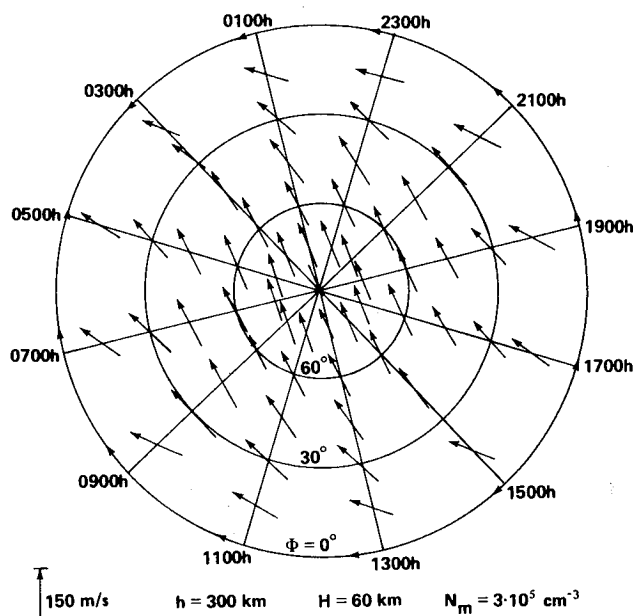


Figure II-30. The atmospheric wind system in the northern hemisphere calculated for an altitude of 300 km when the peak electron density is  $3 \times 10^5 \text{ cm}^{-3}$ .

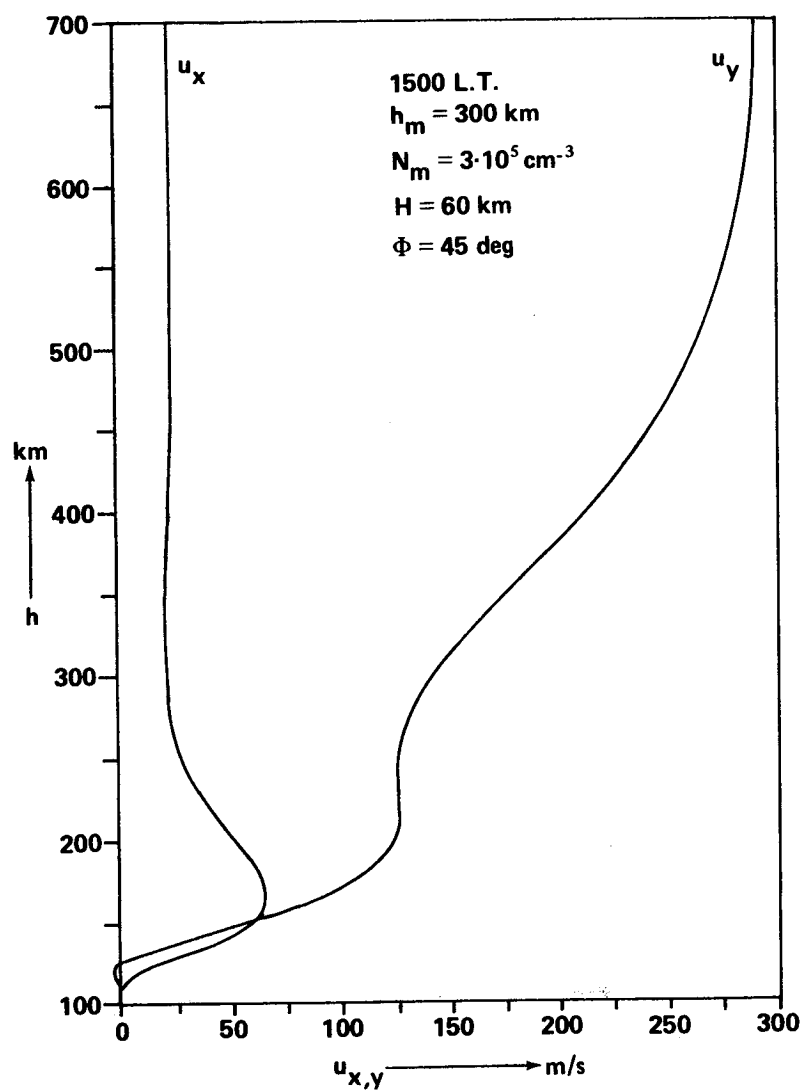


Figure II-31. The variation with height of the horizontal velocity components at 15.00 L.M.T. at a latitude of 45 degrees.

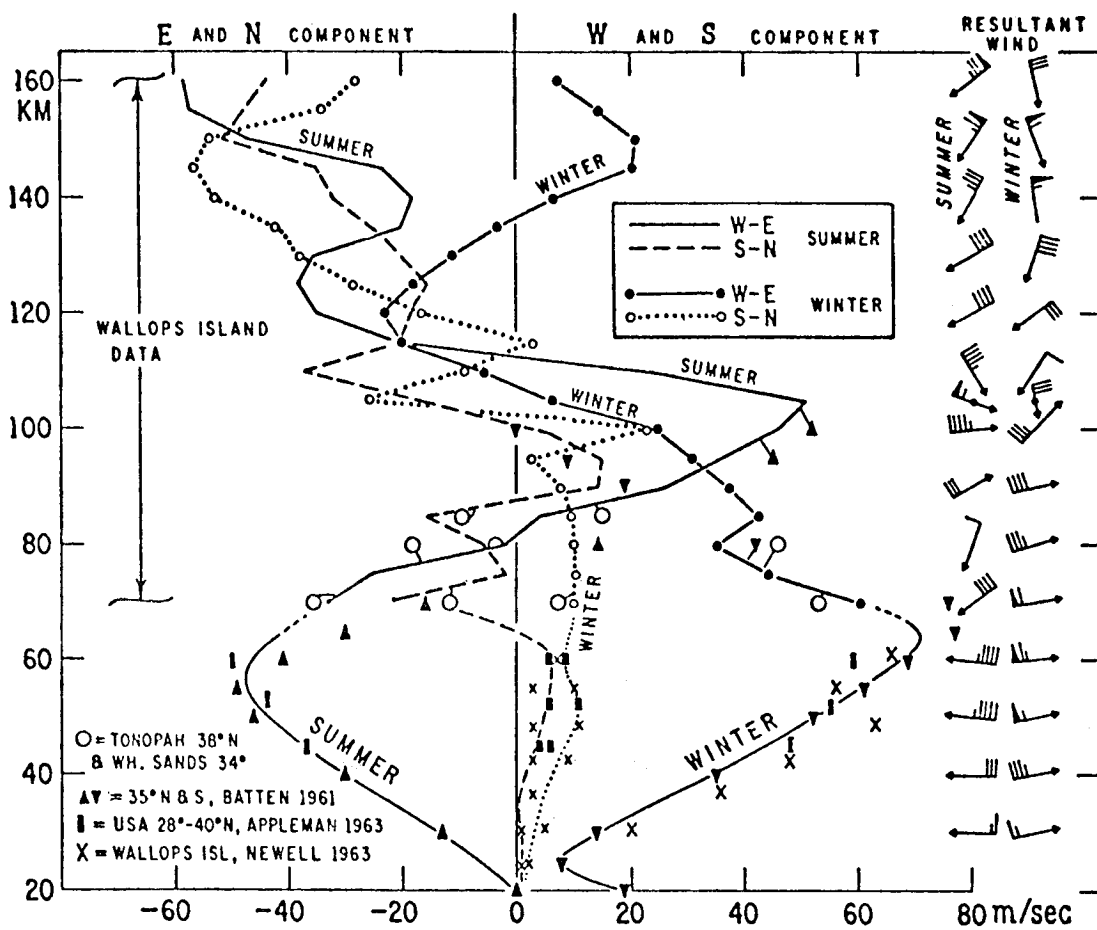


Figure II-32. Resultant components of the wind near latitude 38 degrees N. (The upper part is based on 25 sodium cloud experiments from Wallops Island. Arrows indicate the resultant wind.)

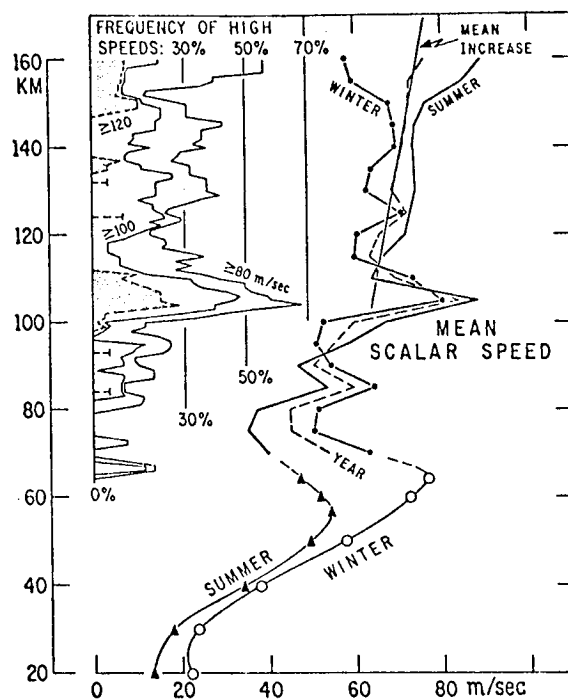
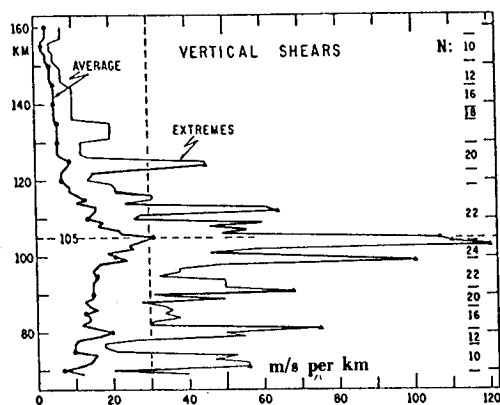


Figure II-33. Averages of the absolute value of wind velocity regardless of direction (i.e. the mean scalar speed), based on the same data as Figure II-32. (Inset: frequency of occurrence of speeds over 80, 100, and 120 m/s.)



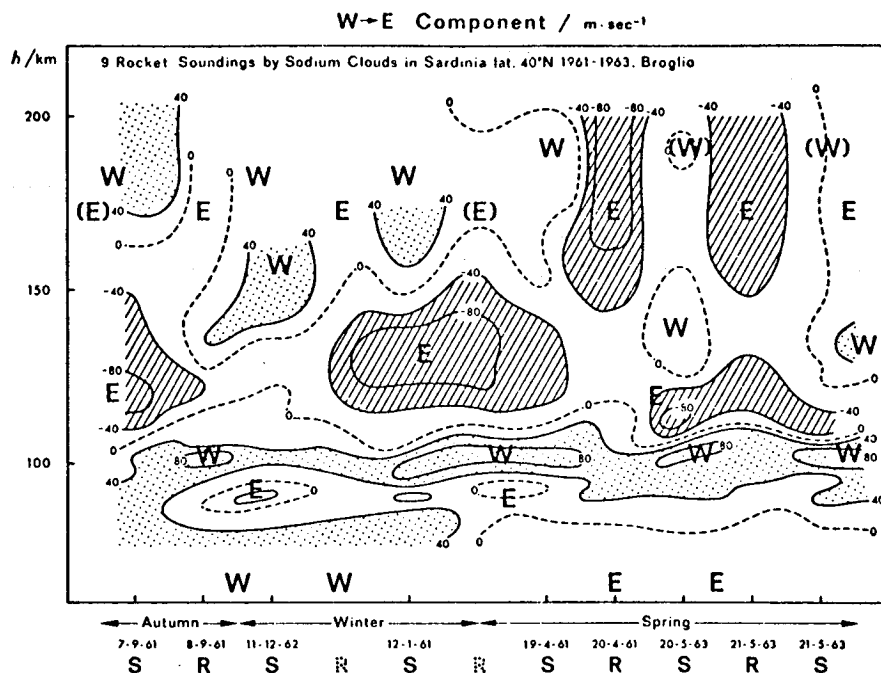


Figure II-35. Results of rocket soundings by sodium clouds in Sardinia 1961-1963, east-west. (Numerical indications give speed in m/s.)

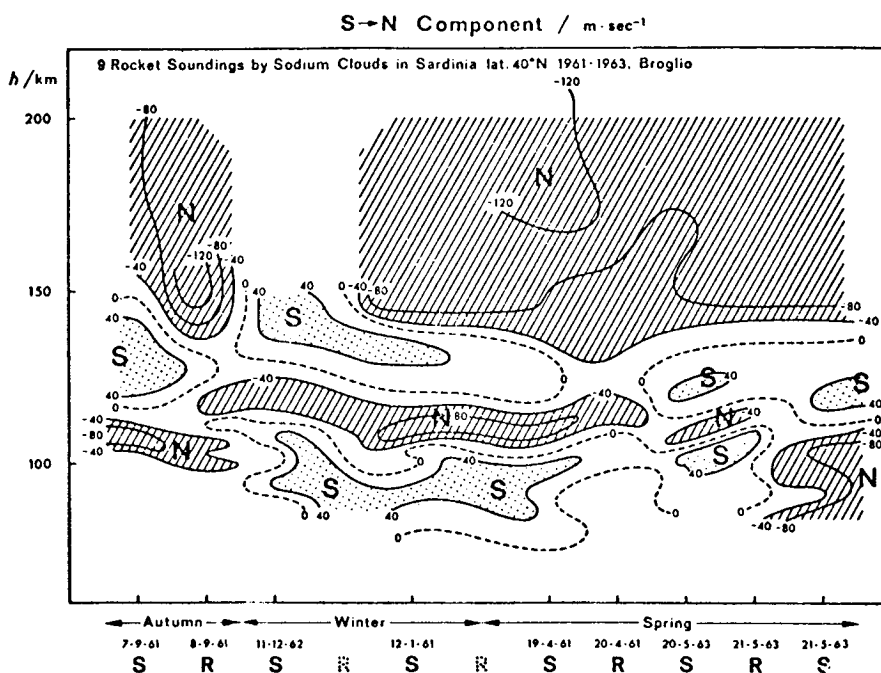


Figure II-36. Result of rocket soundings by sodium clouds in Sardinia 1961-1963, north-south. (Numerical indications give speed in m/s.)

Figures II-32, II-35, and II-36 show that above 150 km a rather persistent equatorward flow is observed and that a weak westward flow observed in the winter gives way to a stronger eastward flow in spring and summer. Kochanski [II-38] indicates that a general equatorward flow occurs for both summer and winter in the region above 100 km, whereas Fedele and Zanela [II-40] (Fig. II-36) indicate that some seasonal variation is observed in the meridional winds between 100 and 150 km. In addition, Kochanski in Figure II-32 indicates that the zonal component changes from westward (90 to 115 km) to eastward (115 to 140 km) with increasing altitude for both seasons, whereas Fedele and Zanela indicate a more complicated seasonal variation.

Data from chemiluminescent cloud experiments give instantaneous wind profiles at specific locations. The data are complicated by the fact that many dynamic processes contribute to the observed profile. Data from these experiments are obtained at widely separated locations and times. Consequently, the data give little indication of global fields or processes. Neither do the data give good measure of mesoscale variability of the winds. Thus, these data give a general indication of the types of magnitudes of motion one should expect to find in probing the lower thermosphere, but no information on the general distribution of the winds as do those studies using the global distribution of density to derive horizontal winds.

### 2.8.3 Winds Above 150 km

Above 150 km, the principal source of wind data is observation of variations of the inclination angle of satellites in orbit. King-Hele has studied these variations over the past 8 years to determine the eastward rotation rate of the upper atmosphere. Figure II-37 summarizes the results of these studies.<sup>4</sup>

In Figure II-37,  $\Lambda$  is the rotation rate of the atmosphere, where  $\Lambda = 1$  is the rotation rate of the earth. To determine the zonal velocity  $u_x$  relative to the earth at an altitude  $z$  and latitude  $\phi$  we have

$$u_x = \omega(\Lambda - 1)(r_E + z) \cos \phi,$$

where  $r_E$  is the radius of earth and  $\omega$  is the rotation rate,

$$\omega = 7.292116 \times 10^{-5} \text{ rad/s.}$$

---

4. D. G. King-Hele, "Measurement of Upper-Atmospheric Rotational Speed from Changes in Satellite Orbits," Space Res., 14, 1971 (Unpublished).

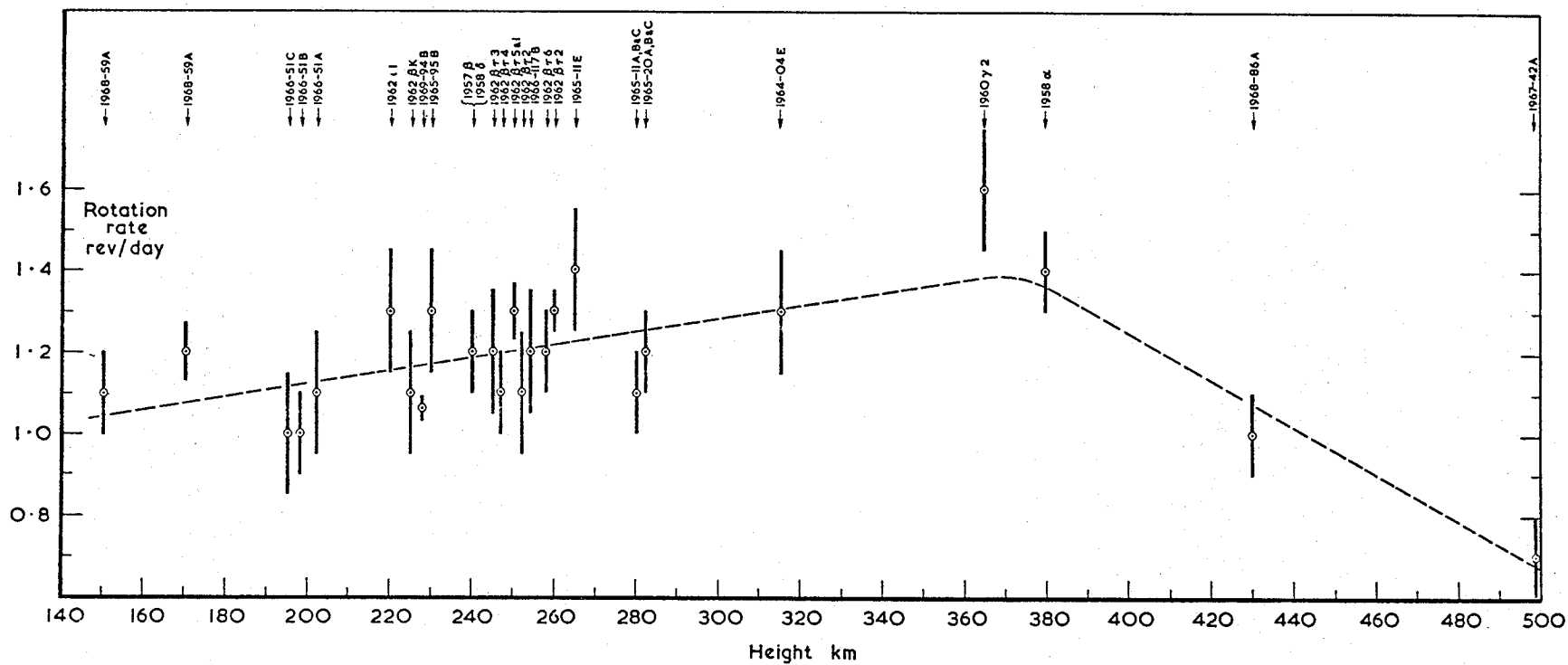


Figure II-37. Mean upper-atmosphere rotation rate, derived from analysis of 29 satellite orbits.



With these definitions, Figure II-37 indicates that the atmosphere is rotating faster than the earth above 140 km to about 450 km. The average eastward winds are indicated to increase from a band 40 m/s at 200 km to 160 m/s at 350 km at 30-degree latitude. Above 450 km, a reversal exists of the wind direction as  $\Lambda < 1$ .

Challinor [II-41] believes that the apparent mean rotation of the upper atmosphere is caused by an eastward daytime motion which is primarily confined to equatorial latitudes. The satellite observations are weighted toward low latitude and daytime conditions. A number of other explanations have been offered for these observations of the super-rotation of the upper atmosphere.

#### 2.8.4 Vertical Winds

The vertical velocities are about two orders of magnitude less than the horizontal velocities. Dickinson and Geisler [II-42] in a study based on Geisler's [II-32] earlier work find the vertical velocities generally to be less than 10 m/s.

#### 2.8.5 Anomalous Strong Winds

Increases in the density of the upper atmosphere during geomagnetic storms have been observed many times. On one occasion near the auroral oval a horizontal wind speed on the order of  $1.5 \text{ km sec}^{-1}$  was observed to occur at approximately 150 km altitude simultaneously with a large increase in the ambient density during a very large geomagnetic storm. Theoretical calculations support this observation and also postulate the possibility of vertical wind speeds on the order of  $50 - 75 \text{ ms}^{-1}$ . Large changes in the composition of the neutral upper atmosphere have been observed during geomagnetic storms. Users should contact the Aerospace Environment Division's Space Environment Branch if a specific design problem arises which might be affected by these anomalous occurrences.

#### 2.8.6 Design Criteria

For design purposes, the following scalar wind speeds ( $\text{ms}^{-1}$ ) should be used:

<u>Altitude (km)</u>	<u>Speed (ms<sup>-1</sup>)</u>	
	<u>Mean</u>	<u>Maximum</u>
90 to 150	200	325
150 to 200	200	250
200 to 300	150	200
300 to 400	150	200

These wind speeds are referenced to a coordinate system fixed to and rotating with the earth's surface.

Satellites other than those at geosynchronous altitude will be affected by a combination of these winds and the winds caused by the rotation of the earth which can be calculated from:

$$u_x = \omega(R_E + z) \cos \varphi \quad \text{ms}^{-1}$$

where

$$\omega = 7.292116 \times 10^{-5} \text{ rad s}^{-1}$$

$$R_E = 6378.1 \text{ km}$$

$z$  = geometric altitude (km) above the earth

$\varphi$  = geocentric latitude.

These winds will always be from the west and at the equator they will have the following values:

<u>z(km)</u>	<u>Speed (ms<sup>-1</sup>)</u>
0	465
100	472
200	480
300	488
400	495

These wind speeds are referenced to a nonrotating coordinate system fixed at the center of the earth.

The winds driven by the pressure gradients are influenced strongly by the electron density profiles distributions; therefore, for problem areas requiring directional wind inputs or detailed information of the winds at these altitudes, users should contact the Aerospace Environment Division's Space Environment Branch.

## REFERENCES

- II-1. Weidner, D. K., West, G. S., and Swenson, G. R.: Variations in Orbital Altitude Atmospheric Density for MSFC 1971-1976 Space Station Programs. NASA TM X-53815, February 1969.
- II-2. Models of Earth's Atmosphere (120 to 1000 km). NASA SP-8021, May 1969.
- II-3. Weidner, D. K., and Swenson, G. R.: Diurnal Variations in the Thermosphere from a Series of Marshall-University of Michigan Probes. Journal of Geophysical Research, vol. 74, 1969, pp. 4755-4763.
- II-4. The Earth's Ionosphere. NASA SP-8049, March 1971.
- II-5. Chan, K. L., and Colin, L.: Global Electron Density Distribution from Topside Soundings, Proceedings of IEEE, vol. 57, no. 6, June 1969, pp. 990-1004.
- II-6. Frihagen, J. (Ed.): Electron Density Profiles in Ionosphere and Exosphere. North Holland Publishing Co., Amsterdam, 1966.
- II-7. Beard, B. D. and Johnson, F. S.: Charge and Magnetic Field Interaction with Satellites. J. Geophys. Res., Vol. 65, 1960, p. 1.
- II-8. Drell, S. D., Toley, H. M., and Ruderman, M. A.: Drag and Propulsion of Large Satellites in the Ionosphere; An Alfvén Propulsion Engine in Space. J. Geophys. Res., vol. 70, 1965, p. 3131.
- II-9. Burrell, M. O., Wright, J. J., and Watts, J. W.: An Analysis of Energetic Space Radiation and Dose Rates. NASA TN D-4404, February 1968.
- II-10. Brandli, H. W.: The Natural Environment of a Satellite in a Synchronous Circular Orbit. Technical Report 192, Air Weather Service, USAF, June 1967.
- II-11. Vette, J. I. et al.: Models of the Trapped Radiation Environment. vols. 1 and 2, NASA SP-3024, 1966.

## REFERENCES (Continued)

- II-12. Vette, J. I. et al.: Models of the Trapped Radiation Environment. vol. 3, NASA SP-3023, 1967.
- II-13. Johnson, F. S.: Satellite Environment Handbook. Second Edition, Stanford University Press, Stanford, California, 1965.
- II-14. Haverly, G.: Design Values of Solar Radiant, Earth Albedo and Earth Radiant Flux for Near-Earth Orbiting Satellites. Technical Information Series No. 63SD201, Reentry Systems Department, General Electric, February 25, 1963.
- II-15. Kaplan, J.: Near-Earth Electromagnetic Radiation Environment. Scientific Report No. 4, General Electric GE-9500-ECS-SR-4, December 1968.
- II-16. Raschke, E., and Bandeen, W. R.: The Radiation Balance of the Planet Earth from Radiation Measurements of the Satellite Nimbus II. Journal of Applied Meteorology, vol. 9, April 1970, pp. 215-238.
- II-17. Earth Albedo and Emitted Radiation. NASA SP 8067, July 1971.
- II-18. McIlwain, C. E.: Coordinates for Mapping the Distribution of Magnetically Trapped Particles. J. Geophys. Res., vol. 66, November 1961, pp. 3681-3691.
- II-19. Jensen, D. C., and Cain, J. C.: An Interim Geomagnetic Field. Abstract, J. Geophys. Res., vol. 67, August 1962, pp. 3568-3569.
- II-20. Thede, A. L.: OV 3-4 Dose Rate and Proton Spectral Measurement. AFWL-TR-68-128, AF Weapons Laboratory, January 1969.
- II-21. White, T. T., Robbins, D. E., and Hardy, A. C.: Radiation Environment for the 1975-1985 Space Station Program. NASA/MSC Document No. MSC-00183-A, November 1969.
- II-22. Suomi, V. E., and Vonder Haar, T. H.: Satellite Observations of the Earth's Radiation Budget. Science, vol. 163, February 1969, pp. 3868.
- II-23. Raschke, Ehrhard: The Radiation Balance of the Earth-Atmosphere System from Radiation Measurements of the Nimbus II Meteorological Satellite. NASA TN D-4589, Washington, D. C., July 1968.

## REFERENCES (Continued)

- II-24. Allen, C. W.: Astrophysical Quantities. Athlone Press, University of London, 1963.
- II-25. Meteoroid Environment Model - 1969 (Near-Earth to Lunar Surface). NASA SP-8013, March 1969.
- II-26. International Geomagnetic Reference Field 1965.0. Journal of Geophysical Research, vol. 74, no. 17, August 1969, p. 4407.
- II-27. Magnetic Fields Earth and Extraterrestrial. NASA SP-8017, March 1968.
- II-28. Spacecraft Magnetic Torques. NASA SP-8018, March 1969.
- II-29. Melbourne, W. G., Mulholland, J. D., Sjogren, W. L., and Sturms, F. M., Jr.: Constants and Related Information for Astrodynamic Constants, 1968. Technical Report 32-1306, Jet Propulsion Laboratory, July 1968.
- II-30. Apollo Navigations Working Group. Apollo Missions and Navigation Systems Characteristics, Technical Report No. AN-1.3, Revision 2, October 1969.
- II-31. Lundquist, C. A., and Veis, G.: Geodetic Parameters for a 1966 Smithsonian Institution Standard Earth, Volume I. Smithsonian Astrophysical Observatory, Special Report 200, 1966.
- II-32. Geisler, J. E.: Atmospheric Winds in the Middle Latitude F-Region. J. Atmos. Terr. Phys., vol. 28, 1966, pp. 703-720.
- II-33. Kohl, H., and King, J. W.: Atmospheric Winds Between 100 and 700 km and Their Effects on the Ionosphere. J. Atmos. Terr. Phys., vol. 29, 1967, pp. 1045-1062.
- II-34. Jacchia, L. G.: Static Diffusion Models of the Upper Atmosphere with Empirical Temperature Profiles. Special Rpt. 170, Smithsonian Astrophysical Observatory, 1964, p. 50.
- II-35. Jacchia, L. G.: The Temperature Above the Thermopause. Space Res., vol. 5, 1965, pp. 1152-1174.

## REFERENCES (Concluded)

- II-36. Geisler, J. E.: A Numerical Study of the Wind System in the Middle Thermosphere. *J. Atmos. Terr. Phys.*, vol. 29, 1967, pp. 1469-1482.
- II-37. Jacchia, L. G., and Slowey, J.: The Shape and Location of the Diurnal Bulge in the Upper Atmosphere. *Space Res.*, vol. 7, 1967, pp. 1077-1090.
- II-38. Kochanski, A.: Atmospheric Phenomena in the Height Region from 70 to 160 km. WMO Tech. Note No. 70, World Meteorological Organization, Geneva, 1965, pp. 140-169.
- II-39. Kochanski, A.: Atmospheric Motions from Sodium Cloud Drifts of Four Locations. *Monthly Weather Rev.*, vol. 94, 1966, pp. 199-212.
- II-40. Fedele, D., and Zanela, A.: Atmospheric Structure Between 30 and 120 km. Winds and Turbulence in Stratosphere, Mesosphere and Thermosphere, K. Rawer, ed., North-Holland Publishing Co., Amsterdam, pp. 1-33.
- II-41. Challinor, R. A.: The Apparent Rotation of the Upper Atmosphere. *Planet. Space Sci.*, vol. 16, 1968, pp. 557-566.
- II-42. Dickinson, R. E., and Geisler, J. E.: Vertical Motion Fields in the Middle Thermosphere from Satellite Drag Densities. *Monthly Weather Rev.*, vol. 94, 1968, pp. 606-616.

## BIBLIOGRAPHY

Webber, W. R.: An Evaluation of the Radiation Hazard Due to Solar-Particle Events. Technical Report D2-90496, The Boeing Company, Seattle, Washington, December 1963.





## SECTION III. CISELUNAR SPACE

### 3.1 Definition

Cislunar space is defined as that region between the earth and moon that extends from 65 000 to 344 400 km. The outer limit of this region is 40 000 km inside the mean lunar orbital distance and is considered to be the outer limit (from the moon) of the moon's sphere of influence.

### 3.2 Gas Properties

Same as Interplanetary Space (see Paragraph 1.2).

### 3.3 Radiation Environment

Same as Interplanetary Space (see Paragraph 1.3).

### 3.4 Meteoroid Environment

The meteoroid environment model encompasses particles of only cometary origin and is composed of sporadic meteoroids in the mass range between 1 and  $10^{-12}$ g and stream meteoroids in the mass range from 1 to  $10^{-6}$ g.

#### 3.4.1 Average Total Meteoroid Environment

Same as Terrestrial Space (see Paragraph 2.5.1).

#### 3.4.2 Sporadic Meteoroids

The average sporadic meteoroid environment is to be used in conjunction with the specific stream meteoroid environment in design of a vehicle with a specified mission period (launch date and duration).

#### 3.4.2.1 Particle Density

The mass density is  $0.5 \text{ g/cm}^3$  for all sporadic particle sizes.

#### 3.4.2.2 Particle Velocity

The average sporadic particle velocity is  $20 \text{ km/s}$  with the distribution as given in Figure III-1.

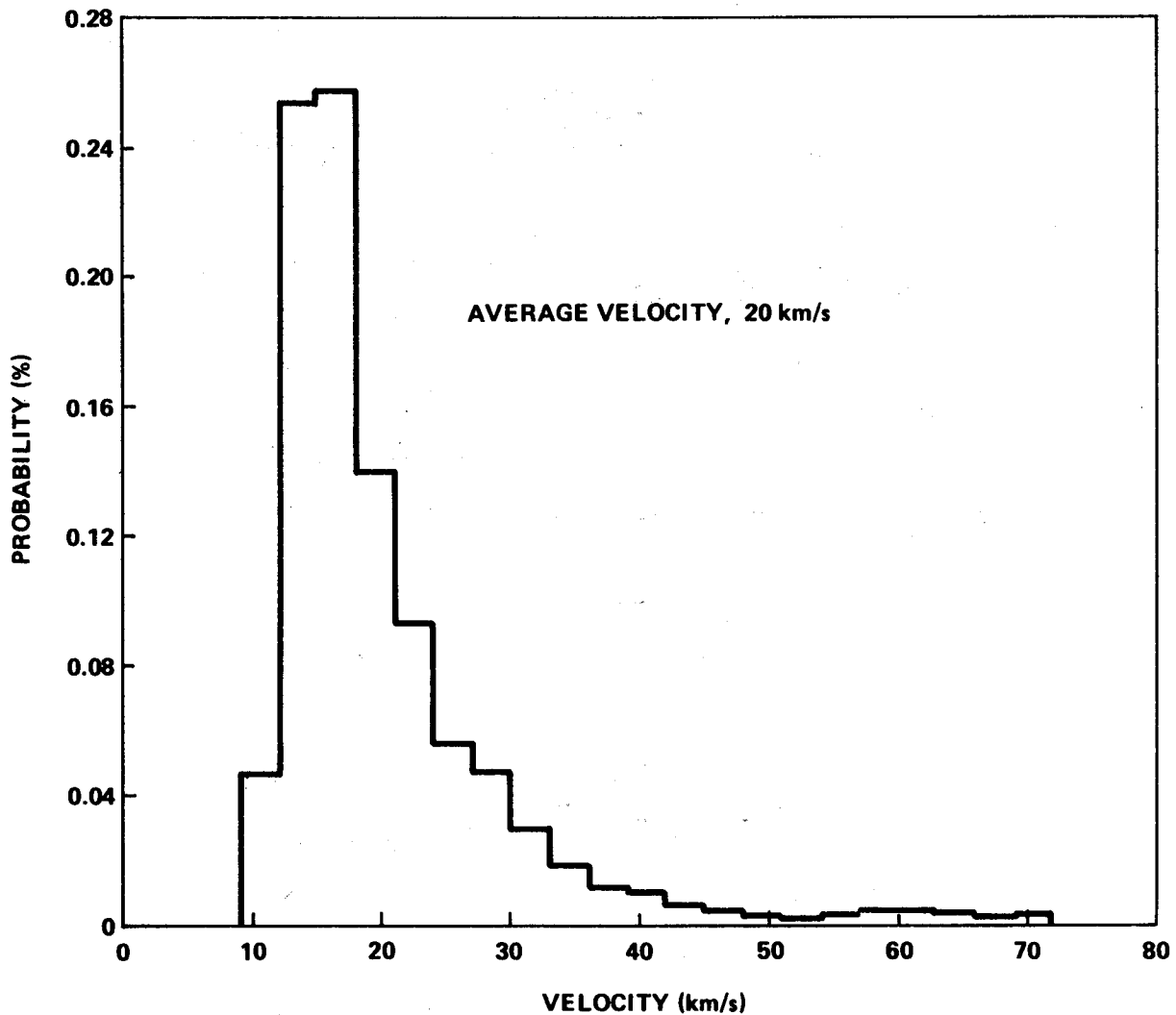


Figure III-1. Probability velocity distribution for sporadic meteoroids.

### 3.4.2.3 Flux-Mass Model

The flux ( $N_{sp}$ ), in number/m<sup>2</sup>/s, of sporadic cometary meteoroids of mass  $m$  or greater on a randomly tumbling surface is: For  $10^{-6} \leq m \leq 10^0$

$$\begin{aligned} \log N_{sp} = & 14.41 - 1.22 \log m + \log \left( 1 + \frac{0.035}{m} \right) + \log G_E \\ & + \log \left[ \frac{1 + \sqrt{1 - 1/r_e^2}}{2} \right] + \log \left[ \frac{1 + \sqrt{1 - 1/r_m^2}}{2} \right] \\ & + \log F_{\text{seasonal}}. \end{aligned}$$

For  $10^{-12} \leq m \leq 10^{-6}$ ,

$$\begin{aligned} \log N_{sp} = & -14.339 - 1.584 \log m - 0.063 (\log m)^2 + \log G_E \\ & + \log \left[ \frac{1 + \sqrt{1 - 1/r_e^2}}{2} \right] + \log \left[ 1 + \frac{0.035}{m} \right] \\ & + \log \left[ \frac{1 + \sqrt{1 - 1/r_m^2}}{2} \right] + \log F_{\text{seasonal}}, \end{aligned}$$

where

$G_E$  = the defocusing factor for the earth and is applicable to all missions

$$G_E = 0.568 + \frac{0.432}{r_e}$$

$r_e$  = the distance from the center of the earth in units of the earth's radius

$r_m$  = the distance from the center of the moon in units of the moon's radius

$m$  = mass in g

$F_{\text{seasonal}}$  = a seasonal factor obtained from the tabulation below.  
(The factor is obtained by taking the average of monthly factors listed for the months of the mission duration.)

Monthly Factors

January	0.6
February	0.4
March	0.5
April	0.6
May	1.1
June	1.6
July	1.8
August	1.6
September	1.1
October	1.1
November	0.9
December	0.7

3.4.3 Stream Meteoroids

Same as Terrestrial Space (see Paragraph 2.5.3).

#### 3.4.4 Additional Information

For additional information relative to the cislunar meteoroid environment, see Reference III-1.

### 3.5 Geomagnetic Environment

Same as Interplanetary Space (see Paragraph 1.5).

## REFERENCES

- III-1. Meteoroid Environment Model - 1970. NASA SP-8038, Interplanetary and Planetary, October 1970.

## SECTION IV. MOON

The information presented in this section is based upon Surveyor and Orbiter data generated before the flight of Apollo 11 and upon data generated in a preliminary analysis of the Apollo lunar samples. As more detailed information from the Apollo missions becomes available and as data are obtained by future missions, this section will be revised accordingly.

### 4.1 Atmospheric Environment

#### 4.1.1 Gas Properties

The moon has a tenuous atmosphere that will have a negligible effect on spacecraft except for problems associated with the effects of vacuum on components and materials.

##### 4.1.1.1 Pressure

Pressure should be considered to be  $10^{-13}$  times the earth's sea level pressure for design purposes.

##### 4.1.1.2 Density

Based on measurements involving radio star occultations, the density is estimated to be less than  $10^{-13}$  times the mean density of the atmosphere at the earth's surface. Minimum density at very small solar flux excluding  $\text{SO}_2$  and  $\text{CO}_2$  is  $5.5 \times 10^4$  particles/cm<sup>3</sup>.

##### 4.1.1.3 Composition [IV-1]

<u>Constituent</u>	<u>Particles/cm<sup>3</sup></u>
H <sub>2</sub>	$5.30 \times 10^3$
He	$3.67 \times 10^4$
H <sub>2</sub> O	$1.7 \times 10^3$
Ar	$5.4 \times 10^4$
Kr	$1.7 \times 10^{-2}$
Xe	$1.87 \times 10^{-3}$
H <sup>+</sup>	$3.3 \times 10$

<u>Constituent</u>	<u>Particles/cm<sup>3</sup></u>
He <sup>++</sup>	$5.9 \times 10^{-2}$
H <sub>2</sub> O <sup>+</sup>	$3.0 \times 10$
Ar <sup>+</sup>	$3.41 \times 10^2$

SO<sub>2</sub> and CO<sub>2</sub> should be present, but there are no definite estimates on the amounts.

#### 4.1.2 Radiation Environment

##### 4.1.2.1 Galactic Radiation

Use criteria given in Paragraph 1.3.1.

##### 4.1.2.2 Trapped Radiation

None.

##### 4.1.2.3 Solar Proton Events

Use criteria given in Paragraph 1.3.2.

##### 4.1.2.4 Thermal Radiation [IV-2]

The thermal radiation from the lunar surface varied from 565 W/m<sup>2</sup> at 200 km to about 5 W/m<sup>2</sup> at 20 000 km.

$$Q = FAI \quad ,$$

where

Q.= thermal radiation flux incident upon vehicle

F = view factor (varies with altitude above the planet and vehicle shape)



A = cross-sectional area of exposed spherical surface

I = lunar thermal radiation flux (324.35 W/m<sup>2</sup>).

#### 4.1.2.5 Albedo Radiation [IV-2]

This varies from 151 W/m<sup>2</sup> at 200 km to 1 W/m<sup>2</sup> at 20 000 km. The albedo radiation is determined from the general equation for albedo radiation flux:

$$Q = FASa \quad ,$$

where

Q = incident radiation flux

F = view factor

A = cross-sectional area of exposed spherical surface

S = solar constant at the moon

a = lunar albedo.

#### 4.1.3 Meteoroid Environment

##### 4.1.3.1 Average Total Meteoroid Environment

The average annual cumulative meteoroid model on the lunar surface is described mathematically as follows: For  $10^{-6} \leq m \leq 10^0$ ,

$$\log N_t = -14.597 - 1.213 \log m.$$

For  $10^{-12} \leq m \leq 10^{-6}$ ,

$$\log N_t = -14.566 - 1.584 \log m - 0.063 (\log m)^2,$$

where

$N_t$  = number of particles/m<sup>2</sup>/s of mass  $m$  or greater

$m$  = mass in g.

The gravitationally focused unshielded flux,  $N_t$ , must be multiplied by an appropriate defocusing factor for the moon,  $G_m$ , and, if applicable, by the shielding factor (Fig. IV-1). The  $G_m$  factor applies to all missions and may be obtained from the equation given below. The body-shielding factor for randomly oriented spacecraft may be calculated by the method given in Figure IV-1 and applied to all missions. For oriented spacecraft, the effects of body shielding on the number of impacts as seen by the parts of the spacecraft must be determined on a unique basis.

The defocusing factor for the moon,  $G_m$ , may be calculated by

$$G_m = 0.966 + \frac{0.034}{r},$$

where  $r$  is the distance from the center of the moon in units of lunar radius.

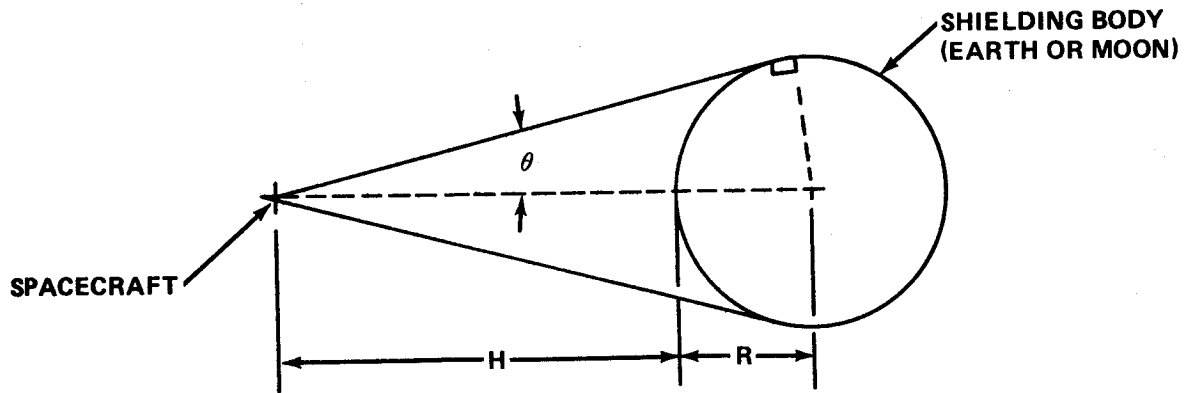
#### 4.1.3.2 Sporadic Meteoroids

##### 4.1.3.2.1 Particle Density

The mass density is 0.5 g/cm<sup>3</sup> for all sporadic particle sizes.

##### 4.1.3.2.2 Particle Velocity

The average sporadic particle velocity is 20 km/s with the distribution as given in Figure IV-2.



BODY SHIELDING FACTOR,  $\zeta$  (DEFINED AS RATIO OF THE SHIELDED TO UNSHIELDED FLUX)

$$\zeta = \frac{1 + \cos \theta}{2}$$

WHERE:

$$\sin \theta = \frac{R}{R + H}$$

R = RADIUS OF SHIELDING BODY

H = ALTITUDE ABOVE SURFACE

Figure IV-1. Method for determining body shielding factor for randomly oriented spacecraft.

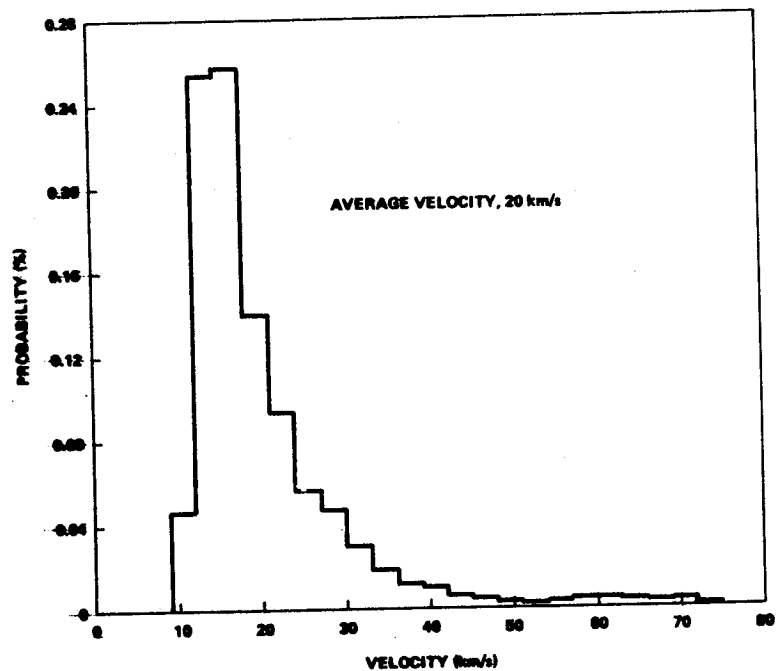


Figure IV-2. Probability velocity distribution for sporadic meteoroids.

#### 4.1.3.2.3 Flux-Mass Model

The flux-mass model for sporadic meteoroids is described mathematically as follows: For  $10^{-6} \leq m \leq 10^0$ ,

$$\begin{aligned} \log N_{sp} = & 14.41 - 1.22 \log m + \log \left( 1 + \frac{0.035}{r} \right) \\ & + \log \left( \frac{1 + \sqrt{1 - 1/r^2}}{2} \right) + \log F_{seasonal} . \end{aligned}$$

For  $10^{-12} \leq m \leq 10^{-6}$ ,

$$\begin{aligned} \log N_{sp} = & 14.339 - 1.584 \log m - 0.063 (\log m)^2 \\ & + \log \left( 1 + \frac{0.035}{r} \right) + \log \left( \frac{1 + \sqrt{1 - 1/r^2}}{2} \right) \\ & + \log F_{seasonal} , \end{aligned}$$

where

$N_{sp}$  = number of particles/ $m^2/s$  of mass  $m$  or greater  
encountered by a randomly oriented surface

$m$  = mass in g

$r$  = distance from the center of the moon in units of the lunar  
radius

$F_{seasonal}$  = seasonal factor obtained from the table below.  
(The factor is obtained by taking the average of  
monthly factors listed for the months of the  
mission duration.)

### Monthly Factors

January	0.6
February	0.4
March	0.5
April	0.6
May	1.1
June	1.6
July	1.8
August	1.6
September	1.1
October	1.1
November	0.9
December	0.7

#### 4.1.3.3 Stream Meteoroids

Same as given in Paragraph 2.5.3.

#### 4.1.3.4 Lunar Ejecta Environment [IV-3]

The lunar ejecta environment encompasses the lunar particles ejected from impacts of meteoroids on the lunar surface. In addition to the hazard of meteoroids in extravehicular activities and other operations on or near the lunar surface, lunar ejecta must be considered. The lunar ejecta environment given herein is to be used from the lunar surface to an altitude of 30 km. The effects of the ejecta environment must be considered separately from meteoroids because of their different velocity regimes.

##### 4.1.3.4.1 Particle Density

The mass density is  $2.5 \text{ g/cm}^3$  for all ejecta particle sizes.

##### 4.1.3.4.2 Particle Velocity

The average ejecta velocity is 0.1 km/s for all ejecta particle sizes.

#### 4.1.3.4.3 Flux-Mass Models

##### 4.1.3.4.3.1 Average Total Ejecta Flux-Mass Model

An average annual total cumulative flux-mass model for the lunar ejecta is to be used in preliminary design and is described as follows:

$$0 \leq V_{ej} \leq 1.0, \quad \log_{10} N_{ej_t} = -10.75 - 1.2 \log_{10} m$$

where

$N_{ej_t}$  = number of particles/m<sup>2</sup>/s of mass m or greater

m = mass in g.

The average ejecta velocity, 0.1 km/s, is to be used with this distribution model.

##### 4.1.3.4.3.2 Individual Ejecta Flux-Mass Models

An average annual individual cumulative lunar ejecta flux-mass distribution for each of three velocity intervals should be used in detailed consideration of the ejecta hazard. These three distributions are:

$$0 \leq V_{ej} \leq 0.1 \quad (V_{ej} = 0.1 \text{ km/s}); \quad \log_{10} N_{ej} = -10.79 \\ - 1.2 \log_{10} m$$

$$0.1 \leq V_{ej} \leq 0.25 \quad (V_{ej} = 0.25 \text{ km/s}); \quad \log_{10} N_{ej} = -11.88 \\ - 1.2 \log_{10} m$$

$$0.25 \leq V_{ej} \leq 1.0 \quad (V_{ej} = 1.0 \text{ km/s}); \quad \log_{10} N_{ej} = -13.41 \\ - 1.2 \log_{10} m$$

#### 4.1.3.5 Additional Information

Additional information relative to the meteoroid environment is given in Reference IV-3.

#### 4.1.4 Geomagnetic Environment

##### 4.1.4.1 Magnetic Field

The lunar total magnetic field strength at the equator is considered to be approximately 35  $\gamma$ . Apollo 15 data have revealed differences in the far-side field strength.

#### 4.1.5 Astrodynamic Constants [IV-4]

##### 4.1.5.1 Lunar Constants

Mean lunar radius:<sup>1</sup>

$$R_m = 1738.09 (\pm 0.07) \text{ km.}$$

Inertial rotational rate of the moon:

$$\omega_m = 0.00015250437 \text{ deg/s.}$$

##### 4.1.5.1.1 Principal Axes

$$a = 1738.57 (\pm 0.07) \text{ km}$$

$$b = 1738.21 (\pm 0.07) \text{ km}$$

$$c = 1737.49 (\pm 0.07) \text{ km}$$

where a is directed toward the mean center of the lunar disk, c is coincident with the moon's rotational axis, and b is perpendicular to a and c.

- 
1. Recent Apollo 15 data show that on the average the back-side elevation of the moon is 2 to 4 km above the mean lunar radius.

#### 4.1.5.1.2 Gravitational Parameter

$$\mu_m = GM_m = 4902.78 (\pm 0.06) \text{ km}^3/\text{s}^2.$$

#### 4.1.5.1.3 Earth-Moon Mass Ratio

$$M_e/M_m = 81.3010 (\pm 0.001) \quad .$$

#### 4.1.5.1.4 Sidereal Period, True Period of Rotation and Revolution

27.322 days.

#### 4.1.5.1.5 Synodic Period, New Moon to New Moon

29.531 days.

#### 4.1.5.2 Gravitational Potential Function of Moon<sup>2</sup>

$$U(r, \phi, \theta) = \frac{\mu_m}{r} \left[ 1 - \frac{J_2}{2} \left( \frac{R_m}{r} \right)^2 (3 \sin^2 \phi - 1) + 3C_{22} \left( \frac{R_m}{4} \right)^2 \cos^2 \phi \cos 2\theta \right] ,$$

where

$r$  = magnitude of selenocentric radius vector, km

$\phi$  = selenocentric latitude

---

2. Lunar orbiter and Apollo 15 tracking data are currently being analyzed by NASA scientific personnel. Upon the completion of these analyses this paragraph may require revision. Confirmation on applicability of this model should be obtained prior to use in design studies.



$\theta$  = selenocentric longitude (positive eastward)

$R_m$  = mean lunar radius = 1738.09 ( $\pm 0.07$ ) km

$J_2 = 2.07108 (\pm 0.05) \times 10^{-4}$

$C_{22} = 0.20716 (\pm 0.05) \times 10^{-4}$ .

#### 4.1.5.3 Gravitational Acceleration

The mean equatorial gravitational acceleration on the surface of the moon has been estimated to be 162.3 cm/s<sup>2</sup>.

## 4.2 Surface Environment

Engineering models of the lunar surface are needed in mission planning and in the design of landing and exploration vehicles and lunar bases. Models of terrain and soil mechanical properties assist in the evaluation of vehicle landing performance, descent engine plume-surface interactions, and exploration vehicle performance and power requirements. Crater and block (rock) models aid in assessing hazardous landing conditions and obstacles encountered in typical traverse missions. Optical models help in establishing camera design parameters and in determining visual capabilities of astronauts. Dielectric models aid in radar system design. Chemical, bearing strength, density, and thermal models are used in design of surface and subsurface base structures and surface vehicles.

The lunar surface models presented here are based on state of the art; they upgrade and extend the earlier engineering models developed by Vaughan [IV-5] and Vaughan and Costes.<sup>3</sup> They are founded on a review and interpretation of available literature and lunar data as well as discussions with scientists familiar with data provided by the Ranger, Surveyor, Orbiter programs, the Russian Luna probes, and the Apollo program in addition, these engineering models reflect, where possible, the consensus of the NASA Lunar Trafficability Model Working Group which is composed of members of NASA centers and other government agencies working on lunar exploration programs.

---

3. O. H. Vaughan and N. C. Costes, Document Exhibit 1 to Lunar Roving Vehicle Request for Proposals "MSFC Natural Environment Design Criteria Guidelines for use in the Design of Lunar Exploration Vehicles," December 11, 1969.

#### 4.2.1 Physical Properties

Many physical properties of the moon have been known for years. The method of their determination and the values presented here are taken mainly from Reference IV-6.

#### 4.2.2 Morphologic Subdivisions

Two fundamental large-scale morphologic types of lunar terrain are clearly evident — Mare and Upland regions. Well-formed young craters are superimposed on both of these surface types and constitute a widely distributed third basic surface.

The Mare surface is characterized by relatively gentle topography with low normal albedo and features, such as craters, ridges, rilles, domes, ray systems, and scarps. In contrast, the Uplands have higher albedo and are rugged with complex superimposed craters.

Besides Mare and Upland, more detailed terms (smooth Mare, rough Mare, hummocky Upland, and rough Upland) are used.

Since most lunar regions are composite, the morphologic term applied to any region describes the predominant type of terrain. Hence, a smooth Mare may contain subregions that are rougher than some subregions in a rough Mare.

The topographies of lunar surfaces are characterized by craters of various sizes and ages. Ideally, the surfaces can be grouped into two types:<sup>4</sup> (1) the young surface where the frequency distribution directly reflects the rate of crater production, and (2) the steady state surface which is the result of the combined effects of crater production and erosion-infilling produced by extensive cratering (crater saturation). Crater frequencies can be expressed approximately by equations of the form  $N_0 = K D^n$  where  $N_0$  is the cumulative number of craters per unit area greater than diameter  $D$ , and  $K$  and  $n$  are constants. The exponent,  $n$ , is about -3 for the young surface in which the craters are fresh and uneroded. For the steady-state surface (ranging from fresh, well-preserved craters to those

---

4. Moore, H. J., "Some Observations of the Lunar Trafficability Problem," U.S. Geological Survey, Nov. 1968 (working paper).

so eroded and filled that they are barely discernible), the exponent,  $n$ , is about -2 and the coefficient  $K$  is  $10^{-1}$ .

#### 4.2.3 Topography

McCauley [IV-7] and Rowan [IV-8] demonstrated with earth-based photography that the median slope was related to the slope length<sup>5</sup> for both terrestrial and Mare topography (a linear relation on a log-log plot). The relationship thus obtained from earth-based lunar observations predicted the mean slope which was later measured from Ranger 7 photographs (when the 0.75-km resolution was extrapolated to 1 m). With Orbiter data, Pike<sup>6</sup> extended the work of Rowan and McCauley and developed relations between the mean lunar slope and slope length for the smooth Mare, rough Mare, hummocky Upland, and rough Upland.

In addition, Pike's study of terrestrial slope distributions indicated identical cumulative distributions when normalized to the mean slope, regardless of the gentleness or steepness of the mean slope. By assuming that lunar slopes have the same characteristic distributions, Pike developed a basic distribution model using photoclinometry data obtained from 7 lunar regions (data read to 0.6-m resolution, but most likely are valid only above 1 m). The slope distribution model presented herein is a current estimate from a continuing investigation by Pike and others at the Center of Astrogeology, U.S. Geological Survey.

Lunar topography studies are also being conducted by the Mapping Sciences Laboratory at the NASA Manned Spacecraft Center (MSC) in support of the Apollo Program, primarily for the landing sites in the Mare regions. Cumulative slope distributions are presented<sup>7</sup> for slope lengths of about 1 and 10 m for various locations in the Mare region. The data demonstrate that the slope distributions, for a single slope length, vary from site to site, even though, within the context of the morphological subdivisions,

- 
5. The slope length is the incremental horizontal distance between two elevations over which the slope is to be determined. It is also referred to as sample cell length by Rowan and McCauley.
  6. Pike, R. J., "Preliminary Models of Slope Distributions on the Moon," U.S. Geological Survey, Branch of Astrogeologic Studies, Oct. 29, 1968.
  7. Anon.: "A Preliminary Analysis of Photometric/Computer Terrain Data for Lunar Trafficability Models," Mapping Sciences Laboratory, NASA Manned Spacecraft Center, Oct. 4, 1968.

the region might be termed a smooth Mare region. Therefore, within a given morphologic region, a distribution exists for the mean lunar slope for any single slope length. The nominal lunar surface model presented in this document provides an estimate of the most likely value of the mean slope for a given slope length.

Variations in the distribution of the average slope for a single base length can be inferred from data in Reference IV-7 and unpublished MSC data (private communication). These MSC data consisted of about 50 lunar slope cumulative frequency distributions for Apollo landing site II P-8 in Sinus Medii. From the data, the mean slope and standard deviation were computed to be 4.5 and 1.2 deg, respectively, for the lunar module base length of about 8.5 m (distance between foot pads). These results were used in establishing the relation between slope standard deviation and mean slope.

The United States Air Force Aeronautical Chart and Information Center also uses photometric techniques to determine lunar topography. Topographic charts included in Reference IV-9 show 1 m contour lines for Lunar Orbiter site II S-2.

Figures IV-3 through IV-6 show the mean lunar slope for various slope lengths. The standard deviation of the mean slope distribution for a single slope length is approximately 0.3 times the mean slope.

The lunar surface roughness models are described in terms of power spectral density (PSD) and were derived from data obtained from Pike (USGS) and Rozema [IV-10]. Similar data have been obtained by the NASA Manned Spacecraft Center although its interest has been concerned primarily with the smooth Mare regions in the Apollo belt. In Reference IV-11, Jaeger and Schuring present power spectral density data for the Mare Cognitum. They also present a procedure that utilizes PSD data to determine the dynamic response of a vehicle moving over the lunar surface.

According to Pike's data, the Mare regions contain both the smoothest and roughest regions on the moon with the Upland roughness falling in between two extremes. Even though the Mare has rougher regions than the Uplands, the steepest slopes are found in the Upland regions. Figures IV-7 through IV-10 present lunar surface roughness in terms of power spectral density ( $\text{m}^2/\text{cycle}/\text{m}$ ). Table IV-1 presents data on lunar surface features which are representative of large-scale slopes and should be considered in the design of lunar roving vehicles.

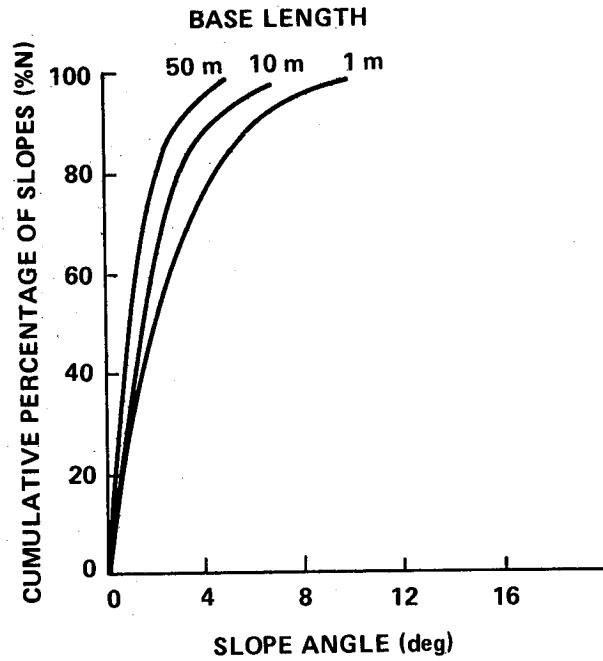


Figure IV-3. Smooth Mare cumulative slope frequency distribution for three base lengths.

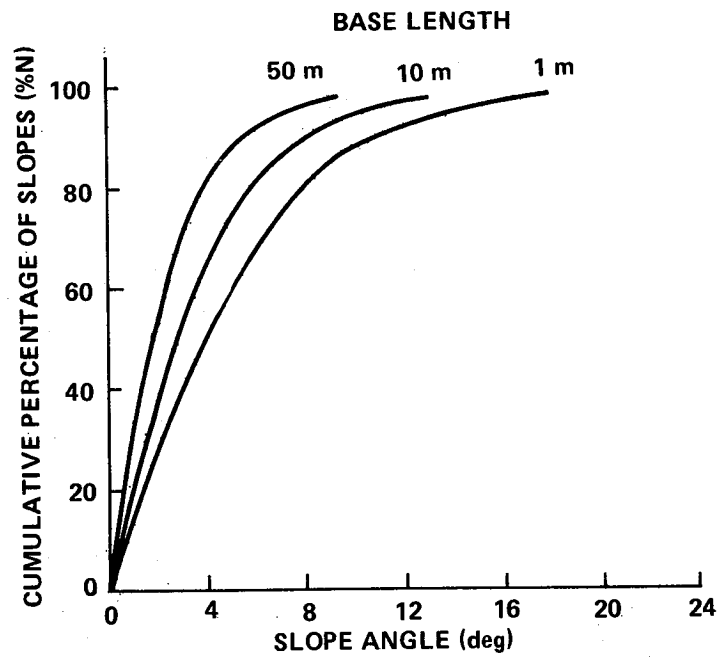


Figure IV-4. Rough Mare cumulative slope frequency distributions for three base lengths.

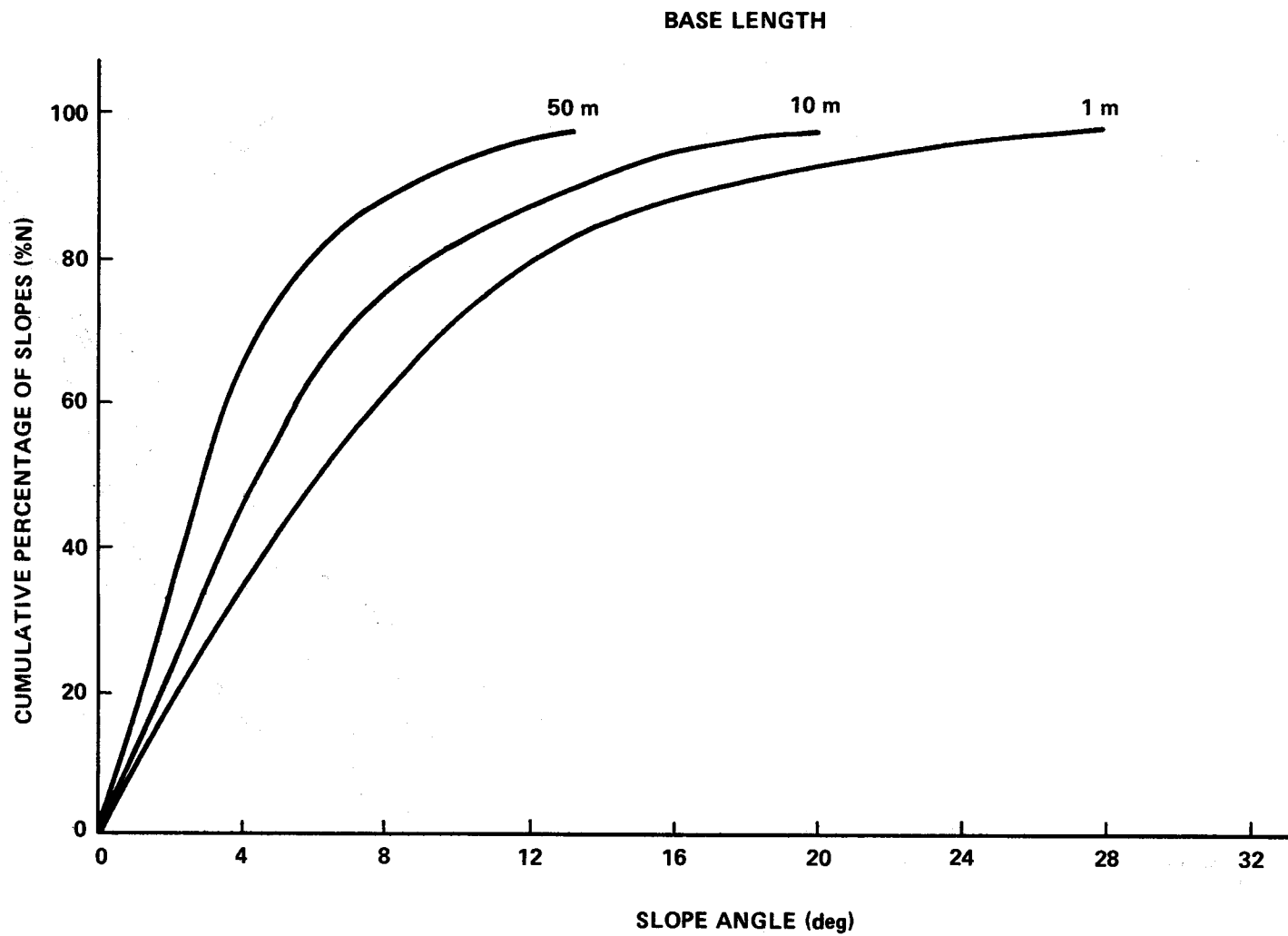


Figure IV-5. Hummocky Uplands cumulative slope frequency distributions for three base lengths.

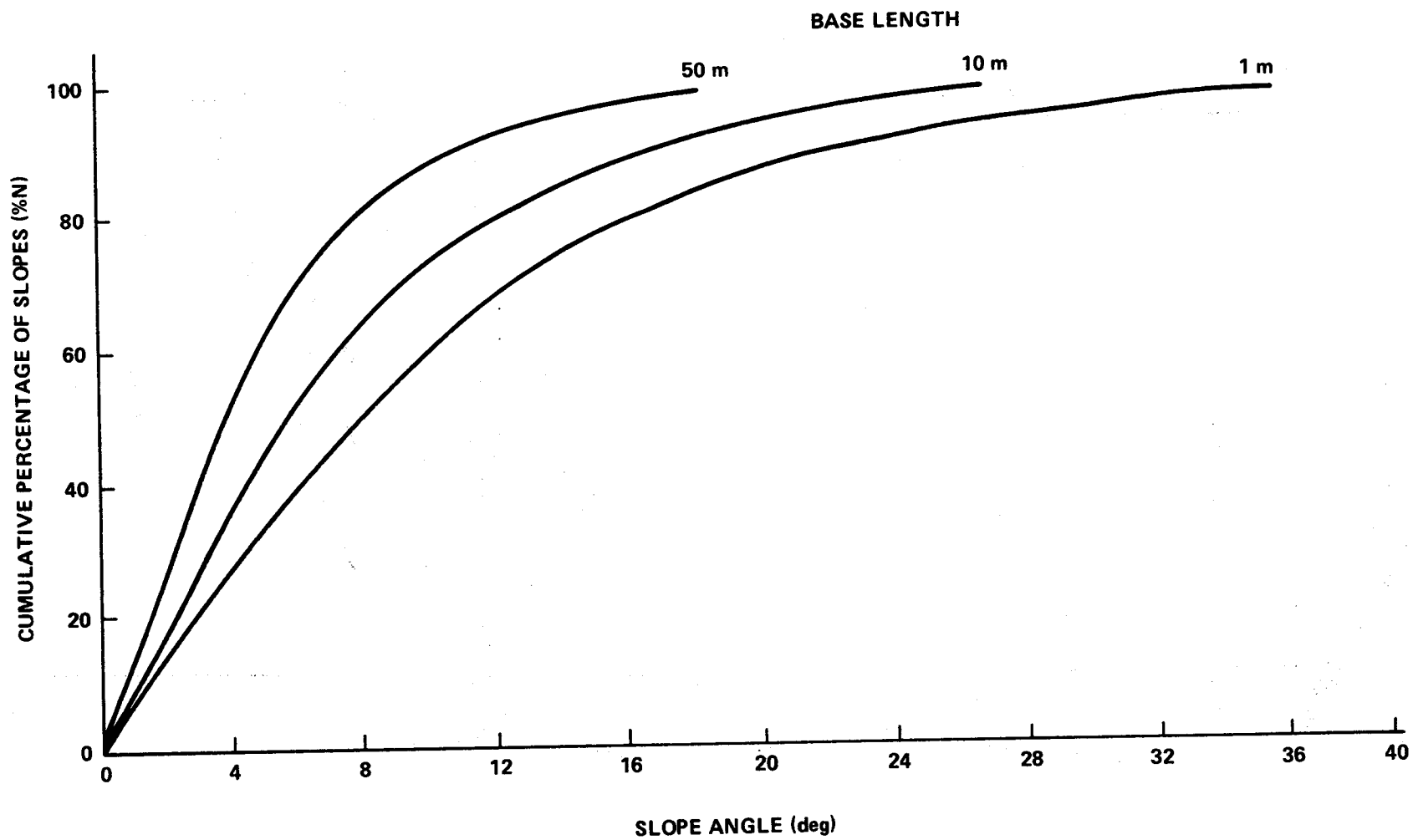


Figure IV-6. Rough Uplands cumulative slope frequency distributions for three base lengths.

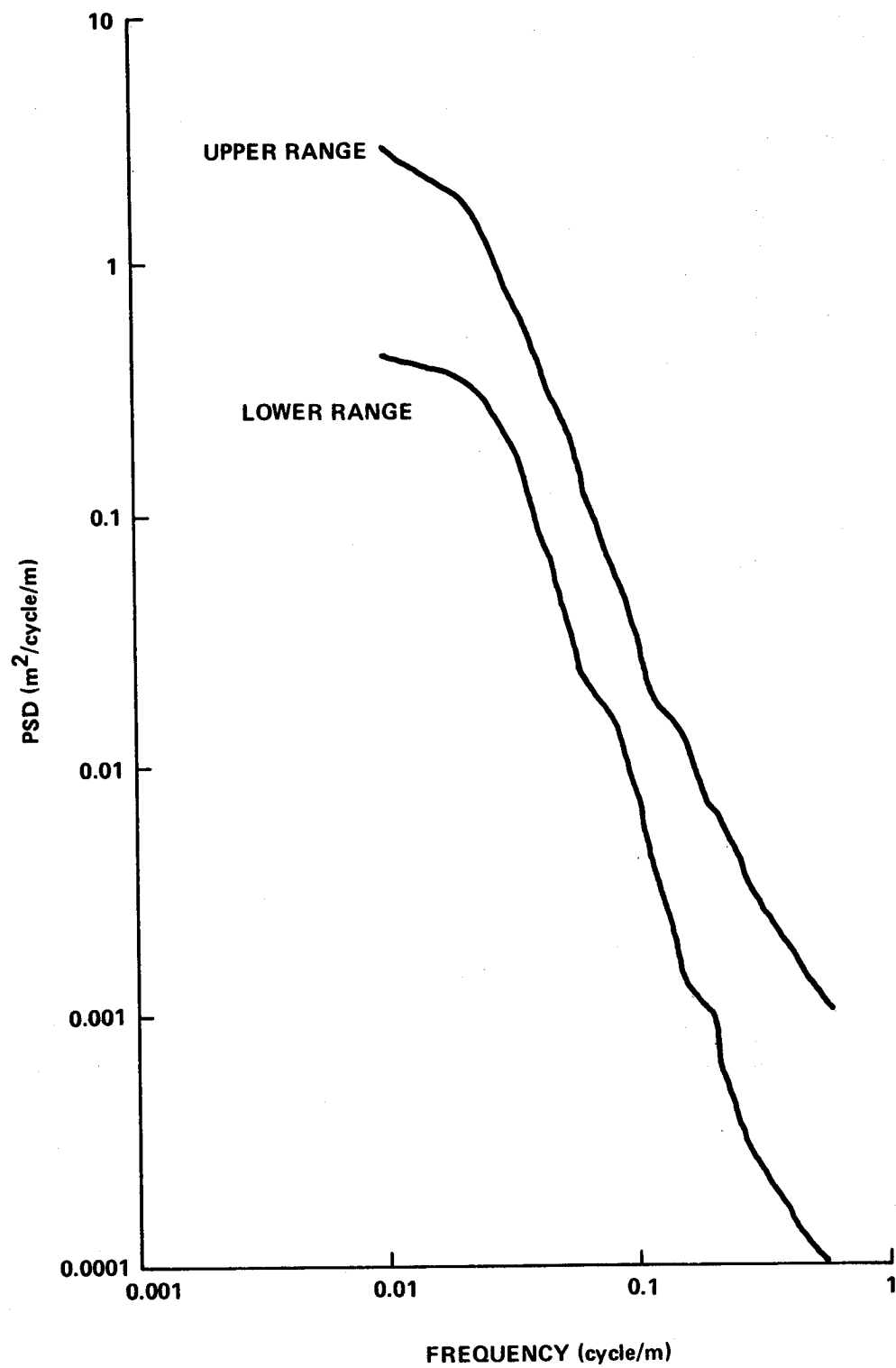


Figure IV-7. Smooth Mare power spectral density versus frequency.



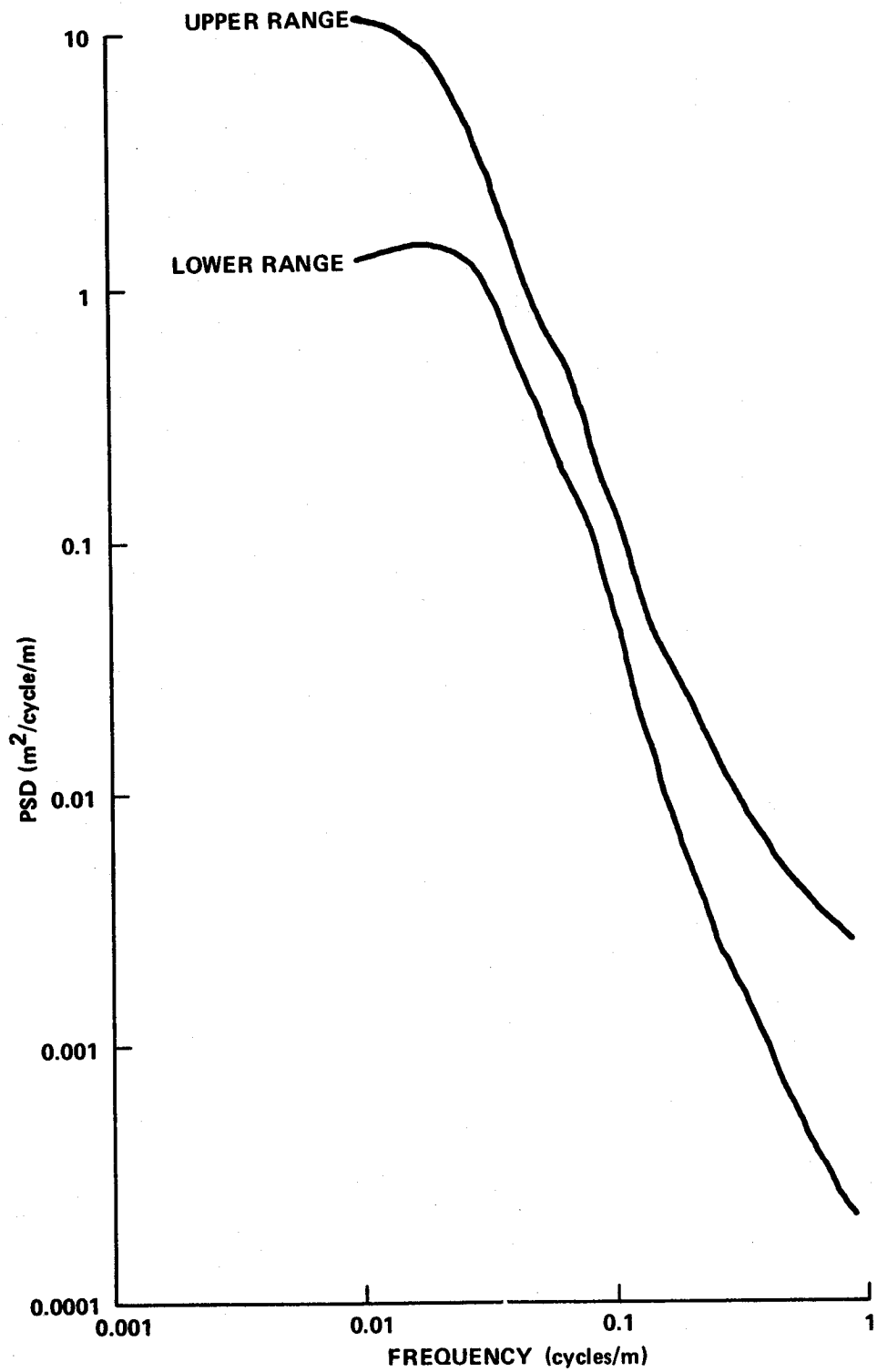


Figure IV-8. Rough Mare power spectral density versus frequency.

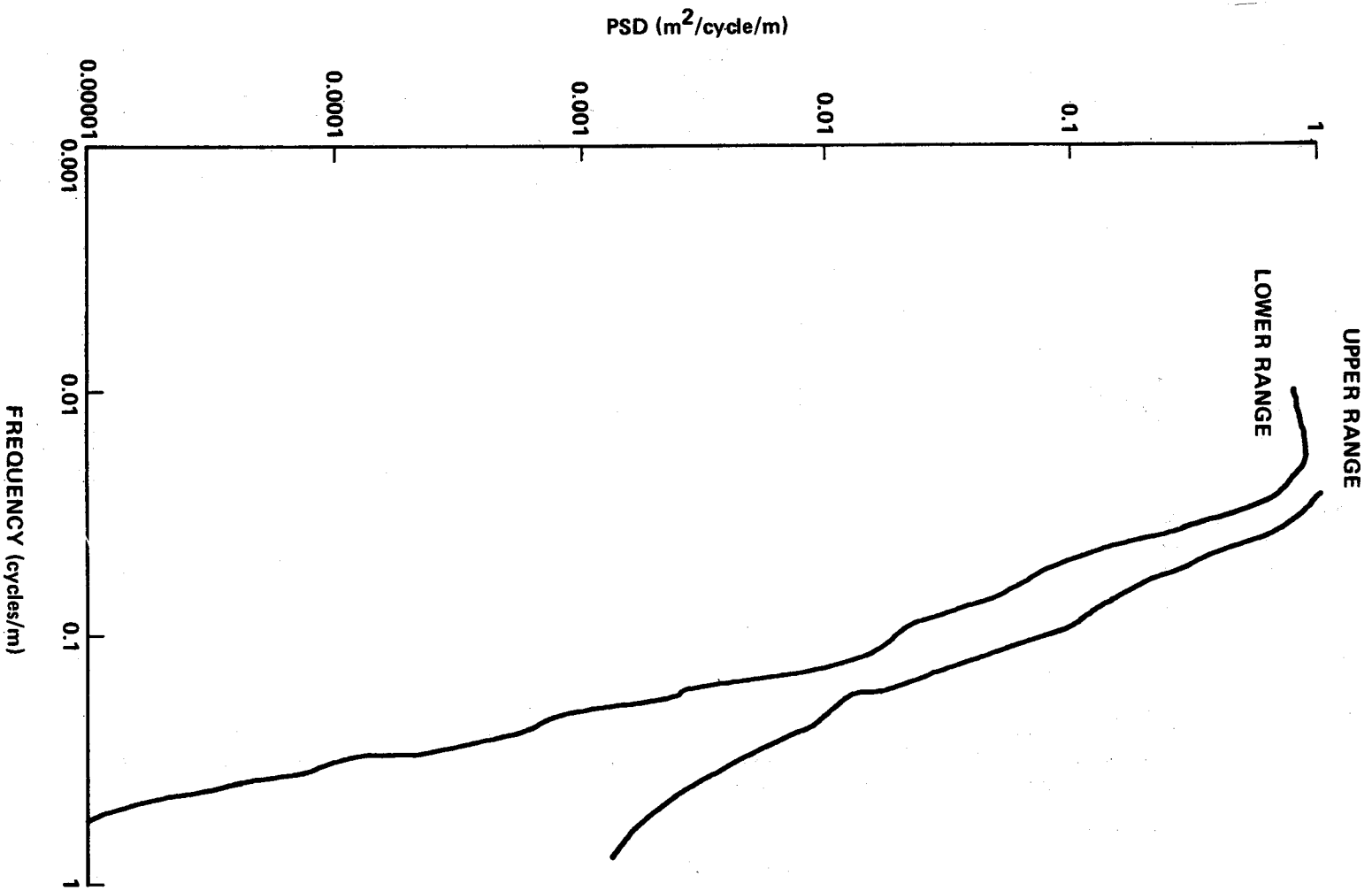


Figure IV-9. Hummocky Upland power spectral density versus frequency.

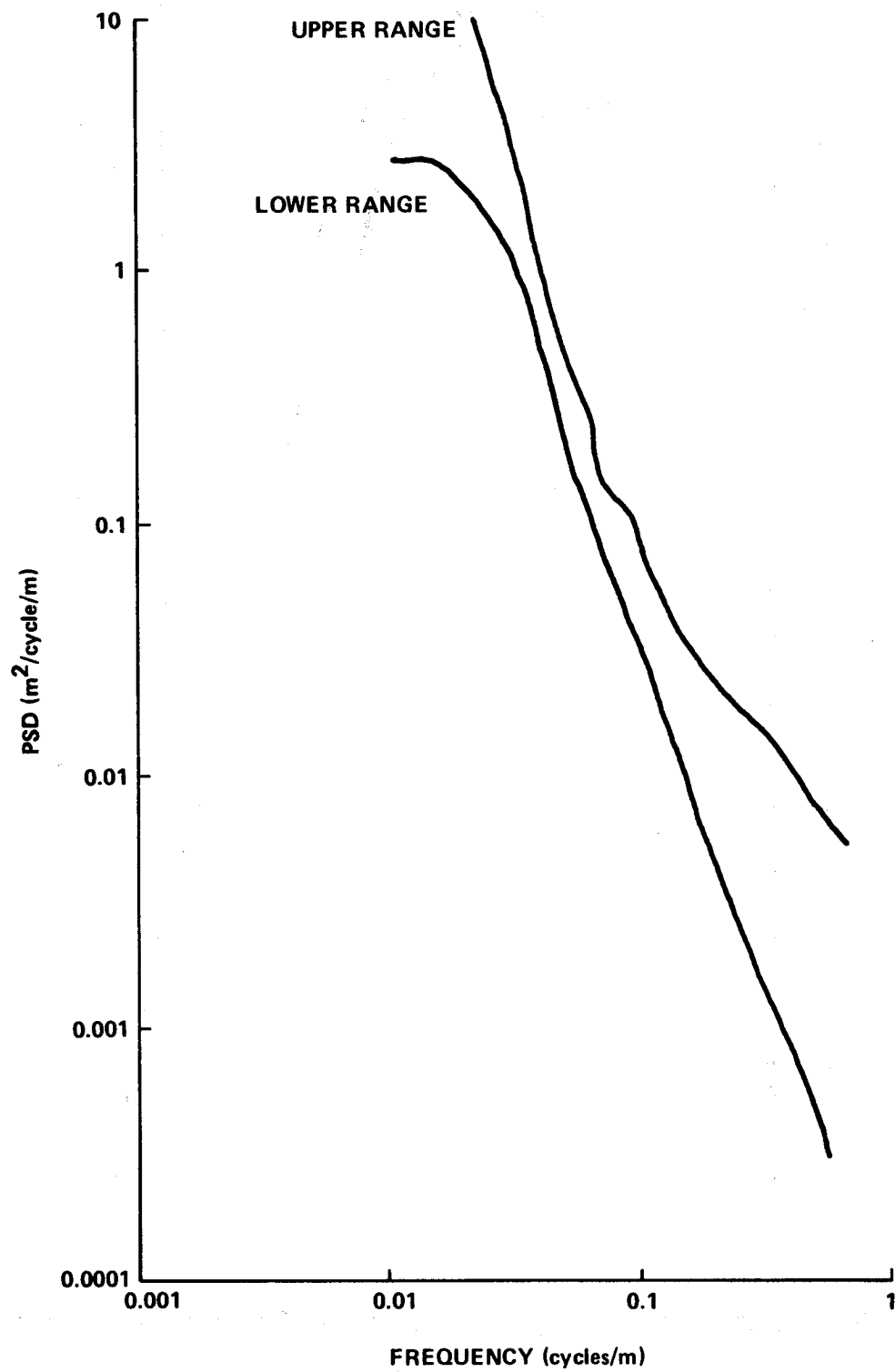


Figure IV-10. Rough Upland power spectral density versus frequency.

TABLE IV-1. LARGE-SCALE SLOPES AND  
OTHER DATA FOR LUNAR FEATURES<sup>a</sup>

<p>Harbinger Mountains</p> <p>Local Slopes on Rille Wall, 39 deg</p> <p>Long Slopes of Rille Wall, 22 deg</p> <p>Long Slope on Upland Ridge, 13 to 19 deg</p> <p>Relief of Ridges, 200 to 400 m</p> <p>Slopes on Small Rille Walls, 15 deg</p> <p>Relief of Small Rilles, 200 to 400 m</p>
<p>Schröters Valley</p> <p>Long Slope of Rille Wall, 31 deg for 1 km</p> <p>Relief, 663 m</p>
<p>Near Aristarchus (Slope of Upper to Lower Plateau)</p> <p>Long Slope, 22.5 deg for 3 km</p>
<p>Small Crater (180-m dia) in Schröters Valley</p> <p>Relief, 26 m</p> <p>Slopes of Upper Walls near 29 to 31 deg</p>
<p>Domical Hill</p> <p>Width of Crest, 4 km</p> <p>Typical Relief</p> <p>850 m Drop in 2.5 km</p> <p>850 m Rise in 3.5 km</p> <p>Comment — Most hills are hummocky at 1- to 10-m wavelengths and many of the dome-type features and ridges and/or rills will be strewn with block fields and small craters with blocky ejecta.</p>

- a. Moore, H. J., "Some Observations of the Lunar Trafficability Problem," U.S. Geological Survey Nov. 1968 (working paper).

#### 4.2.4

#### Block and Crater Frequencies

Most of the block (protuberance) and crater data models given here were derived from data furnished by H.J. Moore. These models also included results obtained by E. Shoemaker and E. Morris of USGS and R. Choate of JPL. Often, the block counts by various investigators differed substantially, probably because different lunar regions and different sizes were used in making the counts. Block frequency data here reflect a compromise between the two block frequency curves in Figures III-42 and IV-34 of Reference IV-12.

##### 4.2.4.1

##### Craters

Table IV-2 illustrates idealized crater shapes with depth and rim height data for various age groups. Figure IV-11 shows the cumulative crater frequency distribution for the "steady-state" surface for various age groups. The lower line indicates the cumulative frequency for only fresh craters. The next higher line indicates the cumulative frequency for both fresh and young craters. The highest line shows the frequency for all crater types. The figure also indicates the percent of original relief remaining for each age group. Figure IV-12 shows the range of crater cumulative frequency distributions for the smooth Mare, rough Mare, and Upland terrains.

##### 4.2.4.2

##### Blocks

For mobility studies, the obstacle height should be considered equal to one-half the block diameter.

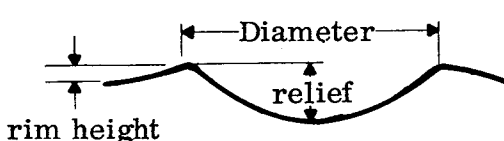



##### 4.2.4.2.1

##### Block Properties

The dimension and shapes of blocks encompass a wide range. A standard lunar block is considered as one having a ratio of its longest dimension to its shortest dimension in the range of 1/1 to 1/5. Surfaces may be rounded or rectangular, and may be pitted, eroded, or vesiculated. The standard height is considered to be equal to one-half the block diameter.

The blocks are gray in color. Most are brighter than the fine soil material and have a normal albedo of 14 to 22 percent. Light reflected from some rocks showed polarization up to 30 percent at phase angles near 120 deg.

TABLE IV-2. IDEALIZED CRATER SHAPES IN RELATION TO THEIR MORPHOLOGY<sup>a</sup>

Crater Type	Typical Profile	Depth to Dia Ratio	Rim Height to Dia Ratio
Fresh		0.23 to 0.25	0.022 to 0.06
Young		0.17 to 0.19	0.016 to 0.045
Mature		0.11 to 0.13	0.008 to 0.03
Old			

a. Moore, H.J., "Some Observations of the Lunar Trafficability Problem," U.S. Geological Survey, Nov. 1968 (working paper).

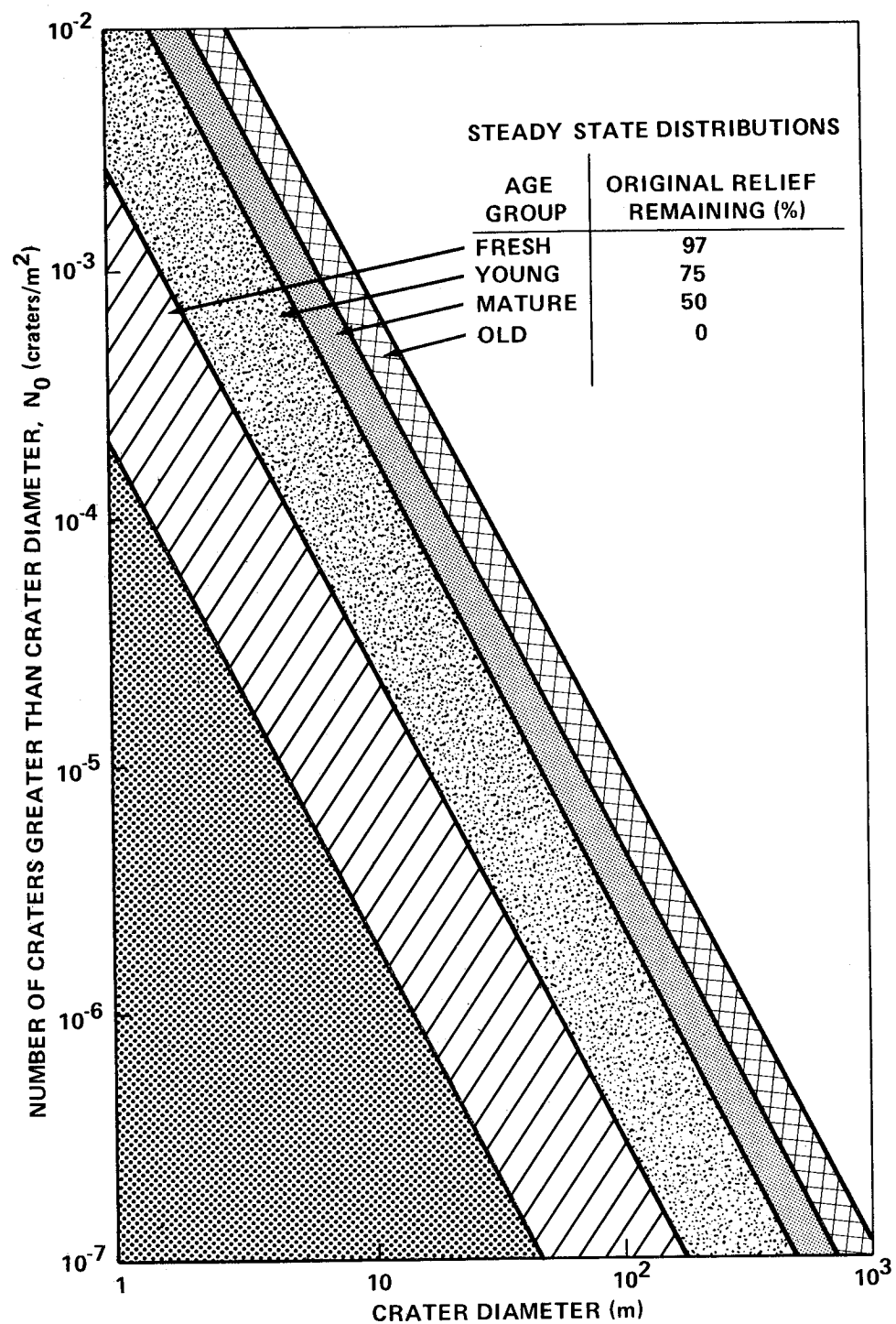


Figure IV-11. Cumulative frequency and relief of craters for various age groups that occur on the smooth Mare, rough Mare, and Upland terrains.

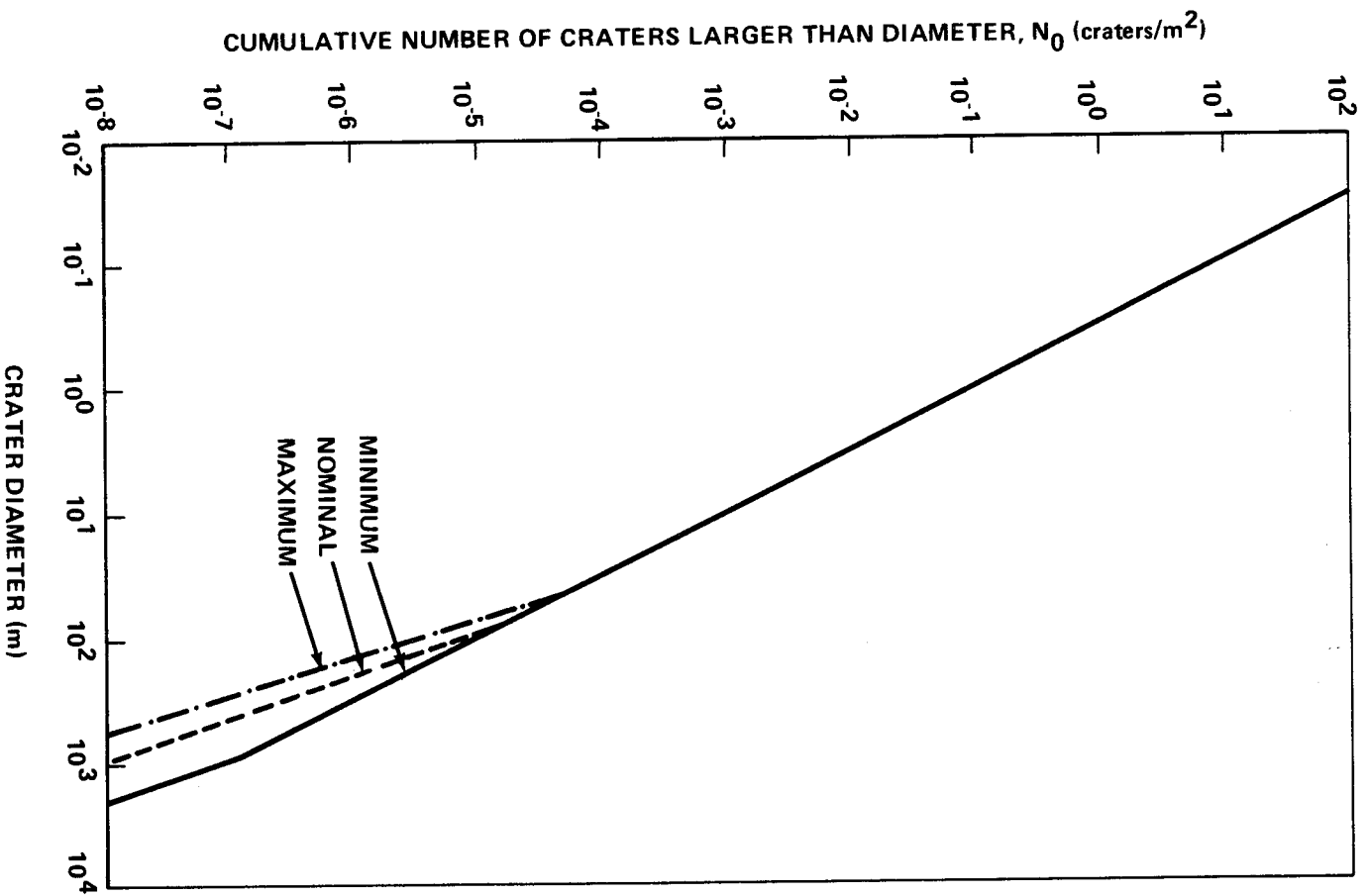


Figure IV-12. Cumulative crater distribution for smooth Mare, rough Mare, and Upland terrains.



It is estimated that a typical lunar block has a density of 2.8 to 2.9 g/cm<sup>3</sup> and a shearing strength of about 200 N/cm<sup>2</sup>.

#### 4.2.4.2.2 Block Distributions in the Intercrater Region

Figure IV-13 shows the cumulative distribution of blocks in the intercrater regions, while Figure IV-14 shows the percent of area covered by blocks of a given diameter/m<sup>2</sup>.

#### 4.2.4.2.3 Block Distributions Around Craters

Block distributions around craters vary from crater to crater. For interim design purposes the models shown in Figures IV-15 and IV-16 are considered representative of blocky craters.

Figure IV-15 shows typical cumulative frequency distribution of blocks in the annular region between the crater rim and a distance two radii from the crater center (between R and 2R for a fresh crater). Figure IV-16 shows the corresponding percent of this area covered by blocks of a given diameter.

#### 4.2.4.2.4 Block Fields

Studies by H. J. Moore of dense block fields indicate the distributions may be higher than those shown in Figure IV-15. However, Moore's data also show that there are often paths 50 m or wider through even dense block fields which are relatively free of blocks.

#### 4.2.5 Soil Characteristics

Cameras on the Surveyor spacecraft with about 1 mm resolution [IV-12 through IV-17] and Luna spacecraft with a resolution of several mm [IV-18] have provided detailed information on the lunar surface material in both Mare and Upland regions. Surveyors 1 and 3 and Lunas 9 and 13 landed in a rough Mare region (Oceanus Procellarum, Western limb), Surveyor 5 landed in a smooth Mare region (Mare Tranquillitatis, Eastern limb), Surveyor 6 landed between the rough and smooth Mare regions (Sinus Mefii, middle region), and Surveyor 7 landed in the Uplands near Tycho. Data from both U.S. and U.S.S.R. spacecraft indicate the surface material to be a matrix of fine, partially cohesive particles less than 1 mm in diameter with a few rocks scattered in and on the matrix. The data from the Apollo program show that the lunar soil is characterized by a brownish, medium-gray, slightly granular soil largely composed of bulky grains in the silt-to-fine-sand range and exhibiting adhesive characteristics. In general the

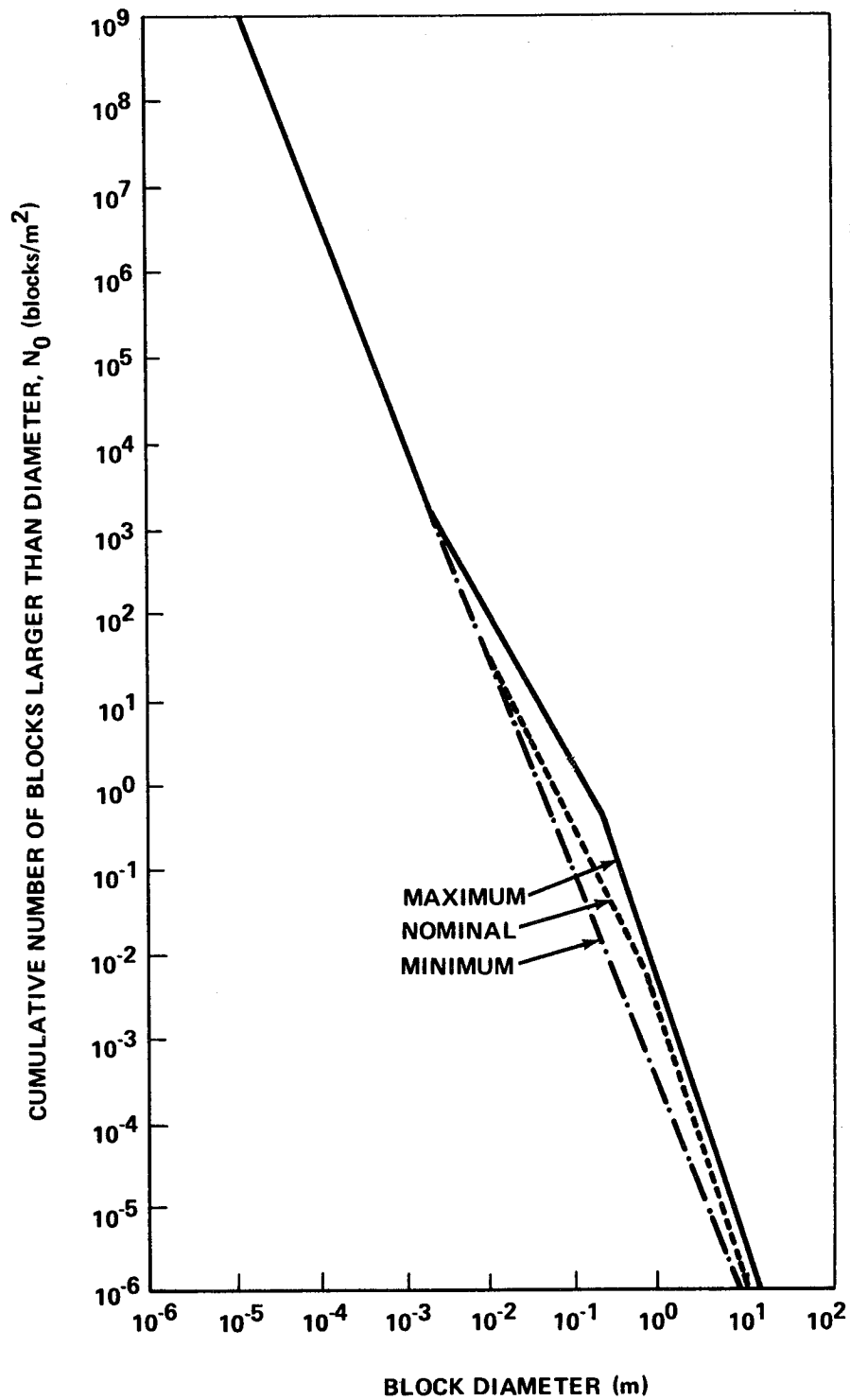


Figure IV-13. Cumulative number of blocks in intercrater region of smooth Mare, rough Mare, and Upland terrains.

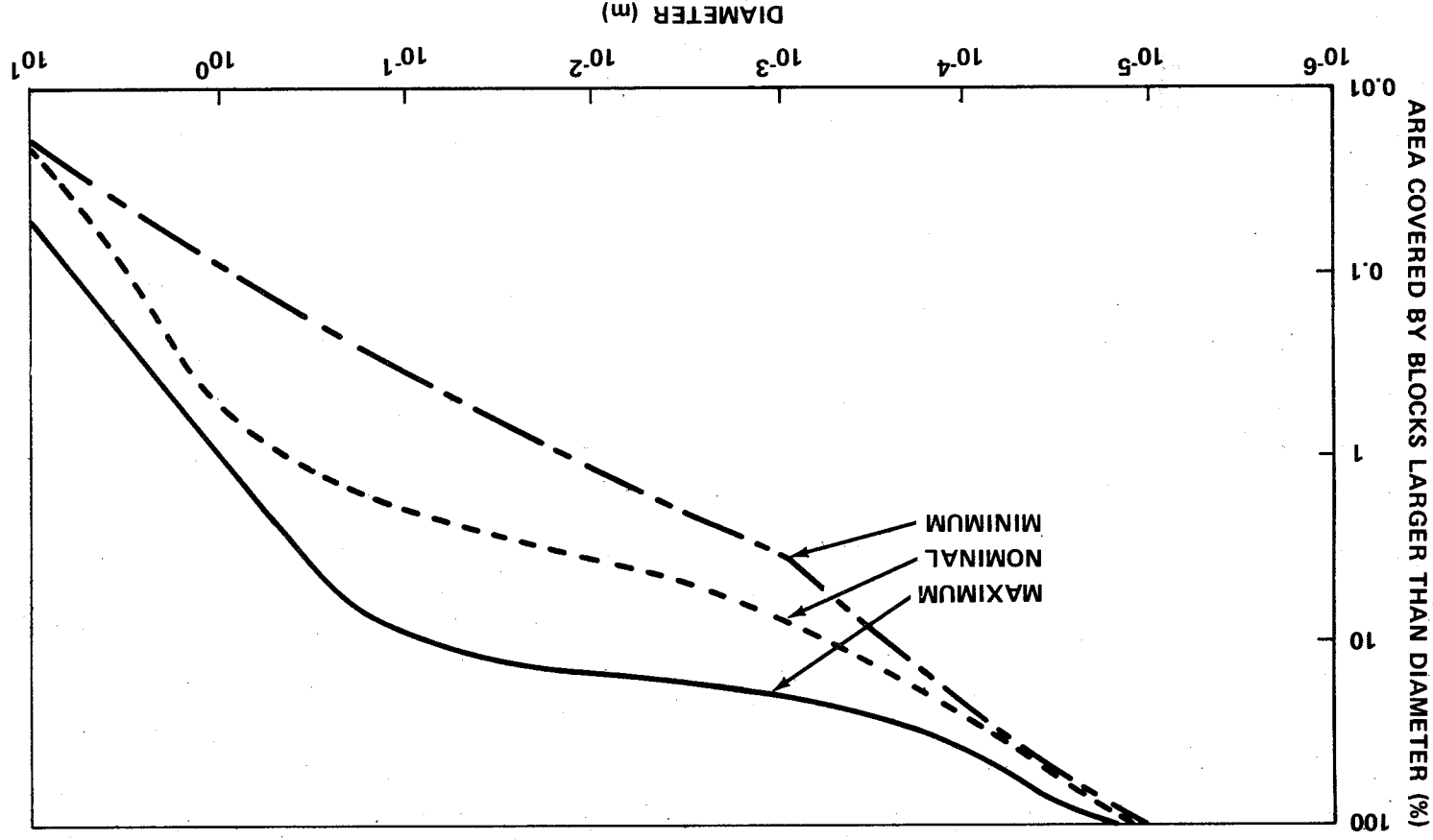


Figure IV-14. Percent of intercrater area of smooth Mare, rough Mare, and Upland terrains which are covered by blocks.

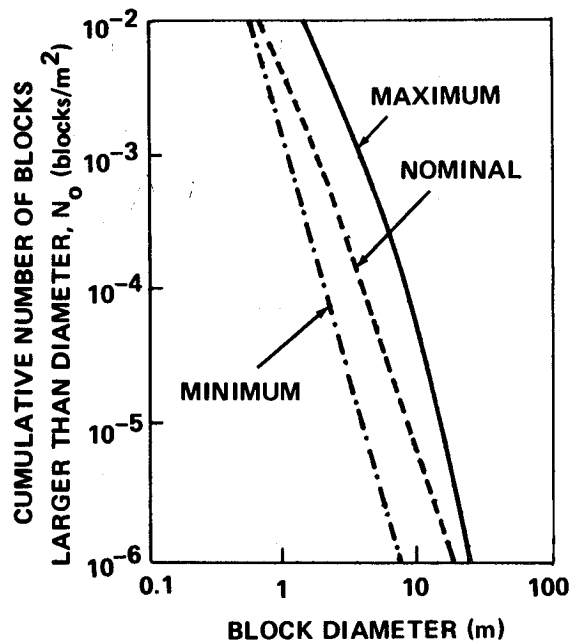


Figure IV-15. Cumulative distribution of blocks between crater rim and two crater radii as seen around craters in smooth Mare, rough Mare, and Upland terrains.

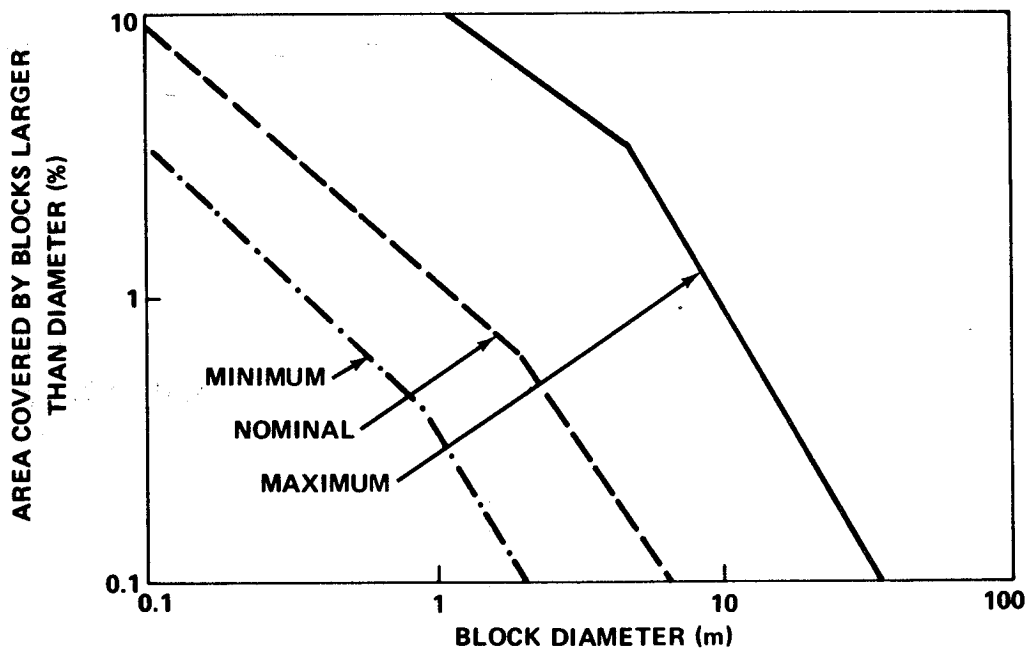


Figure IV-16. Percent of area covered by blocks between crater rim and two crater radii as seen around craters in smooth Mare, rough Mare, and Upland terrains.

particle size range from 0.01 to 5 mm and the density and porosity are the most important characteristics controlling the physical behaviors. Substantial regional and local density variations and changes in density with depth have been observed.

#### 4.2.5.1 Soil Parameters

Table IV-3 presents the average soil parameters.

#### 4.2.6 Thermal Properties

Infrared (10 to 12 $\mu$ ) and photometric (0.45 $\mu$ ) measurements were made by Saari and Shorthill from earth-based observations; their results are presented in the form of isothermal and isophotic charts for 23 phase angles [IV-19]. The infrared temperatures as measured are not independent of the observation angle (as they are for a Lambertian surface), but have a directional effect; References IV-20 and IV-21 point out these directional characteristics as one of the most anomalous characteristics of the surface. Montgomery et. al. [IV-22] concluded the directionality effects are caused by roughness of the surface. A mathematical expression relating infrared temperature to incident and observational directions has been developed from experimental data by Ashby and Burkhard [IV-23].

Calvert [IV-24] fitted a Fourier series to the equatorial brightness temperature measurements of Murray and Wildey [IV-21], Low [IV-25], and Sinton [IV-26] over a complete lunation and presented the coefficients through the fiftieth order. Surface temperature anomalies<sup>8</sup> for local regions much hotter or cooler than the surrounding regions have been detected and closely examined by Shorthill and Saari [IV-19]. The brightness temperature differs from the actual surface temperature in three ways. First, the lunar surface is assumed to be a blackbody. Second, the thermal radiation is measured only over the 10- to 12- $\mu$  portion of the infrared band. Third, the thermal energy measured by the detector is an average of the radiation from distribution of temperatures over a region of the moon's surface. The size of the region changes with the location being viewed. The region is a circular area from 14 to 17 km in diameter when viewed at the center of the moon's disk. The Planck radiation equation is then used with the 10- to 12- $\mu$  band radiation and corrected for atmospheric absorption to determine the brightness temperature. The derived brightness temperature and actual surface temperature can be regarded as approximately equal.

---

8. Over 400 anomalies have been recorded. Mare Humorum typically showed 10°K enhancement above the surrounding Uplands.

TABLE IV-3. SOIL PARAMETERS

Parameter	Value
Composition (Atomic Percent)	
Oxygen	60
Silicon	20
Aluminum	7
Iron Content (Percent)	
Mare Terrain	5
Upland Terrain	2
Grain Size ( $\mu$ )	2 to 60
Cohesion ( $\text{N/cm}^2$ )	0.02 to 0.2
Nominal	0.05
Internal Friction Angle (deg)	31 to 39
Effective Friction Coefficient (Nondimensional)	
Metal to Soil or Rock	0.4 to 0.8
Adhesive Strength ( $\text{N/cm}^2$ )	0.0025 to 0.01
Permeability ( $\text{cm}^2$ )	$1 \times 10^{-8}$ to $7 \times 10^{-8}$
Seismic Velocities (m/s)	
Compressional Wave	30 to 90
Shear Wave	15 to 35
Bulk Density ( $\text{g/cm}^3$ )	
at 5 cm	1.6
at 40 cm	2.0
Porosity (Nondimensional) at 5-cm Depth	0.465

#### 4.2.6.1 Brightness Temperature

A Fourier series representation of measured equatorial brightness temperature ( $T_E$ ) over a complete lunation period  $P$  is given by Reference IV-21.

$$T_E = A_o + \sum_{n=1}^{50} A_n \cos \frac{2n\pi t}{P} + B_n \sin \frac{2n\pi t}{P} \quad .$$

The Fourier coefficients ( $A_n$  and  $B_n$ ) are listed in Table IV-4. Below a depth of about 1 m, the temperature remains constant at about 230° K [IV-6].

A first-order approximation for the variation of temperature with latitude ( $\beta$ ) on the sunlit surface is given by

$$T = T_E \cos^{1/4} \beta \quad .$$

Lunar surface temperatures based on mathematical models for various values of the thermal inertia parameter ( $\gamma$ ) are shown in Figure IV-17. Saari and Shorthill [IV-19] give isothermal and isophotic charts for 23 different phase angles.

#### 4.2.6.2 Brightness Temperature Directionality

An empirical expression, considering the directional aspects [IV-23], has been developed for predicting the surface brightness temperature ( $T_B$ ) of the sunlit portion in the infrared spectrum as follows:

$$T_B = \left( \frac{\pi I_o}{\sigma} \right)^{1/4}$$

where

TABLE IV-4. FOURIER SERIES COEFFICIENTS

$A_0 = 227.194$								
n	$A_n$	$B_n$	n	$A_n$	$B_n$	n	$A_n$	$B_n$
1	172.959	16.710	18	1.287	-0.2525	35	-0.6859	-1.395
2	30.978	-2.828	19	-2.292	-1.712	36	-0.6548	0.1242
3	-32.580	-5.861	20	-1.104	0.1936	37	0.5814	1.387
4	-11.958	1.437	21	1.990	1.620	38	0.6360	-0.1012
5	15.280	3.794	22	0.9928	-0.2003	39	-0.5067	-1.370
6	6.405	-0.8830	23	-1.707	-1.590	40	-0.6452	0.0698
7	-9.454	-2.819	24	-0.9227	0.1567	41	0.4118	1.351
8	-4.129	0.6055	25	1.486	1.522	42	0.6612	-0.0093
9	6.595	2.317	26	0.8615	-0.1585	43	-0.2845	-1.339
10	2.885	-0.5805	27	-1.235	-1.500	44	-0.6237	0.0645
11	-5.097	-2.161	28	-0.7767	0.1743	45	0.2027	1.369
12	-2.246	0.3976	29	1.063	1.499	46	0.5865	-0.01564
13	4.041	1.968	30	0.7044	-0.1354	47	-0.1762	-1.356
14	1.789	-0.3521	31	-0.9409	-1.457	48	-0.6448	-0.01454
15	-3.312	-1.921	32	-0.6887	0.1051	49	0.05244	1.329
16	-1.526	0.2377	33	0.8296	1.409	50	0.3160	0.000041
17	2.731	1.744	34	0.6733	-0.1237			



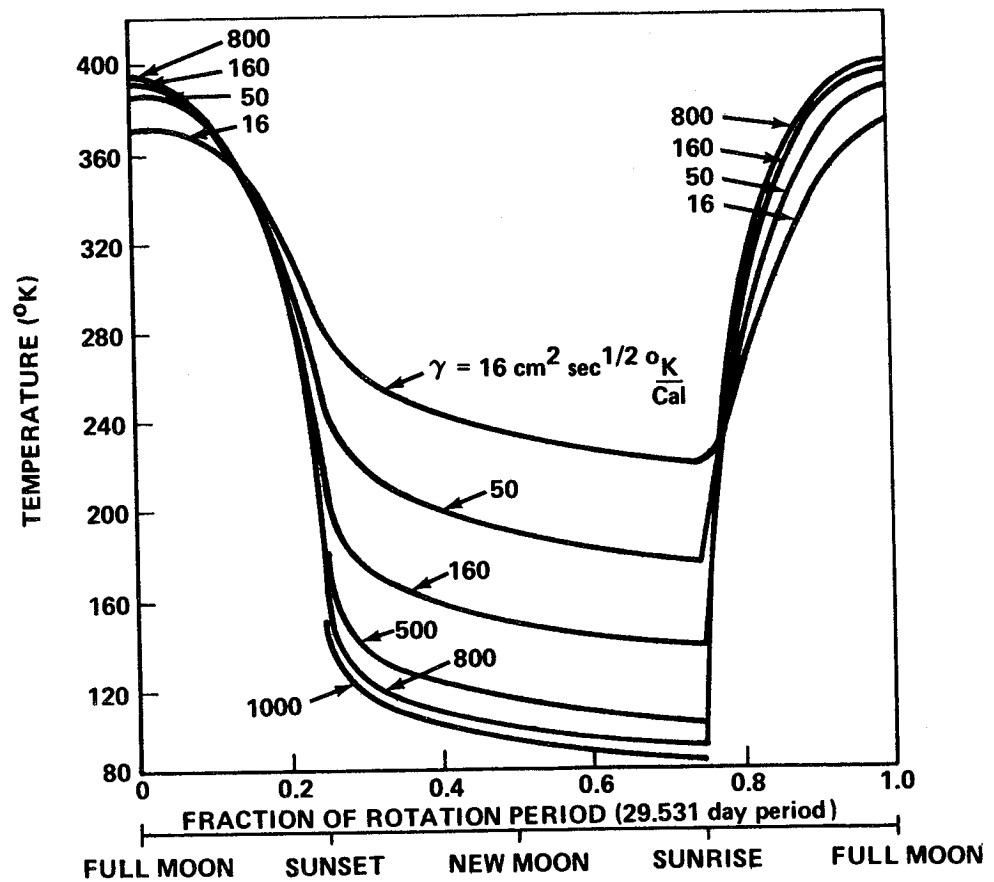
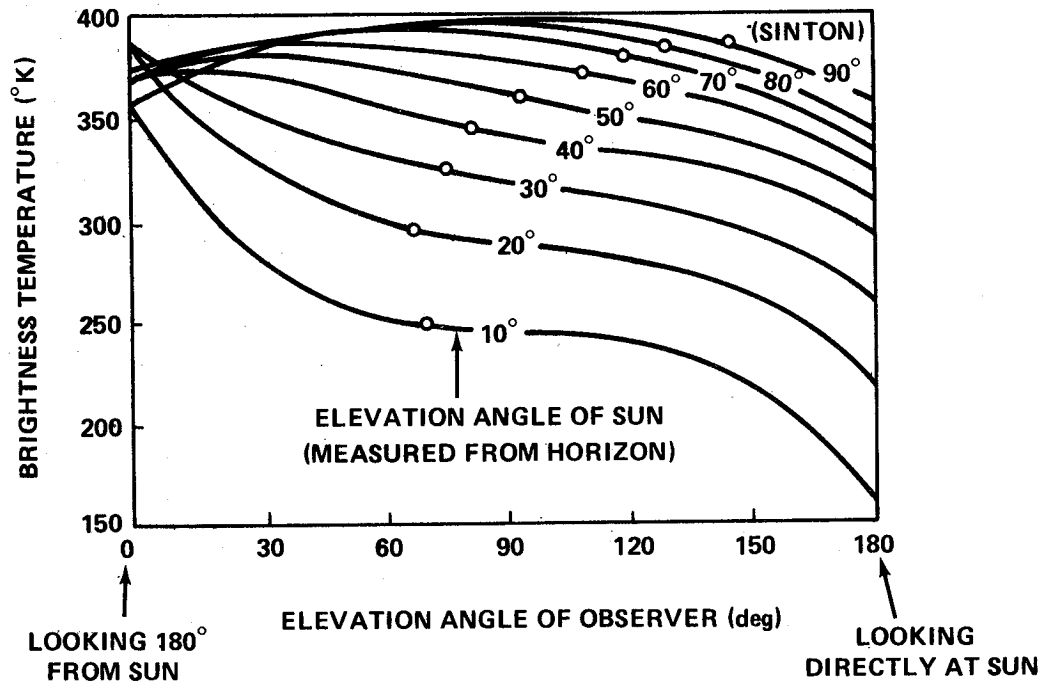


Figure IV-17. Temperatures nearest surface for different thermal parameter values.

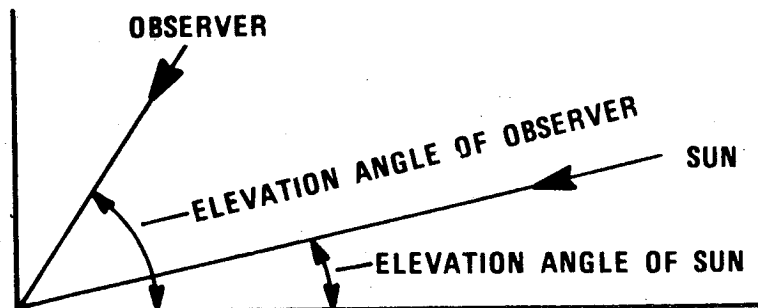


The brightness directionality effect along the thermal meridian is shown graphically in Figure IV-19 [IV-20] as functions of sun angle and elevation angle of observation. In terms of an observer on the surface as shown below, the 90 deg observer elevation angle corresponds to his looking vertically downward at the surface, 0 deg elevation angle to his looking at the horizon with the sun on his back, and the 180 deg elevation angle to his looking at the horizon facing the sun.



NOTE: THE DATA FOR 90° SUN ANGLE REPRESENT SINTON'S (39) OBSERVATIONS OF THE SUBSOLAR POINT. THE LAMBERT TEMPERATURE IS INDICATED BY THE OPEN CIRCLES (33). (DATA (10°-80°) FITTED BY LEAST SQUARE POLYNOMIAL APPROXIMATIONS-SAARI AND SHORTHILL DATA)

Figure IV-19. Brightness temperature versus observer's elevation angle to the surface with the sun at different elevation angles.



#### 4.2.6.3 Surface Thermal Properties

Thermal conductivity,  $k$ , should be considered temperature-dependent and can be expressed as

$$k = k_0 + k_1 T^3$$

where  $T$  is the temperature, and  $k_0$  and  $k_1$  are the conductive and reflectivity constants, respectively.

Laboratory data [IV-27] for powdered pumice and basalt are used for the estimates of the conductivity constant,  $k_0$ , and reflectivity constant,  $k_1$ , given here.

$$2.5 < k_0 \times 10^6 < 21 \text{ W/cm}^\circ\text{K}$$

$$0.88 < k_1 \times 10^{13} < 3.57 \text{ W/cm}^\circ\text{K}^4.$$

These ranges should be considered as representative of the lunar soil.

The specific heat,  $c$ , is likely to be temperature dependent, and the density,  $\rho$ , is depth dependent. However, constant material thermal properties are useful as average properties for data comparison and environmental criteria.

Table IV-5 lists recommended ranges for the thermal inertia parameter,  $\gamma$ , specific heat,  $c$ , conductivity,  $k$ , and density,  $\rho$ .

#### 4.2.6.4 Thermal Radiation

The thermal radiation from the lunar surface is about  $310 \text{ W/m}^2$  at 1 AU with an average albedo of 0.110 [IV-28].

An attempt to determine effective constant material thermal properties for the Maria and Uplands with earth-based measurements has been unsuccessful [IV-29] because variations within a region (Maria or Upland) are as great as the average variation between regions. For this reason, the lunation cooling curves derived from experimental infrared

TABLE IV-5. LUNAR SURFACE THERMAL PROPERTIES

Surface Material	Parameter, $\gamma$ $\text{cm}^1 \text{ s}^{1/2} \text{ }^\circ\text{K}/\text{joule}$ ( $\text{cm}^2 \text{ s}^{1/2} \text{ }^\circ\text{K}/\text{cal}$ )	Density, $\rho$ $\text{kg}/\text{m}^3$ ( $\text{g}/\text{cm}^3$ )	Specific Heat, $c$ $\text{joule}/\text{kg } ^\circ\text{K}$ ( $\text{cal}/\text{g } ^\circ\text{K}$ )	Conductivity, $k$ $\text{W}/\text{m } ^\circ\text{K}$ ( $\text{cal}/\text{cm s } ^\circ\text{K}$ )
Total Range	5.97 to 334 (25 to 1400)	500 to 3000 (0.5 to 3)	755 to 1007 (0.18 to 0.24)	$2.14 \times 10^{-3}$ to 1.13 ( $5.1 \times 10^{-6}$ to $2.7 \times 10^{-3}$ )
Range for Particulate Material Heavily Mixed With Blocks	57.2 to 119 (240 to 500)	1200 to 2000 (1.2 to 2.0)	837 (0.20)	$7.12 \times 10^{-3}$ to $1.8 \times 10^{-2}$ ( $1.7 \times 10^{-5}$ to $4.3 \times 10^{-5}$ )
Blocks (Rocks)	7.2 (30)	2500 (2.5)	837 (0.20)	$9.22 \times 10^{-1}$ ( $2.2 \times 10^{-3}$ )
Range, Excluding Blocks	95.5 to 238 (400 to 1000)	500 to 1100 (0.5 to 1.1)	837 (0.20)	$4.18 \times 10^{-3}$ to $1.17 \times 10^{-2}$ ( $1 \times 10^{-5}$ to $2.8 \times 10^{-5}$ )
Average Maria	95.5 to 191 (400 to 800)	800 to 1500 (0.8 to 1.5)	837 (0.20)	$4.18 \times 10^{-3}$ to $8.8 \times 10^{-2}$ ( $1 \times 10^{-5}$ to $2.1 \times 10^{-5}$ )

measurements taken from the earth are not uniquely determined, but may be combined statistically to obtain an average cooling curve.

Surveyor spacecraft instrument compartment temperature data have been used to infer values of the soil thermal inertia,  $\gamma = (k\rho c)^{-1/2}$ , where  $k$  is thermal conductivity,  $\rho$  is density, and  $c$  is specific heat. The Surveyor data indicated a constant  $\gamma$  cannot adequately represent earth-based measurements during both eclipse and post-sunset. Winter and Saari [IV-30] recently developed a particulate lunar soil model which agrees with both eclipse and post-sunset cooling. Surveyor data [IV-17] indicated a value of  $\gamma$  of about 800 agreed best with the equatorial landing sites. Eclipse data, which give an estimate of  $\gamma$  for the insulating surface material, indicate a value for  $\gamma$  of about 1100 to 1400. Figure IV-14 in Reference IV-17 shows the directionality effect at a sun angle of 60 deg.

#### 4.2.7 Optical Properties

A review of the history of lunar photometry is presented by Minnaert [IV-31]. Basic visual and photometric quantities are discussed by Ziedman [IV-32] who also gives analytical procedures for assessing detection of lunar surface obstacles.

The parameter commonly used to express the diffuse reflectivity of the full moon is called the normal albedo. Published albedo values for various lunar surface features are not entirely in agreement. Errors in determining the normal albedo, for example, may arise because of uncertainty in the photometric function, extrapolations to zero phase angle, luminescence, and limitations or errors in recording and measuring instruments. Early measurements of normal albedo values are presented in References IV-31, IV-33, and IV-34. Reference IV-35 gives more recent measurements of normal albedo for more than 300 lunar surface locations, comparable to those published earlier but not including the brightness surge effect at zero phase. Reference IV-36 lists normal albedo values after an extrapolation to zero phase, which consider the brightness surge effect. These investigators state that the brightness-phase relations show a nonlinear surge close to zero phase and that the brightness may increase by as much as a factor of 2 from  $\pm 5$  to 0 deg phase angle. For example, they give the average Mare and Upland normal albedos as 0.13 and 0.27, respectively. In contrast to these, Minnaert [IV-31], while quoting Sytinskaya's data, gives the normal albedo as 0.065 and 0.105 for the Mare and Upland regions, respectively.

Pohn and Wildey [IV-37] obtained other normal albedo data by using a combined photographic and photoelectric technique with improved photo processing methods. The albedo measurements indicated on the photoelectric-photographic map of the normal albedo to the moon in Reference IV-37 appear to be higher than those in References IV-31, IV-33, IV-34, and IV-35, but lower than those in Reference IV-36. (Pohn and Wildey stated in a private communication that their albedo measurements included the surge effect.) Gehrels et al. [IV-36] give the normal albedo of Mare Crisium as 0.082 to 0.092 in the ultraviolet region ( $3600 \text{ \AA}$ ), 0.194 to 0.218 in the infrared region ( $9400 \text{ \AA}$ ), and 0.08 to 0.15 over the visible region ( $3800$  to  $7800 \text{ \AA}$ ).

Preliminary estimates of the average normal albedo values for the back side of the moon have been made by J. Dragg of NASA, MSC (personal communication), from Orbiter photographs. He indicates the average normal albedo to be 0.217 for the back side of the moon.

#### 4.2.7.1 Normal Albedo

Normal albedo values for the front and rear faces of the moon are listed in Table IV-6. Table IV-7 gives normal albedo values for some prominent features on the front face.

TABLE IV-6. NORMAL ALBEDO VALUES OF FRONT AND BACK FACES OF THE MOON

Regions	Normal Albedo		
	Minimum	Maximum	Average (peak value)
Front Side			
Mare	0.07	0.12	0.095
Upland	0.108	0.24	0.150
Entire face	0.07	0.24	0.110
Back Side			
Entire face			0.217

TABLE IV-7. NORMAL ALBEDO FOR SELECTED LUNAR FEATURES

Lunar Feature	Reference 46	Reference 48	Reference 50
Darkest Point	0.05	0.0516	0.070
Brightest Point	0.18	0.2190	0.240
Mare Crisium	0.062	0.0631 to 0.0784	0.085 to 0.096
Mare Fecunditatis	0.069	0.0655	0.090 to 0.108
Oceanus Procellarum	0.051 to 0.070	0.0533 to 0.0737	0.079 to 0.096
Sinus Iridum	0.065	0.0674	0.085 to 0.096
Mare Tranquillitatis	0.066	0.0571 to 0.0668	0.085 to 0.108
Mare Serenitatis	0.070	0.0585 to 0.0692	0.090 to 0.114
Mare Frigoris	0.089	0.0738	0.102 to 0.127
Mare Imbrium	0.054 to 0.074	0.0632	0.086 to 0.102
Mare Vaporum	0.060	0.0657	0.090 to 0.108
Mare Nubium	0.062 to 0.073	0.0627 to 0.0705	0.090 to 0.108
Tycho	0.154	0.0742 to 0.1737	0.150 to 0.169

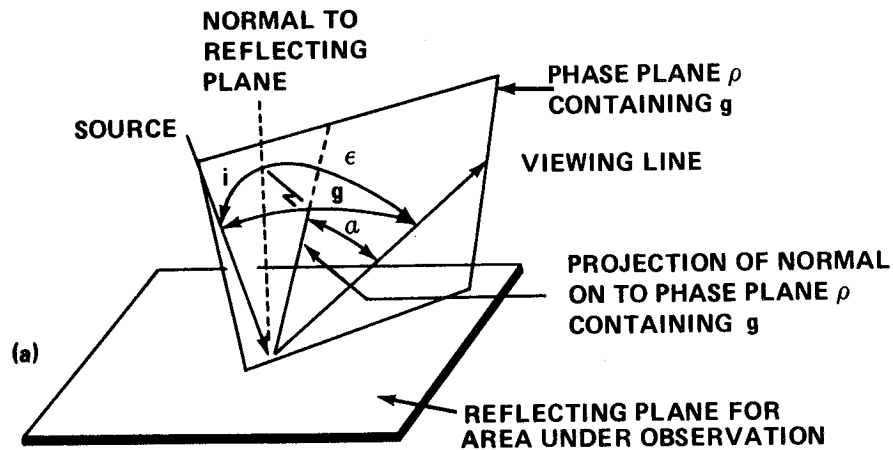
## 4.2.7.2 Photometric Model

The luminance,  $B$ , of the lunar surface is related to the photometric function,  $\phi$ , the solar constant,  $E$  (1400 W/m<sup>2</sup> at 1 AU), and the normal albedo,  $\rho_o$ , by the equation

$$B = \frac{E}{\pi} \rho_o \phi$$

where the function,  $\phi$ , depends on the phase angle,  $g$ , and surface orientation angle,  $\alpha$ , as shown in Figure IV-20.





$i$  = ANGLE OF INCIDENCE  
 $\epsilon$  = ANGLE OF EMITTANCE  
 $g$  = PHASE ANGLE  
 $\alpha$  = PROJECTION OF ANGLE  $\epsilon$  ONTO PHASE PLANE  $\rho$

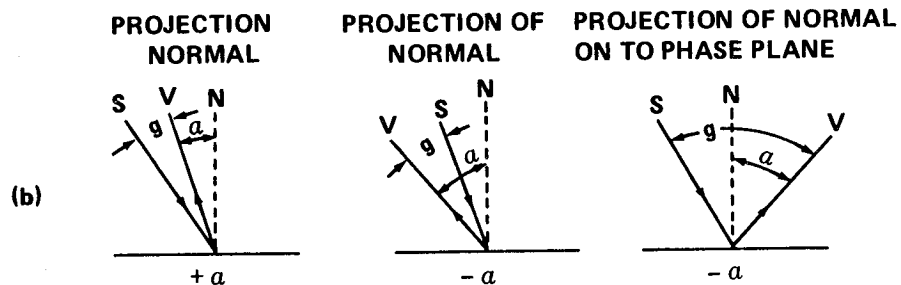


Figure IV-20. Photometric model geometry; (a) geometry, (b) positive and negative  $\alpha$ .

Figure IV-20 (a) shows the location of a section of the lunar surface being observed along with the direction of the sunline and observation direction. The sunline and observation direction define a plane, called the phase plane, which is independent of the orientation of the lunar surface plane being observed. The phase angle is the angle in the phase plane (also independent of orientation of observed lunar surface area) between the sunline and line of observation. The angle,  $\alpha$ , is an angle in the phase plane between the viewing direction and a line perpendicular to the line of intersection of the phase plane and lunar surface plane. The angle,  $\alpha$ , is positive when the viewing line lies between the solar vector and the perpendicular line. Illustrations of positive and negative  $\alpha$  are shown in Figure IV-20.

Figures IV-21 and IV-22 display the variation of the photometric function with angles  $g$  and  $\alpha$  [IV-38].

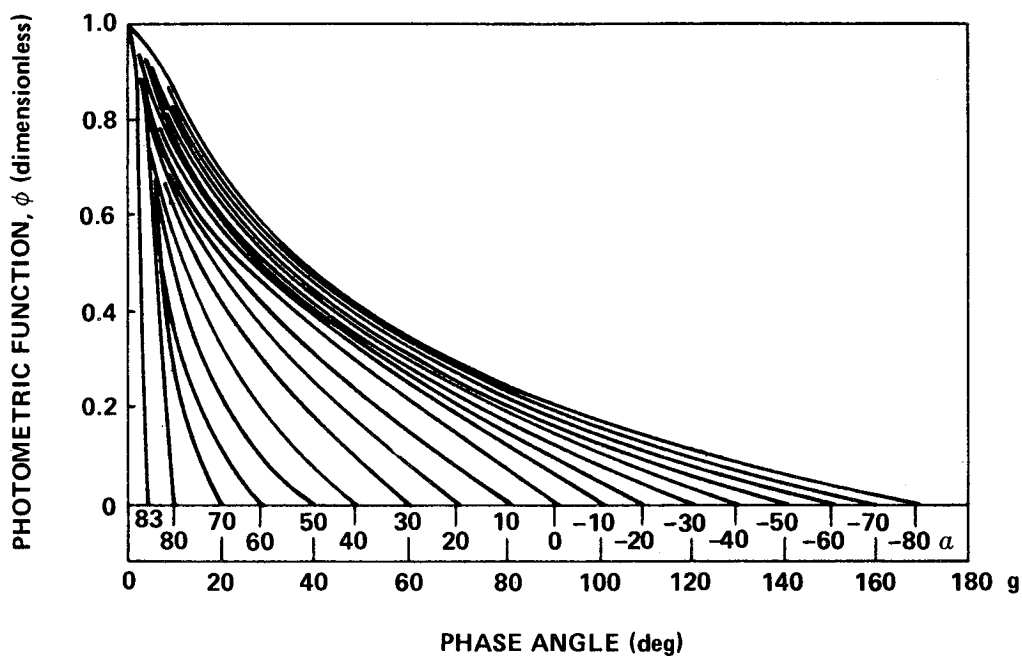


Figure IV-21. Variation of photometric function with phase angle  $g$  and angle  $\alpha$  (after Fedoretz, Ref. IV-38).

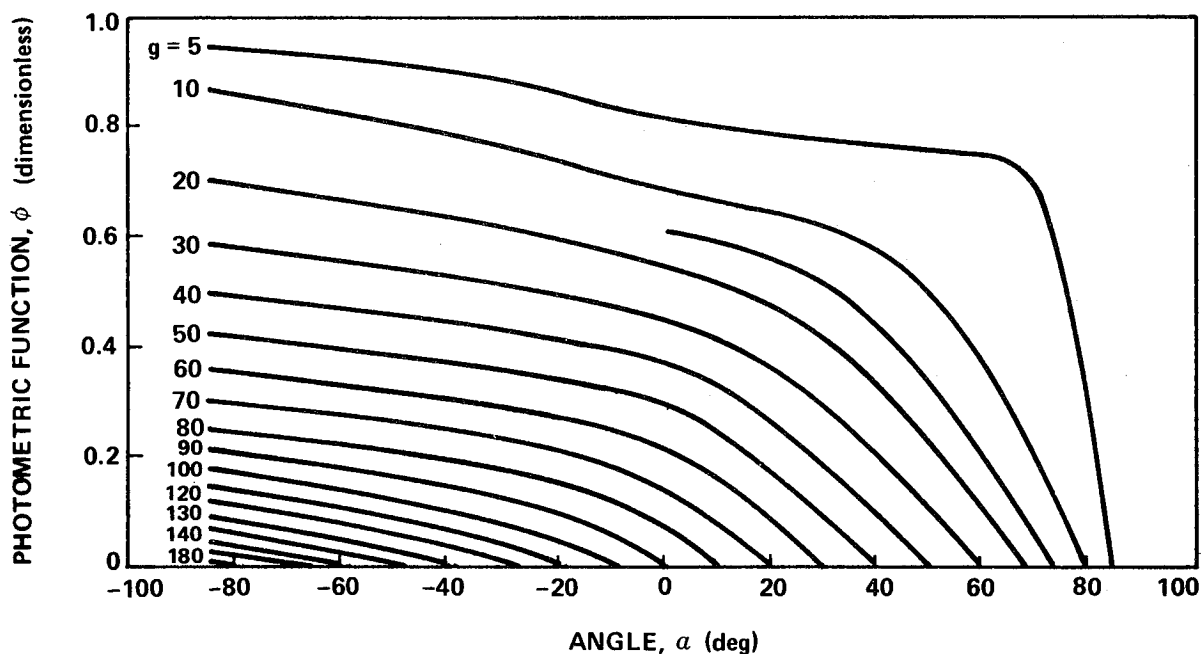


Figure IV-22. Variation of photometric function with angle  $\alpha$  and phase angle  $g$  (after Fedoretz, Ref. IV-38).

#### 4.2.7.3 Polarization of Moonlight

Electromagnetic vibrations in the light emanating from the sun are distributed fairly equal in planes in all directions. After reflection from the moon, the intensities in different planes are no longer equal. The portion of polarized light is defined by

$$P_1 = \frac{I_1 - I_2}{I_1 + I_2}$$

where  $I_2$  is the intensity of the reflected light in the plane defined by the incident and reflected light paths (phase plane) and  $I_1$  is the intensity in the plane at right angles. The polarization curves for the moon shown in Figure IV-23 for both the waxing and waning moon were obtained by Lyot [IV-39], also presented in Chap. 9 of Reference IV-19. The differences in polarization are attributed to the distributions of the Maria which have unusually large polarization and occupy about twice as much area at the last quarter as at the first quarter. The polarization changes in roughly inverse proportion to the albedo.

For different areas of the moon, there are variations in the photometric function. This function relates the brightness of the lunar surface to the viewing angle and solar incidence angle. Two basic photometric functions (based on different assumptions) have been derived from earth-based observations. The first was derived by Hapke [IV-40] by fitting data to a theoretical scattering model of the lunar surface. The model was later revised in 1966 [IV-41]. The second, based entirely on Fedoretz' lunar photographic data [IV-38], was derived empirically by Herriman, Washburn, and Willingham in 1963 [IV-42]. Since the data exhibited a large data scatter for small phase angles, Willingham developed a revised model with data from Sytinskaya and Sharanov in 1964 [IV-43]. These four photometric functions are compared by Watson in Reference IV-44. Efforts are in progress to develop a more accurate photometric function. The function presented herein is that which is developed in Reference IV-38 and is commonly called the Fedoretz function.

#### 4.2.8 Dielectric Constant

The dielectric constant of lunar material has been estimated from the reflection at the surface of microwave emission and from radar return data. Radar observations and observations of the natural radio emission of the

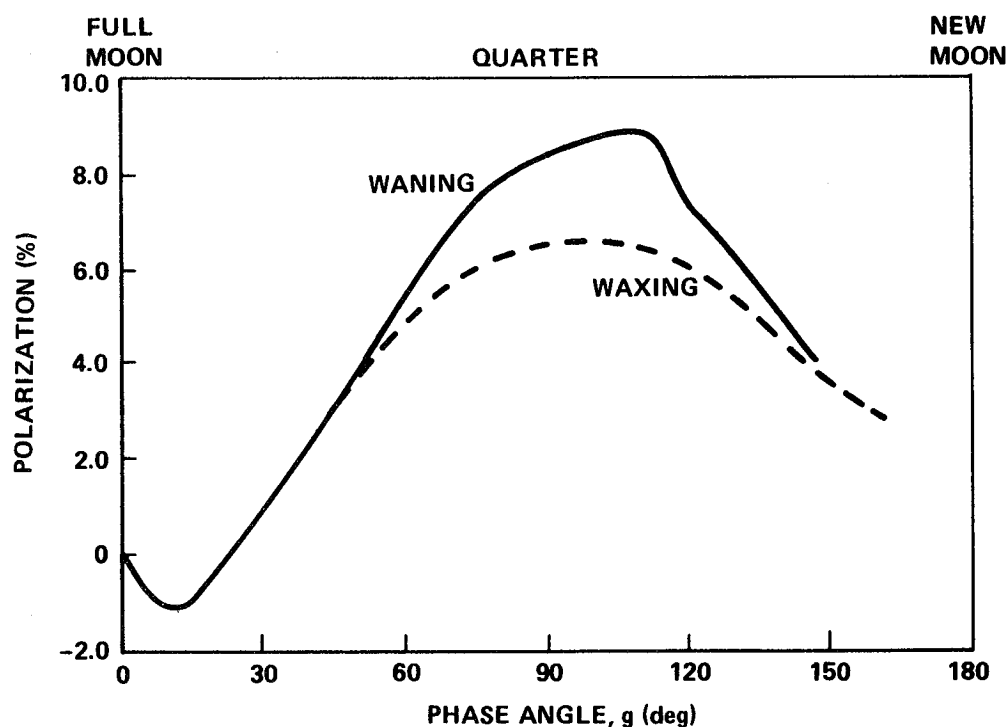
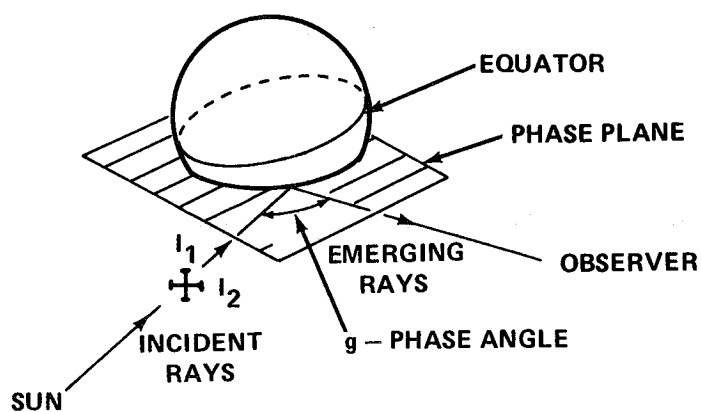


Figure IV-23. Polarization of lunar surface as a function of phase angle  $g$  (after Lyot, Ref. IV-39).

moon led Matveev [IV-45] to conclude that the most probable values for the effective dielectric constant were 1.7 at a 3 cm wavelength, 2.25 averaged over the wavelength range of 0.8 to 12 cm, and 3.2 averaged over the wavelength range of 33 to 784 cm.

Earth-based data obtained by Thompson [IV-46] indicated the dielectric constant in the Uplands is about twice that in the Mare. On the basis of Explorer 35 data obtained near the moon, Tyler [IV-47, IV-48] has estimated the effective dielectric constant to be 3.2 in the Mare and 2.8 in the Uplands at a 2.2 m wavelength at depths of about 25 cm to a depth of many meters. Later, on the basis of radar return data from the Surveyor spacecraft at a 2 to 3 cm wavelength (appropriate for surface estimates), Muhleman [IV-17] estimated the surface dielectric constant to be from 1.84 to 2.47 in the Mare (Surveyors 1, 3, 5, and 6) and from 2.88 to 3.68 in the Upland (Surveyor 7).

Estimates of the dielectric constant by Russian investigators [IV-26, IV-49] do not differentiate between Mare and Upland regions. In Reference IV-49, the dielectric constant estimate is about 3 at a 1.7-m wavelength. In Reference IV-50, the dielectric constant is expressed as a function of wavelength and soil density. For a soil density of 1.5 to 2.5 g/cm<sup>3</sup>, the corresponding dielectric constant lies in the range 2 to 3 at the Surveyor wavelength (2 to 3 cm) and in the range 3 to 4.9 at the Explorer wavelength (2.2 m). Additional laboratory measurements of dielectric and loss tangent values on various terrestrial soils and rocks are given in References IV-27 and IV-51; earlier lunar measurements are presented in Reference IV-24. Other data for the electrical properties of rocks can be found in a recent paper by Campbell and Ulrichs.

#### 4.2.8.1 Dielectric Constant and Loss Tangent

The complete range of values for the dielectric constant is about 1 to 8 where the high values are for solid material. The probable range is from 2 to 4 with the average value about 3. At a 2 to 3 cm wavelength, the value is about  $2.4 \pm 0.5$  on the Mare and  $3.3 \pm 0.4$  in the Upland [IV-17]. The relationship to the wavelength can be approximated by the equation [IV-50]:

$$\epsilon = [1 + \rho \xi(\lambda)]^2, \quad \xi(\lambda) = 0.5 + 0.045 \ln\left(\frac{\lambda}{3}\right)$$

for  $0.03 \text{ m} < \lambda < 200 \text{ m}$ . The loss tangent,  $\tan \phi$ , lies in the range from 0.02 to 0.06, assuming a density of 1 to 2 g/cm<sup>3</sup> [IV-14].

One of the important problems in designing for or predicting vehicle mobility over lunar terrain involves consideration of the soil and vehicle interaction. Currently, designers of lunar roving vehicles have had to rely on approaches developed to predict terrestrial off-road performance capability or trafficability. A recent survey by Cornell Aeronautical Laboratories of the state of the art in terrestrial off-the-road locomotion [IV-52] concluded that there were two general approaches to assessing off-road mobility performance of wheel and track vehicles: one theory initially developed by Bekker [IV-53, IV-54] and modified by personnel at the Land Locomotion Laboratory (LLL), Army Tank Automotive Center; the other theory developed by the U.S. Army Engineering Waterways Experiment Station (WES). The latter approach gives a "go" or "no-go" prediction from an interpretation of cone penetrometer tests in a soil along with empirical formulas; it is primarily applicable to quick predictions of the trafficability of fine-grained soils and sands. Being based on historical performance data of conventional vehicle designs, both methods have limited use for new and different vehicles incorporating unconventional design concepts for operation in a lunar environment.

The Bekker method examines mobility from a more fundamental viewpoint to obtain performance predictions and thrust requirements. The procedure assumes a combined frictional-cohesive soil and then develops wheel-soil equations describing wheel sinkage and tractive force (soil thrust). The relations involve several semi-empirical moduli for the soil. The Cornell survey [IV-52] mentions that there is no comparable work to match the Bekker-LLL approach in depth. Also, when it is applied with judgment to real problems, it often yields reasonable results. However, one major shortcoming of the Bekker-LLL theory is that it was only developed for mobility over flat terrains.

Soil cohesion is another factor affecting the mobility of a vehicle operating on the lunar surface. Halajean [IV-55] considers the influence of cohesion and gravity field on vehicle performance on level terrain. His results show cohesion has a negligible influence in low cohesive soils compared to the soil frictional contributions in earth's gravity field. However, in a lunar gravity field the relative importance of cohesion is much greater.

Soil cohesion takes on added importance in assessing vehicle performance of slopes [IV-56]. At high slope angles (approaching the angle of soil repose), the soil's strength and rigidity because of its frictional character tend to disappear, leaving mainly the cohesive component for load support.

Soil adhesion is an additional factor affecting the design and mobility of a lunar roving vehicle. The clogging of soil on wheels and tracks and the entrance of the soil into bearings that are not completely enclosed could cause problems in the lunar vacuum environment.

The design criteria for the lunar roving vehicle (LRV) were based on the data obtained from the Surveyor and Orbiter programs, and the vehicle performance estimates were based on data using simulated lunar materials (ground basalt).

The LRV, which operated on the lunar surface during the Apollo 15 mission, provided a wealth of information which is being analyzed and is not yet available for design criteria.

## REFERENCES

- IV-1. Hinton, B., and Taeusch, D.R.: The Lunar Atmosphere  
University of Michigan, College of Engineering, Dept. of Electrical  
Engineering, Space Physics Research Lab., Scientific Report No.  
KS-1, October 1962.
- IV-2. Ballinger, J.C., and Christensen, E.H.: Environmental Control  
Study of Space Vehicles. General Dynamics, Convair Research  
Program No. 111-9121, January 20, 1961.
- IV-3. Meteoroid Environment Model — 1970. NASA SP-8038 (Interplane-  
tary and Planetary), October 1970.
- IV-4. Apollo Missions and Navigation Systems Characteristics. Apollo  
Navigations Working Group Technical Report No. AN-1.3, Revision  
2, October 1969.
- IV-5. Vaughan, O.H.: Lunar Environment: Design Criteria Models for  
Use in Lunar Surface Mobility Studies. NASA TM X-53661,  
September 28, 1967.
- IV-6. Glasstone, S.: Sourcebook on the Space Sciences. D. Van Nostrand  
Company, Inc., Princeton, New Jersey, 1965.
- IV-7. Rowan, L.C., and McCauley, J.R.: Lunar Terrain Analysis. Lunar  
Orbiter-Image Analysis Studies Report, U.S. Geological Survey  
Report, May 1, 1965 to January 31, 1966, pp. 89-129.
- IV-8. McCauley, J.F.: Terrain Analysis of the Lunar Equatorial Belt.  
U.S. Geological Survey Open-File Report, July 1, 1964.
- IV-9. Anon.: Photometric Techniques for Mapping Orbiter Site II S-2.  
Aeronautical Chart and Information Center, NASA Defense Purchase  
Request No. T-55866, February 1968.
- IV-10. Rozema, W.: The Use of Spectral Analysis in Describing Lunar  
Surface Roughness. Interagency Report: Astrogeology 12, U.S.  
Geological Survey, December 1968.



## REFERENCES (Continued)

- IV-11. Jaeger, R.M., and Schuring, D.J.: Spectrum Analysis of Terrain of Mare Cognitum. J. Geophys. Res., vol. 71, no. 8, April 1966, pp. 2023-2028.
- IV-12. Anon: Surveyor VII Mission Report, Part II: Scientific Results. Jet Propulsion Lab., Tech. Rept. 32-1264, March 15, 1968.
- IV-13. Anon: Surveyor I Mission Report, Part II: Scientific Results. Jet Propulsion Lab., Tech. Rept. 32-1023, September 10, 1966.
- IV-14. Anon: Surveyor III Mission Report, Part II: Scientific Results. Jet Propulsion Lab., Tech. Rept. 32-177, June 1, 1967.
- IV-15. Anon: Surveyor V Mission Report, Part II: Scientific Results. Jet Propulsion Lab., Tech. Rept. 32-1246, November 1, 1967.
- IV-16. Anon: Surveyor VI Mission Report, Part II: Scientific Results. Jet Propulsion Lab., Tech. Report 32-1262, January 10, 1968.
- IV-17. Anon: Surveyor Project Report. Jet Propulsion Lab., Tech. Rept. 32-1265.
- IV-18. Vingradov, A.P., Surkov, Yu. A., Cherkasov, I.I., and Shvarev, V.V.: Lunar Surface Explorations with Soviet Automatic Stations "Luna-9" to "Luna-13." Presented by the Government of the USSR to the U.N. Conf. on the Exploration and Peaceful Uses of Outer Space, May 1968.
- IV-19. Saari, J.M., and Shorthill, R.W.: Isothermal and Isophotic Atlas of the Moon (Contours through a Lunation). NASA CR-855, September 1967.
- IV-20. Saari, J.M., and Shorthill, R.W.: Review of Lunar Infrared Observations. Physics of the Moon, S.F. Singer, ed., vol. 13, AAS Science and Technology Series, 1967, pp. 57-99.
- IV-21. Murray, B.C., and Wildey, R.L.: Surface Temperature Variations During the Lunar Nighttime. Astrophysical J., vol. 139, 1964, pp. 734-750.

## REFERENCES (Continued)

- IV-22. Montgomery, C.G., Saari, J.M., Shorthill, R.W., and Six, N.F., Jr.: Directional Characteristics of Lunar Thermal Emission. Brown Engineering Res. Labs., Technical Note R-213, and Boeing Document DI-82-0568, 1966.
- IV-23. Ashby, N., and Burkhard, D.G.: A Study of Radiative Aspects of Lunar Materials. NASA CR-61481, January 1967.
- IV-24. Calvert, T.A.: Thermal and Dielectric Properties of a Homogeneous Moon Based on Microwave and Infrared Temperature Observations. NASA TM X-1734, February 1969.
- IV-25. Low, F.J.: Lunar Nighttime Temperatures Measured at 20 Microns. *Astrophysical J.*, vol. 142, 1965, pp. 806-808.
- IV-26. Sinton, W.M.: Temperatures on the Lunar Surface. *Physics and Astronomy of the Moon*, Z. Kopal, ed., Academic Press, 1962, pp. 407-427.
- IV-27. Wechsler, A.E., and Simon, I.: Thermal Conductivity and Dielectric Constant of Silicate Materials. Arthur D. Little, Inc., Contract Report NAS8-20076, December 1966.
- IV-28. Ballinger, J.C., and Christensen, E.H.: Environmental Control Study of Space Vehicles. General Dynamics, Convair Research Program No. 111-9121, January 20, 1961.
- IV-29. Wildey, R.L., Murray, B.C., and Westphal, J.A.: Reconnaissance of Infrared Emission from the Lunar Nighttime Surface. *J. Geophys. Res.*, vol. 72, no. 14, July 15, 1967, pp. 3743-3749.
- IV-30. Winter, D.F., and Saari, J.M.: A New Thermophysical Model of the Lunar Soil. Document DI-82-0725, Boeing Scientific Research Laboratories, 1968.
- IV-31. Planets and Satellites. G.P. Kuiper and B.M. Middlehurst, eds., *The Solar System III, Photometry of the Moon*, Chap. 6 by M. Minnaert, University of Chicago Press, 1961.

## REFERENCES (Continued)

- IV-32. Ziedman, K.: Lunar Surface Visibility. Report prepared by TRW Systems for the Manned Spacecraft Center under Contract NAS 94810, Report No. 05952-6011-R000, August 3, 1966.
- IV-33. Sytinskaya, N.N., and Sharonov, V.V.: Study of the Reflecting Power of the Moon's Surface. Trudy Leningrad Obs., vol. 16, 1952 (Translated by STL, Inc., STL-TR-61-5110-23, May 1961).
- IV-34. Van Digglen, J.: Photometric Properties of Lunar Crater Floors. Res. Astr. Obs., Utrecht, Netherlands, vol. 14, no. 2, 1959. (Translated, NASA-TT-F-209, August 1964.)
- IV-35. Shorthill, R.W., Saari, J.M., Baird, F.E., and LeCompte, J.R.: Photometric Properties of Selected Lunar Features. Report prepared by The Boeing Company for the NASA Manned Spacecraft Center under Contract NAS 9-7665, September 1968.
- IV-36. Gehrel, T., Coffeen, T., and Orvings, D.: Wavelength Dependence of Polarization. III. The Lunar Surface. The Astron. J., vol. 69, no. 10, December 1964, pp. 826-852.
- IV-37. Pohn, H.A., and Wildey, R.L.: A Photoelectric-Photographic Map of the Normal Albedo of the Moon. Astrogeologic Studies Annual Progress Report, July 1, 1965 to July 1, 1966, U.S. Geological Survey, pp. 211-234.
- IV-38. Fedoretz, V.A.: Photographic Photometry of the Lunar Surface. Reports of the Astron. Observatory of the Charkow State University, vol. 2, 1952.
- IV-39. Lyot, B.: Ann. Obs. Meudon. 8, 1929; also in Tech. Transl. F-187 (NASA, Washington, D.C., 1964); Dollfuss, A.; Ann. Astrophys. vol. 19, no. 71, 1956.
- IV-40. Hapke, B.: A Theoretical Photometric Function for the Lunar Surface. J. Geophys. Res., vol. 68, 1963, pp. 4571-4586.
- IV-41. Hapke, B.: An Improved Theoretical Lunar Photometric Function. Astron. J., vol. 7, no. 5, 1966, pp. 333-339.

## REFERENCES (Continued)

- IV-42. Herriman, A., Washburn, H., and Willingham, D.: Ranger Preflight Science Analysis and the Lunar Photometric Model. Jet Propulsion Lab., Tech. Rept. 32-384, 1963.
- IV-43. Willingham, D.: The Lunar Reflectivity Model for Ranger Block III Analysis. Jet Propulsion Lab., Tech. Rept. 32-664, 1964.
- IV-44. Watson, K.: Photoclinometry From Spacecraft Images. U.S. Geological Survey Professional Paper 559-B, 1968.
- IV-45. Matveev, Y. G., Suchkin, G. L. and Troitskii, V. S.: Change of Lunite Density with Depth in the Surface Layer. Soviet Astronomy, vol. 9, no. 4, January-February 1966, pp. 626-631. (Translated from *Astronomicheskii Zhurnal*, vol. 42, no. 4, July-August 1965, pp. 810-816.)
- IV-46. Thompson, T.W.: A Study of Radar-Scattering Behavior of Lunar Craters at 70 cm. Research Report RS 64, Cornell University Center for Radio-physics and Space Research, Ithaca, New York, 1965.
- IV-47. Tyler, G.L.: Oblique-Scattering Radar Reflectivity of the Lunar Surface: Preliminary Results from Explorer 35. *J. Geophys. Res.*, vol. 73, no. 24, December 15, 1968, pp. 7609-7630.
- IV-48. Tyler, G.L.: Brewster Angle of the Lunar Crust. *Nature*, vol. 219, no. 5160, September 21, 1968, pp. 1243-1244.
- IV-49. Yakovlev, O.E., and Yefimov, A.E.: An Investigation of the Reflection of Meter Radio-Waves from the Surface of the Moon. *Doklady, Akademiia, Nauk, SSSR*, vol. 174, 1967, pp. 583-584 (in Russian).
- IV-50. Tikhonova, T.V., and Troitskii, V.S.: The Spectrum of the Reflection Coefficient with Changing Lunar Material Properties Into the Depth. Presented at the Symposium of Physics of the Moon and Planets, Academy of Sciences of the USSR, Kiev, Ukraine, October 15, 1968.

## REFERENCES (Concluded)

- IV-51. Fensler, W.E., Knott, E.F., Olte, A., and Siegel, K.M.: The Electromagnetic Parameters of Selected Terrestrial and Extraterrestrial Rocks and Glasses. The Moon, A. Kopal and Z.K. Mikhailov, eds., Academic Press, 1962, pp. 545-565.
- IV-52. Anon: Survey and Program Definition for Off-Road Mobility Research. Cornell Aeronautical Laboratories, TR CAL VJ-2330-G-1, March 7, 1967.
- IV-53. Bekker, M.G.: Theory of Land Locomotion. The University of Michigan Press, Ann Arbor, Michigan, 1962.
- IV-54. Bekker, M.G.: Mechanics of Off-the-Road Locomotion. James Clayton Lecture presented at an Ordinary Meeting of the Institution of Mechanical Engineers, London, November 13, 1962.
- IV-55. Halajian, J.: Vehicle-Soil Mechanics on the Moon. Paper No. 63213 presented at the Automotive Engineering Congress, January 1963.

## BIBLIOGRAPHY

Anon: Apollo 11 Preliminary Science Report. NASA SP-214.

Anon: Apollo 12 Preliminary Science Report. NASA SP-235.

Anon: Apollo 14 Preliminary Science Report. NASA SP-272.

Anon: A Study of Lunar Traverse Missions. Jet Propulsion Lab., Document 760-26, September 16, 1968.

Anon: Collection of Papers on Apollo 11 Lunar Science Conference. Science, Houston, Texas, vol. 167, no. 3918, January 5-8, 1970.

Anon: Collection of Papers on Apollo 15 Scientific Mission Results. Science, vol. 175, no. 4020, January 28, 1972, pp. 363-375, 407-443.

Cherkasov, I. I., and Shvarev, V. V.: First Results of the Intimate Investigations of the Lunar Soil. Academia Nauk SSSR, 1968.

Cherkasov, I. I., Vakhnin, V. M., Kemurjian, A. L., Mikhlov, L. N., Mikheyev, V. V., Musatov, A. A., Smorodinov, M. I., and Shvarev, V. V.: Determination of the Density and Mechanical Strength of the Surface Layer of the Lunar Crust at the Landing Site of Luna 13 Automatic Lunar Landing Station. Paper presented at the 10th plenary meeting of Cospar, London, July 1967; published in Kosmicheskie Issledovaniia, 5, 1967, pp. 746-757.

Gault, D. E., Quaide, W. L., and Oberbeck, V. R.: Interpreting Ranger Photographs from Impact Cratering Studies. Chapter 6, The Nature of the Lunar Surface, W. N. Hess, ed., The Johns Hopkins Press, Baltimore, Maryland, 1966.

Gringauz, K. I., Bezrukikh, V. V., Khakhlov, M. Z., Zaternker, G. N., Remizov, A. P., and Musatov, L. S.: The Results of Experiments for Determining the Lunar Ionosphere Conducted by the First Artificial Luna Satellite. Doklady, Akademiya, Nauk SSSR, vol. 170, no. 6, 1966 (in Russian).

Jaffe, L. D.: Results of the Surveyor Lunar Landings. Presented at the Symposium of Physics of the Moon and Planets, Academy of Sciences of the USSR, Kiev, Ukraine, October 15, 1968.

Jones, B. P.: Density-Depth Model for the Lunar Outermost Layer. J. Geophys. Res., vol. 73, no. 24, December 15, 1968, pp. 7631-7635.

## BIBLIOGRAPHY (Continued)

- Karafiath, L. L., and Nowatski, E. A.: A Study of the Effect of Sloping Ground on Bearing Strength and the Landing Performance of Space Vehicles. Grumman Research Dept. Memorandum RM-407, March 1968.
- Muller, P. M., and Sjogren, W. L.: Consistency of Lunar Orbiter Residuals with Trajectory and Local Gravity Effects. Jet Propulsion Lab. Tech. Rept. 32-1307, September 1, 1968.
- Oberbeck, V. R., and Quaide, W. L.: Estimated Thickness of a Fragmental Surface Layer of Oceanus Procellarum. J. Geophys. Res., vol. 72, no. 18, September 15, 1967.
- Paterson, N. R.: Seismic Wave Propagation in Poroas Granular Media. Geophysics, vol. XXI, no. 3, July 1956, pp. 691-714.
- Peters, J. D.: Trafficability of the Lunar Surface Considering the Bearing Capacity and Failure Modes of Lunar Surface Materials. Space Age Facilities, ASCE Aero-Space Transport Div. Speciality Conference, Cocoa Beach, Florida, Nov. 17-19, 1965, Proceedings A-67-16606 05-11, New York ASCE, 1966, pp. 163-201.
- Quaide, W. L., and Oberbeck, V. R.: Thickness Determinations of the Lunar Surface Layer from Lunar Impact Craters. J. Geophys. Res., vol. 73, no. 16, August 15, 1968.
- Scott, R. F.: The Density of the Lunary Surface Soil. J. Geophys. Res., vol. 73, no. 16, August 15, 1968.
- Terzaghi, I., and Peck, R. B.: Soil Mechanics in Engineering Practice. John Wiley and Sons, New York, 1964.
- Tolson, R. H., and Gapcynski, J. P.: An Analysis of the Lunar Gravitational Field as Obtained from Lunar Orbiter Tracking Data. NASA Langley Research Center, Paper presented at the IQSY/COSPAR Assemblies, London, July 17-28, 1967.
- Urey, H. C.: The Contending Moons. Astronautics and Aeronautics, January 1969, pp. 37-41.

## BIBLIOGRAPHY (Concluded)

York, W., and Savely, R. T.: Directory of Standard Geodetic and Geophysical Constants for Gemini and Apollo. NASA General Working Paper No. 10, 020B, Manned Spacecraft Center, April 6, 1966.



## SECTION V. MERCURY

This section contains a summary of the most pertinent facts about Mercury's atmosphere and surface environments. Most of the information given herein have appeared in NASA SP 8085 entitled "The Planet Mercury," or in references cited in the monograph.

### 5.1 Atmospheric Environment

#### 5.1.1 Definition

The atmospheric environment of Mercury is considered to include the region of space between the surface of Mercury and 20 000 km above the surface.

#### 5.1.2 Gas Properties (Surface to 1000 km Altitudes)

##### 5.1.2.1 Temperature

Mercury is the smallest planet of the solar system and is also nearest to the sun. The combination of these two circumstances makes it a hot and gravitationally weak planet. Because of its small orbit and concomitant proximity to the sun, Mercury is a very difficult object to observe. Visual observers long ago agreed that Mercury had a captured rotation with one side always turned toward the sun, estimates of respective bright side and dark side temperatures were extreme, ranging from some 400°C (770° F) on the bright side at perihelion to 110° C (450° F) at the center of the dark side [V-1]. It is now known that Mercury turns on its axis fast enough that no one side perpetually faces from the sun. Present estimates of the temperature on Mercury vary but it is generally agreed that any atmosphere on Mercury is expected to have a very high exospheric temperature because of its nearness to the sun. This characteristic combining with the weak gravitational field implies that all except the extremely heavy molecules should escape from the Mercurian atmosphere efficiently.

On earth, the exospheric temperature varies by about a factor of two over the solar cycle [V-2]. Atmospheric escape occurs almost entirely at higher temperatures, and it appears that an effective mean temperature for escape is about 1500° K [V-3]. Intuitively, one expects the exospheric

temperature on Mercury to vary over a wider range than on earth. References V-3, V-4, and V-5 suggest that at very low pressure ( $\sim 10^{-8}$  mb) the exospheric temperatures depend strongly on the flux of solar ultraviolet radiation and thus vary diurnally and with the solar cycle. Temperatures suggested for the day-side exosphere with  $\text{CO}_2$  being the major atmospheric constituent range between  $980^\circ$  and  $2800^\circ$  K.

Actually, the temperature structure of the Mercurian atmosphere has not been observed. Available information concerning the thermal structure on Mercury is based on various hypothetical atmospheric models. Among others, References V-4 and V-5 provide most of the thorough discussions on the temperature structure because they consider solar ultraviolet radiation, infrared radiative transfer, conduction, convection, dissociation, and escape of atmospheric constituents. These results have been summarized and adopted in the forthcoming NASA SP entitled "The Planet Mercury." It states that in the lower atmosphere, for pressure  $> 0.1$  mb, the surface temperature  $T_s$  forms the lower boundary condition, and the temperature gradient in the Mercurian atmosphere should be approximately adiabatic until the value  $(0.5)^{\frac{1}{4}} T_s$  is reached. Higher temperature gradients that would be required for conductive or radiative heat transport are unstable against convection, which would re-establish a nearly adiabatic gradient. Figure V-1 shows the vertical temperature profiles for sunlit and dark cases for the upper density limit model.

#### 5.1.2.2 Composition

The search for atmospheric gases on Mercury was carried out by Antoniadi [V-6] and later by Kuiper [V-7], but failed to give any positive results. It was therefore generally believed that if an atmosphere exists on Mercury, it must be composed of rare gases, such as argon, which are not observable by spectroscopic techniques. This was indeed proved by Dollfus [V-8] who has produced evidence in the early 1960's that Mercury might be surrounded by a thin layer of argon. In 1965, Moroz [V-9] reported data suggesting that the Mercurian atmosphere might contain some carbon dioxide. Both findings seemed reasonable.

In 1963, Kozyrev [V-10 and V-11] claimed that he had detected the presence of hydrogen through his spectroscopic studies and proposed an all-hydrogen atmosphere for Mercury. However, most other researchers conclude that the anomalies have solar, terrestrial, or instrumental origins

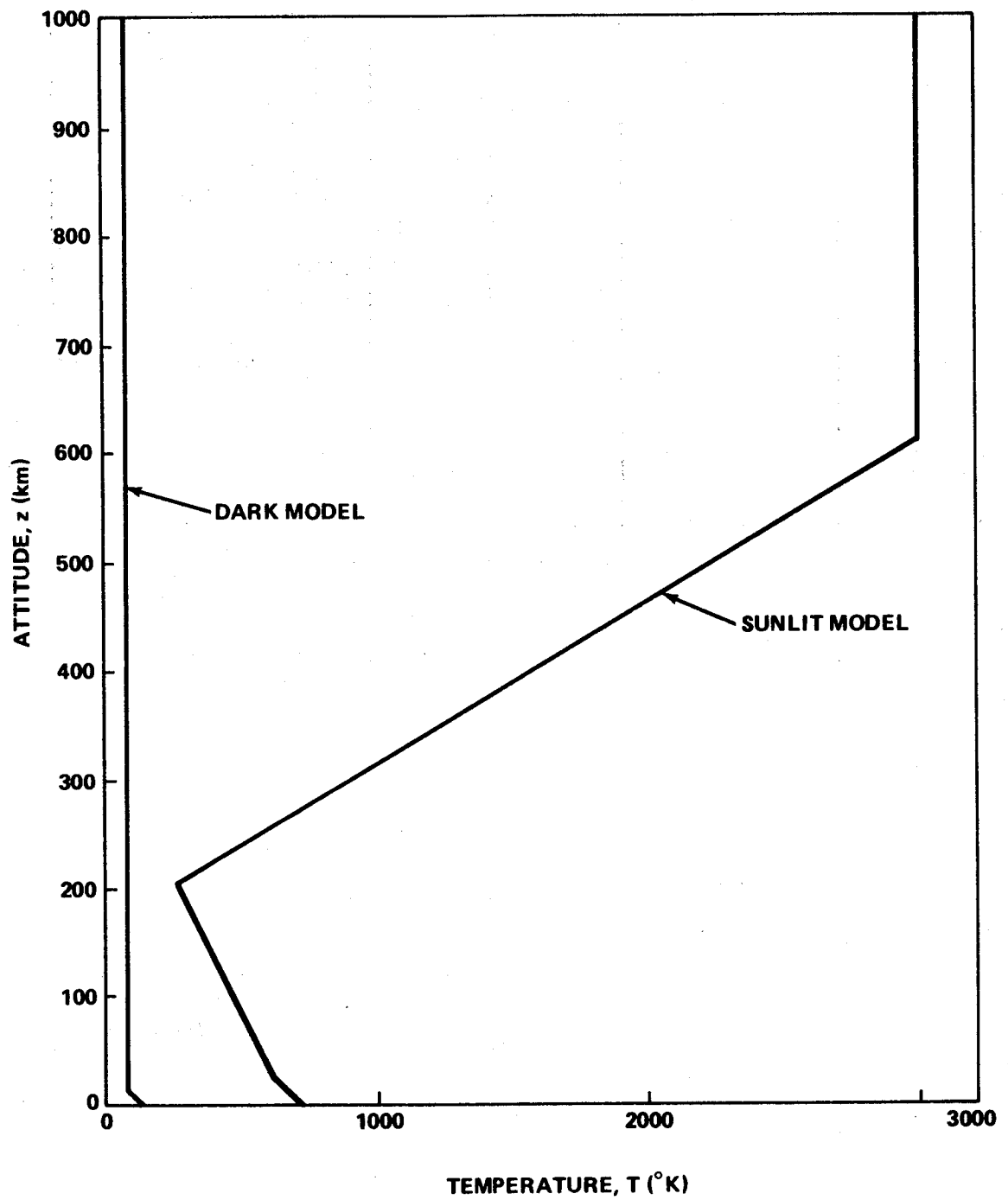


Figure V-1. Range of temperatures between dark and sunlit profiles versus altitude for the Mercury upper density limit model.

[V-12]. Since Mercury has a very high exospheric temperature, it is likely that hydrogen would escape quickly from Mercury. Kozyrev's arguments about the likelihood of a hydrogen atmosphere being cool and replenished from the solar wind are considered inconclusive.<sup>1</sup> Likewise, other lightweight molecules probably have escaped completely from the atmosphere. As a consequence, only those heavy gases such as neon, krypton, argon, and carbon dioxide could exist in the Mercurian atmosphere.

Table V-1 shows the spectroscopic results for Mercury.<sup>2</sup> Note that CO<sub>2</sub> is the only abundant gas presently in the atmospheres of Venus, Earth, and Mars whose molecular weight is equal to or greater than 44 g/mole. The spectroscopic evidence has shown that CO<sub>2</sub> is also existing in the Mercurian atmosphere with the smallest reliable upper limit on the CO<sub>2</sub> partial pressure being 0.04 mb, except for the controversial claim by Moroz.<sup>3</sup> The possibility of the presence of heavy gases in the atmosphere of Mercury other than carbon dioxide and argon has not been ruled out. One can predict that none of the other heavier gases such as oxygen, nitrogen, sulphur vapor, carbon disulphide, sulphur dioxide, neon, krypton or xenon could ever have reached the required escape velocity, with the possible exception of neon. If any of the gases were ever present on Mercury at any time past, they must still be there. Other gases which might be found would include chlorine, hydrogen bromide and iodine vapor [V-17].

Field [V-18] has noted that the terrestrial ratio of the mass of atmospheric argon to the mass of the planet is approximately  $10^{-8}$  with the argon presumably of radiogenic origin. The assumption that this mass ratio corresponds to the terrestrial value results in the partial pressure of argon on Mercury of 1.9 mb. This result suggests that sufficient argon may exist to constitute the difference between the CO<sub>2</sub> partial pressure limit (0.1 mb). A thin atmosphere of 40 percent CO<sub>2</sub> and 60 percent argon probably could remain cool enough through infrared emission to avoid the high temperatures derived by Belton et al. [V-5]. That would cause the rapid loss of a mainly argon atmosphere.

---

1. NASA SP 8085, "The Planet Mercury (1971)."

2. Ibid.

3. Ibid.

TABLE V-1. SUMMARY OF SPECTROSCOPIC RESULTS FOR MERCURY<sup>a</sup>

Wavelength ( $\mu\text{m}$ )	Mole- cule	Abundance (m-atm)	Pressure (mb)	Spectra	Reference	Remarks
0.4102(H $\delta$ ) 0.4861(H $\beta$ )	H <sub>2</sub>	0.8 to 80 <sup>b</sup>	0.003 to 0.3 <sup>b</sup>	Photographic	V-10 and V-11	Detection claimed, <sup>b</sup> abundance not estimated
0.4102(H $\delta$ ) 0.4861(H $\beta$ )	H <sub>2</sub>			Photographic		Reality of detection in references V-10, V-11
Blue ~0.8					V-13	No Mercury lines detected
~0.8 ~0.8 ~0.8	H <sub>2</sub> O O <sub>2</sub> CO <sub>2</sub>	<30 $\mu\text{m}$ <sup>c</sup> < 1.0 <57	<0.05 <4.2		V-14	
1.049	CO <sub>2</sub>	< 5	<0.35	Photoelectric	V-5	
1.203	CO <sub>2</sub>	< 1.0	<0.073	Photographic	V-15	
1.203 1.2177	CO <sub>2</sub> CO <sub>2</sub>	< 0.2 <sup>d</sup> < 0.58	<0.02 <sup>d</sup> <0.04	Photographic	V-15	
1.2177	CO <sub>2</sub>	< 1.4	<0.10	Photographic	V-15	No Mercury lines detected
1.6	CO <sub>2</sub>			IR Spectrometer	V-16	
1.6	CO <sub>2</sub>	1.5-3.5 <sup>b</sup>	0.11-0.26 <sup>b</sup>	PbS Photocell	V-9	Detection claimed <sup>b</sup>
2.12, 2.26 2.26 to 2.32 2.35 3.3	N <sub>2</sub> O NH <sub>3</sub> CO CH <sub>4</sub>	< 0.02 < 0.01 < 0.1 < 0.003	<0.0015 <0.0003 <0.005 <0.0001	PbS Photocell	V-9	No Mercury lines detected

a. NASA Monograph, "The Planet Mercury (1971)," unpublished.

b. Reality of detection questioned by other investigators listed at same wavelength.

c.  $\mu\text{m}$  of precipitable water.

b. Limit suspect because of nearby strong solar and terrestrial absorption lines.

### 5.1.2.3 Pressure

The evidence for an atmosphere on Mercury is based on two observations. Dollfus [V-19] reported an atmosphere of surface pressure  $p_s \sim 1$  mb, from measurements of the polarization at the center and cusps of the planet in the red and green; Moroz [V-9] detected absorption in the  $1.6\text{ }\mu$   $\text{CO}_2$  band in the infrared spectrum of Mercury. By re-analysis of Dollfus's data with laboratory and lunar data from the literature, O' Leary and Rea [V-20] found that the observed polarization properties of Mercury can be expected from laboratory data and are similar to those of the moon. They concluded that no reason exists to suggest any polarimetric evidence for an atmosphere on Mercury and estimate an upper limit of 1 mb for the surface pressure of Mercury from the sensitivity of the polarimetric method. O' Leary and Rea also reason that if the surface of Mercury has been weathered by solar wind and micrometeorite bombardment to produce its present albedo, color, polarization, and photometric properties, then the atmospheric pressure at the surface must be  $\leq 10^{-5}$  mb for the solar protons to penetrate the atmosphere.

Since the spectroscopic measurement of the saturated  $\text{CO}_2$  lines in the  $1.6\text{-}\mu$  band depend on both the effective pressure and the amount of  $\text{CO}_2$ , it is impossible to separate the two by observing only in one band. Therefore, Spinrad, Field, and Hodge [V-14] attempted to measure the intensity of the weak unsaturated lines of  $\text{CO}_2$  at  $8700\text{ }\text{\AA}$  which are not pressure dependent. Combining these measurements with those of Moroz, they expected to get the amount of  $\text{CO}_2$  and the total atmospheric pressure at the surface of the planet. Despite a low detection limit of  $4\text{ m}\text{\AA}$ , they were unable to observe  $\text{CO}_2$  lines in the  $8700\text{-}\text{\AA}$  region. Therefore, Spinrad, Field, and Hodge proposed an upper limit to the  $\text{CO}_2$  content of  $57\text{ m-atm}$ , which corresponds to a maximum possible partial pressure of 4.2 mb on the surface. Combining this upper limit on the amount of  $\text{CO}_2$  with the Moroz observation of the equivalent width of the  $1.6\text{-}\mu$ ,  $\text{CO}_2$  band, they conclude that the surface pressure on Mercury is near 4 mb if the atmosphere is pure  $\text{CO}_2$ .

Evidence of a tenuous atmosphere on Mercury is also supported by the comparison of Mercury's surface properties to the moon's. The apparent similarity of the surface properties of these two is consistent with the hypothesis that their histories and environments are similar because of direct impact by solar wind and solar ultraviolet radiation. If these radiations reach Mercury's surface, a negligible atmosphere is implied.<sup>4</sup> Also, the

---

4. Ibid.

discussion of the properties of the surface layers by Klein [V-21] concludes that the large value derived for the inverse thermal inertia from microwave observation requires that the surface pressure be less than 1 mb. All of these arguments are in good agreement with more recent precise polarimetric results cited by Dollfus [V-22] in which the upper limit total pressure on Mercury has been reduced to 0.1 mb.

#### 5.1.2.4 Atmospheric Models

Based on the available information described in the preceeding subsections, it is clear that Mercury has a tenuous atmosphere with carbon dioxide and argon as possible constituents, and a surface pressure being much less than 1 mb. Two model atmospheres are adopted<sup>5</sup> to illustrate the upper limit pressure and density that could exist on Mercury. The model applicable to sunlit condition uses the CO<sub>2</sub> partial pressure limit of 0.04 mb and the total surface pressure limit of 0.1 mb with argon accounting for the remaining pressure. The resulting composition is 60 percent argon and 40 percent CO<sub>2</sub> by number and implies a mean molecular weight of 41.6 and an adiabatic lapse rate of -4° K/km on Mercury. The appropriate extreme of surface temperature is 700° K and an exospheric temperature of 3000° K. At tropopause, the temperature is  $(0.5)^{\frac{1}{4}} T_S$  which has a value of 590° K. In the upper atmosphere, the warmest temperatures cited in the theoretical literature are approximately 250° K at the mesopause and 3000° K at the critical level (pressure near  $10^{-8}$  mb). To account for the night conditions, a model is specified which yields a still greater density in the first 8 km above the Mercurian surface. Note that the surface pressure of the dark model results from assumed pure argon atmosphere since CO<sub>2</sub> would be frozen out at the prevailing temperature.

Table V-2 shows the values of temperature, pressure, density, pressure scale height, and density scale height as a function of altitude for both sunlit and dark conditions. The table values are terminated at the level where the density has reached a value of approximately  $10^{-16}$  g/cm<sup>3</sup>. Vertical profiles of temperature, pressure, and density are given in Figures V-1 and V-2.

#### 5.1.3 Gas Properties (1000 to 20 000 km Altitude)

Pressure and density decrease exponentially, and temperature increases linearly with increasing altitude to their respective interplanetary

---

5. Ibid.

a

TABLE V-2. MERCURY UPPER DENSITY LIMIT ATMOSPHERIC MODELS

Sunlit (noon)						Dark			
z (km)	T (° K)	P (mb)	$\rho$ (g/cm <sup>3</sup> )	H <sub>p</sub> (km)	H <sub><math>\rho</math></sub> (km)	T (° K)	P (mb)	$\rho$ (g/cm <sup>3</sup> )	H <sub>p</sub> or H <sub><math>\rho</math></sub> (km)
0.0	700	0.1000	$7.15 \times 10^{-8}$	37.4	47.6	100	$600 \times 10^{-2}$	$2.89 \times 10^{-7}$	5.56
5.0	680	0.0873	$6.42 \times 10^{-8}$	36.4	46.2	84	$2.26 \times 10^{-2}$	$1.29 \times 10^{-7}$	4.67
10.0	660	0.0759	$5.76 \times 10^{-8}$	35.3	44.9	84	$7.05 \times 10^{-3}$	$4.04 \times 10^{-8}$	4.67
15.0	640	0.0658	$5.14 \times 10^{-8}$	34.2	43.5	84	$2.42 \times 10^{-3}$	$1.38 \times 10^{-8}$	4.67
20.0	620	0.0567	$4.57 \times 10^{-8}$	33.1	42.2	84	$8.28 \times 10^{-4}$	$4.74 \times 10^{-9}$	4.67
25.0	600	0.0486	$4.05 \times 10^{-8}$	32.1	40.8	84	$2.84 \times 10^{-4}$	$1.63 \times 10^{-9}$	4.67
27.5	590 <sup>b</sup>	0.0450	$3.81 \times 10^{-8}$	31.5	40.1	84	$1.66 \times 10^{-4}$	$9.52 \times 10^{-10}$	4.67
30.0	585	0.0415	$3.55 \times 10^{-8}$	31.3	34.8	84	$9.73 \times 10^{-5}$	$5.58 \times 10^{-10}$	4.67
40.0	566	0.0300	$2.65 \times 10^{-8}$	30.3	33.7	84	$1.14 \times 10^{-5}$	$6.55 \times 10^{-11}$	4.67
50.0	547	0.0214	$1.96 \times 10^{-8}$	29.2	32.6	84	$1.34 \times 10^{-6}$	$7.70 \times 10^{-12}$	4.67
60.0	528	0.0151	$1.43 \times 10^{-8}$	28.2	31.4	84	$1.58 \times 10^{-7}$	$9.04 \times 10^{-13}$	4.67
70.0	509	0.0105	$1.04 \times 10^{-8}$	27.2	30.3	84	$1.86 \times 10^{-8}$	$1.06 \times 10^{-13}$	4.67
80.0	490	0.00725	$7.41 \times 10^{-9}$	26.2	29.2	84	$2.18 \times 10^{-9}$	$1.25 \times 10^{-14}$	4.67
100.0	452	0.00327	$3.62 \times 10^{-9}$	24.1	26.9	84	$3.00 \times 10^{-11}$	$1.72 \times 10^{-16}$	4.67
120.0	413	0.00138	$1.67 \times 10^{-9}$	22.1	24.6				
140.0	375	0.000532	$7.10 \times 10^{-10}$	20.1	22.3				
160.0	337	0.000186	$2.76 \times 10^{-10}$	18.0	20.0				
180.0	299	$5.72 \times 10^{-5}$	$9.58 \times 10^{-11}$	16.0	17.8				
200.0	261	$1.50 \times 10^{-5}$	$2.87 \times 10^{-11}$	13.9	15.5				
205.5	250 <sup>b</sup>	$1.00 \times 10^{-5}$	$2.00 \times 10^{-11}$	13.4	9.8				
210.0	280	$7.29 \times 10^{-6}$	$1.30 \times 10^{-11}$	15.0	11.0				
225.0	381	$3.10 \times 10^{-6}$	$4.07 \times 10^{-12}$	20.4	15.0				
250.0	549	$1.12 \times 10^{-6}$	$1.02 \times 10^{-12}$	29.4	21.6				
275.0	717	$5.34 \times 10^{-7}$	$3.72 \times 10^{-13}$	38.4	28.2				
300.0	886	$2.97 \times 10^{-7}$	$1.68 \times 10^{-13}$	47.3	34.8				
350.0	1222	$1.21 \times 10^{-7}$	$4.97 \times 10^{-14}$	65.3	48.0				
400.0	1559	$6.17 \times 10^{-8}$	$1.98 \times 10^{-14}$	83.3	61.3				
500.0	2232	$2.28 \times 10^{-8}$	$5.10 \times 10^{-15}$	119.3	87.7				
600.0	2905	$1.09 \times 10^{-8}$	$1.88 \times 10^{-15}$	155.3	114.2				
614.19	3000 <sup>b</sup>	$1.00 \times 10^{-8}$	$1.67 \times 10^{-15}$	160.4	160.4				
700.0	3000	$5.856 \times 10^{-9}$	$9.76 \times 10^{-16}$	160.4	160.4				
800.0	3000	$3.14 \times 10^{-9}$	$5.23 \times 10^{-16}$	160.4	160.4				
900.0	3000	$1.68 \times 10^{-9}$	$2.81 \times 10^{-16}$	160.4	160.4				
1000.0	3000	$9.02 \times 10^{-10}$	$1.50 \times 10^{-16}$	160.4	160.4				

a. NASA Monograph, "The Planet Mercury (1971)," unpublished.

b. At these levels the lapse rate  $dT/dz$  changes value.Note: For an isothermal atmosphere  $\frac{d \log T}{d \log P} = \beta = 0$ ,  $H_p = H_\rho$  (App. B).



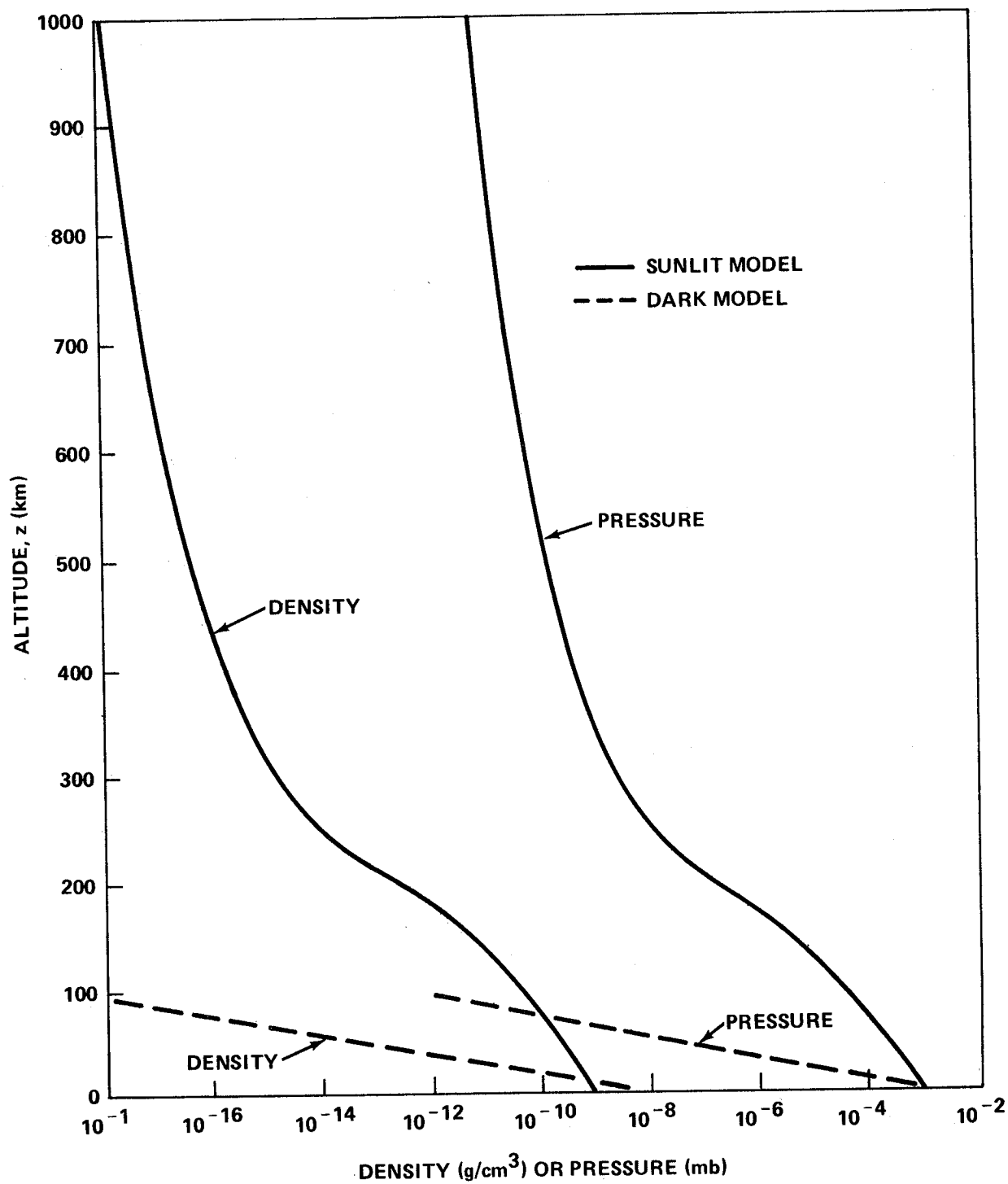


Figure V-2. Dark and sunlit model profiles of density and pressure versus altitude for upper density limit atmospheres.

space values of  $10^{-10}$  dynes/cm<sup>2</sup>,  $10^{-23}$  g/cm<sup>3</sup>, and  $2 \times 10^5$  °K near 20 000 km. Above 20 000 km altitude, all three quantities remain relatively constant with increasing altitude [ V-23 ].

#### 5.1.4 Ionosphere and Charged Particles

Mercury's probable lack of magnetic field and atmosphere indicates the absence of trapped radiation belts and an ionosphere. Thus, the only charged particles of interest are those populating the interplanetary space traversed in Mercury's orbit.<sup>6</sup>

#### 5.1.5 Clouds

Some have been observed [ V-23 ].

#### 5.1.6 Circulation

Information is not available.

#### 5.1.7 Electromagnetic Radiation

The electromagnetic radiation environment near Mercury includes the x-ray, ultraviolet, visible, infrared, and microwave portions of the spectrum.

##### 5.1.7.1 Solar Radiation

The solar radiation environment at 1 AU from the sun is given in Reference V-24 which specifies the spectral irradiance  $P_\lambda$  (the received power per unit area and per unit wavelength interval) for all wavelengths between 1 Å and 100 cm. At the extremes of this range, i.e., the x-ray and microwave regions, the radiation is sporadic; but between 0.1 and 10 μm the radiation is steady with an integrated flux of  $S = 0.1353 \pm 0.0021$  W/cm<sup>2</sup> at 1 AU from the sun; i.e., the solar constant [ V-26 ]. These quantities,  $S$  and  $P_\lambda$ , multiplied by  $r^{-2}$  (where  $r$  is the distance of Mercury from the sun in AU) provide estimates of the radiation at Mercury. Because of the high eccentricity of Mercury's orbit,  $r^{-2}$  ranges between 4.6 and 10.6 AU and, accordingly, the integrated flux  $S/r^2$  ranges between 0.623 and 1.435 W/cm<sup>2</sup> in the sunlight.

---

6. Ibid.

### 5.1.7.2 Mercury Reflected Radiation

Solar radiation reflected from Mercury has been measured visually and photographically by various observers whose results are discussed by Harris [V-26]. The photoelectric measurements of Irvine et al. [V-27] are generally in agreement with the foregoing results at the few angles for which data are published, and are intrinsically more precise. Therefore, they are adopted here.

Mercury's astronomical magnitudes,  $m$ , phase function,  $\phi(\alpha)$ , and geometric albedo,  $p(\lambda)$ , whose definitions are given in References V-26 and V-28, are satisfactorily approximated by the following expressions:

$$m = m_{\odot} - 2.5 \log [p(\lambda)\phi(\alpha)] + 5 \log (rR/R_M)$$

$$\log \phi(\alpha) = \frac{\alpha}{250}^{\frac{1}{2}} \left[ 3.8 + \frac{\alpha}{100} \left( -2.73 + \frac{\alpha}{50} \right) \right]$$

$$\log p(\lambda) = (-0.94 \pm 0.07) + (0.25 \pm 0.05) (2 - \lambda^{-1})$$

These expressions have been adapted from Harris [V-26], Irvine [V-27], and Allen [V-28]. The distance  $r$  from the sun must be expressed in astronomical units, the phase angle  $\alpha$  in degrees, and the wavelength  $\lambda$  in micrometers. The apparent magnitude  $m_{\odot}$  of the sun is given at several wavelengths in Table V-3. Further details of photometric studies are given in References V-29, V-30, and V-31.

The flux of reflected sunlight may be calculated directly from the foregoing values of the phase function,  $\phi(\alpha)$ , and the geometric albedo,  $p(\lambda)$  by the formula

$$F_{\lambda} = \frac{p(\lambda)\phi(\alpha)}{r^2(R/R_M)^2} P_{\lambda}$$

Here,  $P_{\lambda}$  is the solar spectral irradiance specified in Reference V-24 and the distance  $r$  from the sun must be expressed in astronomical units. If the solid angle of the visible, sunlit portion of Mercury's disk is  $\Omega_M$ , the intensity of the surface,  $I_{\lambda}$ , has the average value

$$I_{\lambda} = F_{\lambda} / \Omega_M$$

TABLE V-3. PHOTOMETRIC PARAMETERS FOR THE  
SUN, MOON, AND PLANETS<sup>a</sup>

	Photometric Passband Parameters <sup>b</sup>				
	U	B	V	R	I
Effective Wavelength ( $\mu\text{m}$ )	0.353	0.448	0.554	0.690	0.820
Apparent Magnitude of the Sun ( $m_{\odot}$ )	-28.04	-28.18	-28.81	-29.26	-29.55
Absolute Magnitude of —					
Mercury ( $m_{\odot}$ )	c	+0.57	-0.36	-1.21	-1.73
Venus ( $m_{\odot}$ )	-2.97	-3.47	-4.29	c	c
Earth ( $m_{\odot}$ )	c	-3.67	-3.87	c	c
Moon ( $m_{\odot}$ )	+1.59	+1.13	+0.21	-0.59	-1.05
Mars ( $m_{\odot}$ )	+0.42	-0.16	-1.52	-2.64	-3.02
Jupiter ( $m_{\odot}$ )	-7.94	-8.42	-9.25	-9.75	-9.72
Saturn ( $m_{\odot}$ ) <sup>d</sup>	-7.26	-7.84	-8.88	c	c
Uranus ( $m_{\odot}$ )	-6.35	-6.63	-7.19	-7.04	-6.24
Neptune ( $m_{\odot}$ )	-6.25	-6.46	-6.87	-6.54	-5.74
Pluto ( $m_{\odot}$ )	+0.06	-0.21	-1.01	-1.64	-1.92

a. NASA Monograph, "The Planet Mercury (1971)," unpublished.

b. See Appendix A of Newburn, R. L., and Gulkis, S., 1971, "A Brief Survey of the Outer Planets Jupiter, Saturn, Uranus, Neptune, Pluto, and Their Satellites," Jet Propulsion Laboratory TR 32-1529.

c. Data not available.

d. Can vary with ring inclination up to one magnitude less, i.e., brighter, than specified.

The reflection properties of different portions of the disk imply that an uncertainty factor of 2 in either direction should be applied to the intensity on the basis of lunar analogy [V-32]. The uncertainties specified for the albedo,  $P(\lambda)$ , are large enough so that the uncertainties from substitution of the albedo values into expressions for magnitude,  $m$ , and flux,  $F_\lambda$ , bracket the variations and uncertainties for all wavelengths and phase angles.

The polarization of the light reflected from Mercury varies with phase and position on the disk. The latest measurements reported by Dollfus [V-22] conclude that the polarization is similar to the moon's [V-33].

Although photometric observations of Mercury are not complete enough to permit a determination of the integrated or radiometric albedo [V-34], the similarity of the observed parameters to those of the moon suggests the adoption of lunar values for Mercury. For the moon, the range from 0.07 to 0.24 includes extremes based on differing surface terrains, and the average value is 0.12 [V-35].

#### 5.1.7.3 Mercury Thermal Emission

The observational data from which the characteristics of Mercury's thermal emission have been inferred are discussed in subsection 5.2.4 and summarized in Table V-4. In the wavelength range between  $1 \mu\text{m}$  and  $0.1 \text{ cm}$ , thermal emission occurs within 100 wavelengths of the surface, and is therefore characteristic of the surface temperature and material properties. Although direct measurements of infrared emissivity are not available, it has been estimated as close to unity [V-36] and that value is adopted here. With the infrared emissivity taken as unity, the intensity and flux of thermal radiation are distributed in wavelength according to the Planck function  $B_\lambda(T)$ , which describes blackbody radiation, and the formulas in Table V-5 where  $T$  is the local surface temperature. The integrated flux incident on a spacecraft can be obtained only by integrating the intensities over wavelength and solid angle, but limiting values may be obtained in the form of  $\sigma T^4$  (the integral of the Planck function, Reference V-28) where the limiting values of  $T$  are taken as  $90^\circ$  and  $700^\circ \text{ K}$ . These temperature limits imply limits on the integrated flux of  $0.0004$  and  $1.4 \text{ W/cm}^2$  at Mercury's surface. At larger separations from Mercury ( $R > R_M$ ), the flux limits are proportional to  $(R/R_M)^{-2}$ .

TABLE V-4. INFRARED OBSERVATIONS OF MERCURY  
INTERPRETED AS SURFACE TEMPERATURES<sup>a</sup>

Reference	Wavelength ( $\mu\text{m}$ )	Temperature ( $^{\circ}\text{K}$ )	Interpretation
V-37	8 to 14	600	Subsolar point at mean distance from sun
V-38	8 to 14	613	Same
V-39	8 to 14	180	Night quadrant, after sunset
V-40	8 to 13	<150	Night hemisphere
V-41	3.75 to 11.3	522	Sunlit surface, in- cluding subsolar point
V-41	8.6	205	Sunlit crescent near terminator
V-41	11.8	111 $\pm$ 3	Night hemisphere

a. NASA Monograph, "The Planet Mercury (1971)," Unpublished.

TABLE V-5. ELECTROMAGNETIC RADIATION NEAR MERCURY<sup>a</sup>

	Direct Sunlight <sup>b</sup>	Sunlight Reflected from Mercury <sup>c</sup>	Mercury Thermal, and Radio Emission <sup>d</sup>
Intensity	$I_{\lambda} = \frac{P_{\lambda}}{(6.8 \times 10^{-5} \text{ sterad})}$	$0 < I_{\lambda} < \frac{p(\lambda) P_{\lambda}}{r^2 (\pi \text{ sterad})}$	$I_{\lambda} = B_{\lambda} (T)$
Flux	$F_{\lambda} = P_{\lambda}/r^2$	$0 < F_{\lambda} < \frac{p(\lambda)\phi(\alpha)}{r^2 (R/R_M)^2} P_{\lambda}$	$F_{\lambda} = \frac{\pi B_{\lambda}(T)}{(R/R_M)^2}$
Integrated Flux	$0.62 < F < 1.43 \frac{W}{cm^2}$	$0 < F < \frac{0.35}{(R/R_M)^2} \frac{W}{cm^2}$ (average albedo = $0.12 \times 2 \pm 1$ )	$\frac{0.0004}{(R/R_M)^2} < F < \frac{1.4}{(R/R_M)^2} \frac{W}{cm^2}$

a. NASA SP 8085, "The Planet Mercury (1971)."

b. Beyond shadow of Mercury, take solar spectral irradiance  $P_{\lambda}$ , given in NASA SP-8005 [V-24], and use the distance  $r$  from the sun in astronomical units.

c. Applicable except for conditions of specular reflection of sunlight; then the entries in column 1 are appropriate upper limits. Expressions for  $p(\lambda)$  and  $\phi(\alpha)$  are in footnote a.,  $P_{\lambda}$  is from NASA SP-8005 Reference V-24 and  $r$  is the distance from the sun in astronomical units.

d. For  $\lambda < 0.1$  cm, the range of  $T$  is that of the physical temperature of the observed surface; for  $\lambda > 0.1$  cm the range of  $T$  is that of the brightness temperature  $T_B$  shown in Figure V-3.

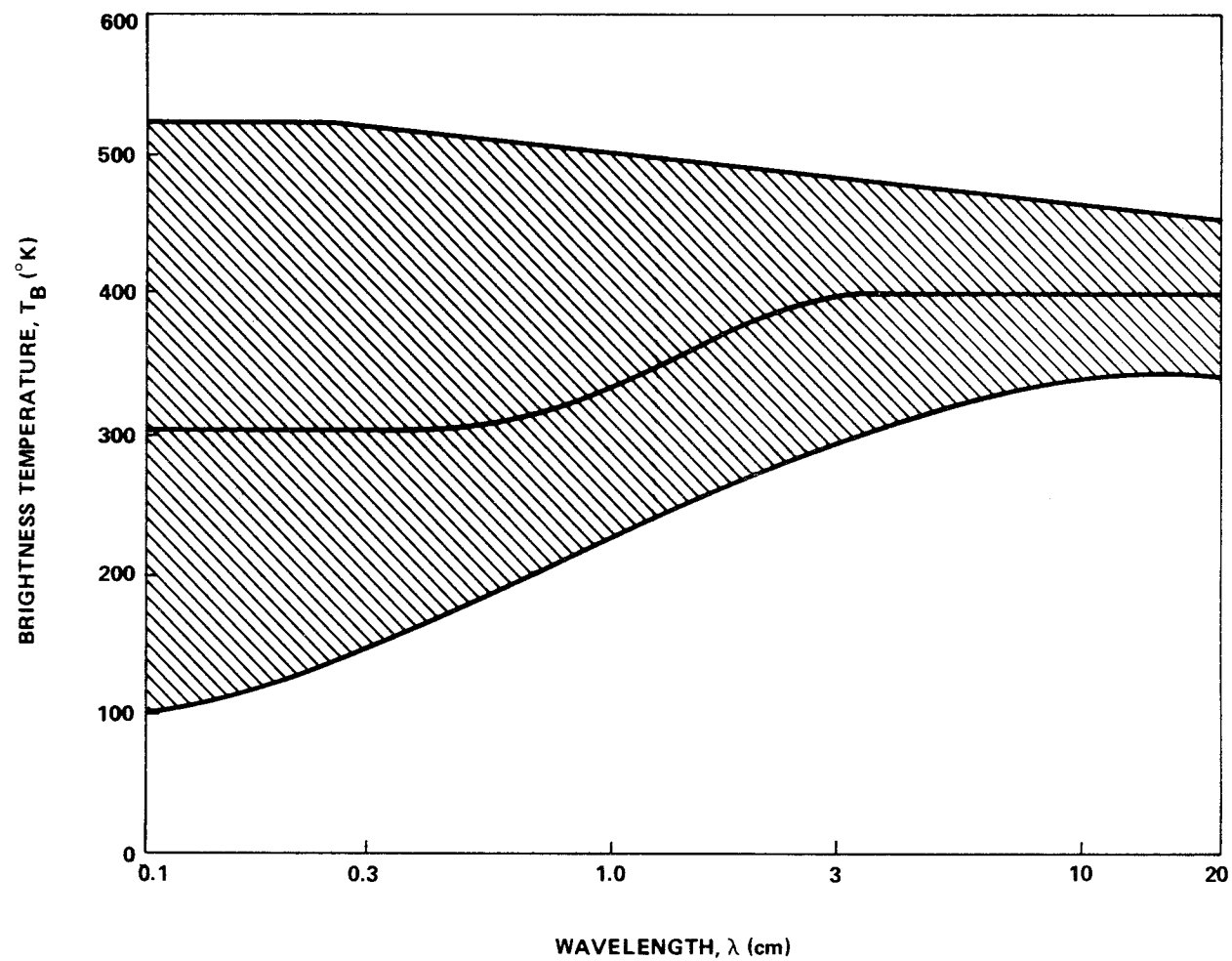


Figure V-3. The range of brightness temperature  $T_B$  for Mercury.  
 (The central line represents the nominal dependence of  $T_B$  on wavelength  $\lambda$ , and  
 the shaded area includes the uncertainties and time variations.)



#### 5.1.7.4 Mercury Microwave Emission

At wavelengths between 0.33 and 11.3 cm, Mercury's radio emission has been detected by several observers, including those listed in Table V-6. The observational data have been interpreted in terms of effective brightness temperature  $T_B$  which is related to the observed flux  $F_\nu$  by the modified Rayleigh-Jeans formula,

$$F_\nu = 2\pi k T_B (R_M / r\lambda)^2 .$$

Where  $k$  is Boltzman's constant,  $R_M$  is the radius of Mercury,  $r$  is the distance from the sun, and  $\lambda$  is the wavelength of electromagnetic radiation. The brightness temperatures exhibit variations with wavelength and time of observation which exceed observational uncertainties and permit derivation of numerical values for physical, thermal, and electrical properties of Mercury's epilith or soil near the surface. The mean brightness temperatures, i.e., those averaged over a long interval of observation, derived at various wavelengths are shown in Table V-6 (adapted from Reference V-47).

At some wavelengths, the data reported in the references cited in Table V-6 indicate strong dependence of the brightness temperature on phase angle and its weaker dependence on heliocentric longitude. Because of the resonance between the periods of Mercury's orbit and rotation, these dependencies can be expressed in terms of the hermographic latitude, longitude, and the local time of that point on Mercury's surface directly beneath a nearby spacecraft.

These considerations are not pertinent to spacecraft design when the encounter circumstances are unspecified, but they do lead to a broad range of possible brightness temperatures at each wavelength. The range adopted here for design purposes is shown as a function of wavelength in Figure V-3. The adopted values are based on the references given in Table V-6. The tabulation of brightness temperatures versus wavelengths in Table V-6 indicates a probable increase of mean brightness temperature with wavelength between a few millimeters and several centimeters [V-47].

If the brightness temperature  $T_B$  is substituted for the physical temperature  $T$  in the formulas for the thermal emission given in subsection 5.1.7.3, the same formulas describe the microwave emission in the wavelengths from 0.1 to 20 cm.

TABLE V-6. SUMMARY OF MERCURY'S RADIO BRIGHTNESS  
TEMPERATURE MEASUREMENTS<sup>a</sup>

Wavelength (cm)	Mean Brightness Temperature, $T_B$ (°K)	Reference
0.33	$296 \pm 30^b$	V-42
0.34	$277 \pm 30$	V-43
0.80	$530 \pm 50$	V-44
1.53	$450 \pm 60$	V-45
1.95	$288 \pm 30$	V-46
1.95	$350 \pm 30$	V-47
2.82	$375 \pm 40^c$	V-47
3.45, 3.75	$400 \pm 80$	V-48
3.75	$380 \pm 20$	V-49
6.00	$385 \pm 30$	V-47
11.3	$300 \pm 40$	V-50

a. NASA SP 8085, "The Planet Mercury (1971)."

b. Uncertainty estimates by Morrison and Klein [V-47] rather than Epstein et al. in most cases.

c. Unpublished results of Medd, cited by Morrison and Klein [V-47].

### 5.1.7.5 Other Radiation Sources

Harris [V-26] describes the light reflected from the moon and planets visible from Mercury. The magnitudes of these objects vary with relative positions (including phase angle) and orientations (including rotation and Saturn's ring inclination) which are specified in the "American Ephemeris and Nautical Almanac [V-50]" or Woolley [V-51]. Uncertainty broad enough to include these variations is implied by the expression for the apparent magnitude

$$m = (m_o \pm 0.3) + 5 \log (r\Delta) + (0.03 \pm 0.02)\alpha .$$

where  $m_o$  is the absolute visual magnitude whose values are specified in Table V-3 and  $\Delta$  is the distance from the reflecting surface to observer in astronomical units. Magnitudes and colors of bright stars may be obtained from standard star catalogs.

The integrated flux from the stars and planets is approximately  $\sigma T^4 = 4.6 \times 10^{-10} \text{ W/cm}^2$  where  $T = 3^\circ \text{K}$ , the equivalent blackbody temperature of space [V-28]. This flux is an appropriate lower limit for all spacecraft surfaces when shadowed from both the sun and Mercury if Mercury is the nearest planet.

### 5.1.8 Meteoroid Environment

#### 5.1.8.1 Cometary Meteoroid Flux [V-23]

The flux ( $F_c$ ), in number per square meter per second, of cometary meteoroids of mass  $m$  or greater on a randomly tumbling surface is: For  $10^{-6} \leq m \leq 10^2$ ,

$$\begin{aligned} \log F_c = & -13.669 - 1.213 \log m + \log \left( 1 + 0.042 \frac{1}{r} \right) \\ & + \log \frac{1}{2} \left[ 1 + \left( 1 - \frac{1}{r^2} \right)^{\frac{1}{2}} \right] . \end{aligned}$$

For  $10^{-12} \leq m \leq 10^{-6}$ ,

$$\begin{aligned} \log F_c = & -13.638 - 1.584 \log m - 0.063 (\log m)^2 \\ & + \log \left( 1 + 0.042 \frac{1}{r} \right) + \log \frac{1}{2} \left[ 1 + \left( 1 - \frac{1}{r^2} \right)^{\frac{1}{2}} \right] , \end{aligned}$$

where  $r$  is the distance of the spacecraft from the center of Mercury (in units of the planet's radius).

#### 5.1.8.2 Average Velocity of Cometary Meteoroids [V-23]

The average velocity of cometary meteoroids relative to the spacecraft is  $31.06 \times 10^3$  m/s.

#### 5.1.8.3 Survival Mass [V-23]

The survival mass for micrometeoroids can be calculated as a function of height in the atmosphere by using the following approximate expression

$$m^{1/3} - m_{\infty}^{1/3} = \frac{\Lambda A \rho_m^{-2/3} v^2}{6\xi \cos Z} \int_{\infty}^h \rho_a dh ,$$

(does not hold for dust balls)

where

$$\text{columnar mass} = - \int_h^{\infty} \rho_a dh$$

$Z$  = zenith angle

$\rho_m$  = density of micrometeoroid ( $3.5 > \rho_m > 0.5$  g/cm<sup>3</sup>)

$v$  = velocity of micrometeoroid

$$(v_{\text{parabolic}} \text{ or } v_{\text{orbital}} > v > v_{\text{escape}})$$

$A$  = shape factor = 1.2 for sphere

$$\Lambda/\xi = 10^{-11.449} .$$

### 5.1.9 Geomagnetic Environment

#### 5.1.9.1 Magnetic Field and Magnetosphere

There are no data that directly indicate existence of an intrinsic magnetic field of Mercury. Three apparently independent estimates of the

surface field strength are of the order of  $10^{-2}$  gauss [V-4, V-52, V-53]. Reiffel [V-54] assumes no intrinsic magnetic field for Mercury because of its slow rotation. (Fast rotation is thought to be significant in the maintenance of the fields of the Earth and Jupiter.) The range of magnetic moments corresponding to the foregoing estimates is between zero and the upper limit  $M_1 = 4 \times 10^{23}$  gauss-cm<sup>3</sup>. The corresponding magnetic field strengths range from the lower limit of  $10\gamma$ , a low interplanetary field estimate near Mercury [V-55], to  $2M_1/R^3$  where  $2M/R_M^3 = 2800\gamma$ .

The boundary of the magnetosphere is fixed by the interaction of the planetary field with the solar wind. For the minimum field estimates, the magnetosphere is nonexistent, but the maximum field estimates yield a magnetosphere boundary one planetary radius above the surface in the solar direction and slightly larger elsewhere. If a magnetosphere exists, its configuration is probably similar to the earth's [V-56], except that the distortions caused by the earth's rotation should be neglected. In these circumstances the simple expression adapted from Good [V-53] can be expected to describe the shape of the magnetosphere's outer boundary as follows:

$$R = R_1 (4 - \cos \theta) / 3$$

Here,  $R_1$  is the sunward extent (for Mercury  $R_1 < 2R_M$ ) and  $\theta$  is the angle from the solar direction.

#### 5.1.10 Astrodynamic Constants (Epoch 1960.0) [V-57]<sup>7</sup>

Parameter	Value
Semi-major axis	$a = 0.3871$ AU
Inclination to ecliptic	$i = 7$ deg
Eccentricity	$e = 0.2056$
Perihelion distance	$a(1-e) = 0.3075$ AU
Aphelion distance	$a(1+e) = 0.4667$ AU
Sidereal period	$T_o = 87.969$ days
Synodic period	115.88 days

---

7. Ibid.

Parameter	Value
Mean motion (orbital angular velocity)	$n = 2\pi/T_o = 8.267 \times 10^{-7} \text{ rad/s}$
Maximum angular velocity	$n(1-e)^{-2} = 1.310 \times 10^{-6} \text{ rad/s}$
Minimum angular velocity	$n(1+e)^{-2} = 5.688 \times 10^{-7} \text{ rad/s}$
Gravitational parameter	$2.1686 \times 10^4 \text{ km}^3/\text{s}^2$
Gravitational potential	$\psi = -(9.10 \pm 0.07 \text{ km}^2/\text{s}^2) (R_M/R)$
Escape velocity at distance R	$V_e = (4.27 \pm 0.02 \text{ km/s}) (R_M/R)^{1/2}$
Period of Keplerian orbit of semi-major axis a	$T_a = (84.5 \pm 0.6 \text{ min}) (a/R_M)^{3/2}$
Surface acceleration of gravity	$g = 374 \pm 4 \text{ cm/s}^2$
Mass	$M_M = (3.32 \pm 0.02) \times 10^{23} \text{ kg}$
Radius	$R_M = 2435 \pm 6 \text{ km}$
Mean density	$\bar{\rho} = 5.5 \pm 0.1 \text{ g/cm}^3$
Period of rotation	$T_r = 58.646 \pm 0.03 \text{ days}$
Angular velocity of rotation	$\omega_r = (1.2400 \pm 0.0006) \times 10^{-6} \text{ rad/s}$
Inclination of rotational pole to normal of orbital plane	$<10 \text{ deg}$

## 5.2 Surface Environment

Because of the lack of good observational evidence for an atmosphere on Mercury, there is now more reason to believe that the surfaces of Mercury and the moon have been conditioned by similar mechanisms. No need would exist to invoke hypotheses such as the presence of radiogenic argon with a low exospheric temperature [V-58], a buildup of a Mercury atmosphere after meteoric erosion [V-14], or a meteoric rain on a Mercurian surface after braking by an atmosphere [V-59]. Rather, support is lent to the hypothesis that bombardment of Mercury by the solar wind and by micro-meteorites may have darkened and roughened its surface, and caused it to evolve to its present albedo, color, polarization, and photometric phase properties.

### 5.2.1 Surface Features

Surface detail is difficult to observe on Mercury for two reasons: (1) the angular extent of its disk is so small as seen from the earth ( $< 13$  arc-sec) that even high magnification does not yield resolution better than about one tenth of a radius which is comparable to that of the moon without magnification, and (2) the bright sky for daytime and long air path length for twilight observations lead to marginal contrast in observed features. These factors are partially responsible for the incorrect derivation of the rotation period from such observations before 1965. Numerous observers interpreted their observations (recorded primarily in the form of drawings) in terms of a single sunlit hemisphere. (Schiaparelli, Fournier, Antoniadi, and Dollfus are widely known for this work.) These drawings and maps created from them are summarized by Sandner [V-60]. Since 1965, the drawings and some photographs obtained at the Pic du Midi and New Mexico Observatories have been reinterpreted on the basis of the 59-day rotation period. The most complete lists of such data have been given by Chapman [V-61] and Camichel and Dollfus [V-62]. These authors have used the data on individual features and comparisons of drawings and photographs to support the 59-day period and prepare maps of Mercury's entire surface except the polar regions. The maps agree in most respects with one another; that from Reference V-62 is reproduced as Figure V-4 because it employs the recently adopted IAU longitude system. The features are positioned only to within about 10 deg accuracy and are not named. They differ in reflectivity by a real factor which, however, cannot be determined because of the impossibility of reliably calibrating drawings and plates made under the foregoing conditions of observation.

Radar observations reported by Goldstein [V-63] detected surface features but did not provide definite locations and properties. Smith et al. [V-64] find no evidence in their radar data for height variations on horizontal scales of 400 km or greater.

Therefore, there is insufficient basis from optical and radar observations to adopt variations in surface properties for different locations on the planet.

### 5.2.2 Physical Conditions

Measurements which relate to Mercury's surface properties indicate marginal differences at most between Mercury and the moon. The photometry (including the absolute and relative albedo, colors, contrast,

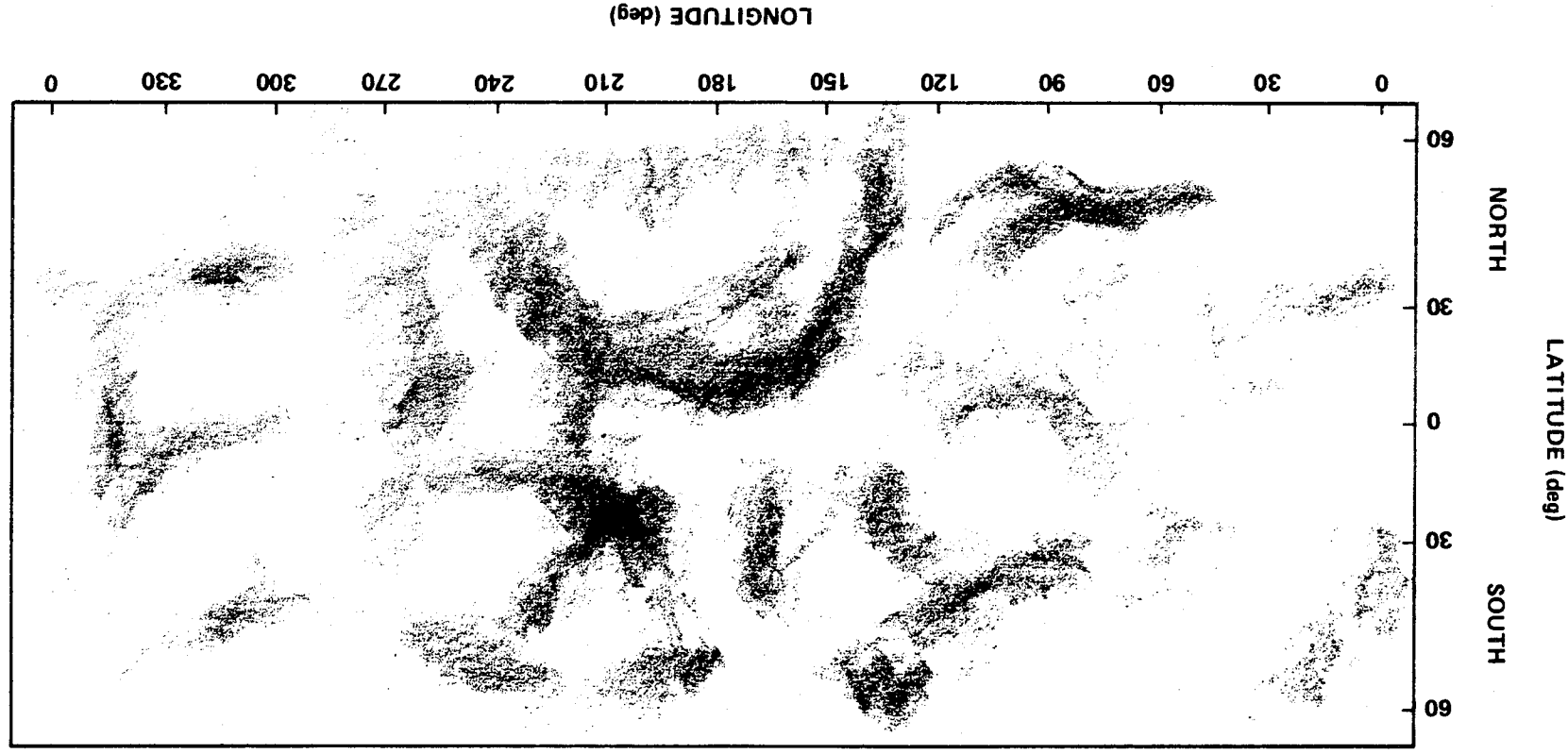


Figure V-4. Map of the surface features of Mercury from Camichel and Dollfus [V-62]. (The Mercator projection is used, South is at the top, and the longitude system is that adopted by the IAU).



and polarization and their dependences on wavelength and phase) is almost indistinguishable from the moon's [V-22, V-26, V-27, V-29, and V-30]. Reflected radar signals show that Mercury's roughness and the ratio of its cross-section to its geometrical area are also indistinguishable from the moon's [V-58, V-63 through V-70] (Table V-7). Analysis of the microwave observations indicates that Mercury's electrical properties are similar to the moon's [V-36]; microwave observations coupled with infrared observations indicate that the thermal response of Mercury's surface is similar to that expected for the moon if placed in Mercury's orbit with its rotation [V-37 through V-41].

TABLE V-7. RADAR INVESTIGATIONS OF MERCURY<sup>a</sup>

Reference	Wavelength (cm)	Chief Subject of Report
V-65	12.5	Surface roughness
V-63	12.5	Surface features (large scale)
V-66	23	Surface roughness
V-67	23, 70	Mass, radius, and ephemeris values
V-68	43	Reflectivity
V-69	70	Rotation rate
V-70	70	Cross-section and reflectivity
V-64		Surface features (large scale)

a. NASA SP 8085, "The Planet Mercury (1971)."

Theoretically, similarity between Mercury and the moon is to be expected on the basis that the qualitative theoretical considerations about the surface histories are the same. These concern the lack of an appreciable atmosphere and the associated surface modification by meteorites [V-71, V-72 and V-73], solar wind [V-59 and V-74], and solar ultraviolet radiation [V-4 and V-5]. The foregoing concept assumes that the original surface compositions and internally-generated orogenic processes were similar.

Therefore, the following sections assume that lunar values for the composition, mechanical properties, and topography can be applied directly to Mercury's surface. Much of material in these sections is taken from Reference 33 which has been corroborated by NASA References 75 and 76 that report Apollo 11 and 12 results.

#### 5.2.2.1 Surface Composition

From the foregoing assumption of similar surface values for the moon and Mercury, the study of Apollo samples [V-77] provided pertinent data on composition of Mercury's rocks and soil. The minerals which make up the bulk of these samples are very similar to those found in terrestrial basalts (namely, plagioclase, pyroxene, and ilmenite) and, less commonly, in anorthosites (primarily plagioclase). The minerals are primarily silicates and other oxides with the major differences from common terrestrial basalts being a larger fraction of ilmenite (containing iron and titanium oxides), the absence of ferric compounds, and the absence of moisture and hydrous minerals. Although Mercury's surface composition doubtless strongly depends on its local geological history, the absence of such data and photometric evidence makes it reasonable to accept the lunar surface composition as similar to Mercury's. One likely difference, however, would be an enhanced ratio of heavy metals, principally iron, in comparison to the earth or moon, to make Mercury's surface composition compatible with its overall high mean density. The magnitude of this difference is indicated by Reynolds and Summers [V-78] in terms of overall iron mass fractions for which representative values of 0.68 for Mercury and 0.13 for the moon are obtained. According to Khodak [V-79], the heavy metals could be present on the surface in the form of a higher fraction of ilmenite than for the moon or of metallic iron and nickel.

#### 5.2.2.2 Soil Mechanical Properties

The mechanical properties of lunar soil have been measured remotely by Surveyor spacecraft, studied from the samples returned by the Apollo missions, and deduced from observations of astronauts and photographs of mobility and sinkage. The pre- and post-Apollo estimates agree in most important respects [V-33, V-80, V-81]. Because these properties are relatively numerous and complex, the lunar values are not discussed in detail here but simply tabulated in Table V-8 and adopted for Mercury's surface. The results of Morrison [V-36] support the tabulated values of density and porosity because loosely-packed rock powders duplicate many of

the properties required to explain the microwave data from Mercury. The other entries in Table V-8 are from Costes et al. [V-33, V-80].

TABLE V-8. SOIL MECHANICS PROPERTIES FOR MERCURY<sup>a</sup>

Properties	Symbols, Values, Units
Bulk density	$1.8 \pm 0.2 \text{ g/cm}^3$
Porosity	0.35 to 0.53
Specific gravity	3.1 to 3.4 $\text{g/cm}^3$
Grain size	2 to 60 $\mu\text{m}$
Cohesion	0.02 to 0.2 $\text{N/cm}^2$ (nominal 0.05 $\text{N/cm}^2$ )
Adhesion	0.0025 to 0.01 $\text{N/cm}^2$
Static Bearing capacity (y = penetration depth in cm)	$(1.0 \pm 0.4)y \text{ N/cm}^2$
Angle of internal friction	31 to 39 deg
Effective coefficient of friction (metal to soil or rock)	0.4 to 0.8

a. NASA SP 8085, "The Planet Mercury (1971)."

#### 5.2.2.3 Topography

The absence of shadows near the terminator, as observed from earth, indicates that large-scale elevation differences are not significantly greater than on the moon. The maximum elevation differences of about 12 km [V-82] are reflected in the uncertainty ascribed to Mercury's radius (subsection 5.1.10). On smaller scales, relief or roughness is conventionally described in terms of the power spectral density function which is defined as the Fourier transform of the autocorrelation function of the surface elevation [V-83]. Figure V-5, adapted from Reference V-33, shows the range of power spectral density versus wavenumber on the moon which is adopted here as the roughness description for Mercury. The similarity in roughness is supported on scales between 10 and 100 cm by the radar data (Table V-7). Slopes on the lunar surface are also specified in Reference V-33 from which Figures V-6 and V-7 are adapted for Mercury.

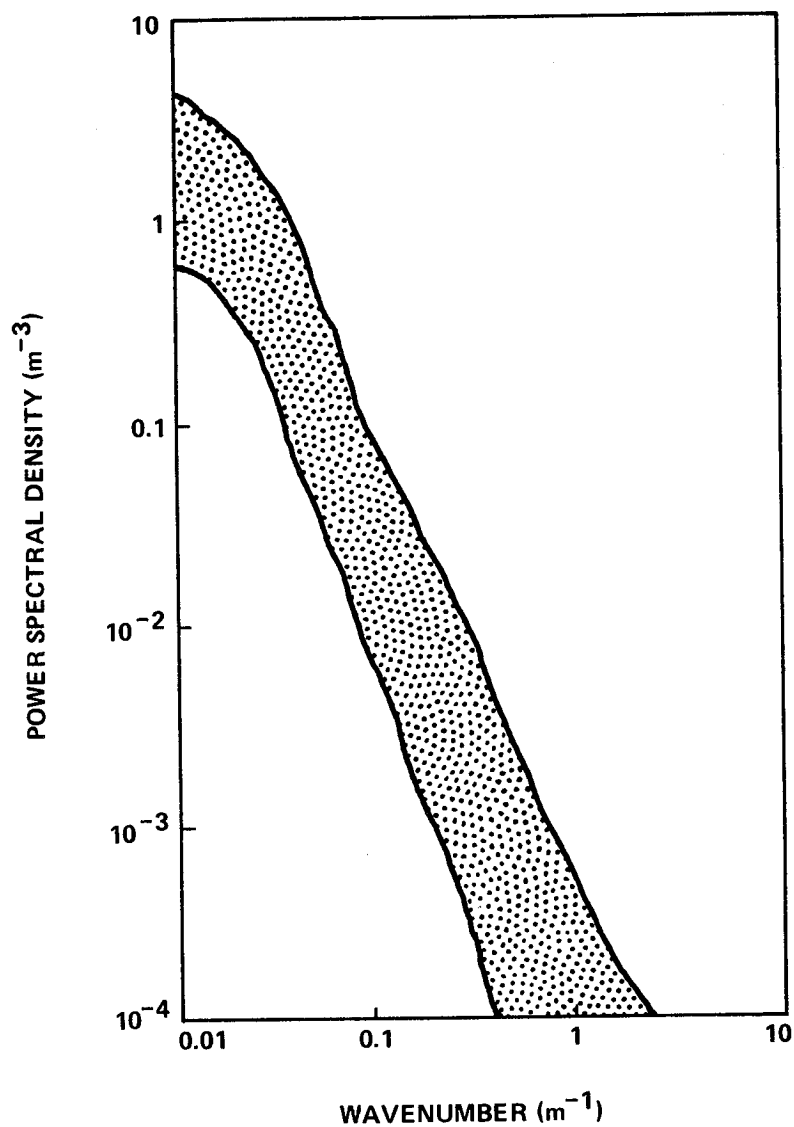


Figure V-5. Roughness of Mercury's surface, given by the power spectral density of the elevation as a function of the wavenumber [V-33].

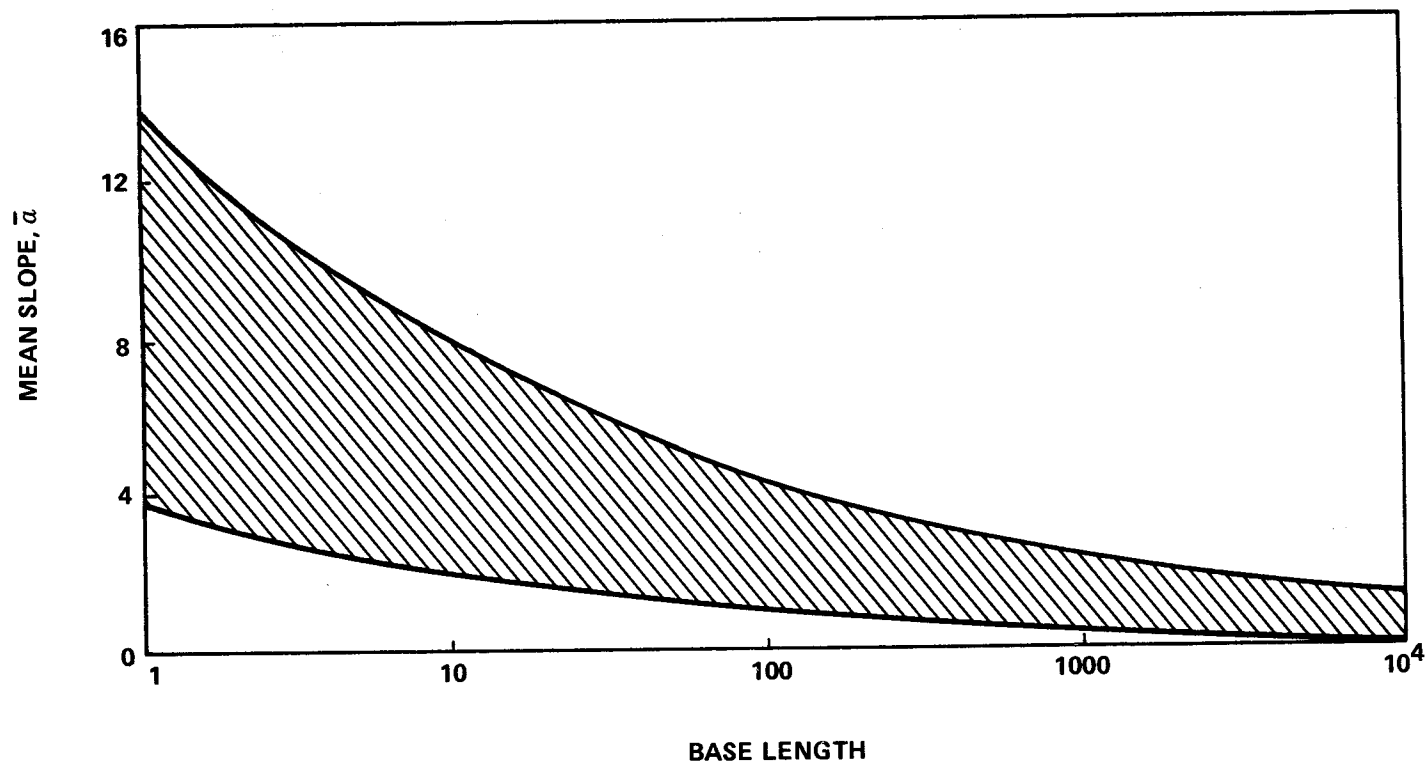


Figure V-6. Variation of mean slope of Mercury's surface with horizontal base length [ V-33 ].

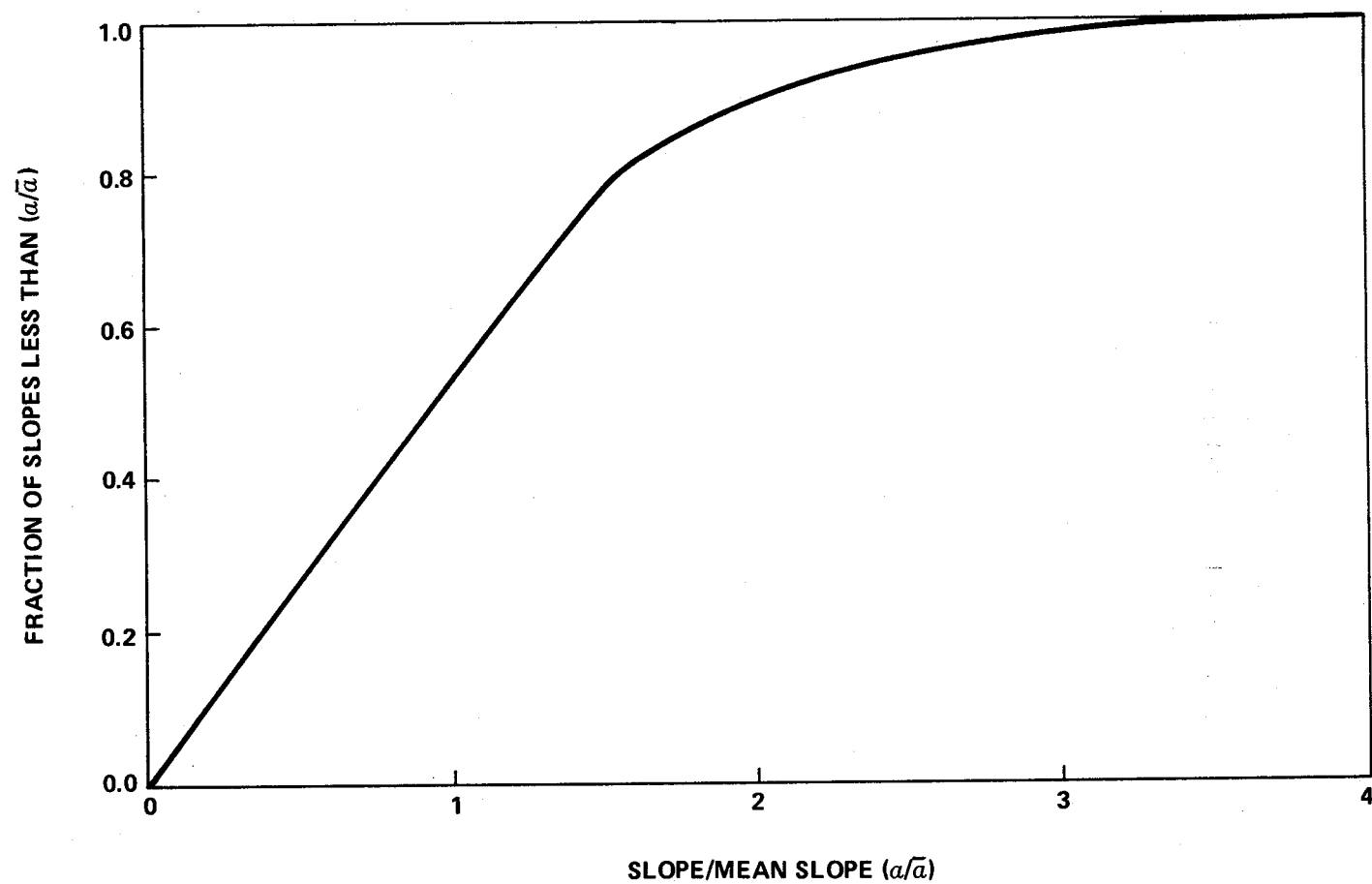


Figure V-7. Relative distribution of slopes on Mercury's surface for use with Figure 8 [V-33].

Crater and block distributions are also specified in Reference V-33 for the moon. The distributions shown in Figure V-8 are taken directly from Reference V-33 for adoption here for Mercury's crater and block frequencies; the Apollo 12 results [V-76] have confirmed these results and extended them to slightly smaller sizes for the craters. Craters outnumber blocks at all sizes shown for craters greater than 1 cm in diameter. For craters, the ratio of depth to diameter is less than 0.25, whereas for blocks the height is nominally 0.5 times the characteristic size [V-33]. For blocks and particles, Figure V-9 from Reference V-33 shows the fraction of the surface area covered and indicates that the entire surface is covered with dust particles greater than 10  $\mu\text{m}$  in size.

### 5.2.3 Electromagnetic Properties

Several radar observations have provided data on the electrical properties of Mercury's surface and the interaction of the surface with electromagnetic radiation. The original articles describing these observations (Table V-7) indicate radar reflection properties for Mercury very similar to those for the moon. These properties include a low radar reflectivity [V-70] which implies a high microwave emissivity. The latter is supported by the analyses of the microwave data obtained by the investigators listed in Table V-6. On the basis of these data and appropriate theoretical considerations, several authors [V-21, V-36, V-42, V-47] have derived values for the electrical as well as thermal parameters of Mercury's surface layers (subsections 5.2.2.2 and 5.2.4). These results are based on the mean value and the amplitude and phase of the periodic variations of the brightness temperature as functions of wavelength and provide effective values for dielectric constant, solar wind flux, and ratio of electrical to thermal skin depths. The ranges adopted in Table V-9 for these parameters bracket not only the effective values cited in the literature but also variations likely to result from inhomogeneities. They are consistent with the composition and mechanical properties (subsection 5.2.2) and with corresponding ranges for the moon [V-36].

### 5.2.4 Temperature and Thermal Properties

Since Mercury has little atmosphere of any kind to diffuse or hold heat, the temperature of the surface in any given area will depend almost entirely upon how much direct sunlight is striking that area when the surface

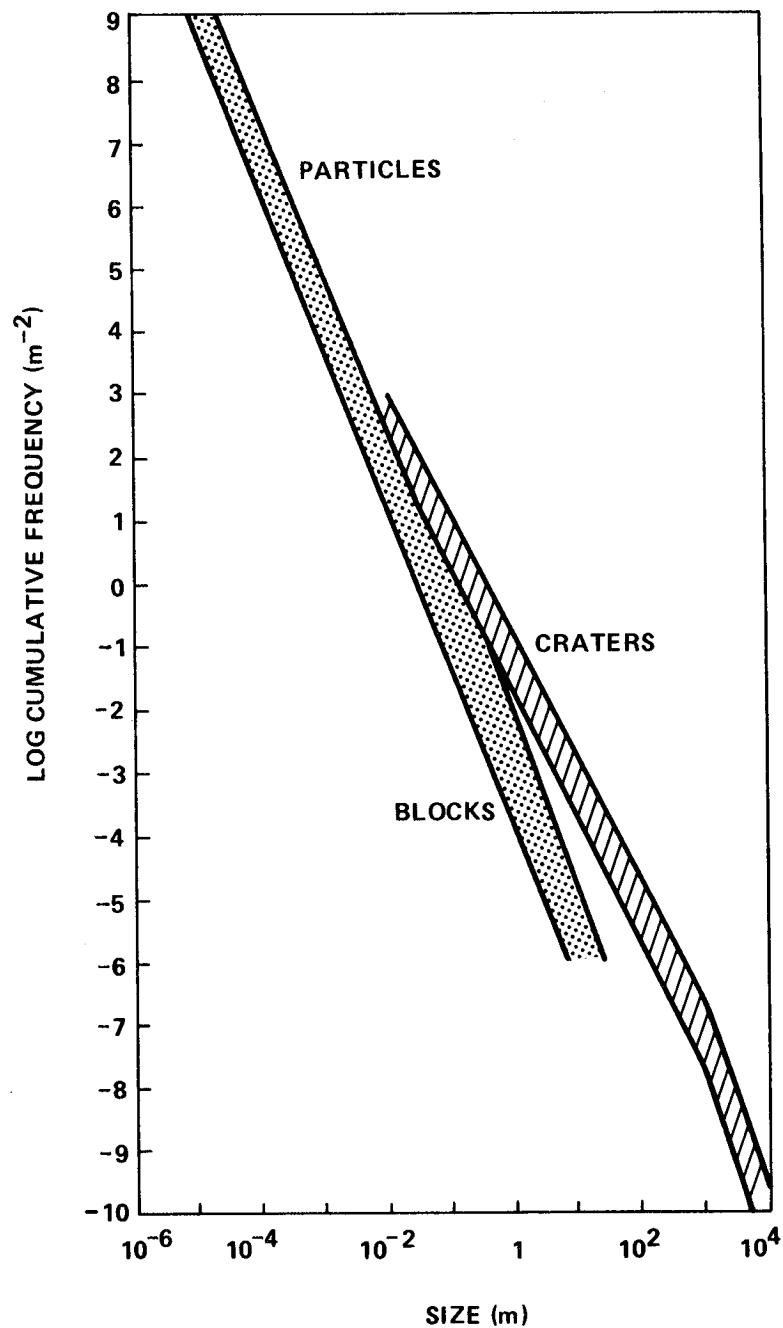


Figure V-8. Number per unit area of blocks, particles, and craters larger than specified characteristic size for the surface of Mercury [V-33, V-80, V-81].



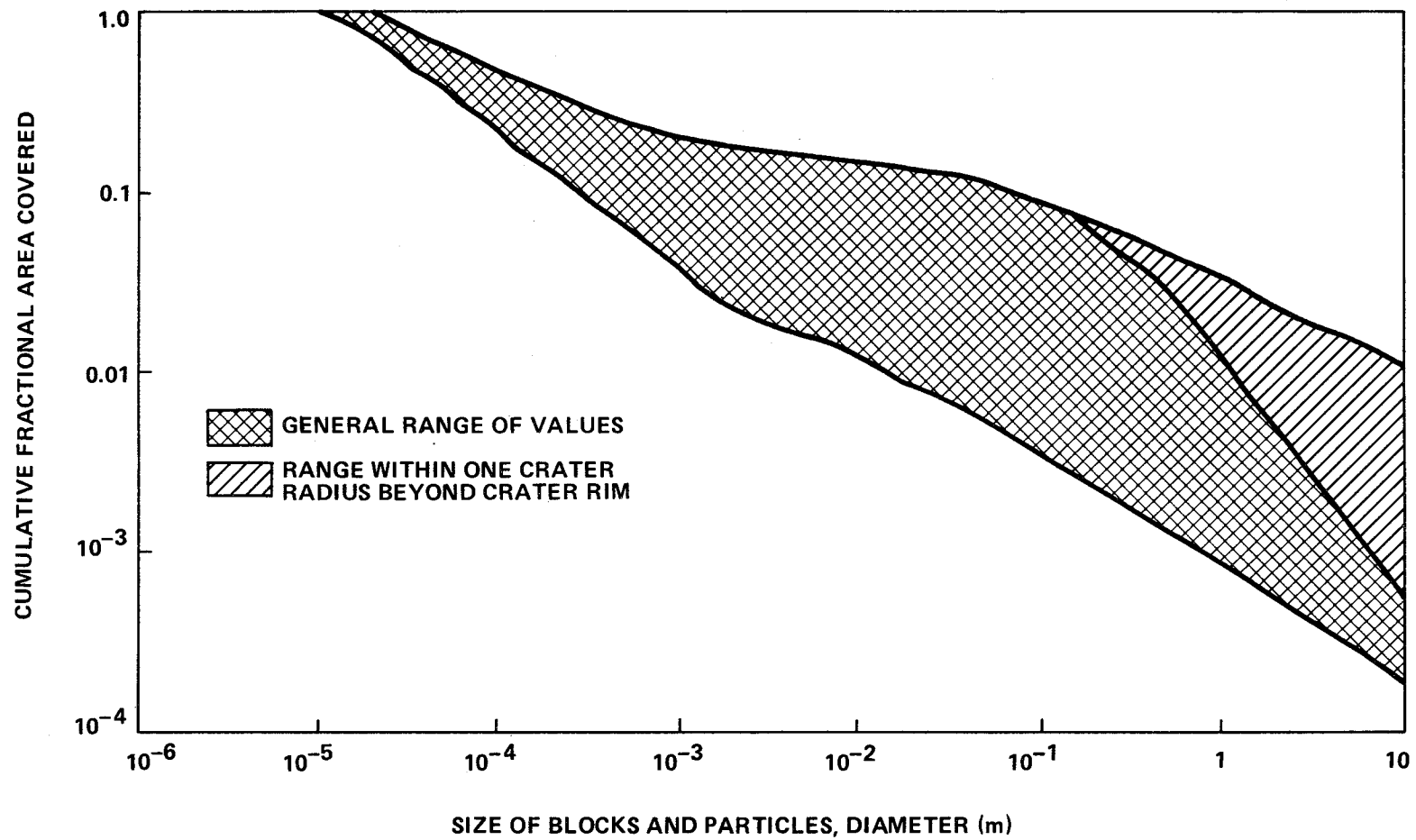


Figure V-9. Fraction of surface area covered by blocks and particles larger than specified characteristic size for the surface of Mercury [V-33].

TABLE V-9. ELECTROMAGNETIC PROPERTIES OF  
MERCURY'S SURFACE LAYERS

Property	Range of Values
Radar reflectivity	$0.06 \pm 0.03$
Microwave emissivity	$0.94 \pm 0.03$
Dielectric constant	$1.6 < \epsilon < 4$
Dielectric loss tangent	$0.0002 < (\tan \phi) < 0.013$
Ratios $\frac{(\text{electrical skin depth})}{(\text{thermal skin depth}) (\text{wavelength})}$	$0.5 < \frac{\delta}{\lambda} < 2.0 \text{ cm}^{-1}$

temperature is measured. To a much smaller degree it will depend upon how long the sunlight has been striking that area as the surface would take some time to heat, and how long the heat is held by the surface after the sunlight is gone.

Temperature measurements of Mercury have been made by recording the thermal emission of the planet in the infrared and microwave regions of the spectrum.

Measurements of Mercury's emission in the infrared, particularly in the 8 to 14- $\mu\text{m}$  region, have been interpreted in terms of the planet's surface temperature. Table V-4 lists the temperature values so derived. All listed values are based on original observations except Soter's which is derived from Pettit and Nicholson's data. Night temperature values are difficult to obtain from the observations because the infrared energy received is susceptible to contamination by sunlight reflected from Mercury's illuminated crescent, the earth's atmosphere, and the observing telescope. Nevertheless, the observations clearly indicate night surfaces are warmer than a permanently dark surface.

The microwave measurements of Mercury discussed in subsection 5.1.7.4 (Table V-6) are also used to derive temperatures. The cited values depend on wavelength and are averages of physical temperatures at and below the surface and over the planet's disk. Thus, the microwave results have a smaller range of temperatures than the infrared ones.

The infrared and microwave temperature measurements have been supplemented by detailed theoretical analyses of the thermal and radio behavior of Mercury's surface layers of which only some highlights follow. Pettit and Nicholson [V-37] showed in calculations using the solar constant and Mercury's albedo that if the temperatures of sunlit surfaces are in equilibrium with the absorbed solar energy, they match the measured temperatures rather well. A detailed calculation is given by Soter and Ulrichs [V-84]. They conclude that in thermal equilibrium, the daytime temperature  $T$  of the sunlit surface is given by

$$T = T_p \left( \frac{r_p}{r} \right)^{\frac{1}{2}} (\cos Z)^{\frac{1}{4}},$$

Here,  $T_p$  equals  $700^\circ \pm 25^\circ \text{ K}$ ,  $r_p$  equals (Mercury's perihelion distance) 0.3075 AU,  $r$  is its actual distance from the sun, and  $Z$  (the zenith angle of the sun) is less than  $90^\circ$ . Both the infrared and microwave data are consistent with temperatures calculated from the above equation. The uncertainty in  $T_p$  is that given by Morrison [V-36].

Surface twilight and night temperatures may be calculated from the theory of heat conduction if appropriate boundary conditions and thermal parameter values are assumed. For materials as dry and porous as Mercury's soil, conduction may occur simultaneously by contact (phonon transport) and radiation (photon transport). Analyses of these phenomena have been applied to Mercury by Soter and Ulrichs [V-84], Morrison [V-36], Winter and Saari [V-85], and Ulrichs and Campbell [V-86]. When the geometrical circumstances of the solar radiation are considered and lunar values for the thermal and electrical properties of the surface are employed, the variations of temperature theoretically predicted are consistent with the results of both the infrared and microwave observations which include part of Mercury's night hemisphere (Tables V-4 and V-6 and the references cited therein). Although some details of the variation of temperature with planetary latitude and longitude, depth below the surface, and time have been published [V-36], they are too complex to be practical for design criteria. Furthermore, although the foregoing results are reasonable for the planet as a whole, they may be unrealistic for particular locations because of surface inhomogenieties. The range from  $90^\circ$  to  $200^\circ \text{ K}$  brackets the observed values and those derived from the theory and is adopted here for the temperature of all surface points for which the sun is invisible (night side or  $Z > 90^\circ$  K)

or for which the predicted temperature  $T$  is less than  $200^\circ \text{K}$  (near the terminator). Within this range, the higher temperatures are appropriate just after sunset and the lower ones from Mercury's midnight to dawn.

Table V-10 lists ranges of thermal property values which include those ascribed to Mercury by the foregoing authors, and to the moon by References V-33, V-87, and V-88. References V-88 and V-89 include results for lunar samples returned by Apollo 11. The ranges cited include both uncertainty and variations of characteristics with temperature and materials; they are deliberately large as contrasted with the range of effective values for the whole disc derived by Klein [V-21] and Morrison [V-36].

TABLE V-10. THERMAL PARAMETER RANGES FOR  
MERCURY CITED IN LITERATURE

Parameter	Range	Units
Specific Heat	$0.07 < C < 0.24$	$\text{cal/g}^\circ \text{K}$
Thermal Conductivity	$2.5 \times 10^{-6} < K < 4 \times 10^{-3}$	$\text{cal/cm sec}^\circ \text{K}$
Inverse Thermal Inertia	$20 < (K\rho c)^{-1/2} < 200$	$\text{cm}^2 \text{sec}^{1/2}^\circ \text{K/cal}$

a. NASA SP 8085, "The Planet Mercury [1971]."

### 5.3 Satellites

None.

## REFERENCES

- V-1. Moroz, V. I.: Physics of Planets. NASA TT F-515, April 1968.
- V-2. Harris, I., and Priester, W.: Time-Dependent Structure of the Upper Atmosphere. J. Atmos. Sci., vol. 19, 1962.
- V-3. Spitzer, L., Jr.: Atmospheres of the Earth and Planets. (G. P. Kuiper, ed.), Chicago, University of Chicago Press, 1952.
- V-4. Rasool, S. I., Gross, S. H., and McGovern, W. E.: The Atmosphere of Mercury. Space Sci. Reviews, vol. 5, no. 5, 1966, pp. 565-584.
- V-5. Belton, M. J. S., Hunten, D. M., and McElroy, M. B.: A Search for an Atmosphere on Mercury, Astrophys. J., vol. 150, no. 3, 1967, pp. 1111-1124.
- V-6. Antoniadi, E. M.: La Planète Mercure. Gauthier-Villars, Paris, 1934.
- V-7. Kuiper, G. P.: Atmospheres of the Earth and Planets. Chicago, University of Chicago Press, 1952.
- V-8. Dollfus, A.: Planets and Satellites. (G. P. Kuiper, ed.), Chicago, University of Chicago Press, 1961.
- V-9. Moroz, V. I.: Infrared Spectrum of Mercury Soviet Astronomy — AJ, vol. 8, no. 6, 1965, pp. 882-889.
- V-10. Kozyrev, N. A.: The Atmosphere of Mercury. Sky and Telescope, vol. 27, 1964, pp. 339-341.
- V-11. Kozyrev, N. A.: Letter to the Editor. Sky and Telescope, vol. 30, 1965, p. 360.
- V-12. Spinrad, H., and Hodge, P. W.: An Explanation of Kozyrev's Hydrogen Emission Lines in the Spectrum of Mercury, Icarus, vol. 4, 1965, pp. 105-108.
- V-13. Dunham, T.: Spectroscopic Observations of the Planets at Mount Wilson. The Atmospheres of the Earth and Planets (G. P. Kuiper, ed.), Revised Edition, Univ. of Chicago Press, Chap. 11, 1952, pp. 288-305.

## REFERENCES (Continued)

- V-14. Spinrad, H., Field, G. B., and Hodge, P. W.: Spectroscopic Observations of Mercury. *Astrophys. J.*, vol. 141, 1965, pp. 1155-1160.
- V-15. Bergstrahl, J. T., Gray, L. D., and Smith, H. J.: An Upper Limit for Atmospheric Carbon Dioxide on Mercury. *Astrophys. J.*, vol. 149, no. 3, 1967, pp. L137-139.
- V-16. Binder, A. B., and Cruikshank, D. P.: Mercury: New Observations of the Infrared Bands of Carbon Dioxide. *Science*, vol. 155, no. 3765, 1967, p. 1135.
- V-17. Nourse, A. E.: *Nine Planets*. New York, Harper & Row, 1970.
- V-18. Field, G. B.: Atmosphere of Mercury, *Astronom. J.*, vol. 67, 1962, pp. 575-576.
- V-19. Dollfus, A.: Visual and Photographic Studies of Planets at the Pic du Midi. *Solar System*, vol. 3, Chap. 15, 1961, pp. 534-571.
- V-20. O' Leary, B. T., and Rea, D. G.: On the Polarimetric Evidence for an Atmosphere on Mercury. *Astrophys. J.*, vol. 148, no. 1, 1967, pp. 249-253.
- V-21. Klein, M. J.: Mercury: Recent Observations at 3.75-cm Wavelength — Summary. *Radio Science*, vol. 5, no. 2, 1970, pp. 397-400.
- V-22. Dollfus, A.: Résultats Récents sur les Planètes Mercure, Vénus et Mars, Obtenus par les Observations Astronomiques au Sol. *La Recherche Spatiale*, vol. 7, no. 1, 1968, pp. 1-12.
- V-23. Weidner, D. K.: Space Environment Criteria Guidelines for Use in Space Vehicle Development (1969 Revision) NASA TM X-53957, August 1970.
- V-24. Anon.: Solar Electromagnetic Radiation. NASA SP-8005, Revised, May 1971.

## REFERENCES (Continued)

- V-25. Thekaekara, M. P.: Proposed Standard Values of the Solar Constant and the Solar Spectrum. *J. Environmental Science*, vol. 13, no. 4, 1970, pp. 6-9.
- V-26. Harris, D. L.: Photometry and Colorimetry of Planets and Satellites, Planets and Satellites. (G. P. Kuiper and B. M. Middlehurst, Eds.), *Solar System*, vol. 3, Univ. of Chicago Press, Chap. 8, 1961, pp. 272-342.
- V-27. Irvine, W. M., Simon, T., Menzel, D. H., Pikoos, C., and Young, A. T.: Multicolor Photoelectric Photometry of the Brighter Planets, III. Observations from Boyden Observatory. *Astronom. J.*, vol. 73, no. 9, 1968, pp. 807-828.
- V-28. Allen, C. W.: *Astrophysical Quantities* (Second Edition). Athlone Press, Univ. of London, 1963.
- V-29. Hämeen-Anttila, K. A.: Surface Photometry of the Planet Mercury. *Ann. Acad. Sci. Fennicae A*, vol. VI, no. 252, 1967.
- V-30. Hämeen-Anttila, K. A., Pikkarainen, T., and Carmichel, H.: Photometric Studies of the Planet Mercury, *The Moon*, vol. 1, 1970, p. 440.
- V-31. de Vaucouleurs, G.: *Photométrie des Surfaces Planétaires*. Surfaces and Interiors of Planets and Satellites. (A. Dollfus, Ed.), Academic Press, New York, Chap. 5, 1970, p. 226.
- V-32. Minnaert, M.: General Conclusions, *La Physique des Planètes*. *Memoires de la Societe Royale des Sciences de Liege*, vol. 24, 1962, p. 597.
- V-33. Anon.: Lunar Surface Models. NASA SP-8023, May 1969.
- V-34. de Vaucouleurs, G.: Geometric and Photometric Parameters of the Terrestrial Planets. *Icarus*, vol. 3, 1964, pp. 187-235.
- V-35. Linsky, J. L.: Models of the Lunar Surface Including Temperature-Dependent Thermal Properties. *Icarus*, vol. 5, 1966, p. 606.

## REFERENCES (Continued)

- V-36. Morrison, D.: Thermophysics of the Planet Mercury. Space Science Reviews, vol. 11, no. 2/3, 1970, pp. 271-307.
- V-37. Pettit, E., and Nicholson, S. B.: Radiation from the Planet Mercury. Astrophys. J., vol. 83, 1936, p. 84-102.
- V-38. Pettit, E.: Planetary Temperature Measurements, Planets and Satellites. Solar System, vol. 3, Univ. of Chicago Press, Chap. 10, 1961, pp. 400-428
- V-39. Soter, S. L.: Mercury — Infrared Evidence for Nonsynchronous Rotation. Science, vol. 153, 1966, pp. 1112-1113.
- V-40. Murray, B. C.: Infrared Radiation from the Daytime and Night-time Surfaces of Mercury. American Geophysical Union Transactions, vol. 48, no. 1, 1967, pp. 148-149.
- V-41. Murdock, T. L., and Ney, E. P.: Mercury: The Dark-Side Temperature. Science, vol. 170, no. 3957, 1970, pp. 535-537.
- V-42. Epstein, E. E., Dworetzky, M. M., Fogarty, W. G., Montgomery, J. W., and Cooley, R. C.: Mercury: Epileth Physical Parameters and a Hermocentric Longitude Dependence of its 3.3-mm Radiation. Radio Science., vol. 5, no. 2, 1970, pp. 401-409.
- V-43. Epstein, E. E., Oliver, J. P., Schorn, R. A., Soter, S. L., and Wilson, W. J.: Mercury: Observations of the 3.4-Millimeter Radio Emission. Science, vol. 157, no. 3796, 1967, pp. 1550-1552.
- V-44. Golovkov, V. K., and Losovskii, B. Ya.: Measurements of the Phase Dependence of the 0.8-cm Radio Emission of Mercury, and Some Properties of its Surface Layer. Soviet Astronomy-AJ, vol. 12, no. 2, 1968, pp. 229-302.
- V-45. Welch, W. J., Thornton, D. D., and Lohman, R.: Observations of Jupiter, Saturn, and Mercury at 1.53 cm. Astrophys. J., vol. 146, no. 3, 1966, pp. 799-809.



## REFERENCES (Continued)

- V-46. Kaftan-Kassim, M. A., and Kellermann, K. I.: Measurements of the 1.9 cm Thermal Radio Emission from Mercury. *Nature*, vol. 213, no. 5073, 1967, pp. 272-273.
- V-47. Morrison, D., and Klein, M. J.: The Microwave Spectrum of Mercury. *Astrophys. J.*, vol. 160, no. 1, 1970, pp. 325-332.
- V-48. Howard, W. E., Barrett, A. H., and Haddock, F. T.: Measurements of Microwave Radiation from the Planet Mercury. *Astrophys. J.*, vol. 136, 1962, pp. 995-1004.
- V-49. Kellermann, K. I.: 11-cm Observations of the Temperature of Mercury. *Nature*, vol. 205, no. 4976, 1965, pp. 1091-1092.
- V-50. American Ephemeris and Nautical Almanac. U.S. Government Printing Office.
- V-51. Woolley, R. v. d. R.: Planetary Co-ordinates for the years 1960-1980. Her Majesty's Stationery Office, London, 1958.
- V-52. Kern, T. W., and Vestine, E. H.: Magnetic Field of the Earth and Planets. *Space Science Reviews*, vol. 3, 1963, p. 136.
- V-53. Good, R. C.: The Magnetosphere of the Planet Mercury as a Scattering Center for Solar Flare Protons. AIAA Paper 67-150, 1967, 8 pp.
- V-54. Reiffel, L.: Trapped Radiation Estimates for the Other Planets. (B. M. McCormack, Ed.), *Radiation Trapped in the Earth's Magnetic Field*, D. Reidel Publ. Co., Dordrecht, Holland, 1966, pp. 256-262.
- V-55. Shatten, K. H., Wilcox, J. M., and Ness, N. F.: A Model of Interplanetary and Coronal Magnetic Field. *J. Solar Physics*, vol. 6, 1969, pp. 442-455.
- V-56. Anon., Magnetic Fields — Earth and Extraterrestrial. NASA SP-8017, March 1969.

## REFERENCES (Continued)

- V-57. Melbourne, W. G., Mulholland, J. D., Sjogren, W. L., and Sturms, F. M.: Constants and Related Information for Astrodynamic Calculations, 1968. Technical Report 32-1306, Jet Propulsion Laboratory, Pasadena, 1968.
- V-58. Muhleman, D. O.: Radar Scattering from Venus and Mercury at 12.5 cm. *J. Research Radio Science*, vol. 69D, no. 12, 1965, pp. 1630-1631.
- V-59. Sagan, C., and Morrison, D.: The Planet Mercury. *Science J.*, vol. 4, no. 12, 1968, pp. 72-77.
- V-60. Sandner, W.: The Planet Mercury. Faber & Faber, London, 1963.
- V-61. Chapman, C. R.: Optical Evidence on the Rotation of Mercury. *Earth and Planetary Science Letters*, vol. 3, no. 4, 1967, pp. 381-385.
- V-62. Camichel, H., and Dollfus, A.: La Rotation et la Cartographie de la Planete Mercure. *Icarus*, vol. 8, no. 2, 1968, pp. 216-226.
- V-63. Goldstein, R. M.: Mercury: Surface Features Observed During Radar Studies. *Science*, vol. 168, no. 3930, 1970, pp. 467-469.
- V-64. Smith, W. B., Ingalls, R. P., Shapiro, I. I., and Ash, M. E.: Surface-Height Variations on Venus and Mercury. *Radio Science*, vol. 5, no. 2, 1970, pp. 411-423.
- V-65. Carpenter, R. L., and Goldstein, R. M.: Radar Observations of Mercury. *Science*, vol. 142, 1963, p. 381.
- V-66. Evans, J. V., Brockelman, R. A., Henry, J. C., Hyde, G. M., Kraft, L. G., Reid, W. A., and Smith, W. W.: Radio Echo Observations of Venus and Mercury at 23 cm Wavelength, 1965. *Astronom. J.*, vol. 70, no. 7, 1965, pp. 486-501.
- V-67. Ash, M. E., Shapiro, I. I., and Smith, W. B.: Astronomical Constants and Planetary Ephemerides Deduced from Radar and Optical Observations. *Astronom. J.*, vol. 72, no. 3, 1967, pp. 338-350.

## REFERENCES (Continued)

- V-68. Kotel'nikov, V. A.: Radar Probes of the Planet Mercury. Doklady Akad. Nauk SSSR, vol. 147, no. 6, 1962, pp. 1320-1323.
- V-69. Pettengill, G. H., Dyce, R. B.: A Radar Determination of the Rotation of the Planet Mercury. Nature, vol. 206, no. 4990, 1965, p. 1240.
- V-70. Pettengill, G. H., Dyce, R. B., and Campbell, D. B.: Radar Measurements at 70 cm of Venus and Mercury. Astron. J., vol. 72, no. 3, 1967, pp. 330-337.
- V-71. Hodge, P.: Interactions of the Planet Mercury with Interplanetary Material, La Physique des Planètes. Memoires de la Société Royale des Sciences de Liège, vol. 24, 1962, pp. 261-268.
- V-72. Hodge, P. W.: The Atmosphere of the Planet Mercury. AGU Transactions, vol. 45, no. 4, 1964, p. 631.
- V-73. Sharonov, V.: Dust Covers on the Surface of Planets and Satellites. Life Sciences and Space Research II, North Holland Publ. Co., Amsterdam, 1964, pp. 171-177.
- V-74. Field, G. B.: The Atmosphere of Mercury. The Origin and Evolution of Atmospheres and Oceans. John Wiley & Sons, New York, 1964, pp. 269-278.
- V-75. Anon.: Apollo 11 Preliminary Science Report. NASA SP-214, 1969.
- V-76. Anon.: Apollo 12 Preliminary Science Report. NASA SP-235, 1970.
- V-77. Wood, J. A.: The Lunar Soil. Scientific American, vol. 223, no. 2, 1970, pp. 14-23.
- V-78. Reynolds, R. T., and Summers, A. L.: Calculations on the Composition of the Terrestrial Planets. J. Geophysical Research, vol. 74, no. 10, 1969, p. 2494.
- V-79. Khodak, Yu. A.: Hermesology—Geology of Mercury. Izvestiya Akad. Nauk CCCP, Seriya Geologiya, no. 10, 1969, pp. 136-142 (U. S. Dept. of Commerce, Joint Publications Research Service 48346, No. 217, Nov. 28, 1969).

## REFERENCES (Concluded)

- V-80. Costes, N. C., Carrier, W. D., Mitchell, J. K., and Scott, R. F.: Apollo 11 Soil Mechanics Investigation. NASA SP-214, 1969, pp. 85-122.
- V-81. Scott, R. F., Carrier, W. D., Costes, N. C., and Mitchell, J. K.: Mechanical Properties of the Lunar Regolith. NASA SP-235, 1970, pp. 161-182.
- V-82. Wright, F. E., Wright, F. H., and Wright, H.: The Lunar Surface: Introduction. The Moon Meteorites and Comets. (B. M. Middlehurst and G. P. Kuiper, Eds.), Solar System, vol. 4, Univ. of Chicago Press, Chap. 1, 1963, pp. 1-56.
- V-83. Bekker, M. G.: Off-the-Road Locomotion. Univ. of Michigan Press, Ann Arbor, 1960.
- V-84. Soter, S., and Ulrichs, J.: Rotation and Heating of the Planet Mercury. Nature, vol. 214, no. 5095, 1967, pp. 1315-1316.
- V-85. Winter, D. F., and Saari, J. M.: A Particulate Thermophysical Model of the Lunar Soil. Astrophys. J., vol. 156, no. 3, 1969, pp. 1135-1151.
- V-86. Ulrichs, J., and Campbell, M. J.: Radiative Heat Transfer in the Lunar and Mercurian Surfaces. Icarus, vol. 11, no. 2, 1969, pp. 180-188.
- V-87. Horai, K., Simmons, G., Kanamori, H., and Wones, D.: Thermal Diffusivity and Conductivity of Lunar Material. Science, vol. 167, no. 3918, 1970, pp. 730-731.
- V-88. Bastin, J. A., Clegg, P. E., and Fielder, G.: Infrared and Thermal Properties of Lunar Rock. Science, vol. 167, no. 3918, 1970, pp. 728-730.

## BIBLIOGRAPHY

- Vaughan, O. H.: Model Atmosphere of Mercury. J. Spacecraft and Rockets, vol 6, no. 10, 1969, pp. 1171-1175.

## SECTION VI. VENUS

### 6.1 Atmospheric Environment

#### 6.1.1 Definition

The atmospheric environment of Venus is defined as the region between the surface and 20 000 km above the surface of Venus.

#### 6.1.2 Gas Properties (Surface to 1000 km Altitude)

##### 6.1.2.1 Temperature

The temperature-versus-altitude profiles illustrated in Figure VI-1 have been idealized from data generated by Mariners II and V, and Venera 4, 5, 6, and 7.

##### 6.1.2.2 Composition

The lower Venus atmosphere is thought to be primarily carbon dioxide with small amounts of water vapor, nitrogen, argon, and oxygen. It is suspected that the upper atmosphere is composed of CO<sub>2</sub>, O<sub>2</sub>, and O and hydrogen and helium from outer space. The molecular weight profile (Fig. VI-2) has been generated from a very extensive review of available literature and a detailed analysis of the average and escape velocities of the constituents in the Venus atmosphere. In developing the profile, the lower atmospheric composition was taken to be 100-percent carbon dioxide, except for the maximum model atmosphere whose composition was assumed to be 97-percent carbon dioxide and 3-percent nitrogen.

##### 6.1.2.3 Surface Pressure

A detailed review of the available literature has indicated the Venus surface pressure to vary from  $6.0 \times 10^4$  to  $12.0 \times 10^4$  mb.

##### 6.1.2.4 Model Atmospheres

Under the assumptions of hydrostatic equilibrium and a perfect gas law relationship among the thermodynamic quantities, a model atmosphere may be generated from a given temperature profile, molecular weight profile, and surface pressure.

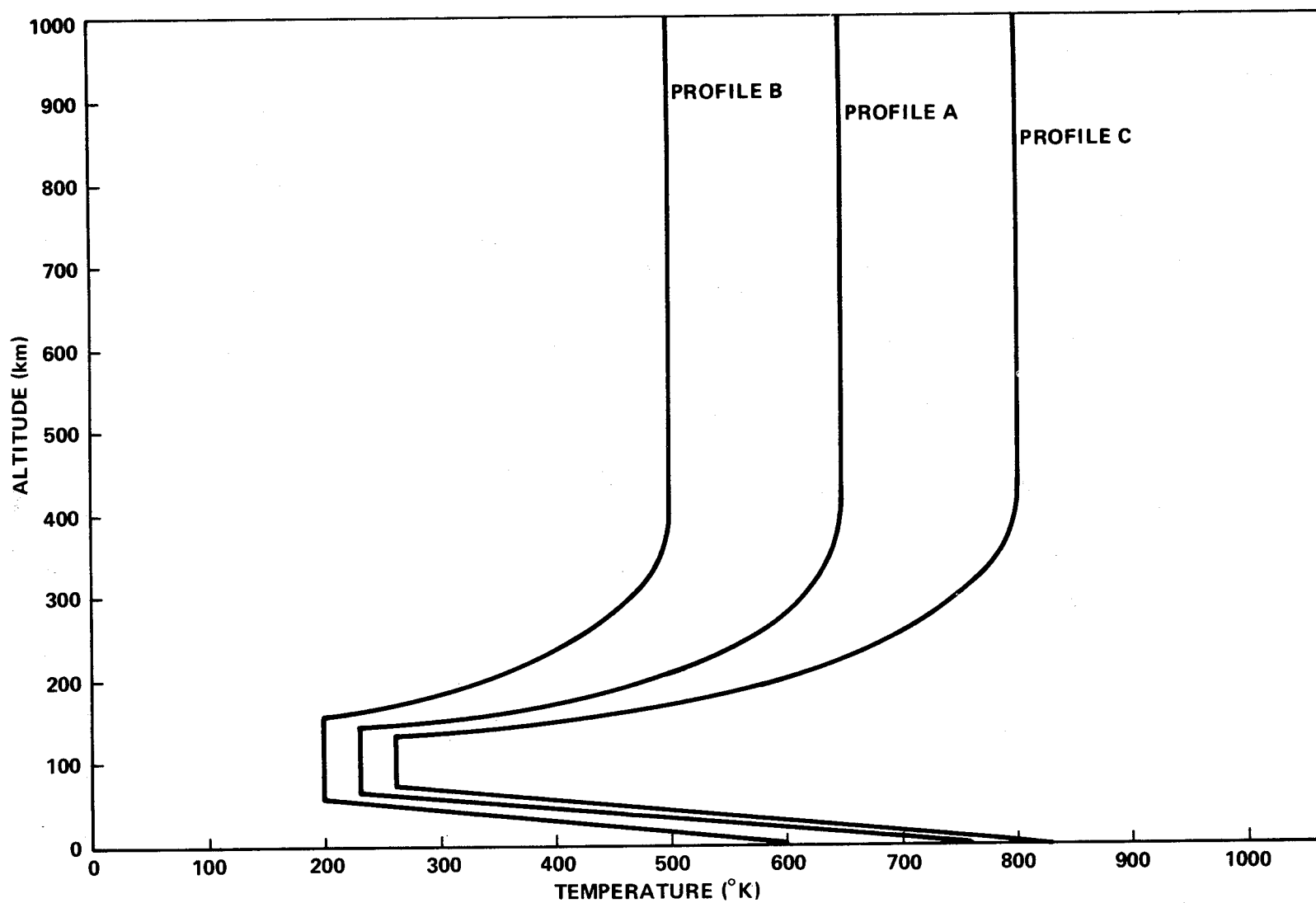


Figure VI-1. Altitude versus temperature for Venus atmosphere.

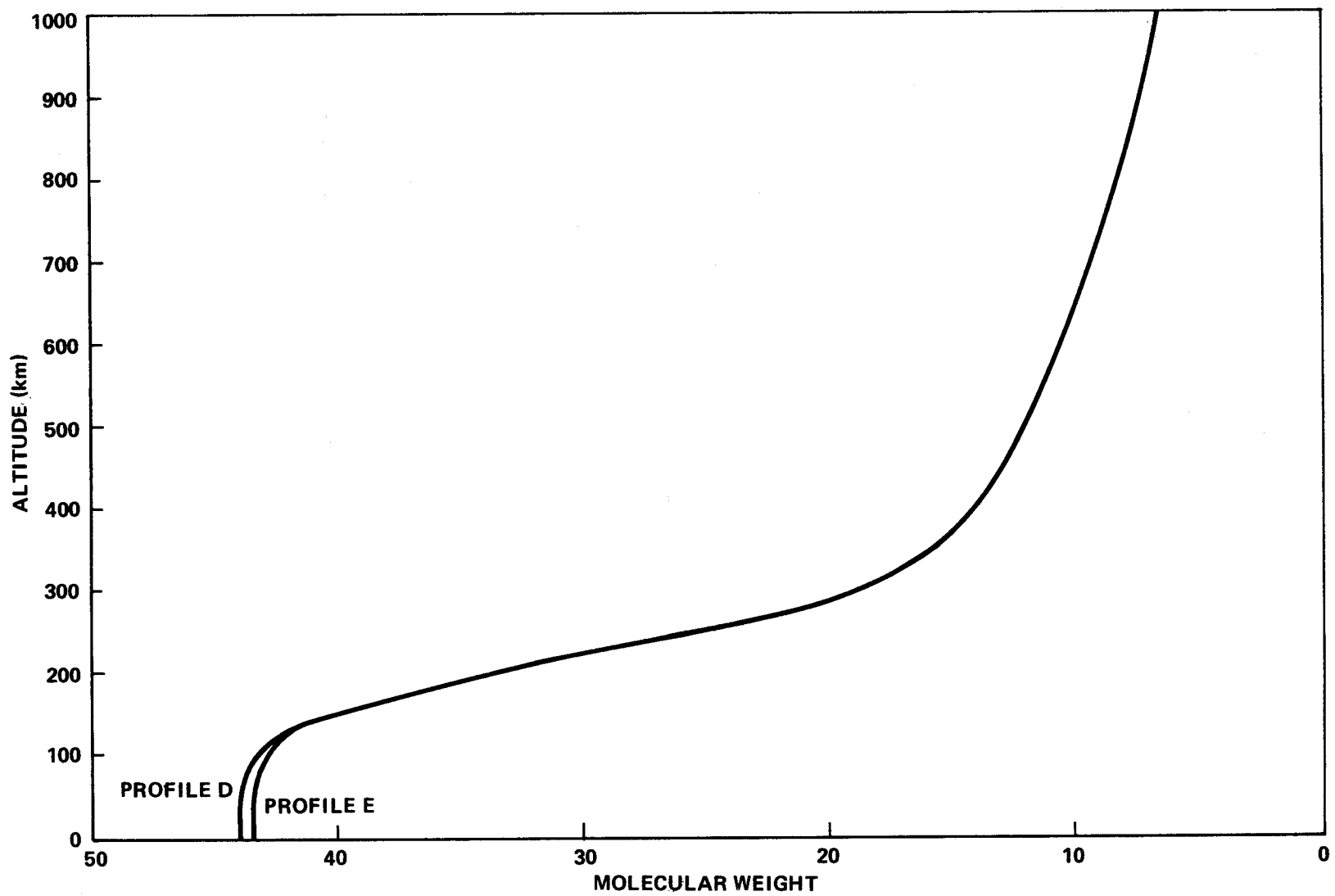


Figure VI-2. Altitude versus molecular weight for Venus atmosphere.

Three such models have been developed with this technique using the following criteria:

a. Mean model atmosphere

1. Temperature - Profile A (Fig. VI-1)
2. Molecular Weight - Profile E (Fig. VI-2)
3. Surface Pressure -  $9.0 \times 10^4$  mb.

b. Minimum model atmosphere

1. Temperature - Profile B (Fig. VI-1)
2. Molecular Weight - Profile D (Fig. VI-2)
3. Surface Pressure -  $6.0 \times 10^4$  mb.

c. Maximum model atmosphere

1. Temperature - Profile C (Fig. VI-1)
2. Molecular Weight - Profile E (Fig. VI-2)
3. Surface Pressure -  $12.0 \times 10^4$  mb.

#### 6.1.2.5 Computed Quantities

The various quantities of the three model atmospheres are tabulated in Tables VI-1, VI-2, and VI-3.

#### 6.1.3 Gas Properties (1000 to 20 000 km Altitude)

Gas pressure decreases exponentially with increasing altitude above 1000 km until it reaches the interplanetary space value of  $10^{-10}$  dynes/cm<sup>2</sup> near 20 000 km. It then remains relatively constant with increasing altitude.

Gas density decreases exponentially above 1000 km altitude to a value of  $10^{-23}$  g/cm<sup>3</sup> near 20 000 km and then remains relatively constant.

Kinetic temperature increases linearly above 1000 km altitude with increased altitude to a value of  $2 \times 10^5$  °K near 20 000 km. It then remains relatively constant with increasing altitude.



TABLE VI-1. MEAN VENUS MODEL ATMOSPHERE

Geometric Altitude (km)	Kinetic Temperature (°K)	Pressure (mb)	Density (g/cm <sup>3</sup> )	Speed of Sound (m/s)	Mol. Wt.	Density Scale Height (km)	Number Density (cm <sup>3</sup> )
.0	747.00	9.000+04	6.376-02	444.54	44.0	19.26	8.729+20
1.0	738.90	8.453+04	6.054-02	442.13	44.0	19.06	8.288+20
2.0	730.81	7.933+04	5.745-02	439.70	44.0	18.85	7.865+20
3.0	722.71	7.440+04	5.448-02	437.26	44.0	18.65	7.459+20
4.0	714.62	6.971+04	5.162-02	434.80	44.0	18.45	7.067+20
5.0	706.53	6.527+04	4.888-02	432.33	44.0	18.25	6.693+20
6.0	698.45	6.106+04	4.626-02	429.85	44.0	18.04	6.334+20
7.0	690.37	5.708+04	4.376-02	427.36	44.0	17.84	5.990+20
8.0	682.29	5.332+04	4.136-02	424.85	44.0	17.64	5.662+20
9.0	674.21	4.977+04	3.906-02	422.33	44.0	17.43	5.348+20
10.0	666.13	4.642+04	3.687-02	419.79	44.0	17.23	5.048+20
20.0	585.53	2.203+04	1.992-02	393.58	44.0	15.20	2.726+20
30.0	505.20	9.437+03	9.886-03	365.58	44.0	13.15	1.353+20
40.0	425.13	3.506+03	4.364-03	335.36	44.0	11.11	5.974+19
50.0	345.32	1.065+03	1.633-03	302.25	44.0	9.04	2.235+19
60.0	266.71	2.397+02	4.742-04	266.04	43.9	7.01	6.492+18
70.0	230.00	3.567+01	8.164-05	247.32	43.8	5.04	1.118+18
80.0	230.00	4.939+00	1.129-05	247.50	43.7	5.07	1.545+17
90.0	230.00	6.916-01	1.574-06	248.01	43.5	5.10	2.155+16
100.0	230.00	9.830-02	2.228-07	248.56	43.3	5.14	3.050+15
110.0	230.00	1.422-02	3.196-08	249.58	43.0	5.18	4.376+14
120.0	230.00	2.106-03	4.691-09	250.71	42.6	5.25	6.422+13
130.0	230.00	3.205-04	7.028-10	252.66	41.9	5.32	9.622+12
140.0	230.00	5.067-05	1.092-10	254.92	41.2	5.43	1.494+12
150.0	260.60	8.669-06	1.615-11	274.14	40.4	5.40	2.211+11
160.0	327.15	2.137-06	3.096-12	310.84	39.4	6.92	4.239+10
170.0	377.15	6.999-07	8.537-13	338.78	38.3	8.65	1.169+10
180.0	414.46	2.670-07	2.862-13	361.45	36.9	9.79	3.918+09
190.0	446.60	1.143-07	1.097-13	381.97	35.6	11.20	1.502+09
200.0	472.41	5.316-08	4.651-14	400.02	34.4	12.23	6.368+08
300.0	605.10	3.828-10	1.563-16	585.56	20.5	25.10	2.140+06
400.0	644.42	2.870-11	8.005-18	708.49	14.9	41.99	1.096+05
500.0	650.00	4.012-12	9.532-19	767.65	12.8	51.49	1.305+04
600.0	650.00	7.681-13	1.601-19	819.51	11.3	60.74	2.192+03
700.0	650.00	1.851-13	3.459-20	865.59	10.1	70.54	4.736+02
800.0	650.00	5.282-14	9.019-21	905.51	9.2	78.55	1.235+02
900.0	650.00	1.741-14	2.700-21	950.10	8.4	87.66	3.697+01
1000.0	650.00	6.523-15	9.265-22	992.80	7.7	98.70	1.268+01

TABLE VI-2. MINIMUM VENUS MODEL ATMOSPHERE

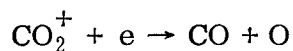
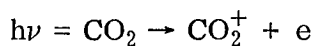
Geometric Altitude (km)	Kinetic Temperature (°K)	Pressure (mb)	Density (g/cm <sup>3</sup> )	Speed of Sound (m/s)	Mol. Wt.	Density Scale Height (km)	Number Density (cm <sup>3</sup> )
.0	600.00	6.000+04	5.292-02	398.41	44.0	15.10	7.245+20
1.0	592.84	5.549+04	4.953-02	396.02	44.0	14.93	6.781+20
2.0	585.68	5.127+04	4.633-02	393.63	44.0	14.75	6.343+20
3.0	578.53	4.733+04	4.330-02	391.22	44.0	14.58	5.927+20
4.0	571.38	4.365+04	4.043-02	388.79	44.0	14.40	5.535+20
5.0	564.23	4.022+04	3.772-02	386.35	44.0	14.23	5.164+20
6.0	557.08	3.702+04	3.516-02	383.90	44.0	14.05	4.814+20
7.0	549.94	3.402+04	3.273-02	381.43	44.0	13.87	4.481+20
8.0	542.80	3.122+04	3.044-02	378.94	44.0	13.70	4.168+20
9.0	535.66	2.863+04	2.829-02	376.44	44.0	13.52	3.872+20
10.0	528.52	2.622+04	2.626-02	373.92	44.0	13.35	3.595+20
20.0	457.27	1.020+04	1.181-02	347.81	44.0	11.59	1.617+20
30.0	386.26	3.410+03	4.672-03	319.66	44.0	9.82	6.397+19
40.0	315.48	9.182+02	1.540-03	288.89	44.0	8.05	2.109+19
50.0	244.93	1.787+02	3.861-04	254.55	44.0	6.26	5.286+18
60.0	200.00	2.120+01	5.599-05	230.25	43.9	4.35	7.666+17
70.0	200.00	2.151+00	5.669-06	230.51	43.8	4.38	7.760+16
80.0	200.00	2.211-01	5.812-07	230.78	43.7	4.40	7.957+15
90.0	200.00	2.305-02	6.035-08	231.27	43.5	4.43	8.262+14
100.0	200.00	2.446-03	6.373-09	231.79	43.3	4.47	8.725+13
110.0	200.00	2.648-04	6.843-10	232.74	43.0	4.51	9.368+12
120.0	200.00	2.944-05	7.541-11	233.79	42.6	4.56	1.032+12
130.0	200.00	3.377-06	8.520-12	235.56	42.0	4.63	1.166+11
140.0	200.00	4.043-07	1.003-12	237.60	41.2	4.73	1.373+10
150.0	200.00	5.076-08	1.228-13	240.57	40.2	4.83	1.681+09
160.0	207.83	6.815-09	1.546-14	248.40	39.2	4.74	2.117+08
170.0	248.03	1.190-09	2.207-15	274.73	38.3	5.70	3.022+07
180.0	281.44	2.835-10	4.473-16	297.85	36.9	6.91	6.124+06
190.0	305.28	8.150-11	1.144-16	315.80	35.6	7.86	1.566+06
200.0	325.92	2.671-11	3.387-17	332.27	34.4	8.67	4.637+05
300.0	457.72	2.997-14	1.603-20	511.64	20.4	20.03	2.194+02
400.00	497.28	1.026-15	3.688-22	623.96	14.9	32.93	5.050+00
500.00	500.00	7.983-17	2.465-23	673.27	12.8	40.31	3.375-01
600.00	500.00	9.306-18	2.522-24	718.76	11.3	47.51	3.453-02
700.00	500.00	1.464-18	3.556-25	759.17	10.1	55.05	4.868-03
800.00	500.00	2.867-19	6.364-26	794.19	9.2	61.46	8.712-04
900.00	500.00	6.774-20	1.366-26	833.30	8.4	68.81	1.870-04
1000.00	500.00	1.890-20	3.490-27	870.74	7.7	77.45	4.778-05

TABLE VI-3. MAXIMUM VENUS MODEL ATMOSPHERE

Geometric Altitude (km)	Kinetic Temperature (°K)	Pressure (mb)	Density (g/cm <sup>3</sup> )	Speed of Sound (m/s)	Mol. Wt.	Density Scale Height (km)	Number Density (cm <sup>3</sup> )
.0	800.00	1.200+05	7.848-02	462.68	43.5	20.62	1.087+21
1.0	792.44	1.132+05	7.477-02	460.49	43.5	20.43	1.035+21
2.0	784.88	1.068+05	7.120-02	458.29	43.5	20.25	9.860+20
3.0	777.33	1.007+05	6.777-02	456.08	43.5	20.06	9.385+20
4.0	769.78	9.487+04	6.448-02	453.86	43.5	19.87	8.929+20
5.0	762.23	8.933+04	6.132-02	451.62	43.5	19.68	8.491+20
6.0	754.68	8.407+04	5.828-02	449.38	43.5	19.49	8.071+20
7.0	747.14	7.907+04	5.537-02	447.13	43.5	19.30	7.668+20
8.0	739.60	7.431+04	5.256-02	444.87	43.5	19.11	7.279+20
9.0	732.06	6.978+04	4.987-02	442.60	43.5	18.93	6.906+20
10.0	724.52	6.549+04	4.729-02	440.31	43.5	18.74	6.549+20
20.0	649.30	3.349+04	2.699-02	416.83	43.5	16.85	3.737+20
30.0	574.32	1.586+04	1.444-02	392.02	43.5	14.95	2.000+20
40.0	499.59	6.785+03	7.105-03	365.63	43.5	13.05	9.839+19
50.0	425.10	2.541+03	3.128-03	337.27	43.5	11.09	4.331+19
60.0	356.12	7.987+02	1.171-03	309.00	43.4	9.23	1.622+19
70.0	287.60	1.978+02	3.584-04	277.97	43.3	7.77	4.964+18
80.0	260.00	3.606+01	7.207-05	264.65	43.2	5.79	9.980+17
90.0	260.00	6.462+00	1.286-05	265.22	43.0	5.83	1.781+17
100.0	260.00	1.173+00	2.325-06	265.81	42.8	5.87	3.220+16
110.0	260.00	2.162-01	4.256-07	266.67	42.6	5.92	5.894+15
120.0	260.00	4.051-02	7.920-08	267.58	42.3	5.98	1.097+15
130.0	260.00	7.732-03	1.496-08	268.96	41.8	6.04	2.072+14
140.0	301.09	1.586-03	2.613-09	291.53	41.2	5.95	3.618+13
150.0	373.88	4.566-04	5.929-10	328.36	40.4	7.68	8.210+12
160.0	439.98	1.672-04	1.802-10	360.48	39.4	9.29	2.495+12
170.0	487.81	7.172-05	6.763-11	385.29	38.3	11.15	9.366+11
180.0	522.76	3.376-05	2.868-11	405.93	36.9	12.31	3.972+11
190.0	554.23	1.713-05	1.325-11	425.51	35.6	13.72	1.834+11
200.0	581.45	9.221-06	6.554-12	443.80	34.4	14.84	9.077+10
300.0	733.41	1.605-07	5.357-14	647.65	20.4	29.93	7.418+08
400.0	793.56	1.936-08	4.362-15	788.21	14.9	50.07	6.040+07
500.0	800.00	3.922-09	7.570-16	851.63	12.8	62.29	1.048+07
600.0	800.00	1.024-09	1.734-16	909.16	11.3	73.55	2.401+06
700.0	800.00	3.222-10	4.891-17	960.29	10.1	85.60	6.773+05
800.0	800.00	1.163-10	1.613-17	1004.58	9.2	95.07	2.234+05
900.0	800.00	4.719-11	5.947-18	1054.05	8.4	105.76	8.235+04
1000.0	800.00	2.125-11	2.453-18	1101.41	7.7	119.14	3.397+04

#### 6.1.4 Ionosphere [VI-1, VI-2, VI-3]

The ionosphere detected by Mariner V is depicted in Figure VI-3 which also contains model values calculated by McElroy [VI-3] under the assumption electrons are produced and removed by:



For design purposes this model should be used.

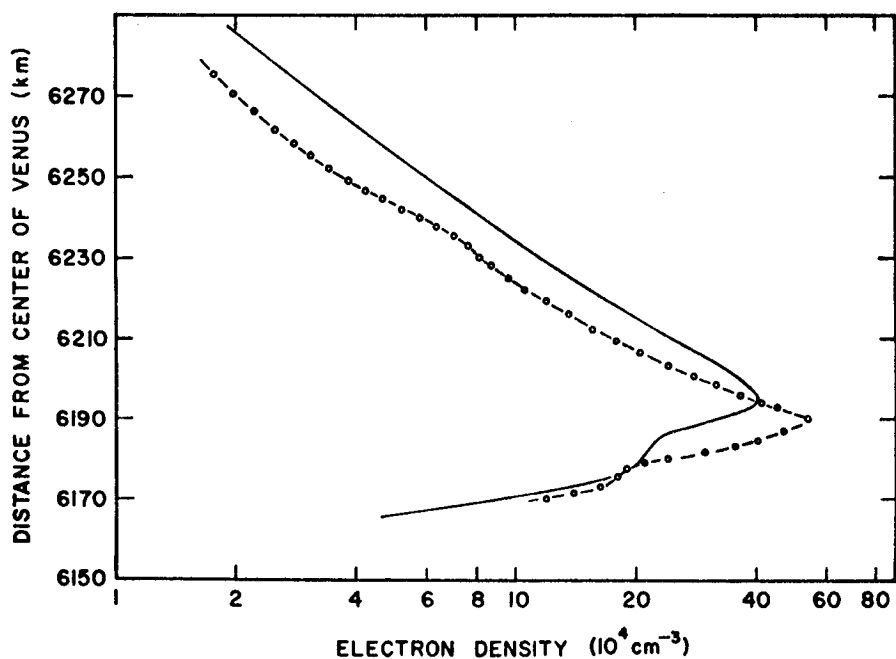


Figure VI-3. A model for the Venus ionosphere. The Mariner data are indicated by circles [VI-3].

#### 6.1.5 Clouds [VI-2]

The very heavy cloud layer that has been observed is thought to be composed of water vapor, ice crystals, dust, carbon suboxide polymers, or suspended hydrocarbons. The top of the cloud layer has been estimated to be from 30 to 65 km above the surface of the planet and is thought to be approximately 10 to 15 km thick.

#### 6.1.6 Circulation [VI-2]

Slow rotational speed will cause the atmosphere fluid to rise near the subsolar point and subside near the antisolar point in a symmetrical regime. However, at higher altitudes, a symmetric regime similar to that of a rotating planet may be predominant; i.e., where ascent occurs near the equator and descent occurs near the poles.

For design purposes the following should be used:

Mean horizontal wind speed at surface	$30 \text{ ms}^{-1}$
Mean horizontal wind speed at cloud altitudes	$100 \text{ ms}^{-1}$
Maximum wind shear	$0.05 \text{ ms}^{-1} \text{ m}^{-1}$

#### 6.1.7 Radiation Environment

##### 6.1.7.1 Galactic Radiation

Same as Interplanetary Space (see Paragraph 1.3.1).

##### 6.1.7.2 Solar Cosmic Radiation

Same as Interplanetary Space (see Paragraph 1.3.2).

##### 6.1.7.3 Magnetically Trapped Radiation

Based on Mariner V and Venera IV data, the apparently small magnetic field of Venus would seem to preclude the existence of any significant radiation belts about the planet as compared to earth.

##### 6.1.7.4 Thermal Radiation

Thermal radiation varies from  $\sim 238 \text{ W/m}^2$  at 200 km to  $\sim 9 \text{ W/m}^2$  at  $\sim 2 \times 10^4 \text{ km}$ . Dark-side radiation is the same as above, although flux is subject to question due to uncertainty in planet atmosphere and surface temperatures. Thermal radiation will consist predominantly of radiation from  $\sim 2$  to 10 microns wavelength.

$$Q = FAI \quad ,$$

where

$Q$  = the thermal radiation flux incident upon vehicle

$F$  = view factor (varies with altitude above the planet and vehicle shape)

$A$  = the cross-sectional area of exposed spherical surface

$I$  = Venus thermal radiation flux ( $160 \text{ W/m}^2$ ) ..

#### 6.1.7.5 Albedo Radiation [VI-2, VI-4]

Albedo radiation varies from  $\sim 3 \times 10^3 \text{ W/m}^2$  at  $\sim 200 \text{ km}$  to  $\sim 90 \text{ W/m}^2$  at  $\sim 2 \times 10^4$  under maximum conditions (zero phase angle and normal to flux). Spectral distribution of albedo radiation is expected to approximate the solar spectrum. Albedo radiation will contribute  $\sim 90$  percent of the total radiation from the planet upon the spacecraft.

$$Q = FASa \quad ,$$

where

$Q$  = the incident albedo radiation flux

$F$  = the view factor

$A$  = the cross-sectional area of exposed spherical surface

$S$  = solar constant at the Venus

$a$  = Venus albedo.

The thermal and albedo radiation values given in this table were calculated with an albedo of 0.76 and a solar constant of  $2676 \text{ W/m}^2$ . More recent literature [VI-5], however, has indicated the solar constant to be  $2586 \text{ W/m}^2$  and the albedo to be 0.70.

Venus Thermal and Albedo Radiation Upon a Spherical Satellite		
Altitude (km)	Thermal W/m <sup>2</sup>	Albedo W/m <sup>2</sup>
200	238	3000
400	208	2660
600	189	2400
1 000	152	1920
4 000	67	770
8 000	35	354
20 000	9	89

#### 6.1.8 Meteoroid Environment

##### 6.1.8.1 Cometary Meteoroid Flux

The flux ( $F_c$ ), in number/m<sup>2</sup>/s<sup>2</sup>, of cometary meteoroids of mass  $m$  or greater on a randomly tumbling surface is : For  $10^{-6} \leq m \leq 10^2$ ,

$$\begin{aligned} \log F_c = & -14.202 - 1.213 \log m + \log \left( 1 + \frac{0.469}{r} \right) \\ & + \log \frac{1}{2} \left[ 1 + \left( 1 - \frac{1}{r^2} \right)^{\frac{1}{2}} \right] + \log V_c . \end{aligned}$$

For  $10^{-12} \leq m \leq 10^{-6}$ ,

$$\begin{aligned} \log F_c = & -14.171 - 1.584 \log m - 0.063 (\log m)^2 \\ & + \log \left( 1 + \frac{0.469}{r} \right) + \log \frac{1}{2} \left[ 1 + \left( 1 - \frac{1}{r^2} \right)^{\frac{1}{2}} \right] + \log V_c , \end{aligned}$$

where  $r$  is the distance of spacecraft from the center of the planet (in units of the planet's radius).

#### 6.1.8.2. Average Velocity of Cometary Meteoroids

The average velocity of cometary meteoroids relative to the spacecraft is  $22.86 \times 10^3$  m/s.

#### 6.1.8.3 Survival Mass [VI-2]

The survival mass for micrometeoroids can be calculated as a function of height in the atmosphere by using the following approximate expression:

$$m^{1/3} - m_{\infty}^{1/3} = \frac{\Lambda A \rho_m^{-2/3} v^2}{6 \xi \cos Z} \int_{\infty}^h \rho_a dh$$

(does not hold for dustballs), where

$$\text{columnar mass} = - \int_h^{\infty} \rho_a dh$$

$Z$  = zenith angle

$\rho_m$  = density of micrometeoroid ( $3.5 > \rho_m > 0.5$  g/cm<sup>3</sup>)

$v$  = velocity of micrometeoroid ( $v_{\text{parabolic}}$  or  $v_{\text{orbital}}$   
 $> v > v_{\text{escape}}$ )

$A$  = shape factor = 1.2 for sphere

$$\Lambda/\xi = 10^{-11.449}.$$



### 6.1.9 Geomagnetic Environment

#### 6.1.9.1 Magnetic Field [VI-6]

From Mariner V data, the upper limit to the magnetic dipole moment of Venus is estimated to be within a factor of 2 of  $10^{-3}$  times that of the earth.

#### 6.1.10 Astrodynamic Constants (Epoch 1960.0) [VI-7]

Distance from sun (average)	$1.082 \times 10^8$ km
Eccentricity of orbit <sup>1</sup>	0.0067921
Inclination of orbit to ecliptic <sup>1</sup>	3 deg 23 ft 39.2 in.
Orbital period (sidereal) <sup>1</sup>	224.70080 days
Radius (equatorial)	6052.0 km
Mass ratio (sun/planet) <sup>1</sup>	408 522 $\pm$ 3
Flattening (dynamic)	Unknown
Average density <sup>1</sup>	5.087 g/m <sup>3</sup>
Rotational period	242.6 days
Gravitational parameter	$3.24860 \times 10^5$ km <sup>3</sup> /s <sup>2</sup>

#### 6.1.11 Additional Information

A more detailed discussion of the Venus atmosphere is given in References VI-5 and VI-8.

---

1. Krause, Helmut G. L.: Astronomical Constants of the Solar System, MSFC, Huntsville, Alabama, 1965 (Unpublished).

## 6.2 Surface Environment

### 6.2.1 Temperature

Measurements from the earth indicate a surface temperature of about 600° to 650° K. Mariner II yielded 700° K, and Venera 7 yielded 747° K. Mariner II detected a large region, slightly cooler than the rest of the disc, that possibly represents the influence of a surface temperature.

### 6.2.2 Features

Since no breaks large enough to reveal the surface have ever been seen in the clouds, no observational data exist. Radar studies have shown areas of enhanced surface roughness.

### 6.2.3 Terrain and Composition

Though the surface has never been seen, it is generally agreed that it is probably dry, dusty, rocky, and windy. One of the explanations of the high surface temperature on the dark side of Venus is that the surface has a very high specific heat capacity. This has led to the conjecture that the surface may consist of a layer of liquid hydrocarbons or a layer of hydrocarbons floating on an ocean of water. However, at temperatures near 700° K, the surface is probably dry and dusty.

### 6.2.4 Dielectric Constant

Radar data indicate a value of 2 to 4 [VI-9]. Recent data by JPL [VI-10] indicate a value of 2.5 as a mean dielectric constant based on data obtained using a high resolution twin-dish interferometer radio telescope.

## 6.3 Satellites

None.

## REFERENCES

- VI-1. Venus: Ionosphere and Atmosphere as Measured by Dual Frequency Radio Occultation of Mariner V. Mariner Stanford Group, Center for Radar Astronomy, Stanford University, Stanford, California, and Stanford Research Institute, Menlo Park, California, Science, vol. 158, December 29, 1967.
- VI-2. Evans, D. E., Pitts, D. E., and Kraus, G. L.: Venus and Mars Nominal Natural Environment for Advanced Manned Planetary Mission Programs. NASA SP-3016, 1965.
- VI-3. McElroy, M. B., The Upper Atmosphere of Venus in Light of the Mariner 5 Measurements, J. Atmos Sci, 25, 574-577, 1968.
- VI-4. Ballinger, John C., and Christensen, E. H.: Environmental Control Study of Space Vehicles, Parts I and II. General Dynamics Corp., Technical Report ERR-AN-004, March 1960.
- VI-5. Koenig, L. R., Murray, F. W., Michaux, C. M., and Hyatt, H. A.: Handbook of the Physical Properties of the Planet Venus. NASA SP-3029, 1967.
- VI-6. Reese, David E., and Swan, R.: Venera 4 Probes Atmosphere of Venus. Ames Research Center and Office of Adv. Res. and Tech., Moffett Field, California, Science, vol. 159, January 25, 1968.
- VI-7. Melbourne, W. G., Mulholland, J. D., Sjogren, W. L., and Sturms, F. M., Jr.: Constants and Related Information for Astrodynamic Constants, 1968. Technical Report 32-1306, Jet Propulsion Laboratory, July 1968.
- VI-8. Models of the Venus Atmosphere. NASA SP-8011, 1968.
- VI-9. Mayer, Cornell H.: Radioastronomy Studies of Venus and Mars. Astronautics and Aeronautics, April 1966.
- VI-10. Kliore, A., Levy, G. S., Cain, D. L., Fjeldbo, G., and Rasool, S. I.: Atmosphere and Ionosphere of Venus from the Mariner V S-Band Radio Occultation Experiment. Science, vol. 158, December 11, 1967.



## SECTION VII. MARS

### 7.1 Atmospheric Environment

#### 7.1.1 Definition

The Martian atmospheric environment is defined as the region between the surface and 20 000 km above the surface of Mars.

#### 7.1.2 Gas Properties (Surface to 1000 km Altitude)

##### 7.1.2.1 Temperature

Considerable information exists on the thermal structure of Mars, among which the data obtained by radiometric and spectroscopic means provide reasonably good temperature measurements. Several methods are available for obtaining planetary temperatures from radiometric measurements. These methods depend on either Planck's or Stefan's laws and make use of the reflected solar radiation from the planet as a calibration standard. The methods that depend on the shape of the Planck curve are sensitive to small variations in the energy measurements; accordingly, the use of Stefan's law, into which the energy enters as a fourth root, seems preferable. Gifford [VII-1], who uses the method of water-cell transmission to reduce radiometric data, analyzes the various sources of error and finds that the individual-tabulated Martian temperature measurements have an observational relative standard error of 10 percent.

Since the Martian atmosphere is believed to be largely transparent to solar radiation, most of the solar energy is not absorbed directly in the atmosphere but rather at the Martian surface. Thus, the calculated temperature from the radiometric measurement can be interpreted as applying to the Martian surface. One should remember that the temperature a few feet above the surface probably decreases at a superadiabatic lapse rate in the daytime, while at night a temperature inversion may be experienced. For this reason, the near surface temperature should be used to develop the vertical temperature profile instead of the temperature calculated from radiometric measurements. To illustrate the difference between the surface and near surface temperatures, Neubauer [VII-2] finds that the surface may experience a diurnal temperature variation of about 95°K, while the air at an altitude of 0.5 m may experience a variation of only 20°K.

Basically, two approaches can be taken to obtain the vertical temperature distribution on Mars. One approach is the theoretical approach. Since Mars and Earth have nearly equal rotational rates, and nearly equal axial tilts, the differential heating and many other physical structures of these two planets are similar; therefore, the average vertical distribution of temperature in the Martian atmosphere is generally controlled by radiation, convection, and conduction processes as is the case on earth. Horizontal eddy transport and advection of heat, though important at various latitudes and seasons, should not affect the average vertical temperature distribution. Furthermore, the release of latent heat into the atmosphere by condensation of water vapor is probably not important on Mars. Ohring [VII-3], using the assumption of a convective troposphere lying below a radiative equilibrium stratosphere, has shown that the Martian temperature profile is characterized by an adiabatic troposphere extending to about 9 km, above which the temperature continues to decrease with height to an average value of about 90°K for the top-most 5-mb layer, assuming a surface pressure of 25 mb.

The variation of the temperature on Mars as a function of latitude and season has been determined also by theoretical analyses. These analyses are generally based on considerations of radiative, convective, and conductive equilibrium conditions for the Martian atmosphere and surface. The findings of House [VII-4], Ohring and Mariano [VII-5], and Leovy [VII-6] are all in general accord. The major difference between the results of Ohring and Mariano and the result of Leovy is found for latitudes in excess of 50 deg in the winter hemisphere. By considering the possible condensation of CO<sub>2</sub>, Leovy derives a minimum temperature of 145°K for latitudes in excess of 60 deg. Such a consideration was not considered by Ohring and Mariano with the result that their temperatures are allowed to decrease below 145°K.

More recently, Lou and Hung [VII-7] have developed a computerized model to predict the Martian environment in three dimensions. They used Leovy's model with several modifications to calculate the atmospheric temperature; however, an improved model of the surface was incorporated to predict the surface temperature. The computer program was written in such a way that it can be used to predict atmospheric parameters such as temperature, density, geometric height of constant pressure level, wind velocity, solid CO<sub>2</sub> deposited on the ground, etc., at a specific point on Mars in terms of earth time without referring to astronomical tables. This model has been used to predict the Martian surface and atmospheric conditions and polar

cap characteristics corresponding to the flybys of Mariner 6 and 7 [VII-8, VII-9, VII-10], and the results have shown excellent agreement with the observed data.<sup>1</sup>

Another source of obtaining the vertical temperature structure of Mars is based on the Mariners 4, 6, and 7 occultation experiments from which several models of temperature-height profiles have been derived [VII-11 through VII-17]. However, the resulting temperature profile can vary considerably depending on the theoretical assumptions concerning the main ionization layer in the Martian atmosphere.

Based on the theoretical considerations and experimental results, the temperature-versus-height profiles (Fig. VII-1) have been idealized to represent the minimum, mean, and maximum temperature profiles expected to exist in the Martian atmosphere. The lower portion of these profiles (0 to 300 km) is taken from the Mars Engineering Model specifically designed for the Viking 75 Project [VII-18]. In developing these profiles, the altitudes chosen for the tropopause were influenced by the work of Anderson [VII-19], temperature lapse rates were based on both theoretical studies [VII-5, VII-20, VII-21, VII-22] and observed data from Mariner occultation experiments [VII-16, VII-17]. The thermodynamics of atmospheric condensation has been considered; for example, the temperature profile for the Minimum Model Atmosphere lies at slightly lower temperatures than the condensation-sublimation curve of CO<sub>2</sub> at altitudes between 26 and 42 km [VII-18]. The upper portion of the temperature profiles (300 to 1000 km) has been derived assuming that the atmosphere is in hydrostatic equilibrium and that the ideal gas law is valid. The envelope of the exospheric temperature is based on the results of a study by Stewart and Hogan [VII-23].

#### 7.1.2.2 Composition and Molecular Weight

Our present knowledge of the composition of the Martian atmosphere is based on gases observed spectroscopically and on gases theoretically deduced as being present. Additionally, the polarization and occultation measurements exist which provide information on the total amount of gases present. Of the expected major constituents (N<sub>2</sub>, CO<sub>2</sub>, and Ar), only CO<sub>2</sub> has been observed spectroscopically. The CO<sub>2</sub> reported is found to lie within the ranges from 50 to 90 m-atm [VII-20, VII-21, VII-22, VII-24 through VII-29], and the arithmetic mean of CO<sub>2</sub> abundance over the 10 best measurements is 72 m-atm [VII-18].

---

1. Lou, Y. S., and Weidner, D. K.: Comparison of the Mariner 69 Predictions to the Observed Data, S&E-AERO-YS, MSFC (Unpublished).

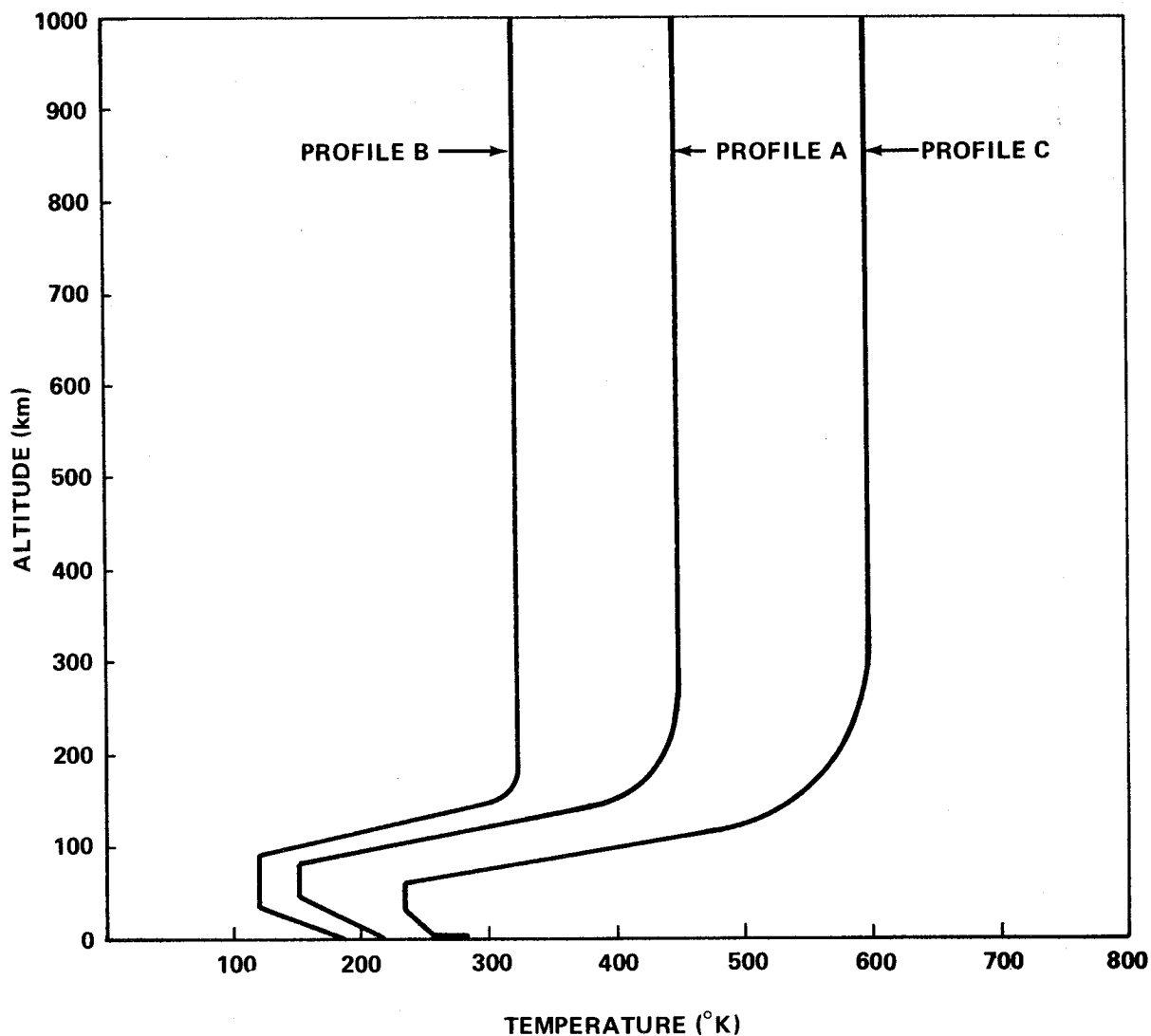


Figure VII-1. Altitude versus temperature for Mars atmosphere.

In the past,  $N_2$  was taken to be the major constituent of the Martian atmosphere on the basis of terrestrial analogy. It is now clear that reasoning by analogy with the earth's atmosphere is entirely inadequate. However, the possibility of a small amount of nitrogen present in the Martian atmosphere cannot be ruled out, even though nitrogen was not detected by the ultraviolet spectrometers on board Mariners 6 and 7. Based on the evidence from Mariners 6 and 7 results, that the ionosphere of Mars is an  $F_1$  type and the ions are  $CO_2^+$ , Goody [VII-30] has pointed out that the nitrogen present in the Martian atmosphere must be less than 10 percent, otherwise the



ions would be  $O^+$  and  $CO^+$ . In the model atmospheres presented in Tables VII-1 to VII-3, nitrogen has been neglected. However, it has been suggested [VII-18] that the presence of 1-percent nitrogen in each of the model atmospheres may be assumed for calculating radio blackout phenomena.

It has been assumed that the Martian atmosphere contains some argon, because there are undoubtedly potassium compounds near the surface of Mars, and some argon will be produced by radioactive decay of potassium-40. The argon present in the Martian atmosphere is probably small. Recent studies [VII-31 through VII-34] indicate that there may be no major constituent other than  $CO_2$ .

The search for water vapor on Mars has been of interest at least partially because of its significance in exobiology, and partly because the polar caps were thought to be  $H_2O$  frost. Early detection of water vapor was credited to Spinrad, Munch, and Kaplan [VII-35] who used the Doppler shift that was produced by the high relative velocity of Mars with respect to earth at quadrature to shift the Martian lines onto the wings of the much stronger telluric lines. An analysis of the line intensities gave an abundance of  $14 \pm 7\mu$  precipitable water, average over the entire planet. This is not a very large amount; e.g., if present in a constant mixing ratio in the atmosphere, the water would give relative humidities at the surface of  $8.5 \times 10^{-5}$  and  $1.4 \times 10^{-5}$  at  $273^\circ K$  and  $300^\circ K$ , respectively, and a dew point of  $-80^\circ C$ .

Other findings of  $H_2O$  were given by Dollfus [VII-36] who gave a value of  $45\mu$  precipitable water that is higher than any other determinations, and by Schorn, et al. [VII-37] who, by studying the lines of  $H_2O$  near  $2800 \text{ \AA}$  using new high-dispersion spectrograms during the 1964-65 apparition, gave an abundance of 10 to  $20 \mu$  precipitable water.

Seasonal and latitudinal variations of water vapor content in the Martian atmosphere have been reported by Tull [VII-38] who found that during the period from mid-summer to mid-autumn the precipitable water vapor reached as much as  $48 \mu m$  in the northern hemisphere and  $20 \mu m$  in the southern hemisphere. Also, Schorn, et al. [VII-39] reported that more precipitable water vapor was found in the northern hemisphere in the northern mid-spring and more in the southern hemisphere in the northern mid-summer.

The only other minor constituent in the Martian atmosphere, in addition to water vapor, was observed recently by Kaplan [VII-40] who made positive identification of  $CO$  in the Martian atmosphere with a preliminary abundance of 10 cm-atm. He states that the  $CO$  is almost certainly well

TABLE VII-1. MEAN MARS MODEL ATMOSPHERE

Geometric Altitude (km)	Kinetic Temperature (°K)	Pressure (mb)	Density (g/cm <sup>3</sup> )	Speed of Sound (m/s)	Mol. wt.	Density Scale Height (km)	Number Density (cm <sup>-3</sup> )
.0	230.00	5.300+00	1.219-05	246.67	44.0	15.32	1.670+17
1.0	225.17	4.862+00	1.143-05	244.07	44.0	15.01	1.564+17
2.0	220.34	4.452+00	1.069-05	241.43	44.0	14.70	1.464+17
3.0	215.51	4.069+00	9.992-06	238.78	44.0	12.96	1.368+17
4.0	213.98	3.712+00	9.180-06	237.93	44.0	11.71	1.257+17
5.0	212.46	3.384+00	8.429-06	237.08	44.0	11.63	1.154+17
6.0	210.95	3.083+00	7.735-06	236.23	44.0	11.55	1.059+17
7.0	209.43	2.807+00	7.094-06	235.38	44.0	11.48	9.712+16
8.0	207.91	2.555+00	6.502-06	234.53	44.0	11.40	8.902+16
9.0	206.40	2.323+00	5.957-06	233.67	44.0	11.33	8.155+16
10.0	204.88	2.111+00	5.454-06	232.81	44.0	11.25	7.466+16
20.0	189.78	7.818-01	2.180-06	224.07	44.0	10.48	2.985+16
30.0	174.77	2.684-01	8.128-07	215.03	44.0	9.71	1.113+16
40.0	159.85	8.437-02	2.793-07	205.64	44.0	8.93	3.824+15
50.0	150.00	2.399-02	8.465-08	199.20	44.0	7.78	1.159+15
60.0	150.00	6.665-03	2.351-08	199.20	44.0	7.83	3.219+14
70.0	150.00	1.865-03	6.580-09	199.20	44.0	7.87	9.008+13
80.0	150.00	5.257-04	1.855-09	199.20	44.0	7.92	2.539+13
90.0	179.36	1.613-04	4.759-10	217.83	44.0	7.98	6.515+12
100.0	215.66	6.181-05	1.498-10	240.36	43.5	9.60	2.051+12
110.0	251.75	2.803-05	5.705-11	262.25	42.6	11.32	7.811+11
120.0	287.58	1.441-05	2.499-11	284.20	41.4	13.11	3.421+11
130.0	323.21	8.194-06	1.219-11	306.81	40.0	15.02	1.668+11
140.0	358.68	5.052-06	6.490-12	330.11	38.3	16.92	8.885+10
150.0	387.26	3.331-06	3.762-12	352.07	36.4	20.26	5.150+10
160.0	403.60	2.301-06	2.353-12	369.99	34.3	23.00	3.221+10
170.0	413.74	1.645-06	1.519-12	389.44	31.8	23.96	2.079+10
180.0	421.01	1.220-06	1.014-12	410.32	29.1	25.56	1.389+10
190.0	427.23	9.344-07	6.929-13	434.50	26.3	27.14	9.486+09
200.0	432.12	7.377-07	4.873-13	460.36	23.7	29.38	6.671+09
300.0	449.70	1.498-07	6.209-14	581.27	15.5	64.13	8.500+08
400.0	450.00	4.654-08	1.624-14	633.36	13.1	83.36	2.224+08
500.0	450.00	1.794-08	5.462-15	678.20	11.4	100.05	7.477+07
600.0	450.00	8.056-09	2.210-15	714.31	10.3	118.97	3.026+07
700.0	450.00	4.038-09	1.008-15	748.85	9.3	136.84	1.380+07
800.0	450.00	2.215-09	5.055-16	783.31	8.5	153.51	6.920+06
900.0	450.00	1.307-09	2.779-16	811.56	8.0	176.13	3.804+06
1000.0	450.00	8.176-10	1.623-16	839.86	7.4	197.07	2.222+06

TABLE VII-2. MINIMUM MARS MODEL ATMOSPHERE

Geometric Altitude (km)	Kinetic Temperature (°K)	Pressure (mb)	Density (g/cm <sup>3</sup> )	Speed of Sound (m/s)	Mol. wt.	Density Scale Height (km)	Number Density (cm <sup>-3</sup> )
.0	180.00	4.000+00	1.176-05	218.22	44.0	9.96	1.610+17
1.0	178.24	3.583+00	1.064-05	217.15	44.0	9.86	1.456+17
2.0	176.47	3.205+00	9.612-06	216.07	44.0	9.77	1.316+17
3.0	174.71	1.865+00	8.678-06	214.99	44.0	9.68	1.188+17
4.0	172.95	2.556+00	7.822-06	213.90	44.0	9.59	1.071+17
5.0	171.19	2.279+00	7.044-06	212.81	44.0	9.50	9.644+16
6.0	169.43	2.029+00	6.337-06	211.71	44.0	9.40	8.675+16
7.0	167.67	1.804+00	5.695-06	210.61	44.0	9.31	7.796+16
8.0	165.92	1.603+00	5.112-06	209.51	44.0	9.22	6.998+16
9.0	164.16	1.422+00	4.584-06	208.39	44.0	9.13	6.276+16
10.0	162.40	1.260+00	4.106-06	207.28	44.0	9.04	5.621+16
20.0	144.91	3.509-01	1.281-06	195.80	44.0	8.11	1.754+16
30.0	127.52	8.411-02	3.490-07	183.67	44.0	7.18	4.778+15
40.0	120.00	1.709-02	7.535-08	178.17	44.0	6.19	1.032+15
50.0	120.00	3.413-03	1.505-08	178.17	44.0	6.23	2.061+14
60.0	120.00	6.883-04	3.035-09	178.17	44.0	6.26	4.156+13
70.0	120.00	1.401-04	6.178-10	178.17	44.0	6.30	8.458+12
80.0	120.00	2.877-05	1.269-10	178.17	44.0	6.34	1.737+12
90.0	120.00	5.965-06	2.630-11	178.17	44.0	6.37	3.601+11
100.0	143.74	1.372-06	4.989-12	196.23	43.5	6.57	6.831+10
110.0	175.08	4.286-07	1.255-12	218.70	42.6	8.11	1.718+10
120.0	206.29	1.670-07	4.034-13	240.71	41.4	9.72	5.523+09
130.0	237.32	7.661-08	1.552-13	262.90	40.0	11.45	2.124+09
140.0	268.10	3.986-08	6.851-14	285.40	38.3	13.22	9.379+08
150.0	295.26	2.292-08	3.398-14	307.33	36.4	15.86	4.652+08
160.0	310.49	1.415-08	1.881-14	324.52	34.3	18.63	2.575+08
170.0	317.25	9.147-09	1.102-14	340.95	31.8	20.06	1.508+08
180.0	320.00	6.170-09	6.881-15	354.31	29.7	20.51	9.421+07
190.0	320.00	4.315-09	4.283-15	375.60	26.4	21.88	5.863+07
200.0	320.00	3.144-09	2.817-15	395.27	23.8	25.69	3.856+07
300.0	320.00	3.422-10	2.003-16	488.99	15.6	48.33	2.743+06
400.0	320.00	6.600-11	3.239-17	534.09	13.1	61.55	4.435+05
500.0	320.00	1.728-11	7.396-18	571.91	11.4	73.99	1.012+05
600.0	320.00	5.602-12	2.162-18	602.36	10.3	87.56	2.959+04
700.0	320.00	2.121-12	7.448-19	631.48	9.3	100.83	1.020+04
800.0	320.00	9.119-13	2.926-19	660.55	8.5	113.80	4.006+03
900.0	320.00	4.343-13	1.298-19	684.37	8.0	129.91	1.777+03
1000.0	320.00	2.245-13	6.265-20	708.23	7.4	145.45	8.578+02

TABLE VII-3. MAXIMUM MARS MODEL ATMOSPHERE

Geometric Altitude (km)	Kinetic Temperature (°K)	Pressure (mb)	Density (g/cm <sup>3</sup> )	Speed of Sound (m/s)	MoL. wt.	Density Scale Height (km)	Number Density (cm <sup>-3</sup> )
.0	280.00	8.000+00	1.485-05	274.67	43.2	19.13	2.070+17
1.0	275.15	7.462+00	1.409-05	272.28	43.2	18.81	1.965+17
2.0	270.31	6.953+00	1.336-05	269.88	43.2	18.49	1.864+17
3.0	265.46	6.466+00	1.265-05	267.45	43.2	18.17	1.765+17
4.0	260.62	6.005+00	1.197-05	265.00	43.2	15.80	1.669+17
5.0	259.59	5.573+00	1.115-05	264.47	43.2	14.11	1.555+17
6.0	258.57	5.170+00	1.039-05	263.95	43.2	14.05	1.449+17
7.0	257.55	4.796+00	9.674-06	263.43	43.2	14.01	1.349+17
8.0	256.54	4.447+00	9.007-06	262.91	43.2	13.96	1.256+17
9.0	255.52	4.123+00	8.383-06	262.39	43.2	13.91	1.169+17
10.0	254.51	3.821+00	7.801-06	261.87	43.2	13.87	1.088+17
20.0	244.39	1.764+00	3.750-06	256.61	43.2	13.39	5.229+16
30.0	234.33	7.921-01	1.756-06	251.28	43.2	12.92	2.449+16
40.0	231.00	3.476-01	7.818-07	249.48	43.2	12.14	1.090+16
50.0	231.00	1.529-01	3.438-07	249.48	43.2	12.21	4.794+15
60.0	231.00	6.755-02	1.519-07	249.48	43.2	12.28	2.119+15
70.0	269.47	3.148-02	6.069-08	269.46	43.2	11.71	8.463+14
80.0	312.39	1.648-02	2.741-08	290.12	43.2	13.66	3.822+14
90.0	355.05	9.412-03	1.377-08	309.30	43.2	15.61	1.921+14
100.0	397.40	5.756-03	7.431-09	329.31	42.7	17.20	1.036+14
110.0	439.59	3.738-03	4.278-09	349.75	41.8	19.11	5.966+13
120.0	481.56	2.554-03	2.599-09	370.89	40.7	21.13	3.624+13
130.0	507.01	1.818-03	1.705-09	386.32	39.5	25.74	2.378+13
140.0	521.15	1.325-03	1.165-09	399.05	38.1	26.92	1.624+13
150.0	532.35	9.874-04	8.093-10	413.31	36.3	28.33	1.128+13
160.0	542.77	7.521-04	5.741-10	428.27	34.4	30.24	8.005+12
170.0	551.00	5.848-04	4.121-10	445.72	32.3	30.85	5.747+12
180.0	556.99	4.652-04	2.964-10	468.77	29.5	31.05	4.133+12
190.0	562.67	3.791-04	2.161-10	495.59	26.7	32.48	3.013+12
200.0	567.99	3.166-04	1.576-10	530.33	23.5	36.11	2.198+12
300.0	594.83	9.402-05	2.962-11	666.68	15.6	81.01	4.130+11
400.0	600.00	3.901-05	1.021-11	731.34	13.1	106.61	1.424+11
500.0	600.00	1.909-05	4.358-12	783.11	11.4	127.72	6.076+10
600.0	600.00	1.047-05	2.154-12	824.81	10.3	152.68	3.004+10
700.0	600.00	6.237-06	1.168-12	864.69	9.3	175.40	1.628+10
800.0	600.00	3.976-06	6.803-13	904.49	8.5	195.48	9.487+09
900.0	600.00	2.677-06	4.267-13	937.11	8.0	225.50	5.950+09
1000.0	600.00	1.882-06	2.802-13	969.78	7.4	252.14	3.907+09

mixed throughout the atmosphere, not just confined to a layer. If CO exists in the Martian atmosphere, then traces of O<sub>2</sub> and O<sub>3</sub> are probably also present. So far, however, they have not been detected.

Several other minor constituents are assumed to exist in the Martian atmosphere, including oxygen, formaldehyde (HCHO), carbonyl sulfide (COS), ammonia (NH<sub>3</sub>), methane (CH<sub>4</sub>), and oxides of nitrogen such as NO<sub>2</sub>, N<sub>2</sub>O<sub>4</sub>, NO, N<sub>2</sub>O, and HNO<sub>2</sub>. Table VII-4 lists the abundance of all observed and assumed constituents.

Based on the Mariner 4 occultation data, Spencer [VII-41] has shown that, for a mean temperature above the occultation point of 140° to 180°K, the allowable mean molecular weight could range from 33.1 to 50. Similarly, Hess and Pounder [VII-42] indicated that while the mean molecular weight is estimated as 33.2 to 39.2, based on the Mariner 4 data, a range of 31.2 to 44 is consistent with reliable spectroscopic data. More recently, both Mariners 6 and 7 occultation experiments indicate that the molecular weight of the Martian atmosphere is close to 44 [VII-16, VII-17]. Thus, the more recent data interpretations are strongly favoring a CO<sub>2</sub> rich atmosphere.

It is suspected that the upper atmosphere of Mars is under constant bombardment by interplanetary space plasma causing the constituents of the upper atmosphere to become mixed with hydrogen and helium from outer space. This mixing of the Martian atmospheric constituents with interplanetary plasma could possibly occur as low as 300-km altitude.

A very extensive review of related literature led to the molecular weight profiles illustrated in Figure VII-2. In this figure, the lower atmospheric composition was taken to be 100-percent CO<sub>2</sub> except for the Maximum Model Atmosphere whose composition was assumed to be 82-percent CO<sub>2</sub> and 18-percent Ar.

#### 7.1.2.3 Surface Pressure

Early estimates of the Martian surface pressure were drawn primarily from photometric and polarization observations. The brightness and polarization were measured as a function of wavelength, position on the disc, and phase angle. Certain assumptions were made about the composition of the atmosphere and the reflecting properties of the surface, and the atmospheric pressure was then derived. The results have been summarized by de Vaucouleurs [VII-43] who discussed the material and concluded that the surface pressure was  $85 \pm 4$  mb. These measurements apply at best to days

TABLE VII-4. OBSERVED AND ASSUMED CONSTITUENTS  
OF THE MARTIAN ATMOSPHERE

Constituent	Abundance	Remarks
CO <sub>2</sub>	72 ± 20 m-atm	Observed
H <sub>2</sub> O	10 to 20 μ-atm	Observed
CO	10 cm-atm	Observed
Ar	<40 m-atm	Assumed
N <sub>2</sub>	<20 m-atm	Assumed
CH <sub>4</sub>	<1 mm-atm	Assumed
NH <sub>3</sub>	<1 mm-atm	Assumed
O	No estimate	Assumed
O <sub>2</sub>	<70 cm-atm	Assumed
O <sub>3</sub>	0.1 μ-atm	Assumed
HCHO	<3 mm-atm	Assumed
COS	<2 mm-atm	Assumed
NO <sub>2</sub>	10 μ-atm	Assumed
N <sub>2</sub> O <sub>4</sub>	10 μ-atm	Assumed
NO	30 cm-atm	Assumed
N <sub>2</sub> O	1 mm-atm	Assumed
HNO <sub>2</sub>	2 mm-atm	Assumed

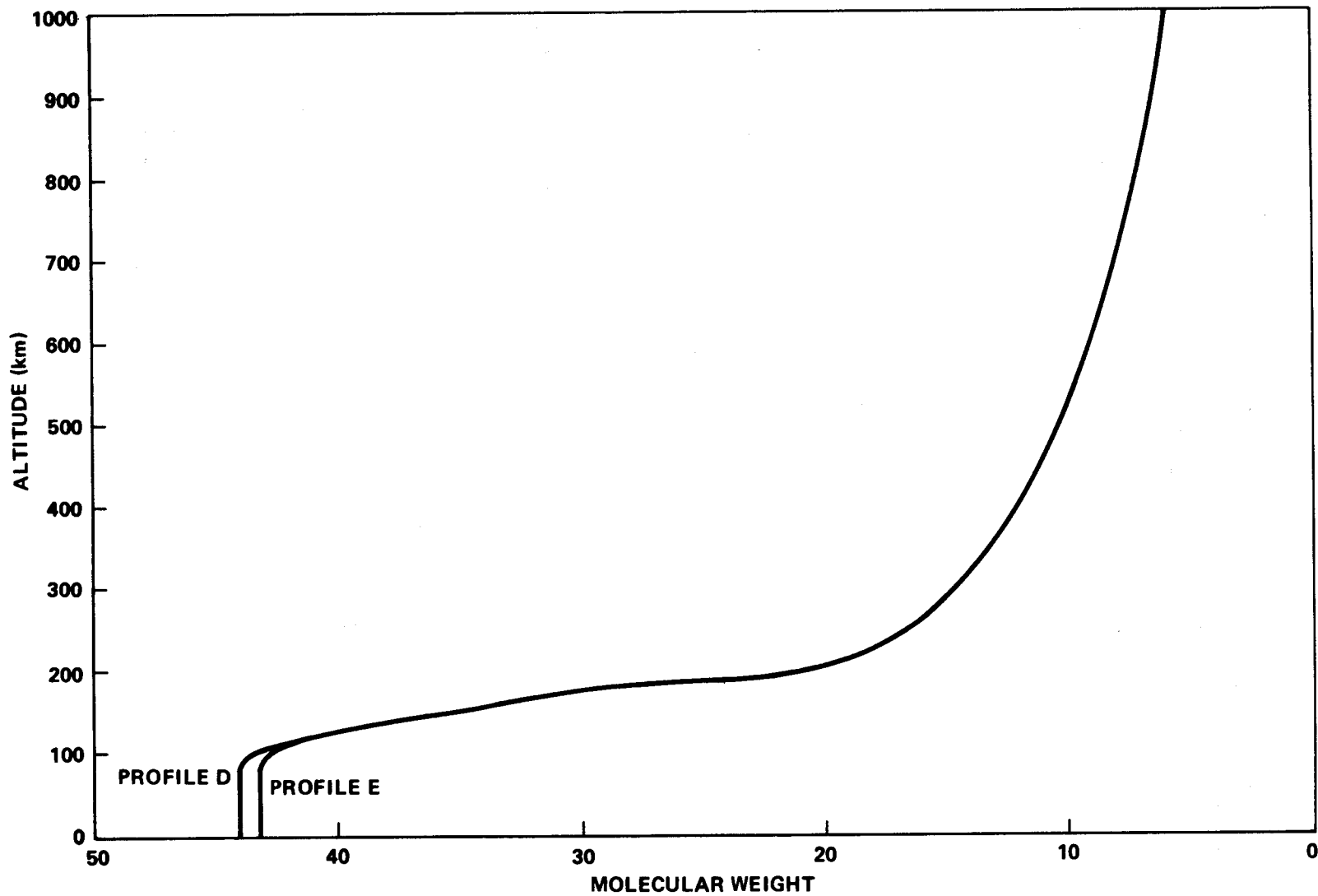


Figure VII-2. Altitude versus molecular weight for Mars atmosphere.

on which the Martian atmosphere is clear of haze or aerosols. The difficulties of these methods have been thoroughly discussed by Chamberlain and Hunter [VII-44] who concluded that even if the polarimetric techniques were perfect in principle, a realistic assignment of errors and their effects indicate that the surface pressure can only be bracketed between 30 to 200 mb.

Modern studies of the Martian atmospheric pressure can properly be stated to have begun in 1963 with the spectroscopic study of Kaplan, Munch, and Spinrad [VII-20]. Their low pressure result signaled the end of the high pressure era and began the current low pressure era. The basis of the spectroscopic method is to utilize two sets of measurements: one measurement is made on a band firmly on the linear part of the curve of growth and the other measurement is made on a fully saturated band. The equivalent width of the former depends only on the abundance of the gas while the equivalent width of the latter depends both on the abundance and the total pressure. A method must be specified for forming these two bands. This technique of modern spectroscopy can be found in References VII-21, VII-22, VII-45, VII-46, and VII-47. The work by Grandjean and Goody [VII-48], who used the observation of  $\text{CO}_2$  to determine a relation between the surface pressure and the fraction of  $\text{CO}_2$ , is of particular interest, although the full significance of their result was not appreciated because of the high pressure generally accepted at that time. Goody [VII-48] noted that a lower limit to the surface pressure followed from the assumption of a pure  $\text{CO}_2$  atmosphere. He obtained 13 mb, while a better analysis made by Belton and Hunter [VII-22] gives  $5.5 \pm 0.5$  mb. Low pressures have also been derived by Musman [VII-49] and Evans [VII-50] from Martian ultraviolet albedoes. Musman used an albedo for the total disc obtained photoelectrically by de Vaucouleurs. Assuming that there are no absorbing atmospheric constituents, no particles in the atmosphere contributing to the albedo, and the surface reflectivity is zero, he calculated the surface pressure of 27 mb for a pure  $\text{N}_2$  atmosphere and 19 mb for a pure  $\text{CO}_2$  atmosphere. On the other hand, Evans used an Aerobee rocket to obtain an ultraviolet spectrum between 2400 and 3500 Å. He found that surface pressures are  $6 \pm 3$  mb for pure  $\text{CO}_2$ ,  $9 \pm 4$  mb for pure  $\text{N}_2$ , and  $12 \pm 6$  mb for pure Ar atmospheres.

Through a careful examination of the most recent 11 spectroscopic measurements, Wood [VII-51] concluded that the values of the surface pressure on Mars fall within the range of 5 to 7 mb with exception of two measurements which yield a pressure of 4.4 and 8.0 mb, respectively. However, the best value of surface pressure would be derived from the spectroscopic measurement of  $\text{CO}_2$  abundance since the nature of the spectroscopic technique is that the abundance of  $\text{CO}_2$  can be measured with more accuracy than the



surface pressure. Wood then derived an arithmetic mean of CO<sub>2</sub> abundance of 72 m-atm from the 10 best measurements of CO<sub>2</sub> abundance by spectroscopy. Since 13.7 m-atm of CO<sub>2</sub> exert a pressure of 1 mb on the Martian surface, the pressure of 72 m-atm of CO<sub>2</sub> is 5.3 mb.

Additional information on the atmospheric pressure was recently obtained from the Mariners 4, 6, and 7 occultation experiments in which changes in the frequency, phase, and amplitude of the S-band radio signal, caused by passage through the atmosphere and ionosphere of Mars, were observed immediately before and after occultation by the planet. Analysis of these effects has yielded estimates of the refractivity and density of the atmosphere near the surface, the scale height in the atmosphere, and the electron density profile of the Martian ionosphere. Based on these data, the surface pressure was estimated in the range 4.2 to 8.0 mb [VII-13, VII-14, VII-16, VII-17, VII-32, and VII-52].

It should be pointed out that the spectroscopic method usually measures an average surface pressure over an area of hundreds of thousands of square kilometers, while the occultation method yields the surface pressure only at a specific point on Mars. Therefore, it has been suggested that the values of the surface pressure differ from one occultation experiment to another and is primarily due to elevation difference. In fact, radar observations have shown that elevation difference on Mars is on the order of 12 km [VII-53, VII-54, and VII-55]. It is interesting to note that the correlation of radar ranging data with results of occultation experiments has strongly indicated that the atmospheric pressure at the mean surface level on Mars is very close to 5.3 mb [VII-51].

Based on modern spectroscopic measurements and Mariner occultation data, the surface pressure of Mars is taken to be 5.3 mb for the Mean Model Atmosphere, and the lower and upper limits of the surface pressure, as used in the Minimum and Maximum Model Atmosphere, are chosen to be 4.0 and 8.0 mb, respectively. One should not misinterpret this limit such that the surface pressure on Mars will not exceed the given envelope; however, the probability of falling beyond this range is believed to be 1 percent or less [VII-18].

#### 7.1.2.4 Model Atmospheres

Under the assumptions of hydrostatic equilibrium and a perfect gas-law relationship among the thermodynamic quantities, a model atmosphere may be generated from a given temperature profile, molecular weight profile,

and surface pressure. Three such models that define the mean atmosphere and the 99-percent confidence envelope for Mars have been developed by this technique, using the computer program described in Appendix C. These models were generated from the following criteria:

a. Mean Model (Table VII-1)

1. Temperature — Profile A (Fig. VII-1)
2. Molecular weight — Profile D (Fig. VII-2)
3. Surface pressure — 5.3 mb.

b. Minimum Model (Table VII-2)

1. Temperature — Profile B (Fig. VII-1)
2. Molecular weight — Profile D (Fig. VII-2)
3. Surface pressure — 4.0 mb.

c. Maximum Model (Table VII-3)

1. Temperature — Profile C (Fig. VII-1)
2. Molecular weight — Profile E (Fig. VII-2)
3. Surface pressure — 8.0 mb.

It should be noted that the model atmospheres presented in Tables VII-1 through VII-3 do not take complete account of diurnal, seasonal, and solar cycle variations. It has been suggested [VII-52] that the effects of these become important at high altitudes: at 100 km above the surface the atmospheric density may vary by one order of magnitude between day and night and by three orders of magnitude between solar maximum and minimum.

#### 7.1.2.5 Computed Quantities

The various computed quantities of the three model atmospheres are tabulated in Tables VII-1, VII-2, and VII-3.

#### 7.1.3 Gas Properties (1000 to 20 000 km Altitude)

Gas pressure decreases exponentially with increasing altitude above 1000 km until it reaches the interplanetary space value of  $10^{-10}$  dynes/cm<sup>2</sup> near 20 000 km. It then remains relatively constant with increasing altitude.

Gas density decreases exponentially with increasing altitude above 1000 km until it reaches the interplanetary space value of  $10^{-23}$  g/cm<sup>3</sup> near 20 000 km. It then remains relatively constant with increasing altitude.

Kinetic temperature increases linearly above 1000 km with increasing altitude to a value of  $2 \times 10^5$  °K near 20 000 km. It then remains relatively constant with increasing altitude.

#### 7.1.4 Ionosphere

It has been speculated that Mars has an ionosphere and that its structure would be similar to that on earth. The truly scientific discussion of the upper atmosphere of Mars, however, has only been possible since the spectacularly successful experiment of Mariner 4. More information was recently provided by Mariners 6 and 7 experiments.

The formation of the ionosphere on Mars and the interpretation of electron number density data acquired from the Mariner experiments are based on analogy to terrestrial atmosphere. In the earth's atmosphere above an altitude of about 50 km, there is a region known as the ionosphere in which four distinct subregions can be identified at different altitudes. These four subregions are designated as D, E, F<sub>1</sub>, and F<sub>2</sub>. The electron and ion densities in these subregions and the dependence on altitude vary with the season, solar activity, and time of day. The ionosphere does not extend below about 50 km because the recombination rate of ions and free electrons to form neutral particles is very rapid in the lower altitudes. In the uppermost altitudes, the free electrons and positive ions do not recombine quickly to form neutral particles because the particle concentrations are extremely low. Moreover, the atomic ions that predominate at these high altitudes recombine with electrons much more slowly than would molecular ions. Hence, even at night when the ionizing radiation is no longer present, these higher subregions of ionosphere continue to exist, although their concentrations of electrons and ions are reduced.

The source of ionization of the D region (50 to 90 km) of the terrestrial ionosphere is believed caused by solar Lyman-alpha radiation acting on the trace constituent, nitric oxide, to form NO<sup>+</sup>, and caused by galactic cosmic rays acting on molecular nitrogen and molecular oxygen to form N<sub>2</sub><sup>+</sup> and O<sub>2</sub><sup>+</sup>. The E region (90 to 150 km) arises mainly because of the ionization of atmospheric molecules by X-rays from the sun. The F<sub>1</sub> region (150 to 250 km) is produced by ultraviolet radiation which causes ionization of some of the heavier species present in the atmosphere in this region. Finally, the F<sub>2</sub> region (above 250 km) is formed by ionization of oxygen atoms.

The photoionization process is expected to occur on Mars to form an ionosphere, except it can have no counterpart to the D region of the terrestrial ionosphere. The height and extent of the Martian ionosphere are also complex functions of the season, solar activity, and time of day. At the uppermost altitudes, the number density of the molecules is too low to produce an appreciable electron density. At lower altitudes, attenuation of the ultraviolet radiation by the atmosphere above and larger electron recombination rates caused by the increased density limit the electron density. These two factors can be expected to cause the Martian ionosphere to occupy a well-defined region. However, the possible atmospheric penetration of the solar wind does not preclude the existence of detectable electron concentration at the Martian surface.

Figure VII-3 shows the distributions of electron number-density in the Martian ionosphere as measured by Mariners 4, 6, and 7 [VII-32, VII-53]. One surprising fact is that the maximum electron densities, at altitudes of 120 km from Mariner 4 measurements and 135 km from Mariners 6 and 7 measurements, are much lower than expected. These densities indicate that the temperature of the Martian atmosphere is considerably less than anticipated.

The measured maximum electron density was  $10^5 \text{ cm}^{-3}$  from Mariner 4 when the solar activity was low and the solar zenith angle was large (67 deg). The Mariners 6 and 7 measurements gave a maximum electron density of  $1.7 \times 10^5 \text{ cm}^{-3}$  when the solar activity was relatively higher than 1965.

Based on these data, it has been concluded [VII-51] that the electron number densities in the Martian ionosphere are not large enough either to affect radio communication to or from a lander that is located on the surface of Mars, or to contribute significantly to the electron number density behind a bow shock wave during entry through the Martian atmosphere. Therefore, the effect of the Martian ionosphere on radio transmission can be disregarded in the design of space vehicle until new evidence shows that such an assumption is not appropriate.

Measurements of the Martian ionosphere made by Mariner 4 probe have three possible interpretations:

- a. The ions are mostly  $\text{O}^+$  ( $\text{F}_2$  model), and the peak electron density of  $10^5 \text{ cm}^{-3}$  occurs at a neutral concentration of  $10^9 \text{ cm}^{-3}$ .

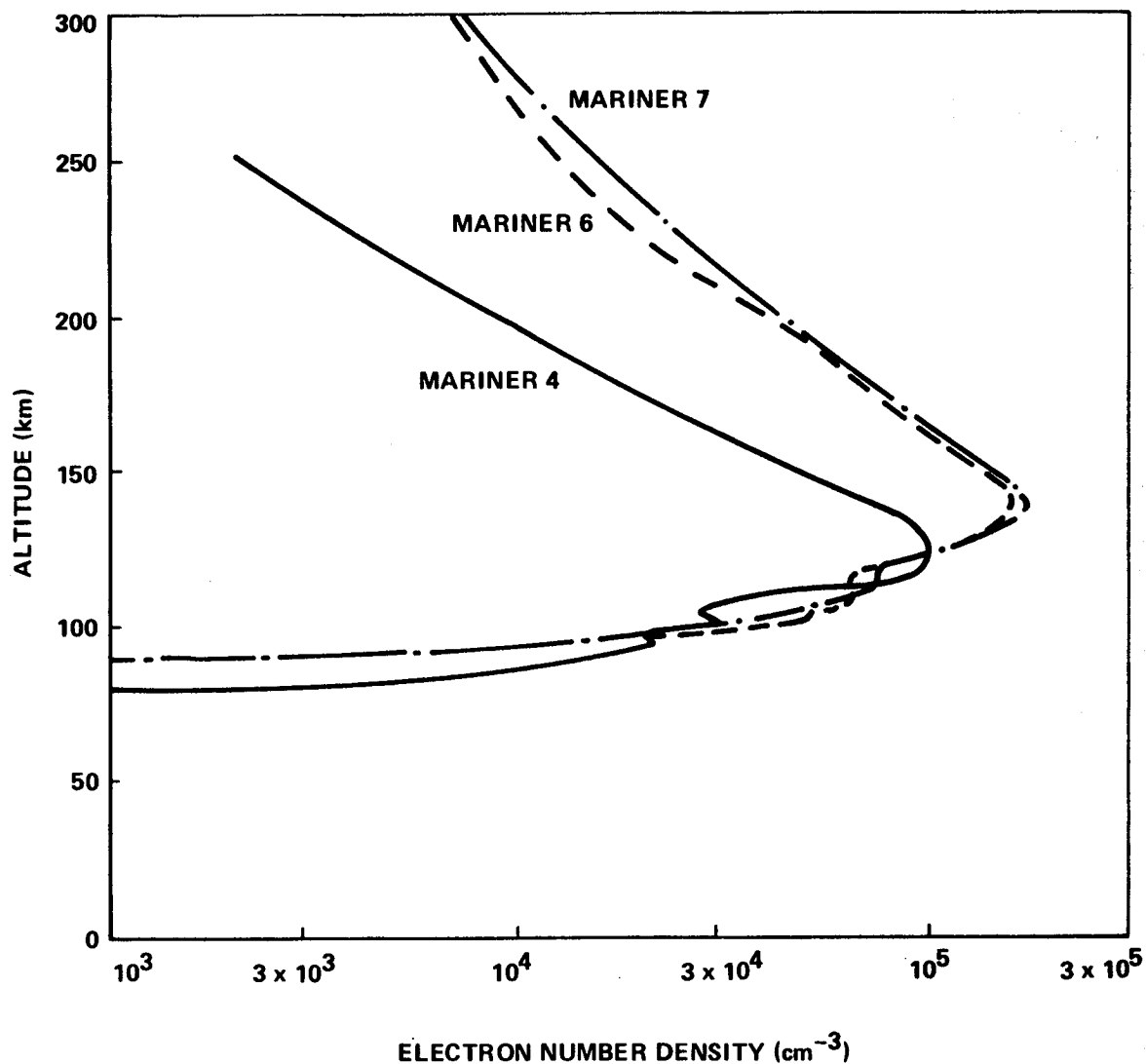


Figure VII-3. Electron number-density distributions measured by Mariners 4, 6, and 7.

b. The ions are mostly  $O_2^+$  (E model), and the peak electron density of  $10^5 \text{ cm}^{-3}$  occurs at a neutral concentration of  $10^9 \text{ cm}^{-3}$ .

c. The ions are predominantly  $CO_2^+$  ( $F_1$  model).

However, the preliminary analysis of the data from the ultraviolet spectroscopy experiments made by Mariners 6 and 7 indicate that  $CO_2^+$  is the

dominant ion in the Martian ionosphere [VII-33]. This implies that the ionosphere is a  $F_1$  type. Physically, the  $F_1$  model would imply  $CO_2^+$  are produced by ionization of the carbon dioxide molecules which are known to be the major constituent of the Martian atmosphere.

#### 7.1.5 Clouds

Even though they were not found to exist during Mariners 6 and 7 observations, the possibility of clouds on Mars should not be eliminated. Martian clouds that have been observed from the earth are summarized in Table VII-5.

Surface details on Mars generally are clearly seen in any light on wavelength greater than 4500 to 4550 Å; i.e., red or yellow light. The so-called "blue haze" is a diffuse, variable phenomenon which occasionally clears and allows surface features to be observed in blue light (blue clearing). The haze itself, which is probably a high-altitude layer, is not blue but causes extinction of solar blue light reflected from the Martian surface while being transparent to longer wavelengths of light. When the effects of observational selection are removed, some correlation of blue clearing with favorable oppositions exist; however, blue clearings have also been observed at unfavorable oppositions, several months from opposition, and on small topographical scales of Mars down to the limit of telescopic resolution.

Some authorities discount the hypothesis that the blue haze is produced by scattering of light by condensed particles, but suggest that the blue haze and its occasional clearing may be accounted for by selective absorption of light by solid particles in the Martian atmosphere.

Others have suggested that solar wind protons interacting with the  $CO_2$  of the Martian atmosphere cause the blue haze by producing molecular ions ( $CO_2^+$  and  $CO^+$ ) which have strong absorption bands in the required energies. Newer and lower Martian density estimates, particularly those obtained from Mariners 4, 6, and 7, would allow a sufficient solar proton flux caused by Mars being in the earth-induced wake of a solar wind magnetohydrodynamic shock might account for the blue clearings observed on Mars. Some authorities point out that the only acceptable explanation of the blue haze phenomenon is that obscuration is largely caused by absorption in blue and violet rather than by scattering. A haze of solid  $CO_2$  or ice is unlikely since neither absorbs in the blue or violet region of the spectrum.

TABLE VII-5. MARTIAN CLOUDS

Composition	Yellow Clouds (Dust)	Blue-White Clouds	Blue Haze or Violet Layer
	Probably dust; 1956 "storm;" color of dust closely matched planet's desert areas (some H <sub>2</sub> O) ?		
Photo Char. In:	(Most can be seen visually)	Blue light shows bright clouds almost always around autumn-winter pole; shows weaker in yellow light; vanish in red light indicating they consist of fine ice crystals.	Obscures surface in blue, especially $\lambda < 4550 \text{ \AA}$ . Begins abruptly at $\sim 450 \text{ \AA}$ .
Blue	Not conspicuous in blue		
Red	Bright & impenetrable in red		
Yellow			
Geo. Locales	Great yellow clouds sometimes extend over vast areas of middle latitudes.	Commonly over poles; various times anywhere on planet; "W" clouds in Tharsis. <sup>a</sup>	Not uniform over entire planet.
Diurnal Var.		"W" clouds are afternoon phenomenon (prominent in blue light, never present before noon).	Quick changes in state; random from opacity to near transparency.
Seasonal Var.		At poles: common at Martian equinox; advent during vernal equinox of S. hemisphere; persist April into May; vanish for summer.	High level phenomenon. Seems to clear at or near oppositions sometimes for a few days at a time--cannot be predicted on present knowledge. Red & yellow photos seem to be totally unaffected by deg. of opacity of blue haze.
Height	1956 blue & yellow photos showed dust clouds higher than blue-white polar winter cloud cover.	Meas. of blue photos 1956 for dia. indicate cloud level ht. at poles & equator differs considerably.	
Motions	Various clouds N 9.66 to 19.3 km/hr; southerly 37.1 km/hr; avg. velocity 32.3 km/hr.	Immobile compared to yellow clouds.	Some observations have shown tenuous band (veils) patterns indicative of a circulatory system (1954).

a. "W" clouds are afternoon phenomenon (prominent in blue light, never present before noon).

#### 7.1.6 Winds

Information concerning the winds on Mars has been obtained from cloud observations and some radiometric measurements of Martian surface temperature from which a flow pattern may be derived based on meteorological principles. The first of such surface temperature and flow pattern maps was constructed by Hess [VII-54]. Other studies of the observed displacements of moving cloud systems on Mars were made by de Vaucouleurs [VII-43] and Kuiper [VII-55]. Based on the life history and motion of clouds and cloud systems, de Vaucouleurs and Kuiper obtained several interesting circulation phenomena on Mars.

Information from Martian cloud observations was also used as direct input for the theoretical study of the circulation on Mars [VII-56] in which the presence of a wave-type circulation regime was found. It has also been suggested that the mean large scale zonal and meridional wind velocities are greater than those observed on earth. A value of 100 m/s or more was obtained for the maximum surface wind, and 13 m/s for the maximum large scale vertical wind. The average zonal and meridional wind were about 25 and 1.3 m/s, respectively.

A comprehensive theoretical investigation of general circulation on Mars was recently conducted by Leovy and Mintz [VII-57] in which calculations of wind velocities were made for northern vernal equinox and southern summer solstice. Their results for the latter case indicate that the meridional component of mean wind has a strong circulation across the equator. This meridional flow has a speed of 10 m/s with the northerly wind at high altitude and the southerly wind at near-surface. Its effective region is between 25°N and 30°S latitudes. As a result of this flow pattern, the air mass is being transferred from the diminishing polar cap to the growing polar cap. The zonal component of the mean wind at near-surface is illustrated in Figure VII-4 where the easterly and westerly winds are plotted against latitudes. The mean flow in the summer hemisphere is expected to be stable and nearly undisturbed. For the winter hemisphere, however, the mean flow becomes baroclinically unstable. They also found that the maximum instantaneous near-surface wind speed occurs at 20°S latitude, and the extremely strong winds at 15-km altitude average at 40°S is about 70 m/s.

Since Mars is subject to large diurnal surface temperature changes, the diurnal variation in wind velocity may be significant. Goody [VII-30] has pointed out that the diurnal variation of wind that is caused by diurnal variation of temperature is complicated by the diurnal variations of the tropopause



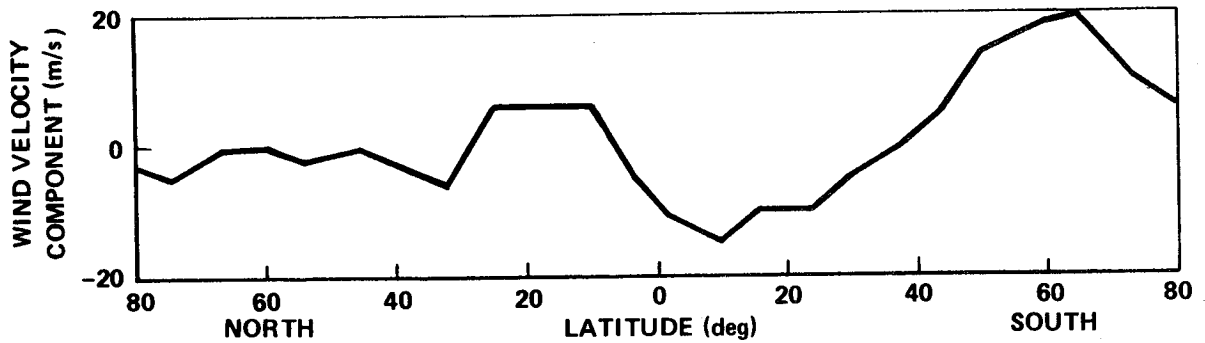


Figure VII-4. Calculated mean zonal (east-west) component of wind near surface (at top of boundary layer). (Positive values are westerlies; negative values are easterlies.) [VII-57].

height, the eddy exchange coefficient, and the unknown behavior of the atmospheric tidal energy. The magnitude of this thermally driven diurnal fluctuation in the vertical momentum exchange can cause a diurnal variation in wind velocity as large as the zonal wind itself which has a magnitude of 40 m/s [VII-58].

The vertical wind vector gradient in the Martian atmosphere has been investigated by Wood [VII-51] who took the results of wind component at two levels provided by Leovy and Mintz and assumed a linear variation of wind with height. His analysis indicates that the vertical wind vector gradient is positive from the top of the boundary layer to 15 km altitude and negative for the altitude region above 15 km. The following near-surface continuous winds are recommended for preliminary design usage.

Surface Pressure	4 mb	10 mb
Mean Speed 1 meter above surface	50 m/s	35 m/s
Peak Speed	145 m/s	100 m/s
Vertical Wind Vector Gradient	6 m/s - km*	
* This is an average wind vector gradient over the entire altitude region specified above. By earth analogy the wind vector gradient in any 1 km layer may be at least six times this value.		

#### 7.1.7 Radiation Environment

##### 7.1.7.1 Galactic Cosmic Radiation

Same as Interplanetary Space (see Paragraph 1.3.1).

#### 7.1.7.2 Solar Cosmic Radiation

Same as Interplanetary Space (see Paragraph 1.3.2).

#### 7.1.7.3 Trapped Radiation

Mariners 4, 6, and 7 measurements did not detect any trapped radiation belts beyond 4 Martian radii, which is their limit of detection.

#### 7.1.7.4 Solar Thermal Radiation

In the vicinity of Mars beyond the Martian atmosphere, the solar radiation will be assumed to have the same spectrum as that of interplanetary space. The integrated intensity will be varying from 490 to 713 W/m<sup>2</sup> [VII-60], depending on the sun-Mars distance at encounter. The significant difference between the Mars spectrum and that of the earth's atmosphere is that it does not have the absorption band in the ultraviolet region because of O<sub>3</sub> and O<sub>2</sub>. Therefore, the solar ultraviolet from 2000 to 3000 Å can penetrate the Martian atmosphere and arrive at the Martian surface.

The average annual radiation from the surface of Mars is 103 W/m<sup>2</sup> which corresponds to an average surface temperature of 206°K if the albedo of Mars is 0.295. This average surface temperature is too low as compared to the result of 220°K obtained by Öpik [VII-61]. However, the average surface temperature will be raised to 215.6°K if the albedo of Mars is 0.159.

Objects on or near the surface of Mars will receive radiation according to their shape, orientation, and distance from the surface. For a spherically shaped object, the following equation may be used to compute the incident flux:

$$Q = FAI,$$

where

Q = flux incident on sphere

F = view factor which depends on altitude

A = cross-sectional area of sphere

I = Mars thermal radiation flux (103 W/m<sup>2</sup>).

Similar equations for a cylinder, hemisphere, and a flat plate are given in Reference VII-62.

#### 7.1.7.5 Albedo Radiation

Albedo radiation varies from  $241 \text{ W/m}^2$  at 200 km to  $4 \text{ W/m}^2$  at  $2 \times 10^4 \text{ km}$  under maximum conditions (zero phase angle and normal to flux) [VII-63]. Albedo radiation will contribute about 70 percent of the total radiation from the planet upon a spacecraft if a planetary integrated albedo of 0.295 is taken. No reliable determinations of the integrated albedo of Mars are available at present; however, when separated from the total spectrum, the albedo is usually considered to be 0.159 [VII-60]. The incident albedo radiation flux,  $Q$ , can be calculated from the following equation:

$$Q = FASa,$$

where

$F$  = the view factor, which varies with altitude

$A$  = cross-sectional area of exposed spherical surface

$S$  = solar constant at Mars orbital position

$a$  = Mars albedo.

#### 7.1.7.6 Albedo

Mars traditionally has been divided into a number of areas which have been visible to the optical astronomers more or less consistently for the last century or so on the basis of albedo differences. The relative albedo range from light areas is found to be 0.18 to  $>0.3$ , and for dark areas to be  $<0.09$  to 0.18 [VII-64]. Based on these data, a contour map of the geometric albedo has been constructed [VII-40].

One should remember that the geometric albedo varies with wavelength. Harris [VII-65] has tabulated the values of geometric albedo for the wavelength from 4050 to  $6360 \text{ Å}$ . If the visual albedo is defined as the albedo at  $5500 \text{ Å}$ , then it has a value of 0.159. However, the average albedo, which is defined as the ratio of the amount of solar radiation reflected over the whole spectrum to the incident radiation, has a value of 0.295 [VII-64].

#### 7.1.7.7 Solar Constant

The solar constant is the rate at which energy is received upon a unit surface, perpendicular to the sun's direction, in free space at the Mars'

mean distance from the sun. It is generally expressed in calories per square centimeter per minute or in watts per square centimeter per minute or in watts per square meter. A recent study indicates that the solar constant for Mars is

	<u>cal/cm<sup>2</sup>min</u>	<u>W/m<sup>2</sup></u>
Perihelion	1.017	708.8
Average	0.836	582.8
Aphelion	0.699	487.0

These values were obtained based on the value of solar constant at 1 AU being 1.94 cal/cm<sup>2</sup> min.

#### 7.1.8 Meteoroid Environment

##### 7.1.8.1 Cometary Meteoroid Flux

The flux ( $F_c$ ), in number per square meter per second, of cometary meteoroids of mass  $m$  on a randomly tumbling surface is [VII-66]: For  $10^{-6} \leq m \leq 10^2$ ,

$$\begin{aligned} \log F_c = & -14.851 - 1.213 \log m + \log \left( 1 + \frac{0.233}{r} \right) \\ & + \log \frac{1}{2} \left[ 1 + \left( 1 - \frac{1}{r^2} \right)^{1/2} \right] + \log V_c . \end{aligned}$$

For  $10^{-12} \leq m \leq 10^{-6}$ ,

$$\begin{aligned} \log F_c = & -14.820 - 1.584 \log m - 0.063 (\log m)^2 \\ & + \log \left( 1 + \frac{0.233}{r} \right) + \log \frac{1}{2} \left[ 1 + \left( 1 - \frac{1}{r^2} \right)^{1/2} \right] \\ & + \log V_c , \end{aligned}$$

where

$V_c$  = average cometary velocity relative to spacecraft in meters per second

$r$  = distance of the spacecraft from the center of the planet (in units of the planet's radius).

#### 7.1.8.2 Average Velocity of Cometary Meteoroids

The average velocity of cometary meteoroids relative to the spacecraft is 15.74 km/s [VII-66].

#### 7.1.8.3 Survival Mass

The survival mass for micrometeoroids can be calculated as a function of height in the atmosphere by using the following approximate expression [VII-63]:

$$m^{1/3} = m_{\infty}^{1/3} = \frac{\Lambda A \rho_m^{-2/3} v^2}{6 \xi \cos Z} \int_{\infty}^h \rho_a dh \quad (\text{does not hold for dustballs})$$

where

$$\text{columnar mass} = - \int_h^{\infty} \rho_a dh$$

$z$  = zenith angle

$\rho_m$  = density of micrometeoroid ( $3.5 > \rho_m > 0.5 \text{ g/cm}^3$ )

$v$  = velocity of micrometeoroid ( $v_{\text{parabolic}}$  or  $v_{\text{orbital}}$ )

$> v > v_{\text{escape}}$ )

$A$  = shape factor = 1.2 for sphere

$$\Lambda / \xi = 10^{-11.449}.$$

### 7.1.9 Geomagnetic Environment

#### 7.1.9.1 Magnetic Field

The results of Mariners 4, 6, and 7 magnetometer measurements indicate the field strength to be less than 0.001 of the earth's magnetic field. From this, it is inferred that the magnetic moment of Mars is less than 0.001 that of the earth and that the equatorial surface magnetic field of Mars is less than 200  $\gamma$ .

#### 7.1.10 Astrodynamic Constants

##### 7.1.10.1 Mars Constants (Epoch 1960.0) [VII-67]

Distance from sun (average)	$2.2794 \times 10^8$ km or 1.5236915 AU
Eccentricity of orbit <sup>2</sup>	0.0933681
Inclination of orbit to ecliptic <sup>2</sup>	1° 50' 59.8"
Orbital period (sidereal) <sup>2</sup>	686.97971 days
Radius (equatorial)	3393.4 km
Mass ratio (sun/planet)	3 098 700 $\pm$ 100
Mass ratio (Mars/earth)	0.1074469
Flattening (dynamic) <sup>2</sup>	1:190.5
Average density <sup>2</sup>	3.879 g/m <sup>3</sup>
Rotational period	24 hr 37 min 22.6689 s
Gravitational parameter	$4.28284 \times 10^4$ km <sup>3</sup> /s <sup>2</sup>
Mean orbital velocity	24.13 km s <sup>-1</sup>

---

2. Krause, H. G. L.: Astronomical Constants of the Solar System. 1965 (unpublished).

#### 7.1.10.2 Gravitational Potential

If Mars is considered to be an oblate spheroid, its gravitational potential function can readily be developed in a spherical harmonic series. Truncating after the first two terms, the gravitational potential function can be expressed as [VII-66]:

$$\phi(R, \theta) = \frac{GM}{R} \left[ 1 - J_2 (R_E/R)^2 P_2^0 \right]$$

and the radial acceleration of gravity as

$$g = -\frac{\partial \phi}{\partial R} = \frac{GM}{R^2} \left[ 1 - 3J_2 (R_E/R)^2 P_2^0 \right]$$

in which

$$P_2^0 = \frac{3}{2} \sin^2 \theta - \frac{1}{2}$$

$\theta$  = latitude

$R_E$  = equatorial radius = 3393.4 km

$GM = 42\,828.4 (\pm 1.4) \text{ km}^3/\text{s}^2$

$J_2 = 0.00197 (\pm 0.00002)$

$R$  = distance from center of Mars (km).

The centrifugal correction to the radial component of gravitational acceleration can be expressed as

$$F_c = \omega^2 R \cos^2 \theta$$

in which  $\omega$  is the Martian angular velocity,  $0.7088218 \times 10^{-4}$  rads/s.

### 7.1.11 Additional Information

A more detailed description of the Mars atmosphere is given in References VII-18, VII-40, VII-63, and VII-68.

## 7.2 Surface Environment

Our present knowledge of the surface environment on Mars comes from earth-based radar and telescopic measurements as well as observations made by Mariners 4, 6, and 7 spacecraft. Because there are only limited information available from these sources, studies of the Martian surface environment are also based on analogy with lunar surface data.

In principle, the radar ranging technique measures the total time required for a radar signal to travel to and from Mars. The variations in the transit time are recorded which are then interpreted as the result solely due to differences in Martian surface elevation. Recent radar measurements have yielded reasonable good results; however, only a narrow latitude band covering 5°N to 25°N has been measured. On the other hand, the telescopic method is easy to operate, but it is limited by the effective optical resolution of available telescopes.

Since spectroscopic measurement and Mariner TV picture became available, data concerning the Martian surface environment have been greatly increased. The following information is based on data obtained from all available sources.

### 7.2.1 Mechanical Properties

#### 7.2.1.1 Surface Roughness

The surface of Mars is covered by numerous meteoritic impact craters, which have a surface roughness with a wavelength of about 1 m at the crater rims [VII-69]. The power spectral density of surface roughness is given in Figure VII-5.

#### 7.2.1.2 Elevations

Differences in elevation between crater floors and surrounding terrain may be as much as 500 m and the difference between crater walls and surrounding terrain as much as 100 m. Crevices and fissures may be



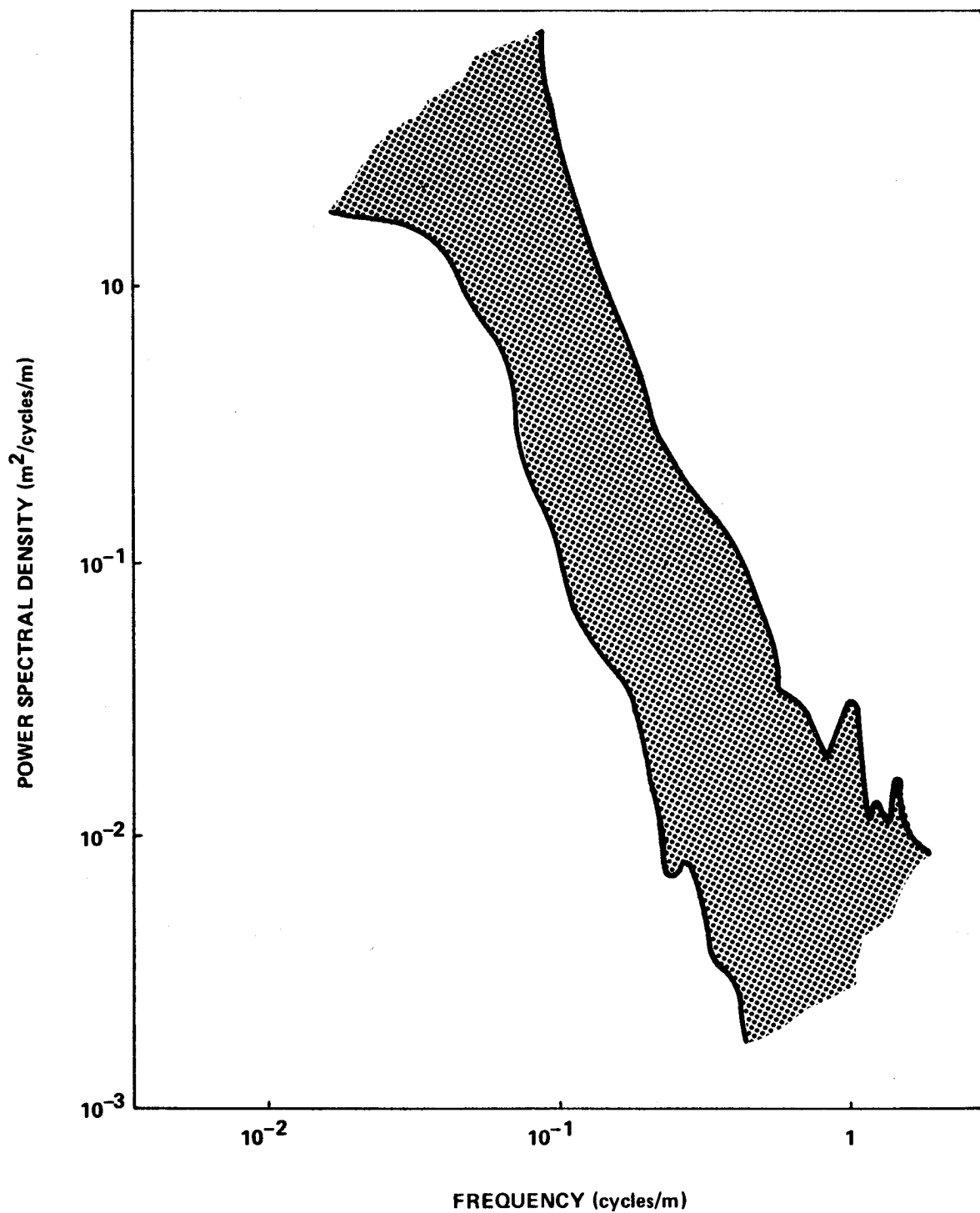


Figure VII-5. Power spectral density function band for Martian surface.

as deep as 25 m, while grabens may have depths up to 1.5 km. Mountain peak heights may exceed 10 km [VII-62].

Further evidence of large elevation differences of up to 11 km has been found along 21.5°N latitude from radar ranging data [VII-70]. The highest areas observed are definitely desert regions, while the Maria lie in low areas or on slopes. The canals identified in the radar ranging data all occur in broad and frequently deep valleys.

Other measurements made by radar ranging technique have been reported by Pettengil, et al. [VII-71] and Rogers, et al. [VII-72]. Their results are summarized in Figure VII-6 where the Martian topographical variations along four latitude circles are shown.

#### 7.2.1.3 Slopes

Radar doppler shift observations indicate a relatively smooth surface on Mars, with an rms slope of about 5 deg on the meter scale [VII-73, VII-74]. Mariner 4 photography suggests an rms slope of about 3 deg on a scale of 3 km or greater [VII-75]. More recent radar observations show that the steepest average slope between points several degrees longitude apart, that is on the order of hundred kilometers, is about 0.5 deg [VII-18].

#### 7.2.1.4 Craters

Early results of television pictures taken by Mariner 4 spacecraft revealed that the surface of Mars was heavily cratered and resembled that of the moon. This discovery was confirmed by pictures taken by the Mariners 6 and 7 cameras, but also revealed distinct differences between Mars and the moon. Preliminary results indicate that at least three distinctive terrains are present on the Martian surface. These are cratered terrain, chaotic terrain, and featureless terrain [VII-33].

Craters with diameter ranging from a few meters to several kilometers are shown on the Mariners 4, 6, and 7 pictures. Two morphological crater types with one large size and flat-bottomed and one small size and bowl-shaped were found. It was also found that large variations in crater morphology exist among different crater terrains. The diameter-frequency distribution is given for the moon and for Mars in Figure VII-7.

#### 7.2.1.5 Particle Size

The particle size distribution is illustrated in Figure VII-8.

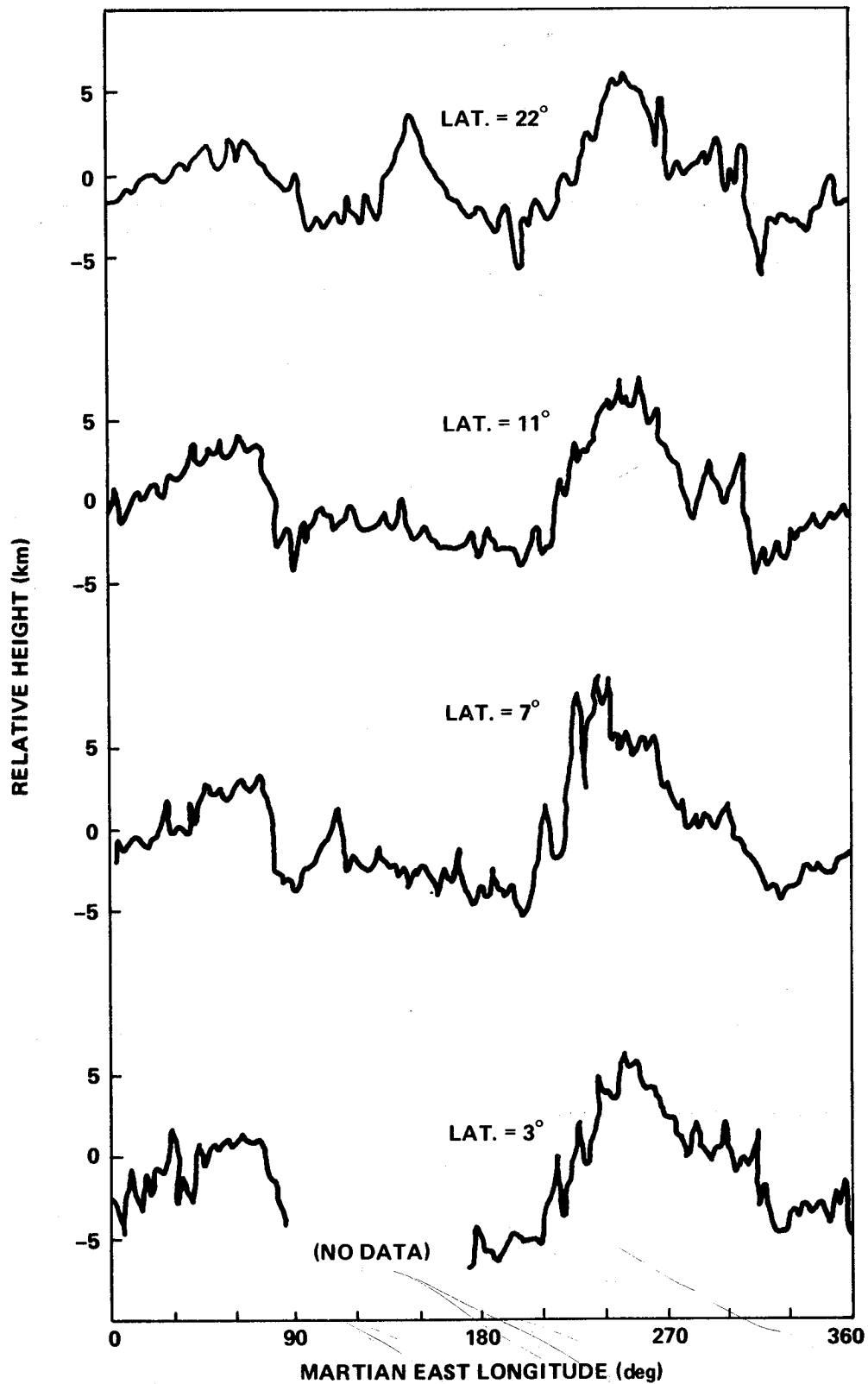


Figure VII-6. Mars topographical variation from radar measurements centered about four latitudes [VII-18].

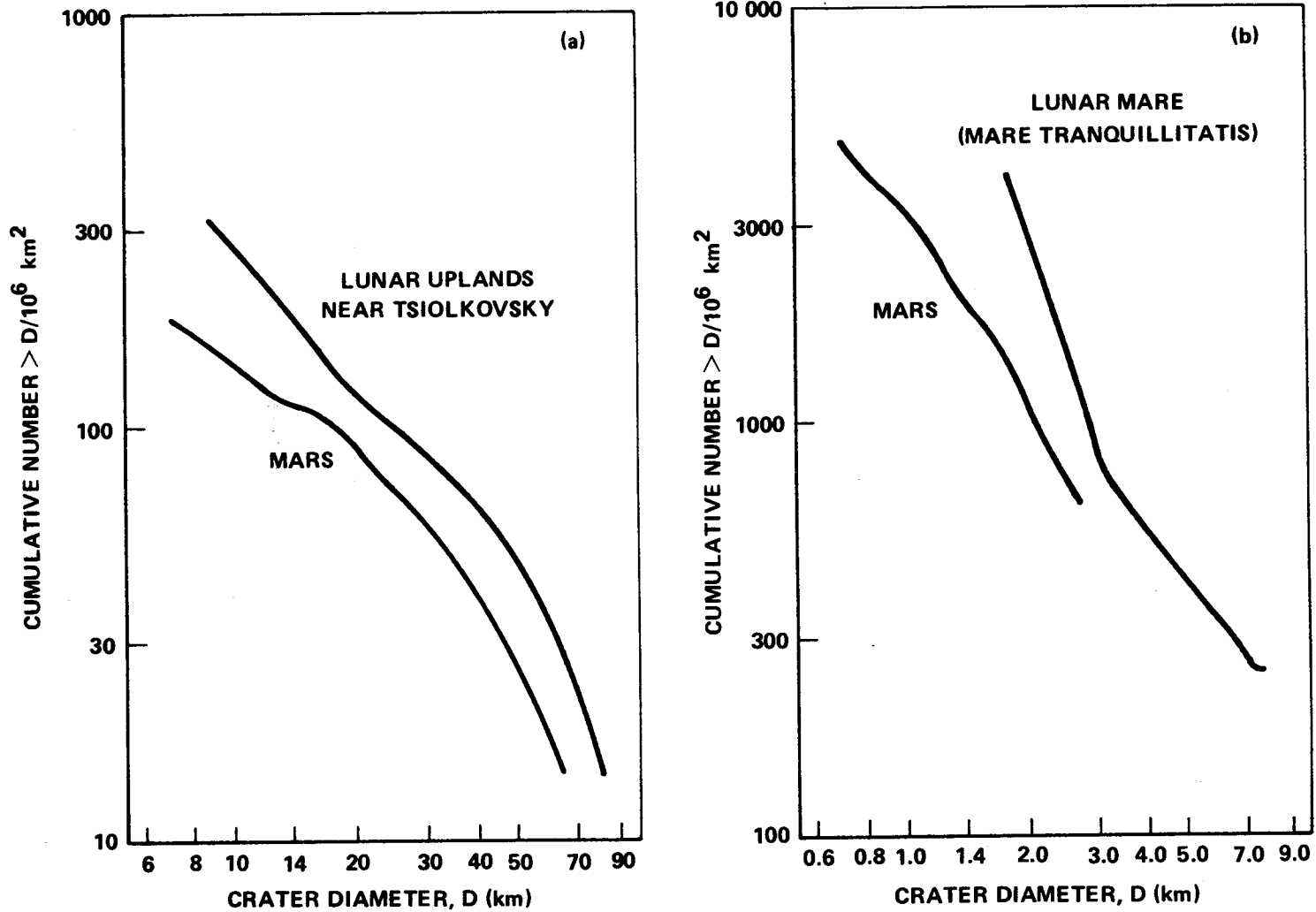


Figure VII-7. Comparisons of Martian and Lunar size distributions: (a) comparison of large craters on Mars with those on the Lunar Uplands, and (b) comparison of small craters on Mars with those on the Lunar Maria.

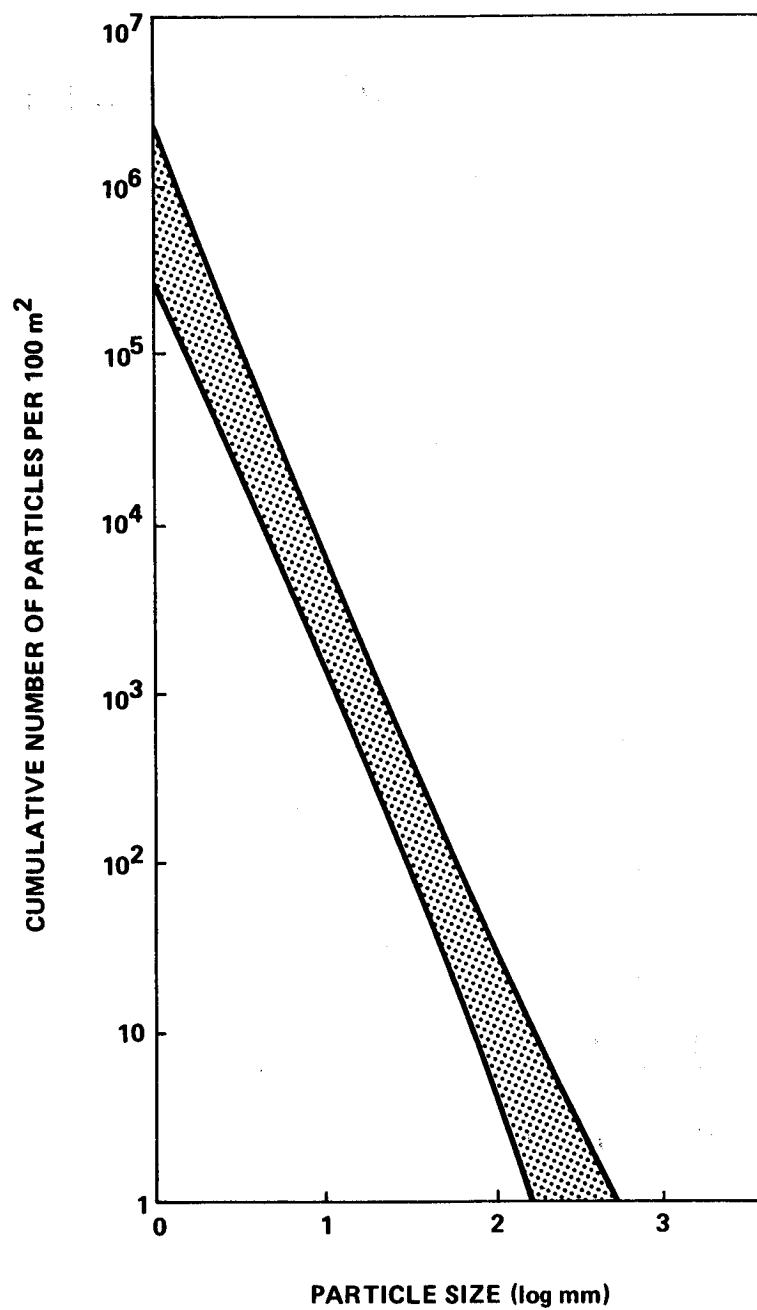


Figure VII-8. Size-frequency distribution on the undisturbed surface [VII-69].

#### 7.2.1.6 Composition

The majority of the rocks are basaltic in nature. The oxides are distributed among compounds by the following percentage ranges:

$\text{SiO}_2$  - 45 to 60

$\text{TiO}_2$  - 0.8 to 2

$\text{Al}_2\text{O}_3$  - 8 to 18

$\text{Fe}_2\text{O}_3$  - 2 to 4

$\text{FeO}$  - 3 to 10

$\text{MnO}$  - 0.2 to 2

$\text{MgO}$  - 3 to 22

$\text{CaO}$  - 6 to 8

$\text{Na}_2\text{O}$  - 2 to 4

$\text{K}_2\text{O}$  - 0.4 to 2

$\text{P}_2\text{O}_5$  - 0.2 to 3.

In decreasing order of abundance, the major mineral compounds present are feldspar (approximately 60 percent of the rock), pyroxenes, olivines, amphiboles, quartz, magnetite, nephelite, and apatite. The presence of limonite or goethite (between 2 and 10 percent) is limited to coatings on surface materials. Some minor amounts of clays, hydroxides of aluminum and iron, and minute amounts of siderite are expected.

#### 7.2.1.7 Other Mechanical Properties of the Martian Surface

The applicable values for the density, porosity, cohesion, Terzaghi soil constants, bearing capacity, Bekker modulus of deformation, sinkage exponent, angle of internal friction, median slopes and slope stability limit, elevation, crater diameters, dust storms velocities, and durations are indicated in Table VII-6.

TABLE VII-6. MECHANICAL PROPERTIES OF MARTIAN  
SURFACE [VII-69]

Properties	Values	
	Bright Areas	Dark Areas
Density ( $\text{g cm}^{-3}$ )	0.6 to 1.9	0.9 to 2.9
Porosity of Combined Top Few cm (%)	15 to 55	15 to 55
Cohesion ( $\text{dyne cm}^{-2}$ )	0 to 100	0 to 100
Soil Stability Factor for Level Ground		
$N_{\gamma}$	10 to 40	10 to 40
$N_Q$	15 to 40	15 to 40
$N_c$	25 to 55	25 to 55
Bearing Capacity Minimum for 10 cm Radius Circular Plate ( $\text{dyne cm}^{-2}$ )	$3 \times 10^5$	$1.3 \times 10^6$
Modulus of Deformation		
$k_{\phi}$	0.5 to 3.5	0.45 to 6
$k_c$	0	0
Sinkage Exponent $\eta$	0.5 to 1.5	1.1 to 1.25
Angle of Internal Friction (deg)	25 to 35	25 to 35
Slope Stability for Cohesionless Soil (deg)	25 to 35	25 to 35
Median Slopes (Fig. VII-9), deg	5 to 7	9 to 11
Average Elevations (km)	-1 to +1	
Elevations in Equatorial Regions (km)		2 to 6
Circular Hellas Type Region Elevation (km)		1 to 2
Average Crater Diameter (km)	3 to 175	3 to 175
Permafrost Elevations (m)	0 to 0.5	0 to 0.5
Dust Storm Speeds ( $\text{km hr}^{-1}$ )	40 to 100	40 to 100
Average Duration of Dust Storms (deg)	2 to 4	2 to 4

### 7.2.2 Electrical Properties [VII-69]

Properties	Values	
	Bright Areas	Dark Areas
Dielectric Constant	1.9 to 8.3	2.4 to 6.4
Dielectric Constant Uppermost Layer	1.5 to 2	1.5 to 2
Tangent Dielectric Loss Angle	0.01 to 0.15	0.001 to 0.15

### 7.2.3 Thermal Properties [VII-69]

Properties	Values		Units
	Bright Areas	Dark Areas	
Thermal Conductivity	$4 \times 10^{-4}$ to $6 \times 10^{-3}$	$4 \times 10^{-4}$ to $6 \times 10^{-3}$	$\text{g cal cm}^{-1} \text{s}^{-1} \text{ } ^\circ\text{K}^{-1}$
Specific Heat	0.17 to 0.19	0.17 to 0.19	$\text{g cal cm}^{-1} \text{ } ^\circ\text{K}^{-1}$ at $0^\circ\text{C}$
Emissivity	0 to 0.8	0 to 0.6	

### 7.2.4 Optical Thickness

The atmosphere of Mars shall be considered to be a plane-parallel, nonabsorbing Rayleigh atmosphere with the optical thickness given below [VII-18]:

<u>Optical Thickness (<math>\tau</math>)</u>	<u>Wavelength (<math>\lambda</math>)</u>
0.100	0.250
0.050	0.300
0.020	0.350
0.010	0.425
0.008	0.450
0.005	0.500



### 7.2.5 Surface Spectral Albedo

The spectral albedo of the surface is expressed as the product of two factors: (1) the relative spectral reflectance of the Mars surface which was obtained by combining the values obtained by Tull and Öpik, and (2) the highest value of spectral albedo for three representative areas [VII-18]:

$$P_{\lambda} = \bar{R}_{\lambda} N,$$

where

$P_{\lambda}$  = surface spectral albedo

$\bar{R}_{\lambda}$  = relative spectral reflectance

$$\bar{R}_{\lambda} = R_{\lambda} / R_{\lambda_{\max}}$$

$R_{\lambda}$  = surface spectral reflectance

$N$  = surface spectral reflectance at  $R_{\lambda_{\max}}$ . Values for  $N$

are as follows:

$$N_L = 0.300 \text{ for light areas}$$

$$N_I = 0.225 \text{ for intermediate areas}$$

$$N_D = 0.150 \text{ for dark areas.}$$

Values for  $\bar{R}_{\lambda}$  are given below:

$\lambda$	$\bar{R}_{\lambda}$	$\lambda$	$\bar{R}_{\lambda}$
0.20	0.010	0.70	0.950
0.30	0.130	0.80	1.000
0.40	0.260	0.90	0.990
0.50	0.410	1.00	0.950
0.60	0.650	1.10	0.963

#### 7.2.6 Surface Photometric Function

The Martian photometric model should be assumed to be very similar to that given for the moon in Section IV.

#### 7.2.7 Surface Temperature

Seasonal maps of the Martian daytime ground-surface temperatures are shown in Figures VII-9 [VII-1]. Seasonal differences noted in these maps are due primarily to the eccentricity of the Mars orbit. Since the southern summer solstice occurs near perigee and the northern summer solstice occurs near apogee, the warm season in the southern hemisphere is shorter and hotter than in the northern hemisphere. The length of seasons and the heliocentric longitudes are given below.

Length of Seasons for Various Heliocentric Longitudes

Heliocentric Longitude	Northern Hemisphere	Southern Hemisphere	Duration	
			Earth Days	Mars Days
87 to 177	Spring	Autumn	199	194
177 to 267	Summer	Winter	182	177
267 to 357	Autumn	Spring	146	142
357 to 87	Winter	Summer	160	156

The daily temperature variation to be expected on the Martian surface near the equator is given in Figure VII-10.

#### 7.2.8 Additional Information

A more complete description of the Martian surface is given in References VII-33 and VII-69.

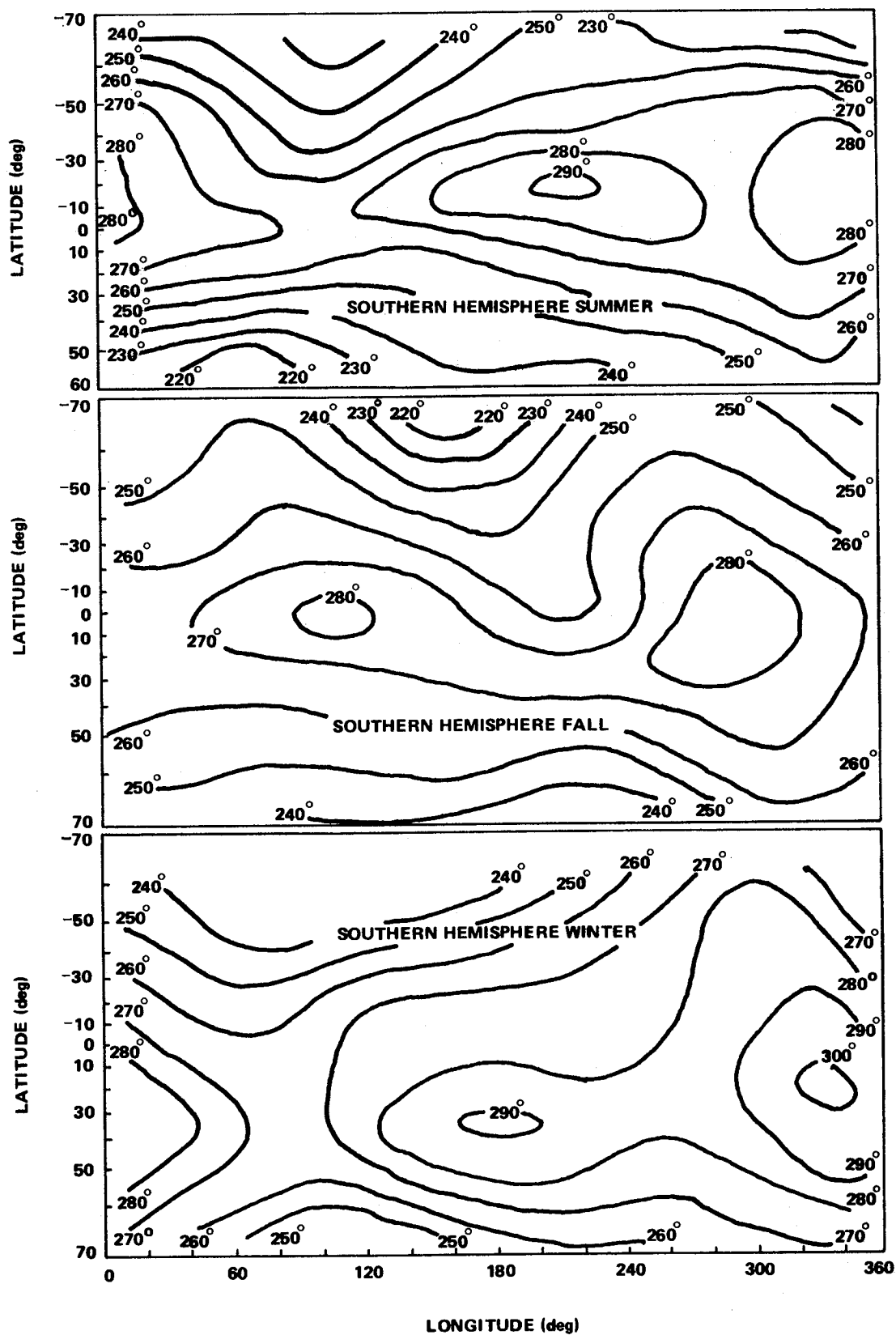


Figure VII-9. Seasonal mean surface temperatures on Mars [VII-1].

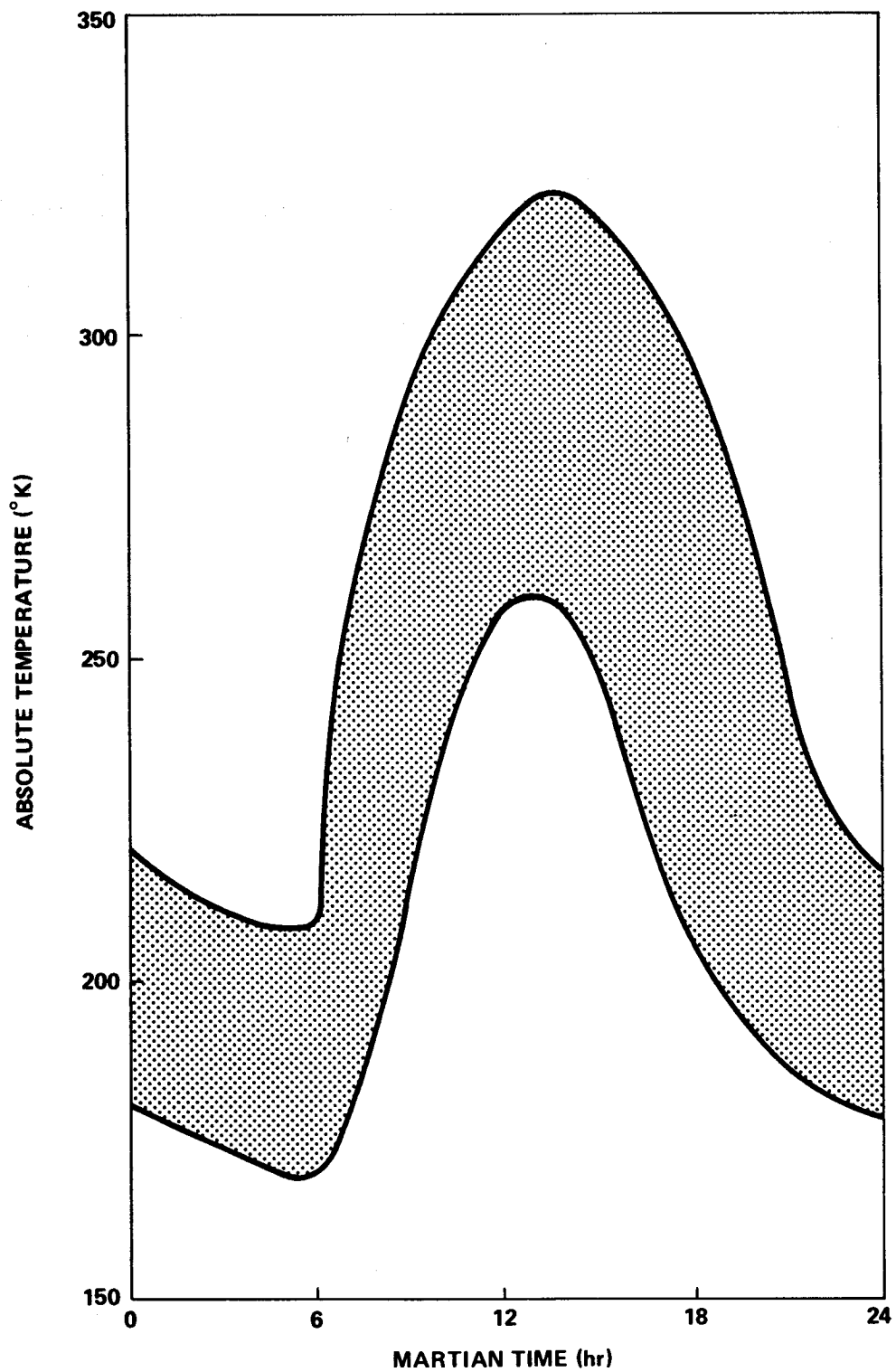


Figure VII-10. Daily temperature variation of surface of Mars at the equator [VII-69].

## 7.3 Satellites

Mars has two known satellites: Phobos and Deimos. Phobos, the larger of the two, has a period of rotation about one-third that of Mars. Thus, Phobos appears to be in retrograde motion as seen from the surface of Mars, though actually it is not (Phobos will rise in the west and set in the east). Deimos, very nearly a synchronous satellite, will rise in the east very slowly and almost half of its phases will be visible in one night, as seen from the surface of Mars. However, both satellites are small, and will appear only as bright stars, Phobos being the brighter of the two. The results of searches for other moons disclosed no detectable satellites. However, objects less than  $1.609 \times 10^5$  cm (1 mile) in diameter would not have been detected. Data for satellites of Mars are summarized in Table VII-7.

TABLE VII-7. DATA SUMMARY FOR SATELLITES OF MARS<sup>a</sup>

Satellite	Discovery		Siderial Period of Revolution ( $P_{sid}$ )		Mean Synodic Period of Revolution ( $P_{syn}$ )		Orbital Mean Motion, $P_{sid}$ ( $^{\circ}/d$ )	Eccen- tricity ( $e$ )
	Discoverer	Date	d	mean solar time	d	mean solar time		
II Phobos	A. Hall	17 Aug. 1877	0.31891031	0 07 39 13.851	0.3190585	0 07 39 26.65	1128.84402	0.021
I Deimos	A. Hall	11 Aug. 1877	1.26244064	1 06 17 54.871	1.2647648	0 06 21 15.68	285.16192	0.002

Satellite	Apparent Distance			Mean Distance from Planet ( $a$ )			Inclination of Orbit to Planet's Equator ( $g$ )	Visual Magnitude at Mean Opposi- tion Distance ( $m_{viz}$ )	Radius, $R$ (km)
	At Unit Distance	As Seen From Sun	At Mean Opposition	( $10^{-3}$ AU)	( $10^3$ km)	In Eq. Radii of the Primary			
II Phobos	12.938	8.491	24.705	0.062725	9.384	2.747	$0^{\circ}57'$	11.6	8
I Deimos	32.373	21.246	61.817	0.15695	23.479	6.873	$1^{\circ}18'$	12.8	4

a. Krause, H. G. L.: Astronomical constants of the Solar System. 1965 (unpublished).

## REFERENCES

- VII-1. Gifford, F. Jr.: The Surface Temperature Climate of Mars. *Astrophys. J.*, vol. 123, January - May 1956, pp. 154-60.
- VII-2. Neubauer, F. M.: Thermal Convection in the Martian Atmosphere. *J. G. R.*, vol. 71, May 15, 1966, p. 2419.
- VII-3. Ohring, G.: A Theoretical Estimate of the Average Vertical Distribution of Temperature in the Martian Atmosphere. *ICARUS*, vol. 1, 1963, pp. 328-33.
- VII-4. House, F. B.: The Seasonal Climatology of Mars. Contribution to Planetary Meteorology, GCA Technical Report No. 66-8-N, March 1966.
- VII-5. Ohring, G., and Mariano, J.: Seasonal and Latitudinal Variations of the Average Surface Temperature Profile of Mars. GCA Technical Report 67-5-N, March 1967.
- VII-6. Leovy, C.: Radiative-Convective Equilibrium Calculations for a Two-Layer Mars Atmosphere. Rand Memo RM-5017, 1966.
- VII-7. Lou, Y. S., and Hung, F. T.: A Method For the Prediction of the Martian Temperature and Some Applications of Meteorological Analysis. Proceedings, Third National Conference on Aerospace Meteorology, American Meteorological Society, 1968, pp. 237-46.
- VII-8. Lou, Y. S., Weidner, D. K., Vaughan, O. H., and West, G. S.: Martian Predictions. *Science*, vol. 165, no. 3890, 1969, p. 234.
- VII-9. Lou, Y. S.: Martian Surface Temperature and Polar Cap Predictions for Mariner V and VII Encounters. Northrop-Huntsville TR-793-9-618, 1969.
- VII-10. Lou, Y. S.: Prediction of the Martian Atmosphere for Mariner VI and VII Occultations. Northrop-Huntsville TR-793-9-632, 1969.
- VII-11. Johnson, F. S.: Atmosphere of Mars. *Science*, vol. 150, 1965, pp. 1445-1448.

## REFERENCES (Continued)

- VII-12. Chamberlain, J. W., and McElroy, M. B.: Martian Atmosphere: The Mariner IV Occultation Experiment. *Science*, vol. 152, no. 3718, 1966, pp. 21-25.
- VII-13. Fjeldbo, G., Fjeldbo, W. C., and Eshleman, V. R.: Models for the Atmosphere of Mars Based on the Mariner IV Occultation Experiment. *J. G. R.*, vol. 71, no. 9, 1966, pp. 2307-2316.
- VII-14. Fjeldbo, G., Fjeldbo, W. C., and Eshleman, V. R.: Atmosphere of Mars: Mariner IV Models Compared. *Science*, vol. 153, 1966, pp. 1518-1523.
- VII-15. Smith, N., and Beutler, A.: A Model Martian Atmosphere and Ionosphere. Report 66-3, University of Michigan, Ann Arbor, Michigan, 1966.
- VII-16. Kliore, A., Fjeldbo, G., and Seidel, B. L.: Mariner 6 and 7: Radio Occultation Measurements of the Atmosphere of Mars. *Science*, vol. 166, 1969, pp. 1393-1397.
- VII-17. Rasool, S. I., Hogan, J. S., and Stewart, R. W.: Temperature Distributions in the Lower Atmosphere of Mars from Mariner 6 and 7 Radio Occultation Data. *J. Atm. Sci.*, vol. 27, 1970, pp. 841-843.
- VII-18. Mars Engineering Model. NASA Langley Research Center, Viking Project Office M75-125-1, December 1970.
- VII-19. Anderson, A. D.: A Model for the Lower Atmosphere of Mars Based on Mariner IV Occultation Data. Lockheed Palo Alto Research Lab. Tech. Memo 6-75-65-62, 1965.
- VII-20. Kaplan, L. D., Munch, G., and Spinrad, H.: An Analysis of the Spectrum of Mars. *Astrophys. J.*, vol. 139, 1964, p. 1.
- VII-21. Gray, L. D.: Transmission of the Atmosphere of Mars in the Region of  $2\mu$ . *ICARUS*, vol. 5, 1966, p. 390.
- VII-22. Belton, M. J. S., and Hunten, D. M.: The Abundance and Temperature of  $\text{CO}_2$  in the Martian Atmosphere. *Astrophys. J.*, vol. 145, 1966, p. 454.



## REFERENCES (Continued)

- VII-23. Stewart, R. W., and Hogan, J. S.: Solar Cycle Variation of Exospheric Temperature on Mars and Venus: A Prediction for Mariner 6 and 7. *Science*, vol. 165, 1969, pp. 386-387.
- VII-24. Owen, T. C.: The Composition and Surface Pressure of the Martian Atmosphere Results from the 1965 Opposition. *Astrophys. J.*, vol. 146, 1966, p. 257.
- VII-25. Spinrad, H., Schorn, R. A., Moore, R., Giver, L. P., and Smith, H. J.: High-Dispersion Spectroscopic Observations of Mars: I. The CO<sub>2</sub> Content and Surface Pressure. *Astrophys. J.*, vol. 146, 1966, p. 331.
- VII-26. Belton, M. J. S., Broadfoot, A. L., Hunten, D. M.: Abundance and Temperature of CO<sub>2</sub> on Mars During the 1967 Opposition. *J. G. R.*, vol. 73, no. 15, 1968, pp. 4795-4806.
- VII-27. Giver, L. P., Inn, E. C. Y., Miller, J. H., and Boese, R. W.: The Martian CO<sub>2</sub> Abundance From Measurements in the 1.05 $\mu$  Band. *Appl. J.*, vol. 153, no. 1, 1968, pp. 285-289.
- VII-28. Carleton, N. P., Sharma, A., Goody, R. M., Liller, W. L., and Roseler, F. L.: Measurement of the Abundance of CO<sub>2</sub> in the Martian Atmosphere. *Appl. J.*, vol. 155, no. 1, 1969, pp. 323-331.
- VII-29. Young, L. D. G.: Interpretation of High Resolution Spectra of Mars, I. CO<sub>2</sub> Abundance and Surface Pressure Derived From the Curve of Growth. *ICARUS*, vol. 11, no. 3, 1969, pp. 386-389.
- VII-30. Goody, R.: The Atmospheres of Mars and Venus. *Naturwissenschaften*, vol. 57, no. 1, 1970, pp. 10-16.
- VII-31. Kaplan, L. D., Connes, J., and Connes, P.: Carbon Monoxide in the Martian Atmosphere. *Appl. J.*, vol. 157, no. 3, 1969, pp. 187-192.
- VII-32. Fjeldbo, G., and Eshleman, V. R.: The Atmosphere of Mars Analyzed by Integral Inversion of the Mariner IV Occultation Data. *Planet Space Sci.*, vol. 16, no. 8, 1968, pp. 1035-1059.

## REFERENCES (Continued)

- VII-33. Mariner-Mars 1969 - A Preliminary Report. NASA SP-225, 1969.
- VII-34. Herr, K. C., Horn, D., McAfee, J. M., and Pimentel, G. C.: Martian Topography from the Mariner 6 and 7 Infrared Spectra. *Astron. J.*, vol. 75, no. 8, 1970, pp. 883-894.
- VII-35. Spinrad, H., Munch, G., and Kaplan, L. D.: The Detection of Water Vapor on Mars, *Astrophys. J.*, vol. 137, 1963, p. 1319.
- VII-36. Dollfus, C. R.: Analyse des Mesured de la quantite de Vapeur d'eau dans l'atmosphere de la planete Mars. *Acad. Sci., Paris*, vol. 261, p. 1603.
- VII-37. Schorn, R. A., Spinrad, H., Moore, R. C., Smith, H. J., and Giver, L. P.: High-Dispersion Spectroscopic Observations of Mars: II. The Water Vapor Variations. *Astrophys. J.*, vol. 147, 1967, p. 743.
- VII-38. Tull, R. G.: High-Dispersion Spectroscopic Observations of Mars IV. The Latitudinal Distribution of Atmospheric Water Vapor. *ICARUS*, vol. 13, no. 1, 1970, pp. 43-57.
- VII-39. Schorn, R. A., Farmer, C. B., and Little, S. J.: High-Dispersion Spectroscopic Studies of Mars: III. Preliminary Results of 1968-1969 Water Vapor Studies. *ICARUS*, vol. 11, no. 3, 1969, pp. 283-288.
- VII-40. Mars Scientific Model. JPL Report No. 606-1, 1968.
- VII-41. Spencer, D. F.: Our Present Knowledge of the Martian Atmosphere. AIAA/AAS Stepping Stones to Mars Meeting, Baltimore, Maryland, March 1966.
- VII-42. Hess, D. S., and Pounder, E.: Voyager Environmental Predictions Document. SE003BB001-IB28, NASA-JPL, October 1966.
- VII-43. de Vaucouleurs, G.: Physics of the Planet Mars. London: Faber & Faber, 1954.

## REFERENCES (Continued)

- VII-44. Chamberlain, J. W., and Hunten, D. M.: Pressure and CO<sub>2</sub> Content of the Martian Atmosphere: A Critical Discussion. Review of Geophysics, vol. 3, 1965, p. 299.
- VII-45. Corlin, W. R.: Space Problems and Planetary Exploration. New York: D. Van Nostrand Company, Inc., 1965.
- VII-46. Kaula, W. M.: An Introduction to Planetary Physics. New York: John Wiley & Sons, Inc., 1968.
- VII-47. Grandjean, J., and Goody, R. M.: The Concentration of Carbon Dioxide in the Atmosphere of Mars. Astrophys. J., vol. 121, 1955, p. 548.
- VII-48. Goody, R. M.: The Atmosphere of Mars. Weather, vol. 12, 1957, p. 3.
- VII-49. Musman, S.: An Upper Limit to a Rayleigh Scattering Atmosphere on Mars. Planet. Space Sci., vol. 12, 1964, p. 799.
- VII-50. Evans, D.: Ultraviolet Reflectivity of Mars. Science, vol. 149, 1965. p. 969.
- VII-51. Wood, G. P.: Mars Environment. Mars Engineering Model for Viking 75 Project, NASA Langley Research Center M75-125-1, 1970.
- VII-52. Mass Atmosphere Definition Final Report: Voyager Spacecraft. NASA CR-61185, 1968.
- VII-53. Fjeldbo, G., Kliore, A., and Seidel, Boris: The Mariner 1969 Occultation Measurements of the Upper Atmosphere of Mars. Radio Science, vol. 5, 1970, pp. 381-386.
- VII-54. Hess, S. L.: Some Aspects of the Meteorology of Mars. J. Meteor., vol. 7, 1950, pp. 1-13.
- VII-55. Kuiper, G. P.: Visual Observations of Mars, 1956. Appl. J., vol. 156. 1957, pp. 307-317.

## REFERENCES (Continued)

- VII-56. Tang, W.: Some Aspects of the Atmospheric Circulation on Mars. NASA CR-262, 1965.
- VII-57. Leovy, C. B., and Mintz, Y.: Numerical Simulation of the General Atmospheric Circulation and Climate on Mars. *J. Atm. Science*, vol. 26, no. 6, 1969, pp. 1167-1190.
- VII-58. Gierasch, P., and Goody, R.: A Study of the Thermal and Dynamical Structure of the Martian Lower Atmosphere. *Planet. Space Sci.*, vol. 16, no. 5, 1968, pp. 615-646.
- VII-59. Henry, R. M.: Wind and Gust Design Criteria for the Martian Atmosphere. *Proceedings, Third National Conference on Aerospace Meteorology*, New Orleans, La., 1968, pp. 356-360.
- VII-60. Lave, E. G., and Drummon, A. J.: Solar Constant: First Direct Measurements. *Science*, vol. 161, 1968, pp. 888-891.
- VII-61. Öpik, E. J.: The Martian Surface. *Science*, vol. 153, no. 3733, 1966, pp. 255-265.
- VII-62. Michaux, C. M.: Handbook of the Physical Properties of the Planet Mars. NASA SP-3030, 1967.
- VII-63. Evans, D. E., Pitts, D. E., and Krause, G. L.: Venus and Mars Nominal Natural Environment for Advanced Manned Planetary Mission Programs. NASA SP-3016, 1965.
- VII-64. de Vaucouleurs, G.: Geometric and Photometric Parameters of the Terrestrial Planets. *ICARUS*, vol. 3, 1964, pp. 187-235.
- VII-65. Harris, D.: Photometry and Colorimetry of Planets and Satellites. *Planets and Satellites*, G. P. Kuiper and B. M. Middlehurst (Eds.) Chicago: University of Chicago Press, 1961, pp. 272-342.
- VII-66. Weidner, D. K. (Ed.): Space Environment Criteria Guidelines for Use in Space Vehicle Development (1969 Revision). NASA TM X-53957, August 20, 1970.

## REFERENCES (Concluded)

- VII-67. Melbourne, W. G., Mulholland, J. D., Sjogren, W. L., and Sturms, F. M.: Constants and Related Information for Astrodynamic Constants. 1968, JPL Technical Report 32-1306, 1968.
- VII-68. Brandt, J. C., and McElroy, M. B.: The Atmospheres of Venus and Mars. New York: Gordon and Breach Science Publishing, Inc., 1968.
- VII-69. The Surface of Mars. NASA SP-8020, 1969.
- VII-70. Binder, A. B.: Topography and Surface Features of Mars. ICARUS, vol. 11, 1969, pp. 24-35.
- VII-71. Pettengill, G. H., Counselman, C. C., Rainville, L. P., and Shapiro, I. I.: Radar Measurements of Martian Topography. Astron. J., vol. 74, 1969, pp. 461-482.
- VII-72. Rogers, A. E., Pettengill, G. H., Shapiro, I. I., Ash, M. E., and Counselman, C. C.: Radar Studies of Mars. Final Report, Lincoln Laboratory, MIT, 1970.
- VII-73. Goldstein, R. M., and Gilmore, W. F.: Radar Observations of Mars. Science, vol. 141, 1963, pp. 1171-1172.
- VII-74. Dyce, R. B., Pettengill, G. H., and Sanchez, A. D.: Radar Observations of Mars and Jupiter at 70 cm. Astron. J., vol. 72, 1967, pp. 771-777.
- VII-75. Leighton, R. B., Murray, B. C., Allen, J. D., and Sloan, R. K.: Mariner IV Pictures of Mars. JPL Tech. Report 32-884, 1967.

## BIBLIOGRAPHY

Counselman, C. C., Pettengill, G. H., and Shapiro, I. I.: Topography on Mars. Trans. Am. Geophys. U., vol. 49, 1968, p. 271.

Kliore, A. J., Fjeldbo, G., and Seidel, B. L.: Summary of Mariner 6 and 7 Radio Ocultation Results on the Atmosphere of Mars. Paper No. M25 presented at the XIII Plenary Meeting of COSPAR, Leningrad, 1970.

Sagan, C., and Pollack, J. B.: Elevation Differences on Mars. J. G. R., vol. 73, 1968, pp. 1373-1387.

## SECTION VIII. JUPITER

### 8.1 Atmospheric Environment

#### 8.1.1 Definition

The atmospheric environment of Jupiter is defined as the region between the surface and 20 000 km above the surface of Jupiter.

#### 8.1.2 Gas Properties

The variable image of the disc of Jupiter, as observed telescopically in visible light, strongly indicates an active atmosphere of sufficient thickness to obscure any features of a solid planetary surface. The presence of methane and ammonia in the absorption bands of the spectrum of Jupiter was discovered approximately 40 years ago. The occultation of  $\sigma$  Arietis by Jupiter was observed photoelectrically by Baum and Code in 1952, and a mean molecular weight of 3.3 was derived for their assumed stratospheric temperature of 86° K which confirmed the dominance of hydrogen and helium in Jupiter's atmosphere. The positive identification of the major component (hydrogen) was reported in 1960 and was accomplished by the spectroscopic detection of molecular hydrogen by means of its quadrupole rotation-vibration spectrum. The next step, the determination of abundances, temperatures, and pressures, for the most dense part of the atmosphere is continuing. Recent papers by Owens [VIII-1] and McElroy [VIII-2] summarize the latest abundance results from visible and infrared spectra in which absorption lines of  $H_2$ ,  $CH_4$ , and  $NH_3$  can be identified as originating in the atmosphere of Jupiter. They conclude that the abundance ratios are consistent with those of a solar mixture of elements which has evolved into simple hydrogen-bearing molecules with modification by saturation and condensation of some species, particularly  $NH_3$  and  $H_2O$ . This conclusion is adopted herein although it must be stressed that absorption lines of He, a presumably important constituent, and minor constituents such as  $H_2O$  and Ne have not been observed in the spectra. In view of the uncertainty thereby introduced and the uncertain solar ratios of elements (particularly He), it is appropriate to consider the fractions by mass of all molecules other than  $H_2$  uncertain by a factor of two in either direction. Atmospheric compositions and other parameters for Jovian model atmospheres are given in Table VIII-1 [VIII-3].

TABLE VIII-1. COMPOSITIONS AND OTHER PARAMETERS  
FOR MODEL ATMOSPHERES OF JUPITER [AFTER REF. VIII-3].

Parameter	Cool Model	Nominal Model	Warm Model
Fractions by mass (or weight)			
H <sub>2</sub>	0.50696	0.75348	0.87674
He	0.46000	0.23000	0.11500
CH <sub>4</sub>	0.00857	0.00429	0.00214
NH <sub>3</sub>	0.00219	0.00109	0.00055
H <sub>2</sub> O	0.01601	0.00800	0.00400
Ne	0.00229	0.00115	0.00057
Others	0.00398	0.00199	0.00100
Fractions by number (or volume)			
H <sub>2</sub>	0.68454	0.86578	0.93754
He	0.31057	0.13214	0.06149
CH <sub>4</sub>	0.00145	0.00062	0.00028
NH <sub>3</sub>	0.00035	0.00015	0.00007
H <sub>2</sub> O	0.00240	0.00102	0.00048
Ne	0.00031	0.00013	0.00006
Others	0.00038	0.00016	0.00008
Mean molecular weight, u (g/mole)	2.70	2.30	2.14
Acceleration of gravity, g (cm/s <sup>2</sup> )	2700	2500	2300
Effective temperature, T <sub>e</sub> (°K)	128	134	140
Troposphere lapse rate parameters $\left\{ \begin{array}{l} \beta_o \\ K_1 \text{ (°K)} \\ K_2 \text{ (°K)} \end{array} \right.$	$\left\{ \begin{array}{l} 0.222 \\ 500 \\ 500 \end{array} \right.$	$\left\{ \begin{array}{l} 0.236 \\ 500 \\ 295 \end{array} \right.$	$\left\{ \begin{array}{l} 0.259 \\ 500 \\ 324 \end{array} \right.$
Correspondence level temperature (°K)	125	125	125
Correspondence level pressure (atm)	0.50	0.30	0.20
Stratosphere temperature (°K)	108	113	118
Stratosphere vertical extent (scale heights)	$\infty$	1.0	1.0
Inversion level temperature (°K)	None	145	500
Inversion level pressure (atm)	None	0.0065	$2 \times 10^{-7}$



The variable appearance of the planet in visible light, analogous to weather patterns on the earth [VIII-4] is attributed to large-scale cloud features which are condensates formed in upward convecting gas. Infrared (thermal) radiation emitted in the lower atmosphere at wavelengths longer than  $5\text{ }\mu\text{m}$  leads to two important conclusions: (1) Jupiter's disc is uniform within 20 percent in brightness between 8 and  $14\text{ }\mu\text{m}$  [VIII-5], and (2) the planet radiates considerably more energy than it receives from the sun [VIII-6]. These conclusions suggest that lower atmospheric parameters need not be specifically associated with planetary latitudes and time of day but that these variations should be included within the uncertainty specified by a single set of models.

#### 8.1.2.1 Model Atmospheres

The lower atmosphere of Jupiter, commencing with the observed large scale cloud features and continuing inward to an indeterminate level, is thought to be in hydrostatic equilibrium and convective to a very great depth [VIII-3]. Lewis [VIII-7] concludes that the three most significant condensates in the upper regions of the lower atmosphere are ammonia ice, ammonium hydrosulfide ( $\text{NH}_4\text{SH}$ ), and water. Despite the pressure of the foregoing condensates, the lapse rate is nearly equal to the condensation free adiabatic value appropriate to a gas composition adapted for a model atmosphere. Another model requirement is a pressure temperature correspondence at some point. Attempts to establish such a correspondence from measurements of spectral line widths, equivalent widths, and their ratios are available but open to serious questions. In particular, "cloud top reflection layer" and ammonia saturation concepts [VIII-4] are not considered satisfactory, and on-going discussions of rotational temperatures and the associated abundance [VIII-8, VIII-9, VIII-10] are incomplete. An alternate approach by Gillett et al. [VII-11] combines the  $125^\circ\text{ K}$  temperature measured near  $12\text{ }\mu\text{m}$  with the calculated opacity of the dominant absorber  $\text{H}_2$  at that wavelength to give an abundance of 12 km-atm  $\text{H}_2$  and a partial pressure of  $1/4\text{ atm H}_2$ . This correspondence and the foregoing composition and lapse rate lead to a reasonable lower atmosphere model, similar to that of Owen [VIII-12], which explains many of the observed features of the reflection and emission spectra.

Jupiter's infrared emission suggests an effective temperature near  $134^\circ\text{ K}$  [VIII-3]. The upper boundary of the lower atmosphere is taken as the level at which the temperature reaches  $113^\circ\text{ K}$  with an isothermal stratosphere overlaying that level and extending upward at least one scale height. The upper atmosphere, as differentiated from the lower atmosphere of Jupiter, extends above the regions of significant radiation reflection,

absorption, and emission. Observational data are meager, but major conclusions are that (1) temperatures are probably near 150° K, but possible solar cycle effects may raise temperatures to as high as 500° K [VIII-3], and (2) molecular hydrogen predominates up to heights ~ 500 km and pressures ~ 10<sup>-6</sup> atm. The model atmospheres used in this document are those presented in Reference VIII-3 and follow the parameters as set forth in Tables VIII-1 through VIII-4 and Figures VIII-1 through VIII-5 for cool, nominal, and hot models.

The nominal model has been constructed with the constant values of  $T_e = 134^\circ \text{ K}$ ,  $g = 2500 \text{ cm/s}^2$ , and  $u = 2.30$  (where  $T_e$  is the effective temperature of Jupiter,  $g$  is the local acceleration of gravity, and  $u$  is the mean molecular weight) which corresponds to the nominal composition and other quantities shown in Table VIII-1. The convective troposphere has an adiabatic lapse rate near  $-2^\circ \text{ K/km}$ , extends indefinitely downward from the tropopause boundary temperature of  $113^\circ \text{ K}$ , and includes the correspondence level established at  $P = 0.30 \text{ atm}$  and  $T = 125^\circ \text{ K}$ . Above the tropopause, an isothermal stratosphere extends upward one scale height (16.3 km). Above the stratosphere an inversion layer of constant  $(P/T)$  ( $dT/dP$ ) is limited by an uppermost level at which  $P = 6.5 \text{ mb}$  and  $T = 145^\circ \text{ K}$ . An isothermal region extends indefinitely upward from the latter level.

The limiting models are cool and warm in the sense that for a given pressure of the nominal model they provide extremes of temperature and density which are thought to bracket the range of possible Jupiter values. The values for model construction were selected as reasonable limits to the nominal values and are given in Table VIII-1. More detailed discussions of the models are available in Reference VIII-3 and the references quoted in that document. The zero altitude is set by earth analogy, at the level at which the pressure  $P$  equals 1 atm in all three models and corresponds to the optical surface or limb of the planet near the ammonia clouds. The zero of altitude is set at  $1.01325 \times 10^6 \text{ dyne/cm}^2$  (pressure of 1 earth atm) and corresponds to the distance from Jupiter's center of  $R_s$ , given by

$$R_s = R_J [1 - \epsilon (\sin \Phi)^2] \quad (\text{VIII-1})$$

where  $R_J = 71\,422 \pm 2000 \text{ km}$ ,  $\Phi$  is the latitude,  $\epsilon$  is the flattening, and  $R_s$  specifies the level of the optical disc of the planet (not a real liquid or solid surface).

TABLE VIII-2. VALUES AT SELECTED PRESSURES FOR  
NOMINAL MODEL ATMOSPHERE OF JUPITER

P (atm)	T (°K)	$\rho$ (g/cm <sup>3</sup> )	z (km)	$H_{\rho}$ (km)	$H_{\rho}$ (km)	w (mg/liter)	Remarks
$2.00 \times 10^{-7}$	145.0	$3.86 \times 10^{-11}$	313.4	21.0	21.0		
$3.00 \times 10^{-7}$	145.0	$5.80 \times 10^{-11}$	304.9	21.0	21.0		
$1.00 \times 10^{-6}$	145.0	$1.93 \times 10^{-10}$	279.7	21.0	21.0		
$3.00 \times 10^{-6}$	145.0	$5.80 \times 10^{-10}$	256.6	21.0	21.0		
$1.00 \times 10^{-5}$	145.0	$1.93 \times 10^{-9}$	231.4	21.0	21.0		
$3.00 \times 10^{-5}$	145.0	$5.80 \times 10^{-9}$	208.3	21.0	21.0		
$1.00 \times 10^{-4}$	145.0	$1.93 \times 10^{-8}$	183.1	21.0	21.0		
$3.00 \times 10^{-4}$	145.0	$5.80 \times 10^{-8}$	160.0	21.0	21.0		
0.00100	145.0	$1.93 \times 10^{-7}$	134.8	21.0	21.0		
0.00300	145.0	$5.80 \times 10^{-7}$	111.7	21.0	21.0		
0.00650	145.0	$1.26 \times 10^{-6}$	95.5	21.0	21.0		Top of inversion layer
0.0100	139.0	$2.02 \times 10^{-6}$	86.7	20.1	18.3		
0.0300	124.8	$6.73 \times 10^{-6}$	65.7	18.1	16.4		
0.0829	113.0	$2.06 \times 10^{-5}$	48.3	16.3	16.3		Stratopause
0.100	113.0	$2.48 \times 10^{-5}$	45.2	16.3	16.3		
0.225	113.0	$5.59 \times 10^{-5}$	31.9	16.3	16.3		Tropopause
0.267	120.0	$6.24 \times 10^{-5}$	29.1	17.4	26.8		
0.300	125.0	$6.72 \times 10^{-5}$	27.0	18.0	27.9	0.00119	Correspondence level
0.350	132.0	$7.44 \times 10^{-5}$	24.1	19.1	29.3	0.00583	
0.406	139.0	$8.20 \times 10^{-5}$	21.2	20.1	30.8	0.0243	
0.469	146.0	$9.00 \times 10^{-5}$	18.3	21.1	32.3	0.0888	NH <sub>3</sub> ice cloud base
1.00	189.1	$1.48 \times 10^{-4}$	0.0	27.3	41.2		Zero of altitude <sup>a</sup>
1.27	205.0	$1.74 \times 10^{-4}$	-6.9	29.7	44.4		
1.80	230.0	$2.20 \times 10^{-4}$	-17.8	33.3	49.5	0.0743	
2.13	243.0	$2.46 \times 10^{-4}$	-23.6	35.1	52.1	0.292	
2.41	253.0	$2.68 \times 10^{-4}$	-28.0	36.6	54.2	0.758	
2.76	264.2	$2.93 \times 10^{-4}$	-33.0	38.2	56.4	2.02	H <sub>2</sub> O ice cloud base
3.00	271.3	$3.10 \times 10^{-4}$	-31.2	39.2	57.8		
10.0	395.8	$7.08 \times 10^{-4}$	-96.7	57.2	82.5		
30.0	550.0	$1.53 \times 10^{-3}$	-168.3	79.6	112.6		
100.0	777.0	$3.61 \times 10^{-3}$	-282.8	112.4	156.3		
300.0	1052.6	$7.99 \times 10^{-3}$	-427.2	152.3	209.1		
1000.0	1452.9	$1.93 \times 10^{-2}$	-643.7	210.1	285.4		

a. The zero of altitude is specified by equation (VIII-1).

TABLE VIII-3. VALUES OF PHYSICAL QUANTITIES AT SELECTED PRESSURES FOR COOL, DENSE MODEL ATMOSPHERE OF JUPITER

P (atm)	T (°K)	$\rho$ (g/cm <sup>3</sup> )	z (km)	$H_{\rho}$ (km)	$H_{\rho}$ (km)	w (mg/liter)	Remarks
$2.00 \times 10^{-7}$	108.0	$6.09 \times 10^{-11}$	192.8	12.3	12.3		
$3.00 \times 10^{-7}$	108.0	$9.14 \times 10^{-11}$	187.8	12.3	12.3		
$1.00 \times 10^{-6}$	108.0	$3.05 \times 10^{-10}$	173.0	12.3	12.3		
$3.00 \times 10^{-6}$	108.0	$9.14 \times 10^{-10}$	159.5	12.3	12.3		
$1.00 \times 10^{-5}$	108.0	$3.05 \times 10^{-9}$	144.6	12.3	12.3		
$3.00 \times 10^{-5}$	108.0	$9.14 \times 10^{-9}$	131.1	12.3	12.3		
$1.00 \times 10^{-4}$	108.0	$3.05 \times 10^{-8}$	116.3	12.3	12.3		
$3.00 \times 10^{-4}$	108.0	$9.14 \times 10^{-8}$	102.7	12.3	12.3		
0.00100	108.0	$3.05 \times 10^{-7}$	87.9	12.3	12.3		
0.00300	108.0	$9.14 \times 10^{-7}$	74.3	12.3	12.3		
0.0100	108.0	$3.05 \times 10^{-6}$	59.5	12.3	12.3		
0.0300	108.0	$9.14 \times 10^{-6}$	46.0	12.3	12.3		
0.100	108.0	$3.05 \times 10^{-5}$	31.1	12.3	12.3		
0.259	108.0	$7.88 \times 10^{-5}$	19.4	12.3	12.3		Tropopause
0.300	111.6	$8.84 \times 10^{-5}$	17.6	12.7	16.4		
0.500	125.0	$1.32 \times 10^{-4}$	10.7	14.3	18.3		Correspondence level
0.833	140.0	$1.96 \times 10^{-4}$	3.0	16.0	20.5	0.0276	
1.00	145.8	$2.26 \times 10^{-4}$	0.0	16.6	21.4	0.0793	Zero of altitude <sup>a</sup>
1.14	150.0	$2.49 \times 10^{-4}$	-2.2	17.1	22.0	0.162	
1.42	157.6	$2.96 \times 10^{-4}$	-6.1	18.0	23.1	0.534	NH <sub>3</sub> ice cloud base
3.00	186.1	$5.30 \times 10^{-4}$	-20.7	21.2	27.3		
10.0	243.1	$1.35 \times 10^{-3}$	-50.0	27.7	35.6	0.406	
16.1	270.0	$1.96 \times 10^{-3}$	-63.8	30.8	39.6	3.00	
22.1	290.0	$2.51 \times 10^{-3}$	-74.1	33.1	42.5	10.3	
30.0	310.2	$3.18 \times 10^{-3}$	-84.5	35.4	45.5	30.4	
32.3	315.4	$3.37 \times 10^{-3}$	-87.2	36.0	46.3	39.2	Solution cloud base (NH <sub>3</sub> -H <sub>2</sub> O)
100.0	405.3	$8.12 \times 10^{-3}$	-133.3	46.2	59.4		
300.0	517.2	0.0191	-190.9	59.0	75.8		
1000.0	675.7	0.0487	-272.3	77.1	99.1		

a. The zero of altitude is specified by equation (VIII-1).

TABLE VIII-4. VALUES AT SELECTED PRESSURES FOR WARM,  
EXTENDED MODEL ATMOSPHERE OF JUPITER

P (atm)	T (°K)	$\rho$ (g/cm <sup>3</sup> )	z (km)	H <sub><math>\rho</math></sub> (km)	H <sub><math>\rho</math></sub> (km)	w (mg/liter)	Remarks
$2.00 \times 10^{-7}$	500.0	$1.04 \times 10^{-11}$	634.8	84.5	75.8		
$3.00 \times 10^{-7}$	477.4	$1.64 \times 10^{-11}$	601.3	80.7	72.4		
$1.00 \times 10^{-6}$	416.1	$6.27 \times 10^{-11}$	510.6	70.3	63.1		
$3.00 \times 10^{-6}$	367.1	$2.13 \times 10^{-10}$	438.0	62.0	55.7		
$1.00 \times 10^{-5}$	320.0	$8.15 \times 10^{-10}$	368.2	54.1	48.5		
$3.00 \times 10^{-5}$	282.3	$2.77 \times 10^{-9}$	312.4	47.7	42.8		
$1.00 \times 10^{-4}$	246.1	$1.06 \times 10^{-8}$	258.7	41.6	37.3		
$3.00 \times 10^{-4}$	217.1	$3.60 \times 10^{-8}$	215.8	36.7	32.9		
0.00100	189.2	$1.38 \times 10^{-7}$	174.5	32.0	28.7		
0.00300	166.9	$4.69 \times 10^{-7}$	141.5	28.2	25.3		
0.0100	145.5	$1.79 \times 10^{-6}$	109.8	24.6	22.1		
0.0300	128.4	$6.09 \times 10^{-6}$	84.4	21.7	19.5		
0.0627	118.0	$1.39 \times 10^{-5}$	69.0	19.9	19.9		Stratopause
0.100	118.0	$2.21 \times 10^{-5}$	59.7	19.9	19.9		
0.171	118.0	$3.77 \times 10^{-5}$	49.1	19.9	19.9		Tropopause
0.179	120.0	$3.88 \times 10^{-5}$	48.2	20.3	31.8	0.000340	
0.200	125.0	$4.17 \times 10^{-5}$	45.8	21.1	33.0	0.00119	Correspondence level
0.223	130.0	$4.47 \times 10^{-5}$	43.5	22.0	34.3	0.00378	
0.248	135.0	$4.78 \times 10^{-5}$	41.1	22.8	35.5	0.0110	
0.270	139.2	$5.05 \times 10^{-5}$	39.2	23.5	36.6	0.0253	NH <sub>3</sub> ice cloud base
0.300	144.6	$5.41 \times 10^{-5}$	36.6	24.4	37.9		
0.756	200.0	$9.85 \times 10^{-5}$	9.9	33.8	51.7	0.00550	
0.871	210.0	$1.08 \times 10^{-4}$	5.0	35.5	54.7	0.0180	
1.00	220.2	$1.18 \times 10^{-4}$	0.0	37.2	56.6	0.0537	Zero of altitude <sup>a</sup>
1.06	225.0	$1.23 \times 10^{-4}$	-2.4	38.0	57.8	0.0867	
1.21	235.0	$1.34 \times 10^{-4}$	-7.3	39.7	60.2	0.221	
1.36	244.7	$1.45 \times 10^{-4}$	-12.1	41.3	62.6	0.505	H <sub>2</sub> O ice cloud base
3.00	318.6	$2.45 \times 10^{-4}$	-49.5	53.8	80.4		
10.0	470.2	$5.55 \times 10^{-4}$	-128.9	79.4	116.2		
30.0	661.4	$1.18 \times 10^{-3}$	-233.0	111.8	160.9		
100.0	949.0	$2.72 \times 10^{-3}$	-395.2	160.4	227.4		
300.0	1306.2	$5.98 \times 10^{-2}$	-602.9	220.7	309.5		
1000.0	1837.3	$1.42 \times 10^{-2}$	-919.9	310.5	413.3		

a. The zero of altitude is specified by equation (VIII-1).

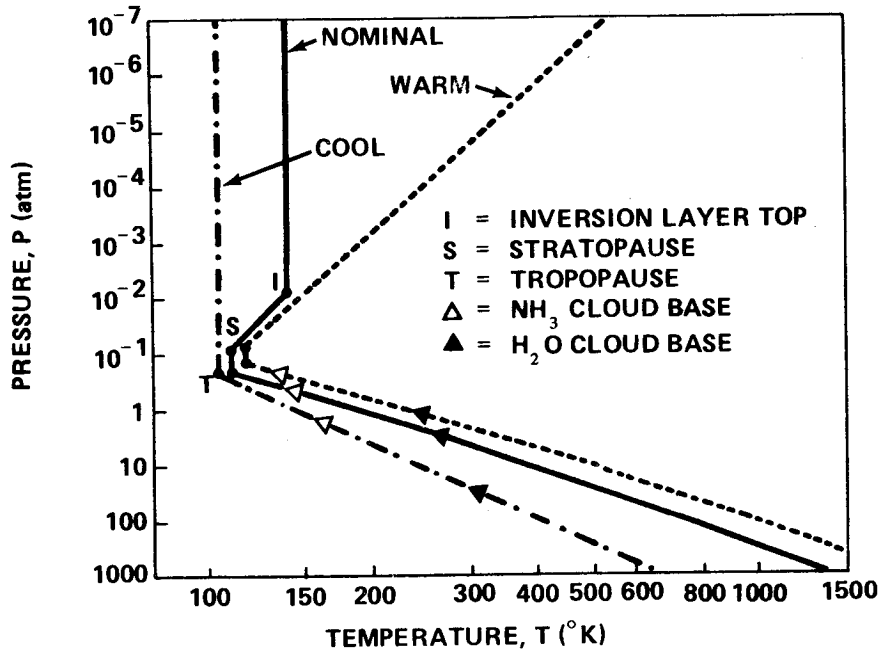


Figure VIII-1. Pressure versus temperature for the Jupiter model atmospheres (after Ref. VIII-3).

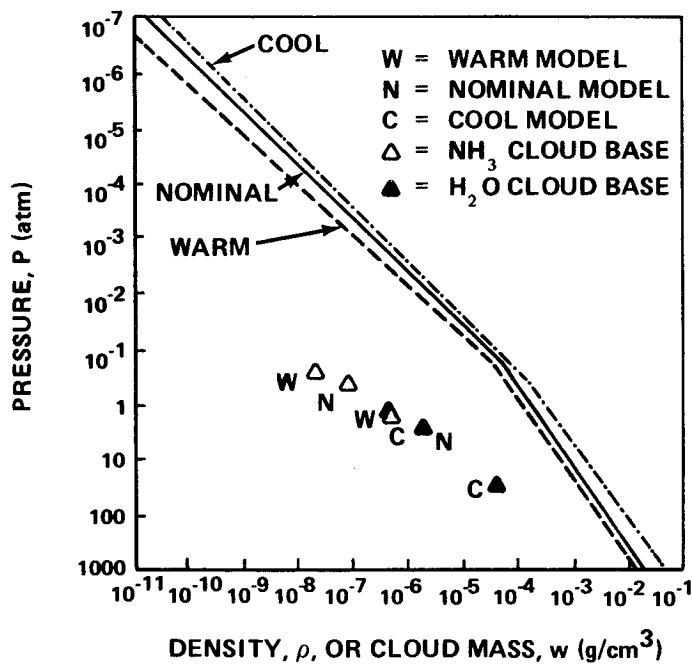


Figure VIII-2. Pressure versus density and cloud masses at cloud bases for the Jupiter model atmospheres (after Ref. VIII-3).

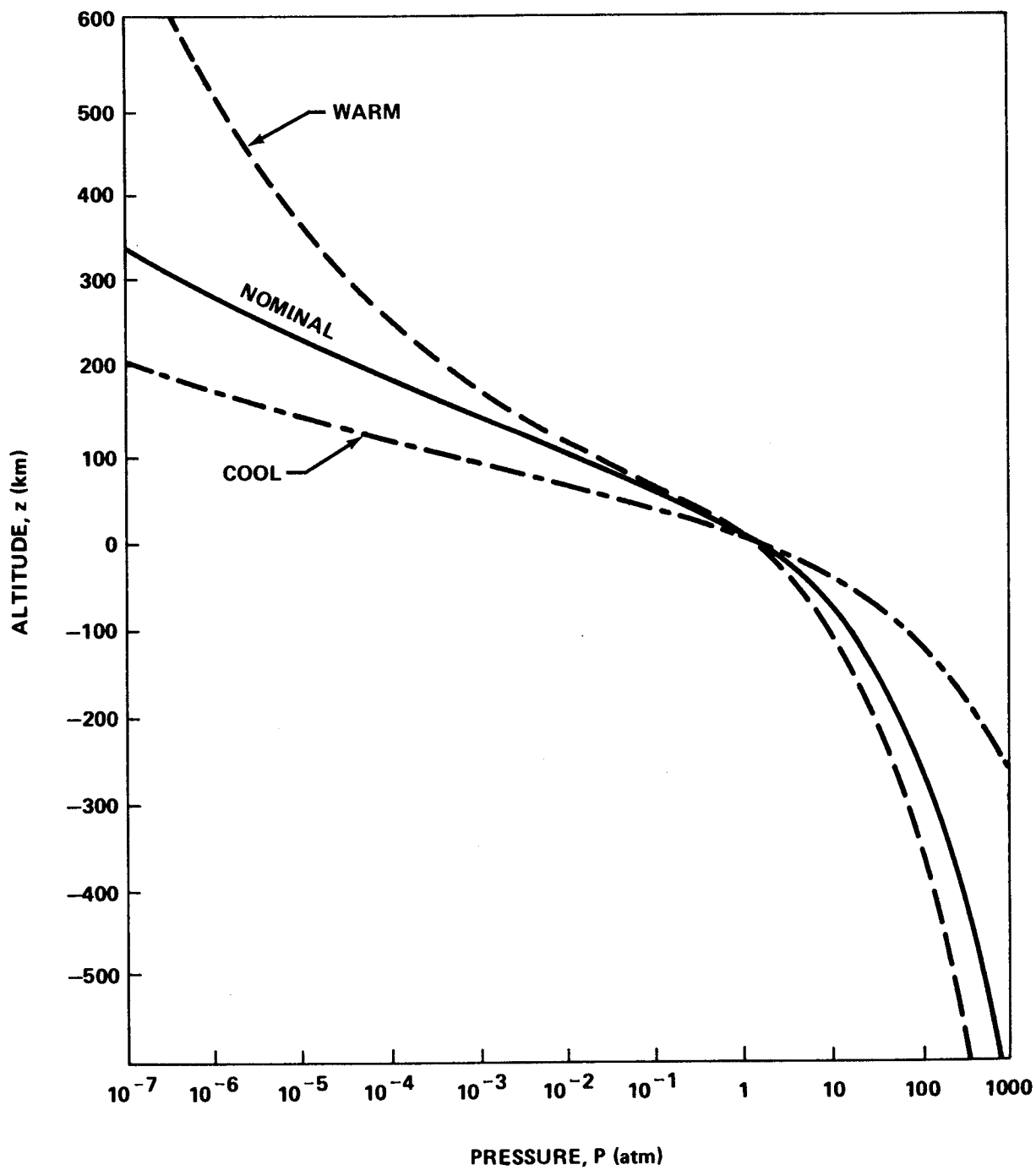


Figure VIII-3. Pressure versus altitude for the Jupiter model atmospheres (after Ref. VIII-3)

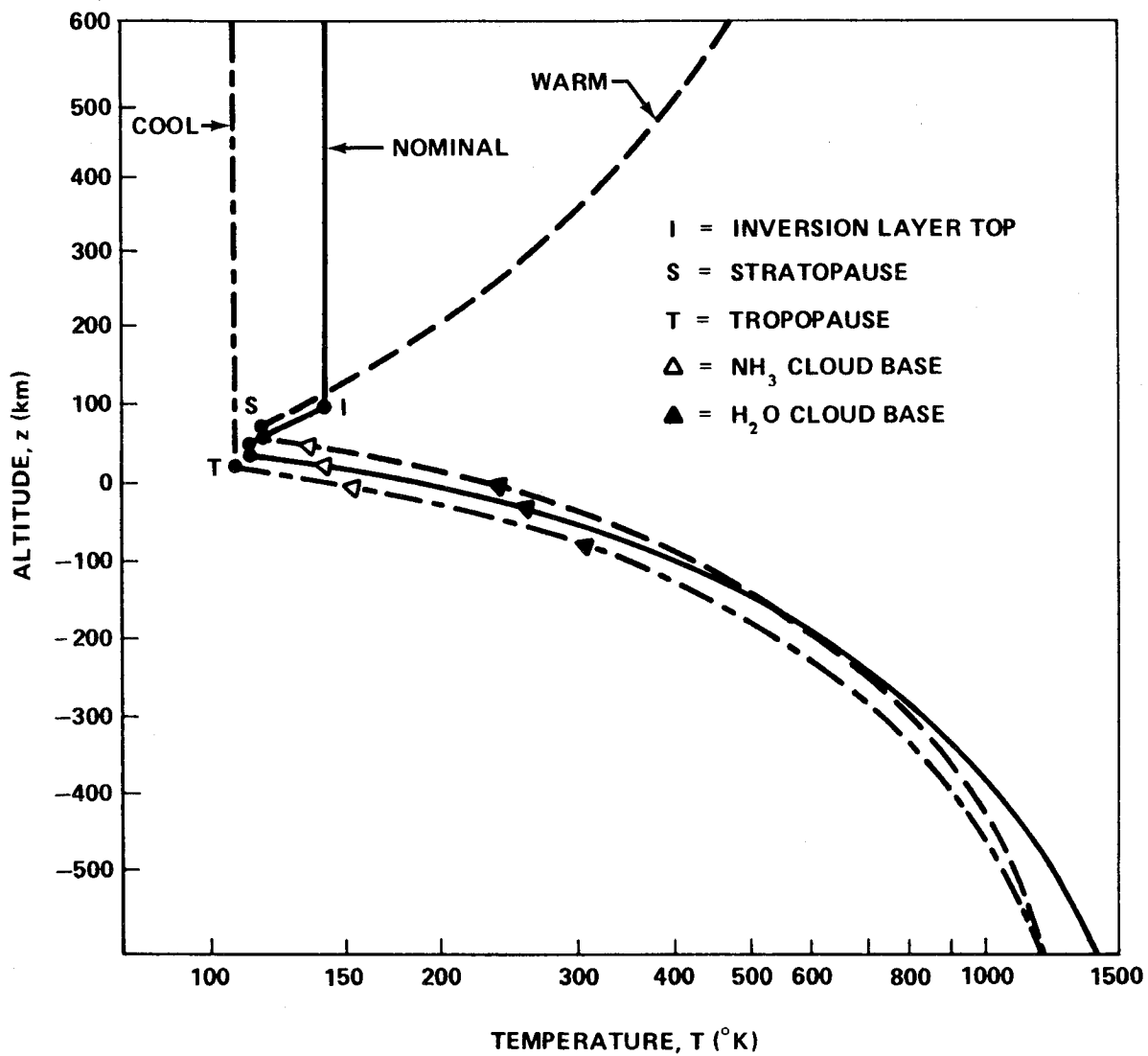


Figure VIII-4. Temperature versus altitude for the Jupiter model atmospheres (after Ref. VIII-3).



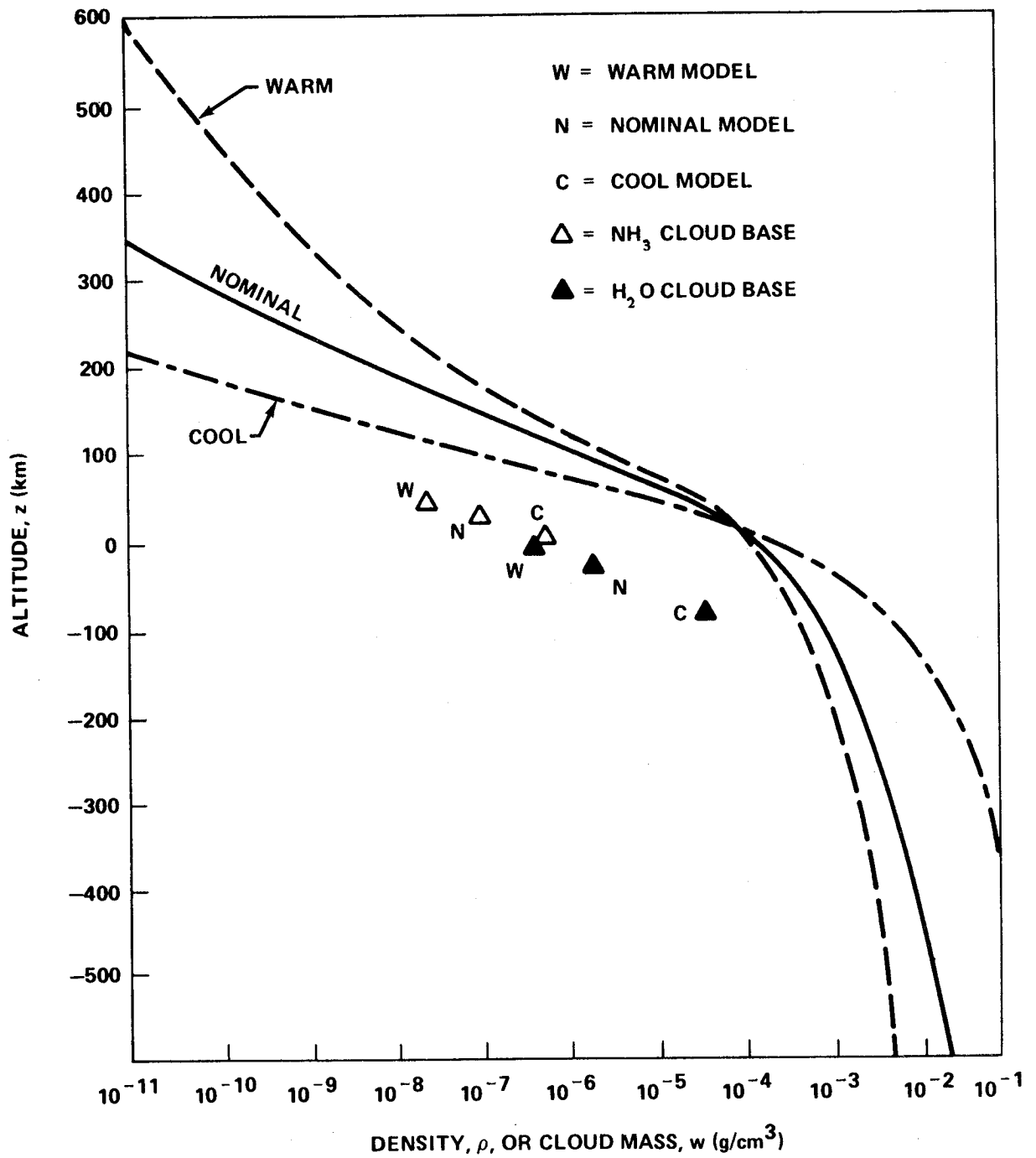


Figure VIII-5. Density versus altitude and cloud masses at cloud bases for the Jupiter model atmospheres (after Ref. VIII-3).

There are two approaches to the description of Jupiter's ionosphere. The first is theoretical in which considerations such as photo-ionization and solar UV flux values (useful in understanding the earth's ionosphere) are applied to Jupiter. The other approach is based on inferences from the HF bursts to which various generation mechanisms and requirements are applied. Within the rather large uncertainties inherent in the two approaches, agreement is quite satisfactory.

The theoretical approach is exemplified by the work of Gross and Rasool [VIII-13]. Their results are supported by those derived by Shimizu [VIII-14], Hunten [VIII-15], Henry and McElroy [VIII-16], and Capone and Barrow [VIII-17] which consider similar processes in less detail. In Reference VIII-13, solar ultraviolet radiation at wavelengths of the order of  $1000 \text{ \AA}$  is responsible for the photoionization of molecular and atomic hydrogen down to those altitudes at which it is fully absorbed. Secondary reactions, e.g., recombination, occur such that the equilibrium abundances of the species  $\text{H}_2$ ,  $\text{He}$ ,  $\text{H}$ ,  $\text{H}^+$ , and  $\text{e}^-$  (listed roughly in order of decreasing concentration) are significant near the maximum of charged particle density, approximately  $10^6 \text{ electrons/cm}^3$  and  $10^6 \text{ protons/cm}^3$ . The local gas pressure at that maximum is approximately  $3 \text{ dynes/cm}^2$ ; atmospheric models suggest that this level occurs within the altitude range  $z_0 = 250 \pm 150 \text{ km}$  (subsec. 8.1.2.1). Below this altitude the electron density becomes negligible within several kilometers, whereas upward the electron density it decreases roughly exponentially with a scale height of approximately  $100 \text{ km}$ . According to the same authors, the ionospheric temperature ranges from  $100^\circ$  to  $200^\circ \text{ K}$ .

Numerous arguments from mechanisms of HF burst generation have yielded electron density values independent of the foregoing considerations. Warwick [VIII-18] suggests that a maximum electron number density of the order of  $10^7 \text{ cm}^{-3}$  may be required to cause reflection of the HF bursts at the ionosphere. Investigations by Ellis [VIII-19] and Papadopoulos and Lerche [VIII-20] use various HF burst mechanisms to derive values within one or two orders of magnitude of the preceding density.

The presence in the earth's ionosphere of several distinct layers of electron and ion concentration suggest that a one-layer model is probably too simplistic for Jupiter. For this reason and on the basis of the foregoing derived values, it is appropriate to adopt a peak number density of  $10^6 \text{ cm}^{-3}$  for electrons and protons and to estimate the uncertainty as an order of magnitude in either direction.

The color, size, and shape of the visible atmospheric layers of Jupiter are constantly changing as winds and clouds alter the various features observed. Beyond approximately  $\pm 50$  deg latitude are the two polar regions which are dark and featureless at the resolution and wavelengths observed from the earth. At lower latitudes the planet has stripes parallel to the equator, classified as zones and belts. As usually observed from the earth in visible light, the zones are bright and the belts dark. Their latitudes and relative and absolute brightnesses vary with longitude, time, and wavelength of observation; i.e., color effects are important. The semipermanent, well-documented, generally uniform belts and zones are occasionally divided by thin bands also parallel to the equator and sometimes are blemished by light or dark spots whose motions in latitude and longitude have provided information on planetary rotation and atmospheric currents. These spots have characteristic horizontal dimensions ranging from 1000 to 10 000 km and lifetimes ranging from a few hours to weeks. Their resolution is marginal from earth observations so that very little is known about their actual properties. The spots are comparable in size and possibly in nature to major weather systems in the earth's atmosphere.

One much larger feature has existed for at least three centuries, namely the Great Red Spot. In a presentation of recent observational results, Solberg [VIII-21, VIII-22] reports that the Red Spot usually contrasts sharply with its surroundings in light of wavelengths  $\lambda < 5000 \text{ \AA}$  (very dark). Its oval shape extends horizontally about 13 000 km in latitude and 40 000 km in longitude, and its area varies by about 50 percent. The latitude of its center is usually within 3 of 22 deg south. Its longitude oscillates with an amplitude near  $0^\circ 8'$  and a period near 90 days, and drifts with respect to longitude system II<sup>1</sup> at a rate of several degrees/year. The Red Spot's nature and how it retains its integrity are enigmatic although Hide [VIII-23] has developed the Taylor column hypothesis in which relatively uniform, stagnant fluid overlies some topographical feature in the rotating fluid which forms Jupiter's deep atmosphere.

Theories of cloud formation and structure have been applied to the vertical distribution of condensates in Jupiter's lower atmosphere (subsec. 8.1.2). Techniques based on the analysis of Lewis [VIII-24] have

- 
1. The artificial Jupiter longitude measurement system in which the meridian at  $96^\circ 58'$  is directed toward the earth at 0<sup>h</sup> Universal Time on 14 July 1897 and has prograde rotation with angular velocity of 870.27 degrees/day. It is applied to the analysis of optical observations at mid-latitudes.

been applied to the models given in subsection 8.1.2.1 with numerical data for the condensates of ammonia and water from the International Critical Tables [VIII-25] and Lange [VIII-26]. Some of the cloud properties are given in Tables VIII-2, VIII-3, and VIII-4 and Figures VIII-1, VIII-2, VIII-4 and VIII-5. Cloud altitudes, masses, and compositions, primarily H<sub>2</sub>O and NH<sub>3</sub> ices with a dilute NH<sub>3</sub>-H<sub>2</sub>O solution replacing H<sub>2</sub>O in the cool model, show broad ranges which may be exceeded in the real atmosphere for any of the following reasons: (1) additional condensates, particularly NH<sub>4</sub>SH and NH<sub>4</sub>Cl, may form clouds of their own or contaminate the ones considered, leading to nonuniform cloud structure and color [VIII-24], (2) convection may carry the condensates to other altitudes, and (3) in downward convecting regions (cooler than upward-moving ones at a given pressure), condensates are likely to be present so there is a reasonable basis for equating downward convecting regions with Jupiter's dark belts. Lastly, by earth analogy, it would not be surprising if storms were occasionally present in regions of high cloud activity, leading to rain, hail, snow, thunder, and lightning within the lower atmosphere.

#### 8.1.5 Atmospheric Motions, Rotation Rate, and Winds

Atmospheric motions are roughly classified as rotation and winds. Vertical motions, motions at polar latitudes, motions above the tropopause, and motions on scales less than 1000 km are inferred from assumptions and theories. Probably the most significant rotation period given for Jupiter is that obtained from radio observations:

$$T_0 = 9^{\text{h}} 55^{\text{m}} 29.73 \pm 0.04.$$

Rotation periods derived from visible features on the planetary disc are averaged and give two distinct periods as follows: Latitudes with  $\pm 10$  deg of equator

$$T_1 = 9^{\text{h}} 50^{\text{m}} 30.003.$$

Latitudes other than those mentioned previously:

$$T_2 = 9^{\text{h}} 55^{\text{m}} 40.632.$$

In accord with Chapman's concept of the horizontal surface motions on Jupiter [VIII-27], it is appropriate to define winds as any motions differing from solid body planetary rotation (assumed to have a period equal to that for Jupiter's radio sources). At latitudes within 50 deg of the equator, visual and photographic observations of the positions of spots and features on the Jupiter disc imply horizontal winds on scales larger than 1000 km that are zonal, i.e., parallel to the equator, and apparently unceasing. According to Chapman [VIII-27], the major winds can be described by (1) a westerly equatorial current between latitudes  $\pm 10$  deg of average speed near 100 m/s, corresponding to the fast System I<sup>2</sup> rotation period  $T_1$ , with local winds up to 10 m/s in any direction with respect to the prevailing wind, (2) local winds between latitudes of 10 and 50 deg N and up to 10 m/s in any direction with a frequent westerly current (the north temperature current) of speeds up to 100 m/s within 10 deg of latitude 25 deg N, (3) local winds between latitudes 10 and 50 deg S up to 20 m/s of which the most prominent and persistent (the circulating current) has an easterly component near 20 deg S and a westerly component near 25 deg S, and (4) a wind having counterclockwise vorticity near the edges of the Great Red Spot of speeds near 10 m/s. Additional details of the winds may be inferred from the observational analysis of Peek [VIII-28] and the theoretical analyses of Hide [VIII-29] and Ingersoll and Cuzzi [VIII-30]. Winds have not been observed on a smaller scale, at latitudes beyond  $\pm 50$  deg, or moving in vertical directions; but a reasonable assumption is that for such winds the characteristic speed of 10 m/s holds. The limits in height and depth to which these winds might extend are unknown, but a reasonable assumption is that the horizontal winds may occur everywhere in the atmosphere, whereas the vertical ones are confined to the troposphere (subsec. 8.1.4). The literature contains no estimate of the magnitude of wind shear.

#### 8.1.6 Radiation Environment [VIII-31]

Three distinct categories of radiation are known to emanate from Jupiter: (1) the centimeter region, (2) the decimeter region, and (3) the decameter range.

Radio emission from Jupiter at wavelengths of a few centimeters is undoubtedly thermal in origin. The 3-cm region is somewhat higher than

- 
2. The artificial Jupiter longitude measurement system in which the meridian at  $47^{\circ} 31'$  is directed toward the earth at  $0^h$  Universal Time on 14 July 1897 and has prograde rotation with angular velocity of 877.90 deg/day. It is applied to the analysis of optical observations at equatorial latitudes.

the infrared temperature, but this can be accounted for if the radiofrequency emission at 3 cm is from regions below the tops of the ammonia clouds.

The radiation from Jupiter in the decimeter wavelength region is mainly nonthermal in character. It is, however, emitted continuously, although the intensity exhibits long-term variations. It has been proposed that this radiation is emitted by electrons of high energy spiraling around the lines of force of the Jovian magnetic field. The electrons trapped are similar to the outer Van Allen zone in the earth's magnetic field. It appears that this is synchrotron radiation from relativistic electrons with energies in the range of 5 to 10 million eV.

In the decameter range, emission is of the noise-storm type; i.e., it occurs in bursts of a 1- or 2-second duration emitted in groups lasting 5 to 10 minutes and continuing intermittently over a period of a few hours. This radiation is circularly polarized and exhibits very complex intensity variations. The probability of this occurrence is inversely related to the sunspot number. Indications exist that occasionally there is strong emission from Jupiter a few days after a strong solar flare. There is also definite correlation of the Jovian longitude at which emission is strongest with the rotation of the planet. As yet, there is no satisfactory explanation of Jupiter's decameter radiation.

#### 8.1.6.1 Electromagnetic Radiation [VIII-3]

##### 8.1.6.1.1 Solar Radiation

Near Jupiter the sun is the dominant source of light which may be direct, reflected, or scattered. NASA SP-8005 [VIII-32] summarizes the direct solar spectrum at 1 AU and specifies  $P_{\lambda}$ , the power per unit area and per unit wavelength interval for wavelengths between 50 Å and 100 cm. The values from Reference VIII-32 and standard relationships for intensity and flux lead to the formulas given for the sun in Table VIII-5.

Above the tropopause (here the tropopause at altitude  $z = 35 \pm 15$  km is the appropriate limit), the formulae in Table VIII-5 specify the ranges of intensities, fluxes, and temperatures associated with the electromagnetic radiation environment under conditions of maximum illumination. Under partial illumination, total shadowing, or eclipse, the values for intensities and fluxes range down to zero from the maximum illumination conditions of Table VIII-5 and temperatures range down to 3°K. The wavelength of interest determines which of the radiation sources listed in Table VIII-5 should be considered. Figure VIII-6 shows the geometric albedo  $p$  and

**TABLE VIII-5. ELECTROMAGNETIC RADIATION PARAMETERS NEAR JUPITER  
WITH MAXIMUM ILLUMINATION**

Parameters	Direct Sunlight <sup>a</sup>	Reflected Sunlight <sup>a</sup>	Thermal Radiation <sup>b</sup>	Synchrotron UHF Radiation <sup>c</sup>
Wavelength	$1 \text{ \AA} < \lambda < 100 \text{ cm}$	$1 \text{ \AA} < \lambda < 10 \text{ }\mu\text{m}$	$1 \text{ }\mu\text{m} < \lambda < 100 \text{ cm}$	$1 \text{ cm} < \lambda < 100 \text{ cm}$
Intensity Power/area wavelength solid angle	$I_{\lambda} = \frac{P_{\lambda}}{(0.000068 \text{ sterad})}$	$I_{\lambda} = \frac{pP_{\lambda}}{(90 \pm 10)}$	$I_{\lambda} = B_{\lambda}(T_{BD})$	
Power/area frequency solid angle			$I_{\nu} = B_{\nu}(T_{BD})$	$I_{\nu} = 2kT_{BS}/\lambda^2$
Flux Power/area wavelength	$F_{\lambda} = \frac{P_{\lambda}}{r^2}$	$F_{\lambda} = \frac{pH_{\lambda}}{(27 \pm 3) (R/R_j)^2}$	$F_{\lambda} = \frac{\pi B_{\lambda}(T_{BD})}{(R/R_j)^2}$	
Power/area frequency			$F_{\nu} = \frac{\pi B_{\nu}(T_{BD})}{(R/R_j)^2}$	$F_{\nu} = \frac{(5 \pm 2) \times 10^8}{4 + (R/R_j)^2} \text{ FU}$
Integrated flux Power/area	$F = \frac{(1.353 \pm 0.021) \times 10^6}{r^2} \left( \frac{\text{erg}}{\text{cm}^2\text{s}} \right)$	$F = \frac{(1.4 \pm 0.2) \times 10^4}{(R/R_j)^2} \left( \frac{\text{erg}}{\text{cm}^2\text{s}} \right)$	$F = \frac{(1.8 \pm 0.3) \times 10^4}{(R/R_j)^2} \left( \frac{\text{erg}}{\text{cm}^2\text{s}} \right)$	$F = \frac{(15 \pm 7) \times 10^{-6}}{4 + (R/R_j)^2} \left( \frac{\text{erg}}{\text{cm}^2\text{s}} \right)$
Brightness Temperature			$T_{BD}$	$T_{BS} = \frac{D\lambda^2}{R_j} (0.30 \pm 0.15)^{\circ}\text{K}$
Effective Temperature	$5800 \pm 15^{\circ}\text{K}$		$T_e = 134 \pm 6^{\circ}\text{K}$	

a. Solar irradiance from NASA SP-8005 [VIII-32], solar distance  $r$  in AU only, and geometric albedo  $p$  from Figure VIII-6.

b. Brightness temperature  $T_{BD}$  from Figure VIII-6 and Planck functions  $B_{\lambda}(T)$  and  $B_{\nu}(T)$  from Allen [VIII-33] or elsewhere.

Use  $\lambda$  in cm only and estimate  $D/R_j$  from Figure VIII-7 with  $D$  being the approximate pathlength of line of sight through the volume. Radiation is up to 30 percent linearly polarized.

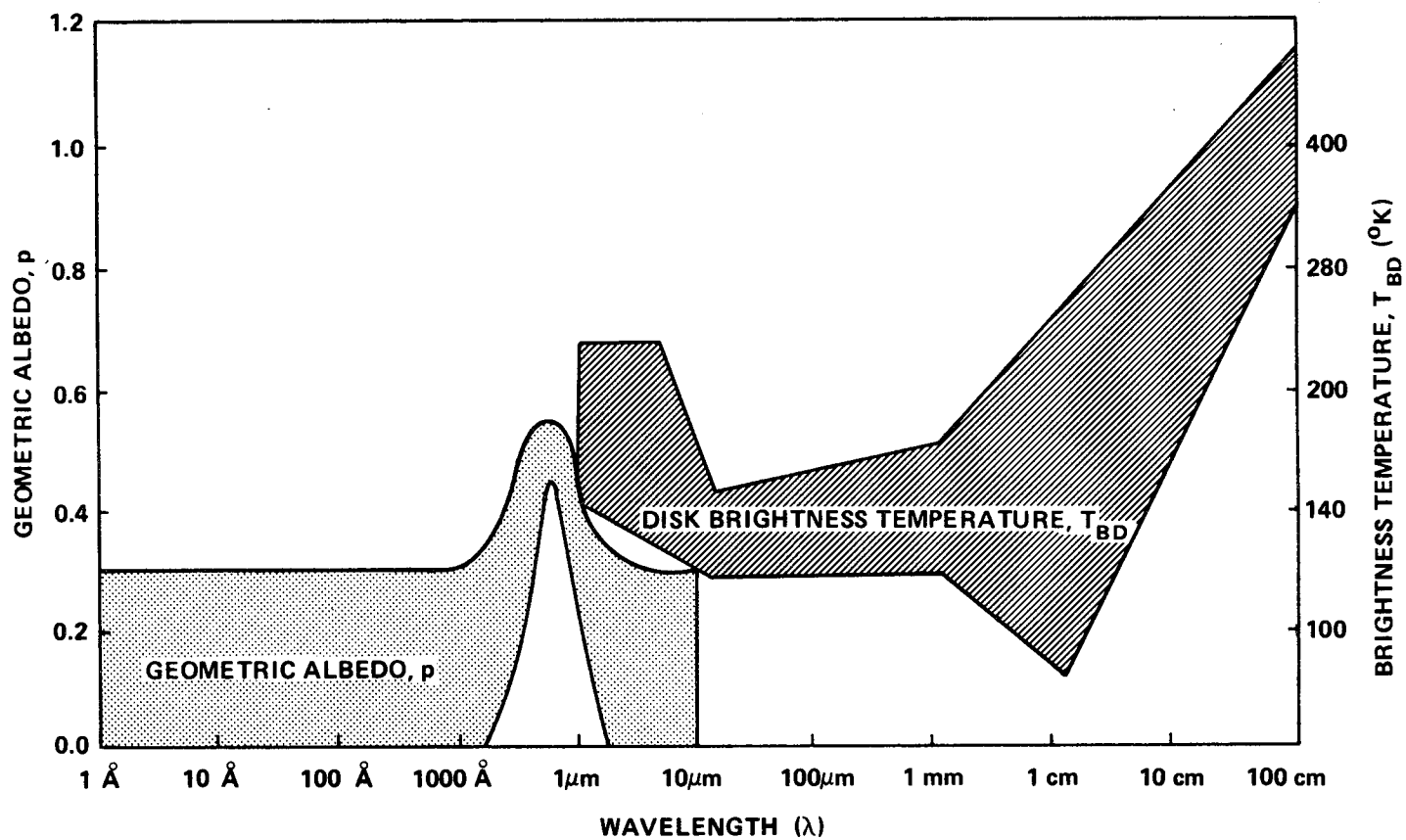


Figure VIII-6. Ranges of geometric albedo and disk brightness temperature as functions of wavelength (after Ref. VIII-3).



brightness temperature  $T_{BD}$  as functions of the wavelength. In Table VIII-5, the quantity  $D$  is the approximate pathlength of the line of sight through the schematic synchrotron emission volume shown in Figure VIII-7.

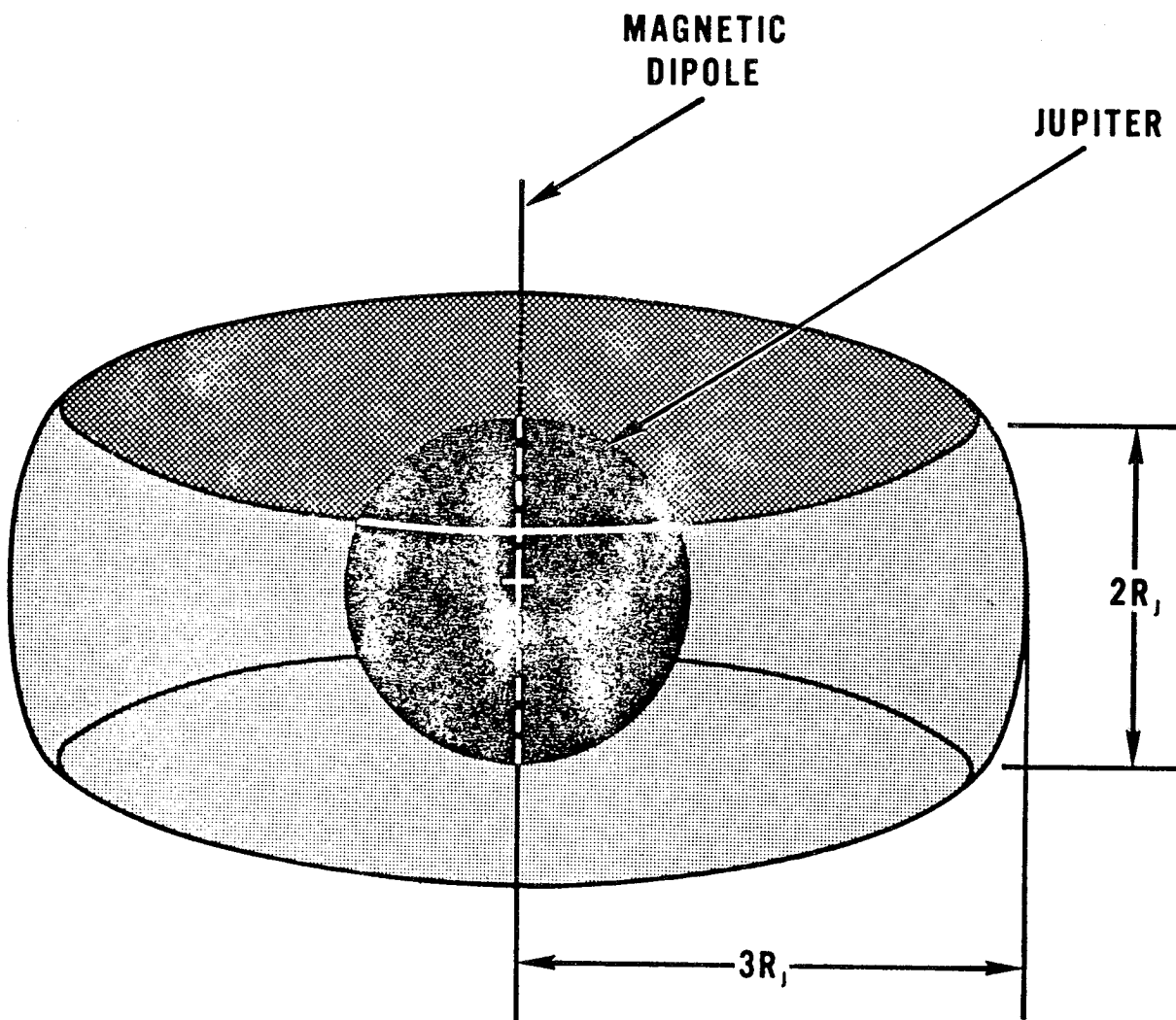


Figure VIII-7. Schematic volume for the calculation of the brightness temperature,  $T_{BS}$ , of Jupiter's synchrotron emission source (after Ref. VIII-3).

In addition, Jupiter's satellites and the other planets constitute light sources, but their fluxes near Jupiter are minor compared to the sources listed in Table VIII-5. Their positions are published annually in the American Ephemeris and Nautical Almanac [VIII-34], and their visual magnitudes and colors are specified by

TABLE VIII-6. MAGNITUDES AND COLORS FOR  
SATELLITES OF JUPITER AND PLANETS

	$m_o$	U-B	B-V
Jupiter V (Amalthea)	6.3	—	—
I (Io)	- 1.90	1.30	1.17
II (Europa)	- 1.53	0.52	0.87
III (Ganymede)	- 2.16	0.50	0.83
IV (Callisto)	- 1.20	0.55	0.86
VI-XII	$\geq 7.0$	—	—
Mercury	- 0.36	—	0.93
Venus	- 4.29	0.50	0.82
Earth	- 3.87	—	0.2
Mars	- 1.52	0.58	1.36
Jupiter	- 9.25	0.48	0.83
Saturn	- 8.88	0.58	1.04
Uranus	- 7.19	0.28	0.56
Neptune	- 6.87	0.21	0.41
Pluto	- 1.01	0.27	0.80

$$m_V = (m_0 \pm 0.3) + 5 \log r \Delta + (0.03 \pm 0.02) \alpha \quad (\text{VIII-2})$$

and the parameters in Table VIII-6 where  $\alpha$  is in degrees, and  $r$  and  $\Delta$  in AU. The radiation from stars and other nonsolar-system objects is identical to that beyond the earth's atmosphere.

Below the tropopause, i.e, altitudes  $z < 35 \pm 15$  km, the maximum contributions of the sun and the synchrotron source are identical to those specified in Table VIII-5 which uses the geometric albedo  $p$  and brightness temperature  $T_{BD}$  given in Figure VIII-6. The reflected sunlight intensity and flux in Table VIII-5 are appropriate but must be considered omnidirectional to account for the maximum scattered light. The thermal radiation is specified by Table VIII-7. In addition, sporadic lightning may require that light-sensitive surfaces be covered when local meteorological conditions are stormy.

TABLE VIII-7. THERMAL RADIATION PARAMETERS BELOW THE TROPOPAUSE IN JUPITER'S ATMOSPHERE

Wavelength	$1\mu\text{m} < \lambda < 100 \text{ cm}$
Intensities	$\begin{cases} I_\lambda = B_\lambda(t) \\ I_\nu = B_\nu(t) \end{cases}$
Fluxes	$\begin{cases} F_\lambda = \pi B_\lambda(t) \\ F_\nu = \pi B_\nu(t) \end{cases}$
Integrated Fluxes	$F = \begin{cases} (1.8 \pm 0.3) \times 10^4 \left( \frac{\text{erg}}{\text{cm}^2\text{s}} \right) & \text{for } T < 134^\circ\text{K} \\ \left( \frac{T}{134} \right)^4 (1.8 \pm 0.3) \times 10^4 \left( \frac{\text{erg}}{\text{cm}^2\text{s}} \right) & \text{for } T > 134^\circ\text{K} \end{cases}$
Brightness Temperature	$t = \text{larger of } T \text{ and } T_{BD}$

Radiation and its effects at wavelengths shorter than  $1 \text{ \AA}$  ( $\gamma$ -rays) should be ignored. The power emitted sporadically in the HF bursts near Jupiter ranges up to  $4 \times 10^{16} \text{ erg/s}$  at wavelengths longer than  $7.5 \text{ m}$ ; intensities at wavelengths longer than  $1 \text{ m}$  are unknown but probably high compared to communications intensities.

#### 8.1.6.1.2 Jupiter Reflected Radiation [VIII-3]

The solar radiation reflected from Jupiter (or its clouds) has been observed only at phase angles less than  $12 \text{ deg}$  and is conventionally described in terms of astronomical magnitudes, colors, and albedos. The definition of geometric albedo  $p$  leads to formulae for the intensity and flux of Jupiter-reflected radiation observed at zero phase angle and jovicentric distance  $R$ ,

$$I_{\lambda} = \frac{p \lambda}{\pi r^2} \quad (\text{VIII-3})$$

and

$$F_{\lambda} = \frac{p \lambda}{r^2 (R/R_j)^2} \quad (\text{VIII-4})$$

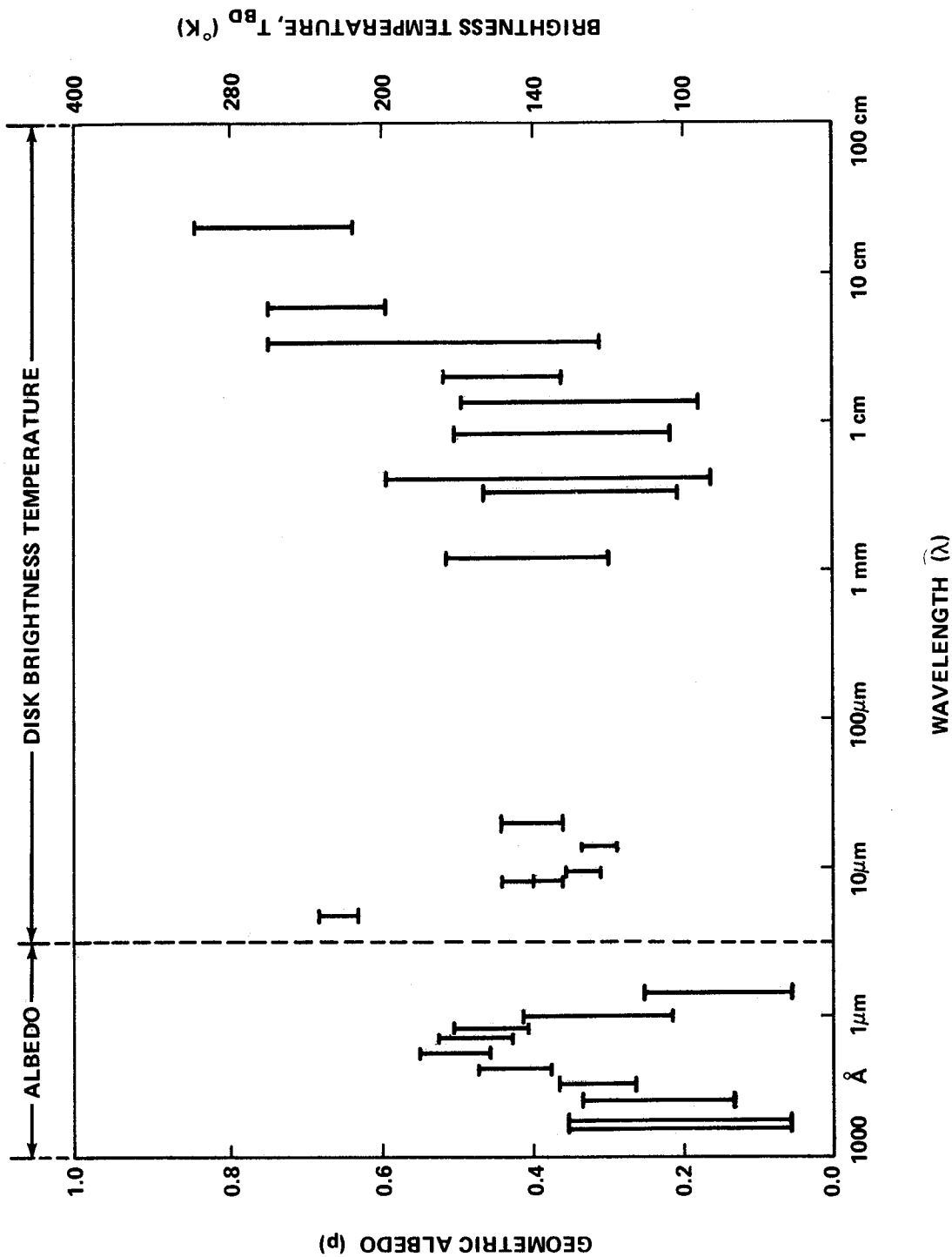
where  $r^2$  evaluated for Jupiter in  $(\text{AU})^2$  has the value  $27 \pm 3$ . For other observable phase angles ( $< 12 \text{ deg}$ ), these quantities are smaller than the results of equations (VIII-3) and (VIII-4). Therefore, it can be inferred that the zero phase angle formulae constitute correct upper limits at all phase angles.

Photoelectric measurements of the geometric albedo  $p$  for Jupiter at wavelengths between  $2000 \text{ \AA}$  and  $1.5 \text{ \mu m}$  are summarized in Table VIII-8. Limiting values from Table VIII-8 are shown in Figure VIII-8, and although the data are restricted to one decade in wavelength, the albedo is apparently decreasing as both ends of the observed range are approached. Thus, a range of values for  $p$  between 0 and 0.3 at unobserved wavelengths in addition to the range from Table VIII-8 is adopted herein. Table VIII-8 also lists the result of a photoelectric determination of the bolometric albedo  $p_b$ . That value and its substitution in the following expression for the integrated reflected flux.

TABLE VII-8. OBSERVED GEOMETRIC ALBEDOS FOR JUPITER

Wavelength <sup>a</sup> (Å)	Geometric Albedo (p)
1730	0.2 ±0.15
2100	0.2 ±0.15
2800	0.23 ±0.1
3530 (U)	0.31 ±0.05
4480 (B)	0.42 ±0.05
5540 (V)	0.50 ±0.05
6900 (R)	0.47 ±0.05
8200 (I)	0.35 ±0.05
10 635	0.31 ±0.1
15 000	0.15 ±0.1
Bolometric Albedo	$P_b = 0.28 \pm 0.03$

a. Letters specify pass bands in the conventional magnitude system.



$$F = \frac{p_b S}{r^2 (R/R_j)^2}$$

are adopted here.

#### 8.1.7 Meteoroid Environment

No direct evidence exists of meteoroidal debris in the environment of Jupiter. Traditionally, the meteoroid environment near a planet has been inferred from the presumed gravitational enhancement of the nearby interplanetary cometary debris [VIII-35]. Although such an enhancement is definitely to be expected, the uncertainties involved in the evaluation of the interplanetary debris distribution and the enhancement characteristics in the case of Jupiter amount to several orders of magnitude.

Another reasonable approach is to consider Jupiter's irregular satellites (Table VIII-9, J VI through XII) as the observable, large body end of a meteoroid distribution analogous to that expected in the asteroid belt. Such an approach assumes that the smaller satellites of Jupiter have individual properties and a mass distribution comparable to those of the asteroids, an assumption which is neither confirmed nor denied by the meager satellite data available.

The masses  $M_n$  in grams and radii  $R_n$  in cm for J V through XII presented in Table VIII-9 are derived from the relationships

$$\log M_n = 26 \pm 1 - 0.6 m_o \quad (\text{VIII-6})$$

and

$$\log R_n = 8.3 \pm 0.3 - 0.2 m_o \quad (\text{VIII-7})$$

TABLE VIII-9. PROPERTIES OF JUPITER'S SATELLITES

Satellite	Orbital Period (days)	Range of Distance from Jupiter (radii of Jupiter, $R_j$ )	Maximum Jovi- centric Latitude (deg)	Orbital Speed (km/s)	Radius, $R_n$ (km)	Mass, $M_n$ (g)
V (Amalthea)	0.498	$2.539 \pm 0.08$	0.4	26	$100 \times 2^{\pm 1}$	$10^{22} \pm 1$
I (Io)	1.76914	5.905	0	17	$1800 \pm 160$	$(7.2 \pm 0.6) \times 10^{25}$
II (Europa)	3.55118	9.396	0	14	$1550 \pm 100$	$(4.7 \pm 0.1) \times 10^{25}$
III (Ganymede)	7.15455	14.99	0	11	$2600 \pm 400$	$(15.5 \pm 0.2) \times 10^{25}$
IV (Callisto)	16.68902	26.36	0	8	$2400 \pm 400$	$(9.6 \pm 0.8) \times 10^{25}$
VI	251	$161 \pm 25$	29	3	$70 \times 2^{\pm 1}$	$10^{21.5 \pm 1}$
VII	260	$164 \pm 23$	28	3	$10 \times 2^{\pm 1}$	$10^{19 \pm 1}$
X	253	$164 \pm 23$	29	3	$7 \times 2^{\pm 1}$	$10^{18 \pm 1}$
VIII	737	$300 \pm 200$	33	2	$8 \times 2^{\pm 1}$	$10^{19 \pm 1}$
IX	758	$330 \pm 120$	23	2	$7 \times 2^{\pm 1}$	$10^{18.5 \pm 1}$
XI	692	$313 \pm 63$	18	2	$7 \times 2^{\pm 1}$	$10^{18.5 \pm 1}$
XII	631	$290 \pm 50$	34	2	$7 \times 2^{\pm 1}$	$10^{18.5 \pm 1}$



which are reasonable for asteroids of absolute magnitude  $m_0$ , mass density  $3.5 \text{ g/cm}^3$ , and visual albedo 0.2. If the positions of the outer seven satellites are distributed uniformly within a volume centered on Jupiter of radius  $500R_j$  and at latitudes within  $\pm 30$  deg, the number per unit volume  $N_M$  of particles of mass  $M \geq 10^{18.5} \text{ g}$  is  $10^{-31 \pm 1} \text{ m}^{-3}$ . This is almost identical to the peak spatial density at this mass in the asteroid belt [VIII-35]. Application of a crude mass distribution similar to that in Reference VIII-35 gives

$$\log N_M = 31 \pm 1 - (0.8 \pm 0.1) (\log M - 18.5). \quad (\text{VIII-8})$$

Equation (VIII-8) requires  $N_M$  in particles/ $\text{m}^3$  and applies for  $10^{-9} \leq M \leq 10^{20} \text{ g}$  within the foregoing given volume near Jupiter.

Omnidirectional fluxes of particles may be computed by multiplying  $N_M$  by  $v/4$  where the speed  $v$  of the particles relative to a spacecraft (with speed  $v_s$ ) is approximately  $v = [v_s^2 + (R_j/R) (40 \text{ km/s})^2]^{1/2}$ . The particle density is  $3.5 \times 2^{\pm 1} \text{ g/cm}^3$ . Lack of relevant data makes it impossible to decide whether such a distribution dominates anticipated cometary debris of lower density, but it is recommended that cometary debris be neglected on the basis of the small fluxes suggested in Reference VIII-35.

### 8.1.8 Geomagnetic Environment

#### 8.1.8.1 Magnetic Field

The characteristics of Jupiter's UHF and HF radiation permit quantitative descriptions of the magnetic field strength and configuration to be formulated although the uncertainties are considerable. UHF data permit

3. The inner boundary for meteoroids could be  $100R_j$  because of sweeping action by the satellites and gravitational forces. However, an inner boundary of  $1R_j$  is assumed herein.
4. The average particle velocity relative to Jupiter is taken here as the orbital velocity ( $40 \text{ km/s}$  at  $R/R_j = 1$ ) which is distinct from the escape velocity given in Reference VIII-35.

an order-of-magnitude determination of the magnetic field in the radiation belts ; the values cited in the literature are near 1 gauss about 2 radii from the dipole [VIII-18, VIII-36, VIII-37] which correspond to field strengths near 10 gauss about 1 radius from the dipole and dipole moment  $M_1$  near  $3 \times 10^{30}$  gauss-cm<sup>3</sup>. The UHF values at 1 radius are compatible with the narrower range commonly derived from the HF bursts if the burst frequency is taken to equal the local electron gyrofrequency at the source location. The local magnetic field strengths corresponding to observed HF frequencies near 30 MHz are near 12 gauss [VIII-18, VIII-19, VIII-38]. The dipole moment obtained from this field strength value depends sensitively on the relative locations of the dipole and the HF burst generation region. If the dipole is centered on the planet and the emission near 30 MHz is generated just above Jupiter's atmosphere in the magnetic equatorial plane, the moment corresponding to the 12-gauss field strength is approximately  $4 \times 10^{30}$  gauss-cm<sup>3</sup>. This value is close to the value of  $4.2 \times 10^{30}$  gauss-cm<sup>3</sup> derived by Warwick [VIII-18, VIII-39], who completed a detailed analysis of the HF burst structure based on a severely offset dipole. To consider published field strength and dipole moment values based on analyses of HF and UHF data [VIII-19, VIII-36, VIII-37, VIII-38, VIII-40], an uncertainty factor of two and a nominal value of  $M_1 = 4 \times 10^{30}$  gauss-cm<sup>3</sup> are adopted in this document. The consequent range of field strengths in the atmosphere is from 6 gauss at the equator to 48 gauss at the poles if the dipole is centered on Jupiter. The dipole and field have the opposite orientation from the earth's as Jupiter's northern hemisphere contains its north-seeking magnetic pole [VIII-18, VIII-41].

#### 8.1.8.2 Magnetosphere

Jupiter's magnetosphere is the region within which Jupiter's own magnetic field and charged particles dominate. In the solar direction the magnetosphere boundary is conventionally fixed by equating the solar wind and planetary magnetic field pressures and consists of both a shock front (at which the solar wind velocity decreases abruptly) and a magnetopause (limiting Jupiter's regular magnetic field). The result is  $50 \pm 20 R_J$  which includes most estimates of the distance of the sunward boundary from Jupiter [VIII-36, VIII-42, VIII-43]. This distance is adopted here as the minimum radius of the magnetosphere. In other directions, additional complex features, including distortion by Jupiter's rotation and a more distant magnetosphere boundary, are expected by analogy with the earth. In the antisolar direction the length of Jupiter's magnetospheric tail is greater than  $100 R_J$  [VIII-36, VIII-44].

### 8.1.9 Charged Particle Environment

In the charged particle environment, the rate at which charge buildup proceeds is dependent on the charging or discharging mechanism, the spacecraft materials, and the net charge present. A distinction should be made in the charge buildup process between highly energetic particles and lower-energy, thermal particles in that the latter are influenced by spacecraft charge. The near-Jupiter region and near-earth region consist of the magnetosphere and the magnetosheath. It is assumed that the near-Jupiter environment follows the same pattern as the near-earth region, so the available data on the near-earth particle environment provide useful background information for predicting the environment surrounding Jupiter, although wide variations between these predictions and reality may exist. A complete discussion and analysis of spacecraft charge buildup is continued in Reference VIII-45.

#### 8.1.9.1 Galactic Cosmic Rays

Near the earth, galactic cosmic ray intensities are modulated by the interplanetary magnetic field. In general, it is expected that this modulation reduces the intensities more severely at lower energies, closer to the sun, and during intervals of greater solar activity. Quantitative predictions of the intensities near Jupiter have not been made, however. Jupiter's own magnetic field may reduce the intensities further, particularly at low energies and latitudes. Thus the approach adopted is to specify the fluxes in the energy range observed (0.1 to  $10^{10}$  GeV) as between zero and a spectrum extrapolated from the highest energies observed for the most abundant particle kinds at times near minimum solar activity. This spectrum can be approximated by the following expression for the flux of particles with kinetic energy greater than E

$$\Phi_E = A (E + m_0 c^2)^{-1.5} \quad (\text{VIII-9})$$

where  $m_0 c^2$  is the rest energy of the particle and E is the particle kinetic energy in GeV (per nucleon for alpha-particles). The summary given by Haffner [VIII-46] specifies the coefficient  $A \approx 10 \text{ cm}^{-2} \text{ s}^{-1}$  for protons and  $A \approx 1 \text{ cm}^{-2} \text{ s}^{-1}$  for alpha-particles; Fanselow [VIII-47] specifies  $A \approx 0.2 \text{ cm}^{-2} \text{ s}^{-1}$  for electrons.

#### 8.1.9.2 Solar Particle Events

Protons and alpha-particles of energy greater than 1 MeV are emitted sporadically by the sun and have been detected by ground-based and spacecraft-borne instrumentation. Their fluxes near the earth vary over several orders of magnitude in time, have both directional and isotropic components, and frequently can be identified with specific solar flares. Properties of sample events observed near the earth are described in Reference VIII-48. The recent theoretical model by Englade [VIII-49] cites the important references which treat the complex processes involved. This literature shows that neither the probability of occurrence of an event nor the variation of the particle fluxes with solar distance can be reliably estimated at this time.

#### 8.1.9.3 Solar Wind

Properties of the solar wind are summarized by Hundhausen [VIII-50]. On the basis of observations from Mariner spacecraft at 0.8 to 1.5 AU from the sun, protons and electrons during quiet solar conditions have concentrations of approximately  $5r^{-2} \text{ cm}^{-3}$  (for  $r$  in AU) and are streaming radially away from the sun at speeds near 320 km/s. Increases in solar activity are accompanied by temporary increases up to factors of 10 in the concentration and 3 in the speed. The applicable theory suggests that the extrapolation of these conditions on the basis of heliocentric distance  $r$  to the orbit of Jupiter is justified. The interaction of the solar wind with Jupiter's magnetic field is responsible for the formation of the outer boundary of Jupiter's magnetosphere.

#### 8.1.10 Astrodynamic Constants

##### 8.1.10.1 Jupiter Constant [VIII-3]

Distance from sun	$r = 5.20 \pm 0.25 \text{ AU}$
-------------------	--------------------------------

Period of revolution about sun	$T = 11.862 \text{ years}$
-----------------------------------	----------------------------

Mass of planet, excluding satellites	$M_j = (1.899 \pm 0.002) \times 10^{30} \text{ g}$
--------------------------------------	--

Equatorial radius	$R_j = 71422 \pm 200 \text{ km}$
Mean density	$\bar{\rho} = 1.32 \pm 0.01 \text{ g/cm}^3$
Flattening (dynamical)	$\epsilon = 0.0645 \pm 0.0008$
Period of rotation	$T_o = 9^{\text{h}} 55^{\text{m}} 29.^{\text{s}}_{73} \pm 0.^{\text{s}}_{04}$
Rotational angular velocity	$\omega_o = (1.758531 \pm 0.000002) \times 10^{-4} \text{ rad/s}$
Angular momentum	$C \omega_o = (4.3 \pm 0.2) \times 10^{45} \text{ g-cm}^2/\text{s}$
Celestial coordinates of North Pole	$\alpha_R = 17^{\text{h}} 52^{\text{m}} 0.^{\text{s}}_{84} + 0.^{\text{s}}_{247} (t-1919.0)$ $\delta_R = +64^\circ 33'34'' 6 - 0.60'' (t-1910.0)$
Moment of inertia about rotational axis	$C = (2.4 \pm 0.1) \times 10^{49} \text{ g-cm}^2$
Moment of inertia about equatorial axes	$A = (2.25 \pm 0.1) \times 10^{49} \text{ g-cm}^2$
Gravitational parameter	$1.267076 \times 10^8 \text{ km}^3/\text{s}^2$

#### 8.1.10.2 Gravitational Potential [VIII-31]

The gravitational potential function can be expressed as

$$\Phi(R, \theta) = \frac{GM}{R} \left[ 1 - J_2 (R_E/R)^2 P_2^0 - J_4 (R_E/R)^4 P_4^0 \right], \quad (\text{VIII-10})$$

and the radial acceleration of gravity as

$$Z = - \frac{\partial \Phi}{\partial R} = \frac{GM}{R^2} \left[ 1 - 3J_2 (R_E/R)^2 P_2^0 - 5J_4 (R_E/R)^4 P_4^0 \right] \quad (\text{VIII-11})$$

where

$R_E$  = equatorial radius

$$GM = 1.267076 \times 10^8 \text{ km}^3/\text{s}^2$$

$$J_2 = 1.471 \times 10^{-2}$$

$$J_4 = -6.75 \times 10^{-4}$$

$$P_2^0 = 3/2 \sin^2 \phi - 1/2 \quad (\phi = \text{latitude})$$

$$P_4^0 = 4.375 \sin^4 \phi - 3.75 \sin^2 \phi + 0.375$$

$R$  = distance from the center of Jupiter (km).

#### 8.1.10 Additional Information

The physical properties of the planet Jupiter are discussed in detail in References VIII-3 and VIII-51.

## 8.2 Surface Environment

The interior of Jupiter is that portion of the planet below the atmospheric altitudes at which radiation of various wavelengths escapes. The only compositions capable of retaining the low mean density of Jupiter at the pressures required by its high gravity consist primarily of hydrogen and possibly include helium and other elements listed in Table VIII-1. Theoretical models of the interior have been constructed by DeMarcus [VIII-52] and refined by Peeble [VIII-53]; thermal effects are included in References VIII-54, VIII-55, and VIII-56. The models suggest the following probable conclusions:

- a. The planet is fluid either everywhere or throughout much of its bulk with the metallic phase of hydrogen being likely in the central regions; a small, heavy-element core is not excluded.
- b. The pressure, density, and temperature increase in moving inward; the rate of increase is uncertain because the equation of state is poorly known. The temperature reaches values near the center of the order of magnitude of  $10^4$ °K.

c. Energy is released to the exterior due to cooling and gravitational contraction.

d. The energy is transported by convection in most layers of the planet, and electron conduction is significant elsewhere.

e. Convection in the rotating, conducting fluid hydrogen interior is responsible for the maintenance of the planetary magnetic field. (The magnetohydrodynamic processes involved are not well understood.)

f. Although phase transitions may occur even in the probable chemically homogeneous interior, they do not constitute a rigid, solid surface at any level but are characterized by density and viscosity graduation over a radial distance scale of kilometers or greater. Therefore, the atmosphere is considered to be an extension of the interior rather than a distinct entity.

## 8.3 Satellites

Four categories of known satellites of Jupiter are listed in Table VIII-9 which specifies some of their properties. Additional photometric data for the Galilean satellites are given in subsection 8.1.7.1.1. Detailed ephemerides may be found in the American Ephemeris and Nautical Almanac [VIII-34] and the references specified there.

## REFERENCES

- VIII-1. Owen, T.: The Atmosphere of Jupiter. *Science*, vol. 167, no. 3926, 1970, p. 1675.
- VIII-2. McElroy, M. B.: Atmospheric Composition of the Jovian Planets. *J. of the Atmospheric Sciences*, vol. 26, no. 5, 1969, p. 798.
- VIII-3. Divine, N. et al.: The Planet Jupiter (1970). NASA SP-8069, August 1971.
- VIII-4. Kuiper, G. P.: Planetary Atmospheres and Their Origin. *The Atmospheres of the Earth and Planets*. G. P. Kuiper, ed., Univ. of Chicago Press, Chap. 12, 1952, p. 306.
- VIII-5. Wildey, R. L.: Structure of the Jovian Disk in the  $\nu_2$  band of Ammonia at 100 000 Å. *Astrophys. J.*, vol. 154, no. 2, 1968, p. 761.
- VIII-6. Aumann, H. H., Gillespie, C. M., Jr., and Low, F. J.: The Internal Powers and Effective Temperatures of Jupiter and Saturn. *Astrophys. J.*, vol. 157, no. 1, 1969, p. L 69.
- VIII-7. Lewis, J. S.: The Clouds of Jupiter and the  $\text{NH}_3 - \text{H}_2\text{O}$  and  $\text{NH}_3 - \text{H}_2\text{S}$  Systems. *Icarus*, vol. 10, no. 3, 1969, p. 365.
- VIII-8. Margolis, J. S., and Fox, K.: Studies of Methane Absorption in the Jovian Atmosphere. I. Rotational Temperature from the  $3\nu_3$  Band. *Astrophys. J.*, vol. 157, no. 2, 1969, p. 935.
- VIII-9. Margolis, J. S., and Fox, K.: Extension of Calculations of Rotational Temperature and Abundance of Methane in the Jovian Atmosphere. *J. of the Atmospheric Sciences*, vol. 26, no. 5, 1969, p. 863.
- VIII-10. Margolis, J. S., and Fox, K.: Studies of Methane Absorption in the Jovian Atmosphere. II. Abundance from  $3\nu_3$  Band. *Astrophys. J.*, vol. 158, no. 3, 1969, p. 1183.
- VIII-11. Gillett, F. C., Low, F. J., and Stein, W. A.: The 2.8-14-Micron Spectrum of Jupiter. *Astrophys. J.*, vol. 157, no. 2, 1969, p. 925.



## REFERENCES (Continued)

- VIII-12. Owen, T.: The Spectra of Jupiter and Saturn in the Photographic Infrared. *Icarus*, vol. 10, no. 3, 1969, p. 355.
- VIII-13. Gross, S. H., and Rasool, S. I.: The Upper Atmosphere of Jupiter. *Icarus*, vol. 3, no. 4, 1964, p. 311.
- VIII-14. Shimizu, M.: The Atomic and Molecular Processes in the Upper Atmospheres of Planets. Report of Ionosphere and Space Research in Japan, vol. 20, no. 3, 1966, p. 271.
- VIII-15. Hunten, D. M.: The Upper Atmosphere of Jupiter. *J. of the Atmospheric Sciences*, vol. 26, no. 5, 1969, p. 826.
- VIII-16. Henry, R.J.W., and McElroy, M.B.: The Absorption of Extreme Ultraviolet Solar Radiation by Jupiter's Upper Atmosphere. *J. of the Atmospheric Sciences*, vol. 26, no. 5, 1969, p. 912.
- VIII-17. Capone, L. A., and Barrow, C. H.: The Upper Atmosphere of Jupiter. *Am. Astronomical Society Bulletin*, vol. 1, no. 2, 1969, p. 214.
- VIII-18. Warwick, J. W.: Particles and Fields near Jupiter. NASA Contractor Report CR-1685, 1970.
- VIII-19. Ellis, G. R. A.: The Decametric Radio Emissions of Jupiter. *J. Research Radio Science*, vol. 69D, no. 12, 1965, p. 1513.
- VIII-20. Papadopoulos, K., and Lerche, I.: Collective Bremsstrahlung from Relativistic Electrons as a Possible Mechanism in Radio Sources. *Astrophys. J.*, vol. 158, no. 3, 1969, p. 981.
- VIII-21. Solberg, H. G., Jr.: Jupiter's Red Spot in 1967-68. *Icarus*, vol. 10, no. 3, 1969, p. 412.
- VIII-22. Solberg, H. G., Jr.: A 3-Month Oscillation in the Longitude of Jupiter's Red Spot. *Planetary and Space Sci.*, vol. 17, no. 9, 1969, p. 1573.
- VIII-23. Hide, R.: Jupiter's Great Red Spot. *Scientific American*, vol. 218, 1968, p. 74.

## REFERENCES (Continued)

- VIII-24. Lewis, J. S.: The Clouds of Jupiter and the  $\text{NH}_3\text{-H}_2\text{O}$  and  $\text{NH}_3\text{-H}_2\text{S}$  Systems. *Icarus*, vol. 10, no. 3, 1969, p. 365.
- VIII-25. Washburn, E. W., ed.: *International Critical Tables*. McGraw-Hill, New York, vol. 3, 1928.
- VIII-26. Lange, N. A., ed.: *Handbook of Chemistry*. Revised Tenth Edition, McGraw-Hill, New York, 1967.
- VIII-27. Chapman, C. R.: Jupiter's Zonal Winds: Variation with Latitude. *J. of the Atmospheric Sciences*, vol. 26, no. 5, 1969, p. 986.
- VIII-28. Peek, B. M.: *The Planet Jupiter*. Faber & Faber, London, 1958.
- VIII-29. Hide, R.: Dynamics of the Atmospheres of the Major Planets with an Appendix on the Viscous Boundary Layer at the Rigid Bounding Surface of an Electrically-Conducting Rotating Fluid in the Presence of a Magnetic Field. *J. of the Atmospheric Sciences*, vol. 26, no. 5, p. 841.
- VIII-30. Ingersoll, A. P., and Cuzzi, J. N.: Dynamics of Jupiter's Cloud Bands. *J. of the Atmospheric Sciences*, vol. 26, no. 5, 1969, p. 981.
- VIII-31. Smith, R. E., and Weidner, D. K.: *Space Environment Criteria Guidelines for Use in Space Vehicle Development (1968 Revision)*. NASA TMX-53798, Marshall Space Flight Center, Huntsville, Alabama, 1968, p. VIII-1.
- VIII-32. Anon.: *Solar Electromagnetic Radiation*. NASA SP-8005, Revised May 1971.
- VIII-33. Allen, C. W.: *Astrophysical Quantities (Second Edition)*. Athlone Press, Univ. of London, 1963.
- VIII-34. *The American Ephemeris and Nautical Almanac*. U. S. Government Printing Office.

## REFERENCES (Continued)

- VIII-35. Anon.: Meteoroid Environment Model-1970 (Interplanetary and Planetary). NASA SP-8038, June 1970.
- VIII-36. Carr, T. D., and Gulkis, S.: The Magnetosphere of Jupiter. Annual Review of Astronomy and Astrophysics, vol. 7, 1969, p. 577.
- VIII-37. Dickel, J. R.: Microwave Observations of Jupiter. Magnetism and the Cosmos, W. R. Hindmarsh, F. J. Lowes, P. H. Roberts, and S. K. Runcorn, editors, American Elsevier Publ. Co., 1967, p. 296.
- VIII-38. Goldreich, P., and Lynden-Bell, D.: Io, A Jovian Unipolar Inductor. Astrophys. J., vol. 156, no. 1, 1969, p. 59.
- VIII-39. Warwick, J. W.: Dynamic Spectra of Jupiter's Decametric Emission, 1961. Astrophys. J., vol. 137, no. 1, 1963, p. 41.
- VIII-40. Luthey, J. L., and Beard, D. B.: The Electron Energy and Density Distribution in the Jovian Magnetosphere. University of Kansas, 1970.
- VIII-41. Berge, G. L.: An Interferometric Study of Jupiter's Decimeter Radio Emission. Astrophys. J., vol. 146, no. 3, 1966, p. 767.
- VIII-42. Ellis, G. R. A.: The Radio Emissions from Jupiter and the Density of Jovian Exosphere. Australian J. of Physics, vol. 16, 1963, p. 74.
- VIII-43. Melrose, D. B.: Rotational Effects on the Distribution of Thermal Plasma in the Magnetosphere of Jupiter. Planetary & Space Sci., vol. 15, no. 2, 1967, p. 381.
- VIII-44. Haffner, J. W.: The Magnetospheres of Jupiter and Saturn. AIAA Paper No. 71-30, 1971.

## REFERENCES (Concluded)

- VIII-45. West, W. S. et al.: Spacecraft Charge Buildup Analysis. NASA SP-276, 1971.
- VIII-46. Haffner, J. W.: Radiation and Shielding in Space. Academic Press, 1967.
- VIII-47. Fanselow, J. L.: The Primary Cosmic-Ray Electron Spectrum Between 0.09 and 8.4 BeV in 1965. *Astrophys. J.*, vol. 152, 1968, p. 783.
- VIII-48. McDonald, F. B., editor: Solar Proton Manual. NASA TR R-169, 1963.
- VIII-49. Englade, R. C.: A Computational Model for Solar Flare Particle Propagation. University of Chicago, July 1970.
- VIII-50. Hundhausen, A. J.: Direct Observations of Solar-Wind Particles. *Space Science Reviews*, vol. 8, No. 5/6, 1968, p. 690.
- VIII-51. Michaux, C. M., Handbook of the Physical Properties of the Planet Jupiter. NASA SP-3031, 1967.
- VIII-52. DeMarcus, W. C.: The Constitution of Jupiter and Saturn. *Astronom. J.*, vol. 63, no. 1, 1968, p. 2.
- VIII-53. Peebles, P. J. E.: The Structure and Composition of Jupiter and Saturn. *Astrophys. J.*, vol. 140, no. 1, 1964, p. 328.
- VIII-54. Smoluchowski, R.: Internal Structure and Energy Emission of Jupiter. *Nature*, vol. 215, no. 5102, 1967, p. 691.
- VIII-55. Hubbard, W. B.: Thermal Structure of Jupiter. *Astrophys. J.*, vol. 152, no. 3, 1968, p. 745.
- VIII-56. Hubbard, W. B.: Thermal Models of Jupiter and Saturn. *Astrophys. J.*, vol. 155, no. 1, 1969, p. 333.

## SECTION IX. SATURN

### 9.1 General

Saturn resembles Jupiter in many respects: the large size, the color bands, and the large number of satellites. Saturn ranks second to Jupiter in size and number of satellites, and has the lowest mean density and greatest oblateness of any planet in the solar system. The combination of a large radius and small density produces a gravitational force on the surface slightly greater than that of the earth.

### 9.2 Composition of the Atmosphere

The atmosphere of Saturn has been estimated from spectroscopic observations to consist of  $\text{CH}_4$ ,  $\text{NH}_3$ ,  $\text{O}_3$ , and  $\text{SO}_2$ . Hydrogen and helium have not been detected spectroscopically; however, it is reasonable to believe that they may be present. Neon and argon probably exist also. Measured infrared radiometer temperature of Saturn at the top of the ammonia clouds is about  $125^\circ\text{K}$ , while microwave radiation at a wavelength of 3.4 cm shows  $106^\circ \pm 21^\circ\text{K}$ . The blackbody temperature as calculated from the solar radiation is  $107^\circ\text{K}$ . Since methane can solidify at these temperatures, it is possible that there may be methane clouds of the cirrus type below the ammonia clouds.

### 9.3 Radiation

Some indications [IX-1] exist that Saturn emits synchrotron radiation in the decimeter wavelength region resulting from the relativistic electrons trapped in the radiation belt, or belts, surrounding the planet. This synchrotron radiation implies that Saturn has a magnetic field that is being generated by a dynamo mechanism resulting from the rotating planet and its liquid core. The radiation, however, has been noted to exhibit a plane of polarization that is perpendicular to the equator rather than parallel to it. This tends to imply that the magnetic axis of the planet is at right angles to the axis of rotation. However, some indications [IX-1] exist that the rings of Saturn may be removing electrons that are in the equatorial region of the radiation belts, thus creating this particular type of field. The visual albedo has been estimated to be 0.76.

## 9.4 Astrodynamic Constants (Epoch 1960.0) [IX-2]

Distance from sun (average)	$1.42699 \times 10^9$ km
Eccentricity of orbit <sup>1</sup>	0.0556818
Inclination of orbit to ecliptic <sup>1</sup>	$2^{\circ} 29' 23.7''$
Orbital period (sidereal) <sup>1</sup>	10759.205 days
Radius (equatorial)	60 401.0 km
Mass ratio (sun/planet)	$3499.2 \pm 0.4$
Flattening (dynamic) <sup>1</sup>	1:10.21
Average density <sup>1</sup>	0.679 g/m <sup>3</sup>
Rotational period <sup>1</sup>	10 hr 14 min
Gravitational parameter	$3.792651 \times 10^7$ km <sup>3</sup> /s <sup>2</sup>

## 9.5 Telescopic Appearance

Saturn, as seen through the telescope, is similar to Jupiter in that the general appearance and albedo are about the same. Both planets have satellites (they appear to be flattened) and exhibit bands parallel to the equator. The brightest band on Saturn is the equatorial band, which is yellowish in color. A greenish band surrounds the poles and is less distinct than the band on Jupiter. These bands are somewhat variable with respect to their intensities as well as to latitude in location and dimension. Occasionally, signs of activity exist in the atmosphere, and clouds or bright spots are seen in the equatorial zone. There does not seem to be a permanent feature as the Red Spot on Jupiter. The period of rotation at the equator is 10 hours and 14 minutes. Although the period of rotation at the poles is considered to be longer than at the equator, it is not exactly known. The most striking feature is the rings which vary in width caused by the equatorial plane being inclined at a large angle to the orbital plane and the plane of the ecliptic. The rings are discussed in the following paragraph,

- 
1. Krause, Helmut G. L.: Astronomical Constants of the Solar System. MSFC, Huntsville, Alabama, 1965 (Unpublished).

## 9.6 Rings [IX-1]

Saturn has three concentric rings in the plane of the equator, designated A, B, and C. The diameter of the entire ring system is 274 000 km. The A ring has an outer diameter of 274 000 km and a width of approximately 16 000 km. This ring is separated from the B ring by a gap of approximately 4000 km. The B or bright ring has a width of 26 000 km. The C or inner ring, called the Crepe, is about 21 000 km in width. Measurements have indicated the thickness of the rings is not more than 16 to 19 km and could be even less. These measurements were made during the time that the rings appear to be edgewise when viewed from the earth. The mass of these rings is not known, but based on observations of perturbations in the orbits of the satellites of Saturn which would be caused by these rings, their mass is then indicated to be as an upper limit somewhat less than the mass of the moon. Infrared spectra suggest that the rings are composed of particles of ice or solid ammonia.

## 9.7 Satellites

Table IX-1 is a summary of data for the satellites of Saturn. Titan is the only satellite in the solar system to have an atmosphere recognized by Kuiper in his spectroscopic studies.

TABLE IX-1. DATA SUMMARY FOR SATELLITES OF SATURN<sup>a</sup>

Satellite	Discovery		Sidereal Period of Revolution (P <sub>sid</sub> )		Mean Synodic Period of Revolution P <sub>syn</sub>		Orbital Mean Motion n <sub>sid</sub> (°/d)	Eccen- tricity (e)
	Discoverer	Date	d	Mean Solar Time	d	Mean Solar Time		
VII Mimas	W. Herschel	18 Sept. 1789	0.942 421 9	0 22 37 05.25	0.942 505	0 22 37 12.4	381.994 519	0.020 1
VI Enceladus	W. Herschel	29 Aug. 1789	1.370 217 8	1 08 53 06.82	1.370 392	1 08 53 21.9	262.731 954	0.004 44
V Tethys	J. D. Cassini	21 March 1684	1.887 802 5	1 21 18 26.14	1.888 134	1 21 18 54.8	190.697 915	0.000 0
IV Dione	J. D. Cassini	21 March 1684	2.736 915 9	2 17 41 09.53	2.737 612	2 17 42 09.7	131.534 915	0.002 21
III Rhea	J. D. Cassini	23 Dec. 1672	4.517 502 6	4 12 25 12.23	4.519 400	4 12 27 56.2	79.690 048	0.000 98
I Titan	C. Huyghens	25 March 1655	15.945 452	15 22 41 27.1	15.969 04	15 23 15 25	22.576 971	0.028 9
VIII Hyperion	G. P. Bond	16 Sept. 1848	21.276 665	21 06 38 23.9	21.318 82	21 07 39 06	16.919 945	0.104
II Iapetus	J. D. Cassini	25 Oct. 1671	79.330 82	79 07 56 23	79.920 09	79 22 04 56	4.537 959	0.028 28
IX Phoebe	W. H. Pickering	16 Aug. 1898	550.441 6	550 10 35 54	523.651 6	523 15 38 18	-0.654 02	0.163 26
X Janus	A. Dolitus	1 Jan. 1967		17.975 hr				

Satellite	Apparent Distance			Mean Distance from Planet (a)			Inclination of Orbit to Planet's Equator (R)	Visual Magnitude at Mean Opposition Distance (m <sub>vis</sub> )	Radius R (km)	Mass M (Primary=1)	Visual Albedo (A <sub>vis</sub> )
	At Unit Distance	As Seen From Sun	At Mean Opposition	(10 <sup>-3</sup> AU)	(10 <sup>3</sup> km)	In Eq. Radii of the Primary					
VII Mimas	255.89	26.826	29.968	1.240 6	185.59	3.067	1 31.0	12.1	250	1:14 960 000	0.29
VI Enceladus	328.29	34.416	38.447	1.591 6	238.10	3.935	0 01.4	11.77	300	1: 7 900 000	0.32
V Tethys	406.40	42.605	47.594	1.970 3	294.75	4.872	1 05.56	10.27	500	1: 876 400	0.49
IV Dione	520.51	54.567	60.958	2.523 5	377.51	6.240	0 01.40	10.44	500	1: 548 000	0.55
III Rhea	726.89	76.203	85.127	3.524 1	527.20	8.714	0 20.49	9.76	800	1: 250 000	0.48
I Titan	1 684.35	176.578	197.257	8.166 0	1 221.62	20.191	0 20.00	8.39	2400	1: 4 147	0.12
VIII Hyperion	2 044.4	214.32	239.42	9.911 5	1 482.8	24.51	0 25.34	14.16	200	1: 5 000 000	
II Iapetus	4 908.6	514.59	574.86	23.797 6	3 360.1	58.84	14 43	11.03 (10.1-11.9)	600		
IX Phoebe	17 861.0	1 872.45	2 091.74	86.592 6	12 954	214.11	150	14.5	120		
X Janus					~97.09				~175		

a. Krause, Helmut G. L.: Astronomical Constants of the Solar System.  
MSFC, Huntsville, Alabama, 1965 (Unpublished).



## REFERENCES

- IX-1. Glasstone, Samuel: The Sourcebook on the Space Sciences. D. Van Nostrand Co., Inc., 1965.
- IX-2. Melbourne, W. G., Mulholland, J. D., and Sturms, F. M., Jr.: Constants and Related Information for Astrodynamic Constants, 1968. Technical Report 32-1306, Jet Propulsion Lab., July 1968.



## SECTION X. URANUS

### 10.1 General

Uranus, when viewed through the telescope, exhibits a greenish color. This planet is unusual in that its equator is inclined at nearly right angles to the plane of the ecliptic. At certain times a whitish equatorial zone and bands, similar to Jupiter and Saturn but somewhat fainter, can be observed.

The atmosphere of this planet, based on spectroscopic data, is composed of large proportions of methane. In addition, some bands of molecular hydrogen have been detected. Other atmospheric constituents [X-1] which have not been identified may be ammonia, helium, neon, and argon.

### 10.2 Astrodynamic Constants (Epoch 1960.0) [X-1]

Distance from sun (average)	$2869.62 \times 10^6$ km
Eccentricity of orbit <sup>1</sup>	0.0472095
Inclination of orbit to ecliptic <sup>1</sup>	$0^{\circ} 46' 23.0''$
Orbital period (sidereal) <sup>1</sup>	30 685.5 days
Radius (equatorial)	23 535.0 km
Mass ratio (sun/planet)	$22\,930 \pm 6$
Flattening (dynamic) <sup>1</sup>	1:16
Average density <sup>1</sup>	$1.440 \text{ g/m}^3$
Rotational period <sup>1</sup>	10 hr 49 min
Gravitational parameter	$5.787722 \times 10^6 \text{ km}^3/\text{s}^2$

---

1. Krause, H. G. L., "Astronomical Constants on the Solar System," MSFC, Huntsville, Alabama, 1965 (Unpublished).

### 10.3 Satellites

Uranus has five satellites. The nearest satellite to Uranus, Miranda, or V, was not discovered until 1948 by Kuiper. Tabular data for the satellites are shown in Table X-1.

TABLE X-1. DATE SUMMARY FOR SATELLITES OF URANUS<sup>a</sup>

Satellite	Discovery		Siderial Period of Revolution (P <sub>sid</sub> )		Mean Synodic Period of Revolution (P <sub>syn</sub> )		Orbital Mean Motion, N <sub>sid</sub> (°/d)	Eccen- tricity (e)
	Discoverer	Date	d	Mean Solar Time	d	Mean Solar Time		
V Miranda	G. P. Kuiper	1 March 1948	1.414	1 09 56	1.414	1 09 56	254.6	0.005
III Ariel	W. Lassell	24 Oct. 1851	2.520 383	2 12 29 21.1	2.520 60	2 12 29 40	142.835 43	0.002 8
IV Umbriel	W. Lassell	24 Oct. 1851	4.144 183	4 03 27 37.4	4.144 73	4 03 28 25	86.868 75	0.003 5
I Titania	W. Herschel	11 Jan. 1787	8.705 876	8 16 56 27.7	8.708 33	8 17 00 00	41.351 38	0.002 4
II Oberon	W. Herschel	11 Jan. 1787	13.463 262	13 11 07 05.8	13.469 17	13 11 15 36	26.739 43	0.000 7

Satellite	Apparent Distance (arc-sec)			Mean Distance from Planet (a)			Inclination of Orbit to Planet's Equator (g)	Visual Magnitude at Mean Opposition Distance (M <sub>vis</sub> )	Radius, R (km)	Mass, M (Primary=1)	Visual Albedo (A <sub>vis</sub> )
	At Unit Distance	As Seen From Sun	At Mean Opposition	(10 <sup>-3</sup> AU)	(10 <sup>3</sup> km)	In Eq. Radii of the Primary					
I Miranda	179.9	9.38	9.89	0.872	130.5	5.25	0	16.5	80	1: 1 000 000	
III Ariel	264.43	13.785	14.544	1.282 0	191.78	7.72	0	14.4	300	1: 70 000	
IV Umbriel	368.38	19.205	20.261	1.786 0	267.18	10.75	0	15.3	200	1: 170 000	
I Titania	604.42	31.510	33.243	2.930 3	438.37	17.64	0	14.01	500	1: 20 000	
II Oberon	808.29	42.138	44.456	3.918 7	586.23	23.59	0	14.20	400	1: 34 000	

a. Krause, Helmut G. L.: Astronomical Constants of the Solar System.  
MSFC, Huntsville, Alabama, 1965 (Unpublished).

## REFERENCES

- X-1. Glasstone, Samuel: The Sourcebook on the Space Sciences. D. Van Nostrand Co., Inc., 1965.

## BIBLIOGRAPHY

Melbourne, W. G., Mulholland, J. D., Sjogren, W. L., and Sturms, F. M., Jr.: Constants and Related Information for Astrodynamic Constants, 1968. Technical Report 32-1306, Jet Propulsion Lab., July 1968.

## SECTION XI. NEPTUNE

### 11.1 General

Neptune appears as a small greenish disk when viewed through the telescope. The location of this planet was predicted by Adams in England in 1846 and LeVERRIER in France independently in the same year. Galle, in 1846, the German astronomer, used these position data and discovered Neptune.

The atmosphere of Neptune as indicated by spectroscopic studies is chiefly methane. Neptune has the largest amount of methane detected for any planet [XI-1]. Hydrogen has also been identified spectroscopically. Although other gases have not been identified, they may be helium, neon, or argon.

### 11.2 Astrodynamic Constants (Epoch 1960.0) [XI-2]

Distance from sun (average)	$4496.64 \times 10^6$ km
Eccentricity of orbit <sup>1</sup>	0.0085747
Inclination of orbit to ecliptic <sup>1</sup>	1° 46'25.5"
Orbital period (sidereal) <sup>1</sup>	60 189.5 days
Radius (equatorial)	22 324.0 km
Mass ratio (sun/planet)	19 260 ± 100
Flattening (dynamic) <sup>1</sup>	1:50
Average density	1.597 g/m <sup>3</sup>
Rotational period	14 hr
Gravitational parameter	$6.890574 \times 10^6$ km <sup>3</sup> /s <sup>2</sup>

### 11.3 Satellites

Tabulated data for satellites are given in Table XI-1.

---

1. Krause, H. G. L., "Astronomical Constants of the Solar System  
MSFC Huntsville, Alabama, 1965 (Unpublished).

TABLE XI-1. DATA SUMMARY FOR SATELLITES OF NEPTUNE<sup>a</sup>

Satellite	Discovery		Siderial Period of Revolution ( <sup>P</sup> <sub>sid</sub> )		Mean Synodic Period of Revolution ( <sup>P</sup> <sub>syn</sub> )		Orbital Mean Motion N <sub>sid</sub> (°/d)	Eccen- tricity (e)
	Discoverer <sup>1</sup>	Date	d	Mean Solar Time	d	Mean Solar Time		
I Triton	W. Lassell	10 Oct. 1846	5.876 833	5 21 02 38.4	5.876 452	5 21 03.25	-61.257 48	0.000 0
II Nereid	G. P. Kuiper	10 May 1949	359.881	359 21 09	361.315	361 07 34	1.000 33	0.749 34

Satellite	Apparent Distance (arc-sec)			Mean Distance from Planet (a)			Inclination of Orbit to Planet's Equator (g)	Visual Magnitude at Mean Opposition Distance ( <sup>M</sup> <sub>vis</sub> )	Radius, R (km)	Mass, M (Primary=1)	Visual Albedo (A <sub>vis</sub> )
	At Unit Distance	As Seen From Sun	At Mean Opposition	(10 <sup>-3</sup> AU)	(10 <sup>3</sup> km)	In Eq. Radii of the Primary					
I Triton	489.82	16.296	16.857	2.374 7	355.25	14.21	159 57	13.55	2 100	1: 757	0.21
II Nereid	7 668.86	255.137	263.917	37.179 7	5 562.03	222.48	27 48.4	18.7	150	1: 3 000 000	

a. Krause, Helmut G. L.: Astronomical Constants of the Solar System.  
MSFC, Huntsville, Alabama, 1965 (Unpublished).



## REFERENCES

- XI-1. Glasstone, Samuel: Sourcebook on the Space Sciences. D. Van Nostrand Co., Inc., 1965.
- XI-2. Melbourne, W. G., Mulholland, J. D., Sjogren, W. L., and Sturms, F. M., Jr.: Constants and Related Information for Astrodynamic Constants, 1968. Technical Report 32-1306, Jet Propulsion Laboratory, July 1968.



## SECTION XII. PLUTO

### 12.1 General

The planet Pluto is the farthest known planet from the sun. Orbital data, brightness, and color give some indication of its characteristics. Astronomers began to search for this planet when the perturbations noted in the orbit motion of Uranus could not be explained even after the influence of Neptune had been considered. Around 1914, Percival Lowell and W. H. Pickering agreed that some other body was causing this perturbation. Both men searched for the object, but it was not discovered until 1930 by C. Tombaugh. Pluto has the most highly eccentric orbit of any planet in our solar system, and at the perihelion, it orbits inside the orbit of Neptune. This planet is so far away from the sun that the sun would appear as a star in the distance. The spherical blackbody average temperature for Pluto has been estimated to be  $40^{\circ}\text{K}$ .

### 12.2 Astrodynamic Constants (Epoch 1960.0) [XII-1]

Distance from sun (average)	$5911.85 \times 10^6 \text{ km}$
Eccentricity of orbit <sup>1</sup>	0.2486438
Inclination of orbit to ecliptic <sup>1</sup>	$17^{\circ} 08' 38.4''$
Orbital period (sidereal) <sup>1</sup>	90737.2 days
Radius (equatorial)	7016.0 km
Mass ratio (sun/planet)	$1\,812\,000 \pm 40\,000$
Flattening (dynamic)	Unknown
Average density <sup>1</sup>	$5.47 \text{ g/m}^3$
Rotational period	6.39 days
Gravitational parameter	$7.324088 \times 10^5 \text{ km}^3/\text{s}^2$

---

1. Krause, H. G. L., "Astronomical Constants of the Solar System," MSFC, Huntsville, Alabama, 1965 (Unpublished).

## REFERENCE

- XII-1. Melbourne, W. G., Mulholland, J. D., Sjogren, W. L., and Sturms, F. M., Jr.: Constants and Related Information for Astrodynamic Constants, 1968. Technical Report 32-1306, Jet Propulsion Laboratory, July 1968.

## APPENDIX A. SOLAR CYCLE PREDICTION TECHNIQUE

Current analyses have shown that properties of the natural atmospheric environment are dependent upon solar activity. This appendix provides a brief description of the method that is currently used at the Marshall Space Flight Center to predict future levels of solar activity.

In 1949, Lincoln and McNish [A-1] suggested that the prediction of a future solar cycle, based on the mean approximation of all past solar cycles, could be improved by adding to the mean a correction proportional to the departure of the earlier values of the cycle from the mean cycle. However, this technique was not recommended for making predictions longer than 1 year in the future.

Using data from two additional solar cycles, Lockheed [A-2] modified the Lincoln-McNish technique so that the Zürich-smoothed sunspot number could be predicted for 10 years in advance, and at quarterly rather than yearly intervals. Recently, another version of the original technique has been programmed that permits evaluation at quarterly, monthly, or 27-day intervals. This allows us to make predictions for shorter intervals and also to incorporate more recent data into the predictions.

The time within each cycle is measured from the minimum which defines the beginning of a cycle. The data are arranged in matrix form; each row consists of a solar cycle and each column consists of the  $j$ th year after the origin of the cycle. A mean cycle is determined by averaging each  $j$ th point of all cycles. The deviation of each  $j$ th point in all cycles from the mean at that point is computed. The products of the deviation columns are summed, and the matrix inversion technique is used to calculate prediction coefficients.

An updated prediction of future solar activity parameters is issued each month by the Aerospace Environments Division, Space Environment Branch, S&E-AERO-YS, MSFC. Table A-1 contains an example of such a prediction based on the data available in December 1971. To ensure that the most current data are used in the space vehicle design studies, copies of the most recent update will be provided upon request.

The following paragraphs are a mathematical description, in terms of input and output, of the sunspot prediction program currently in use at the Marshall Space Flight Center.

TABLE A-1. PREDICTION OF SUNSPOT NUMBERS, SOLAR FLUX AND  
GEOMAGNETIC INDEX (USING DATA AVAILABLE  
IN DECEMBER 1971)

Time	Sunspots		10.7 cm Flux		K <sub>P</sub>	
	Nominal	Percentile (95.)	Nominal	Percentile (95.)	Nominal	Percentile (95.)
1971.583	59.80	66.06	109.33	114.50	2.20	3.02
1971.833	54.16	64.86	104.68	113.51	2.20	3.02
1972.083	51.20	63.49	102.24	112.38	2.20	3.02
1972.333	47.91	60.69	99.53	110.07	2.20	3.02
1972.583	42.82	57.54	95.33	107.47	2.20	3.02
1972.833	39.36	55.85	92.47	106.08	2.20	3.02
1973.083	35.08	53.23	88.94	103.91	2.20	3.02
1973.333	31.67	49.97	86.13	101.22	2.20	3.02
1973.583	29.27	46.97	85.56	98.75	2.20	3.02
1973.833	25.65	42.18	83.39	94.79	2.20	3.02
1974.083	22.48	38.02	81.49	91.37	2.20	3.02
1974.333	19.68	35.46	79.81	89.26	1.80	3.02
1974.583	17.91	34.22	78.74	88.23	1.80	3.02
1974.833	15.64	31.72	77.38	86.17	1.80	3.02
1975.083	14.86	31.21	76.91	85.75	1.80	3.02
1975.333	15.23	36.09	77.14	89.78	1.80	3.02
1975.583	16.17	45.90	77.70	97.87	1.80	3.02
1975.833	18.96	60.34	79.38	109.78	1.80	3.02
1976.083	22.68	74.61	81.61	122.14	2.20	3.54
1976.333	28.11	89.84	84.87	136.88	2.20	3.54
1976.583	34.22	103.73	88.23	150.31	2.20	3.54
1976.833	42.18	117.74	94.80	163.86	2.20	3.54
1977.083	50.48	130.40	101.65	176.09	2.20	3.54
1977.333	57.47	138.11	107.42	183.55	2.20	3.54
1977.583	64.16	145.60	112.93	190.80	2.20	3.54
1977.833	70.28	150.08	117.96	195.13	2.20	3.54
1978.083	78.27	161.31	125.68	205.99	2.20	3.54
1978.333	83.94	169.93	131.17	214.32	2.80	3.54
1978.583	89.02	173.29	136.08	217.57	2.80	3.54
1978.833	92.16	173.89	139.12	218.15	2.80	3.54
1979.083	92.65	170.06	139.59	214.45	2.80	3.54
1979.333	94.35	168.14	141.23	212.59	2.80	3.54
1979.583	93.56	164.21	140.47	208.80	2.80	3.54
1979.833	92.58	160.20	139.53	204.91	2.80	3.54
1980.083	89.10	149.08	136.16	194.16	2.80	3.54
1980.333	84.57	139.32	131.78	184.73	2.80	3.54
1980.583	83.17	133.44	130.43	179.04	2.80	3.54
1980.833	80.11	123.88	127.46	169.79	2.20	3.54
1981.083	77.60	117.20	125.03	163.33	2.20	3.54
1981.333	74.50	109.56	122.04	155.94	2.20	3.54
1981.583	68.97	99.99	116.90	146.69	2.20	3.54
1981.833	63.62	92.16	112.49	139.12	2.20	3.54
1982.083	59.11	85.88	108.76	133.04	2.20	3.54
1982.333	55.26	79.80	105.59	127.16	2.20	3.54
1982.583	51.70	76.12	102.66	123.61	2.20	3.02
1982.833	46.99	71.76	98.77	119.39	2.20	3.02
1983.083	42.94	66.62	95.43	114.43	2.20	3.02
1983.333	40.17	63.70	93.14	112.55	2.20	3.02
1983.583	37.16	60.05	90.66	109.54	2.20	3.02
1983.833	35.23	56.77	89.06	106.84	2.20	3.02
1984.083	32.91	57.16	87.15	107.15	2.20	3.02
1984.333	29.27	53.41	85.56	104.06	2.20	3.02
1984.583	26.71	54.89	84.03	105.28	2.20	3.02
1984.833	24.92	59.08	82.95	108.74	2.20	3.02
1985.083	23.43	62.42	82.06	110.36	2.20	3.02
1985.333	22.97	65.29	81.78	113.13	2.20	3.02
1985.583	22.82	67.84	81.69	115.61	2.20	3.02
1985.833	23.14	70.39	81.88	118.07	2.20	3.02
1986.083	24.12	72.91	82.47	120.51	2.20	3.54

## Input Data

The input to the program includes the Zürich smooth sunspot numbers for cycles 1 through 19 and as many values in the 20th cycle as are available. These values were obtained by the Zürich smoothing method described in the following equation:

$$R_{\ell} = \frac{1}{12} \left[ \sum_{k=\ell-5}^{\ell+5} R_k + \frac{R_{\ell-6} + R_{\ell+6}}{2} \right],$$

where  $R_{\ell}$  is the Zürich-smoothed sunspot at the  $\ell$ th month and  $R_k$  is the monthly relative sunspot number for the  $k$ th month. The monthly mean values and the Zürich-smoothed sunspot numbers for cycles 1 through 19 and the values of the 20th cycle that are available may be obtained from the Aerospace Environment Division, Marshall Space Flight Center.

The smoothed sunspot numbers,  $R_{ij}$ , were obtained for the first month in each cycle and at 3-month intervals thereafter for 12 years. The month and year which currently define the first point in each cycle are defined below.

Cycle No.	First Month	Cycle No.	First Month
1	Mar. 1755	11	Mar. 1867
2	May 1766	12	Dec. 1878
3	June 1775	13	Feb. 1890
4	Sept. 1784	14	Jan. 1902
5	Apr. 1798	15	Aug. 1913
6	July 1810	16	July 1923
7	Apr. 1823	17	Sept. 1933
8	Nov. 1833	18	Feb. 1944
9	July 1843	19	Apr. 1954
10	Dec. 1855	20	Oct. 1964

These data defining the beginning of the cycle were obtained from Reference A-3 for cycles 1 through 19. The beginning date of cycle 20 was computed from the Journal of Geophysical Research Data.

## Computational Procedure

Let  $R_{ij}$  denote the smoothed Zürich sunspot number for the  $i$ th cycle and the  $j$ th time point within the cycle. For the initial point within the cycle,  $j = 1$  and the  $j$ th time points is  $j - 1$  quarters later in time. The mean value for any given point within the cycle is given by

$$\bar{R}_j = \frac{1}{n - n_o} \sum_{i=n_o}^{n-1} R_{ij} ,$$

where  $n$  is the subscript denoting the current cycle and  $n_o$  is the subscript for the first cycle to be used in the regression model. The deviations,  $\Delta R_{ij}$ , from this mean are

$$\Delta R_{ij} = R_{ij} - \bar{R}_j .$$

The first point to be predicted within the  $n$ th cycle will be denoted by the subscript  $m$ . The first known value in the  $n$ th cycle to be used in the prediction will be designated by the subscript  $m_o$ . The sunspot numbers,  $R_{n, m_o}, R_{n, m_o+1} \dots R_{n, m-1}$  will be used to predict  $R_{n, m}, R_{n, m+1}, \dots, R_{n, M}$ , where  $M$  denotes the last sunspot value to be predicted. The following matrix notation will simplify the description of the procedure:

$$a_{jk} = \sum_{i=n_o}^{n-1} \Delta R_{ij} \Delta R_{ik} .$$

$$A = \left\| \begin{matrix} a_{jk} \end{matrix} \right\| , \quad j, k = m_o, m_o + 1, \dots, m - 1$$

$$B = \left\| \begin{matrix} a_{jk} \end{matrix} \right\| , \quad \begin{matrix} j = m_o, m_o + 1, \dots, m - 1 \\ k = m, m + 1, \dots, M \end{matrix}$$



$$m_o = \begin{cases} 1, & m \leq 8 \\ m - 8, & m > 8 \end{cases}.$$

The predicted values are defined by the following  $1 \times (M - m + 1)$  matrix:

$$R_p = \begin{bmatrix} R_{nm} & R_{n\ m+1} & \dots & R_{nM} \end{bmatrix}$$

$$\bar{R} = \begin{bmatrix} \bar{R}_m & \bar{R}_{m+1} & \dots & \bar{R}_M \end{bmatrix}$$

$$\Delta R = \begin{bmatrix} \Delta R_{nm} & \Delta R_{n\ m+1} & \dots & \Delta R_{nM} \end{bmatrix},$$

where

$$R_p = \bar{R} + \Delta R.$$

The values in the  $n$ th cycle that are to be used in the prediction are included in the following  $1 \times (m - m_o)$  matrix:

$$\Delta R_o = \begin{bmatrix} \Delta R_{nm_o} & \Delta R_{nm_o+1} & \dots & \Delta R_{nm-1} \end{bmatrix}.$$

The matrix of predicted values is then described by the following equation:

$$R_p = \bar{R} + \Delta R_o A^{-1}B,$$

where

$$A A^{-1} = I \quad .$$

The current MSFC prediction routine actually predicts Zürich smoothed sunspot numbers. The 10.7 cm solar flux is obtained from the following equations: If  $RZ \geq 70$ ,

$$F = 50 + 0.967 RZ.$$

If  $30 \leq RZ < 70$ ,

$$F = 60 + 0.825 RZ.$$

If  $RZ < 30$ ,

$$F = 68 + 0.6 RZ.$$

The term  $RZ$  is the Zürich-smoothed relative sunspot numbers and  $F$  is the 10.7-cm solar flux. The geomagnetic index,  $K_p$ , is obtained from the following equations: If  $F \geq 130$ ,

$$K_p = 2.8.$$

If  $80 \leq F < 130$ ,

$$K_p = 2.2.$$

If  $F < 80$ ,

$$K_p = 1.8.$$

## Computer Output

The computer printout of this program contains predicted nominal and  $+2\sigma$  values and  $-2\sigma$  values for (1) sunspot numbers, (2) 10.7-cm solar flux, and (3)  $K_p$ , 3-hour geomagnetic index for the remainder of cycles 20 through 21 as shown in Table A-1. Figure A-1 is a graph of the long-range prediction of the quarterly smoothed sunspots showing the nominal, and 95-percentile values.

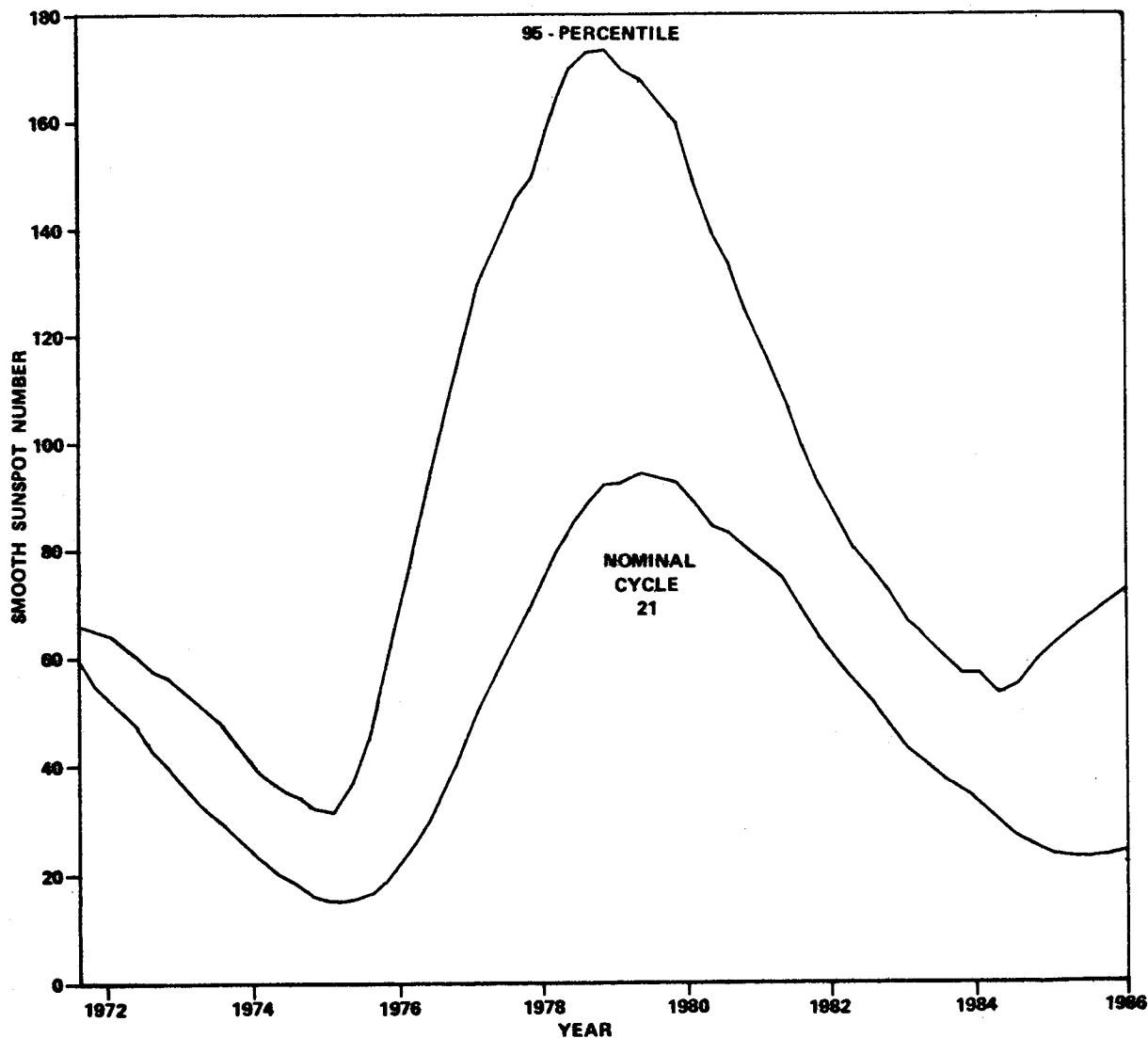


Figure A-1. Prediction of sunspot numbers (using data available in October 1971).

Since the Lincoln-McNish technique [A-1] was originally developed to predict sunspot numbers for only 1 year in advance, it seems at first unreasonable to modify this technique to obtain predictions 15 years in advance. However, after a very detailed analysis of all available data, it was concluded that the 15-year predictions are in excellent agreement with the statistical mean and  $2\text{-}\sigma$  values. These statistical parameters for sunspot numbers and 10.7-cm solar flux are given in Table A-2.

TABLE A-2. MEAN AND STANDARD DEVIATION OF SUNSPOT NUMBERS  
AND 10.7-cm SOLAR FLUX

Quarter Number	Cycles 1 thru 19, Sunspots		Cycles 1 thru 19, 10.7-cm Flux		Cycles 1 thru 18, 10.7-cm Flux	
	Mean	St. Dev.	Mean	St. Dev.	Mean	St. Dev.
1	5.12	3.28	71.07	1.97	71.13	2.01
2	6.49	3.47	71.88	2.08	71.92	2.13
3	8.55	4.10	73.13	2.46	73.15	2.53
4	12.03	5.53	75.22	3.35	75.16	3.42
5	17.07	7.99	78.39	4.98	78.17	5.03
6	23.48	12.20	82.86	8.21	82.18	7.90
7	32.10	17.19	89.26	12.53	87.81	11.21
8	41.97	23.03	96.99	18.02	94.77	15.78
9	52.81	29.60	105.97	24.61	102.70	20.87
10	62.36	35.32	114.15	30.56	109.90	25.34
11	69.88	39.12	120.77	34.62	116.33	29.86
12	79.05	43.42	129.05	39.22	124.30	34.56
13	86.35	45.99	135.70	42.05	130.74	37.40
14	91.95	47.90	140.79	44.19	135.56	39.24
15	95.33	46.90	143.85	43.36	138.34	37.54
16	94.83	44.41	143.32	40.89	137.81	34.48
17	94.47	42.03	142.88	38.63	137.47	31.91
18	91.95	38.52	140.35	35.39	135.42	29.32
19	90.68	37.25	139.04	34.35	134.20	28.29
20	90.58	34.38	138.73	31.93	134.06	25.75
21	86.80	31.94	135.03	29.75	130.66	23.90
22	85.34	29.30	133.56	27.37	129.84	22.96
23	82.51	25.92	130.81	24.16	127.72	20.86
24	76.48	23.23	125.25	21.42	122.50	18.46
25	72.71	20.08	121.78	18.33	119.34	15.54
26	67.73	16.48	117.23	14.77	115.12	12.09
27	61.33	14.31	111.53	12.53	109.89	10.73
28	56.40	12.75	107.31	10.83	106.13	9.87
29	51.05	12.59	102.77	10.25	102.17	10.20
30	46.83	13.96	99.37	11.35	99.12	11.60
31	44.24	13.96	97.39	11.14	97.11	11.38
32	40.17	13.01	94.30	10.06	94.13	10.31
33	36.42	13.71	91.63	10.23	91.55	10.50
34	32.75	13.66	89.02	9.82	88.89	10.07
35	28.86	14.18	86.35	9.99	86.31	10.26
36	26.04	14.33	84.52	9.88	84.42	10.14
37	23.40	13.45	82.69	9.10	82.53	9.33

TABLE A-2. (Concluded)

Quarter Number	Cycles 1 thru 19, Sunspots		Cycles 1 thru 19, 10.7-cm Flux		Cycles 1 thru 18, 10.7-cm Flux	
	Mean	St. Dev.	Mean	St. Dev.	Mean	St. Dev.
38	20.11	12.39	80.46	8.09	80.22	8.24
39	17.54	11.46	78.75	7.34	78.47	7.44
40	16.32	11.02	77.99	7.09	77.90	7.27
41	14.93	10.06	77.13	6.40	77.21	6.56
42	14.23	9.51	76.69	5.95	76.83	6.08
43	14.99	11.27	77.37	7.57	77.57	7.73
44	15.92	15.42	78.24	11.14	78.42	11.42
45	18.38	21.62	80.38	16.67	80.62	17.10
46	22.23	28.73	83.51	23.17	83.86	23.75
47	26.36	33.72	86.79	27.85	87.18	28.56
48	32.15	39.20	91.45	32.94	91.78	33.82

## REFERENCES

- A-1. McNish, A. G., and Lincoln, J. V.: Prediction of Sunspot Numbers. Transactions, American Geophysical Union, vol. 30, no. 5, October 1949.
- A-2. Boykin, E. P., and Richards, T. J.: Application of the Lincoln-McNish Technique to the Prediction of the Remainder of the Twentieth Sunspot Cycle. Lockheed Missiles and Space Company, Technical Memorandum 54/30-89, Huntsville, Alabama, March 1966.
- A-3. Chernosky, E. J., and Hagan, M. P.: The Zürich Sunspot Number and Its Variations for 1700-1957. Journal of Geophysical Research, vol. 63, no. 4, December 1958.

## APPENDIX B. NEUTRAL ATMOSPHERE MODELS

### B.1 Density Variations and Models

Since the advent of the first orbiting satellite in 1957, significant advances have been made in our knowledge of the earth's upper atmosphere. The accepted model of the earth's upper atmosphere at that time was one in which the temperature, pressure, density, and composition varied only with height. Predictions of future sightings (orbital positions) of the first satellites using this invariant atmosphere soon showed that the model was in error. Subsequently, several periodic variations in the density, temperature, and composition of the upper atmosphere have been identified. They are classified as:

- a. Variations with the solar cycle  $\sim 11$  year.
- b. Variations with the daily change in activity on the solar disc.
- c. The diurnal variation.
- d. Variations with geomagnetic activity.
- e. The semiannual variation.
- f. Seasonal-latitudinal variations of the lower thermosphere.
- g. Seasonal-latitudinal variations of helium at all altitudes.
- h. Rapid density fluctuations probably connected with tidal and gravity waves.

The first seven have some regularity and can be modeled with varying degrees of accuracy. Since temperature plays a minor role in comparison with density, current models have been developed to represent, insofar as practical and possible, the variability of the ambient mass density rather than the temperature. The models are based on temperature profiles (Fig. B-1) [B-1] which have been adjusted so as to produce the density values derived from the analyses of satellite orbital decay data.

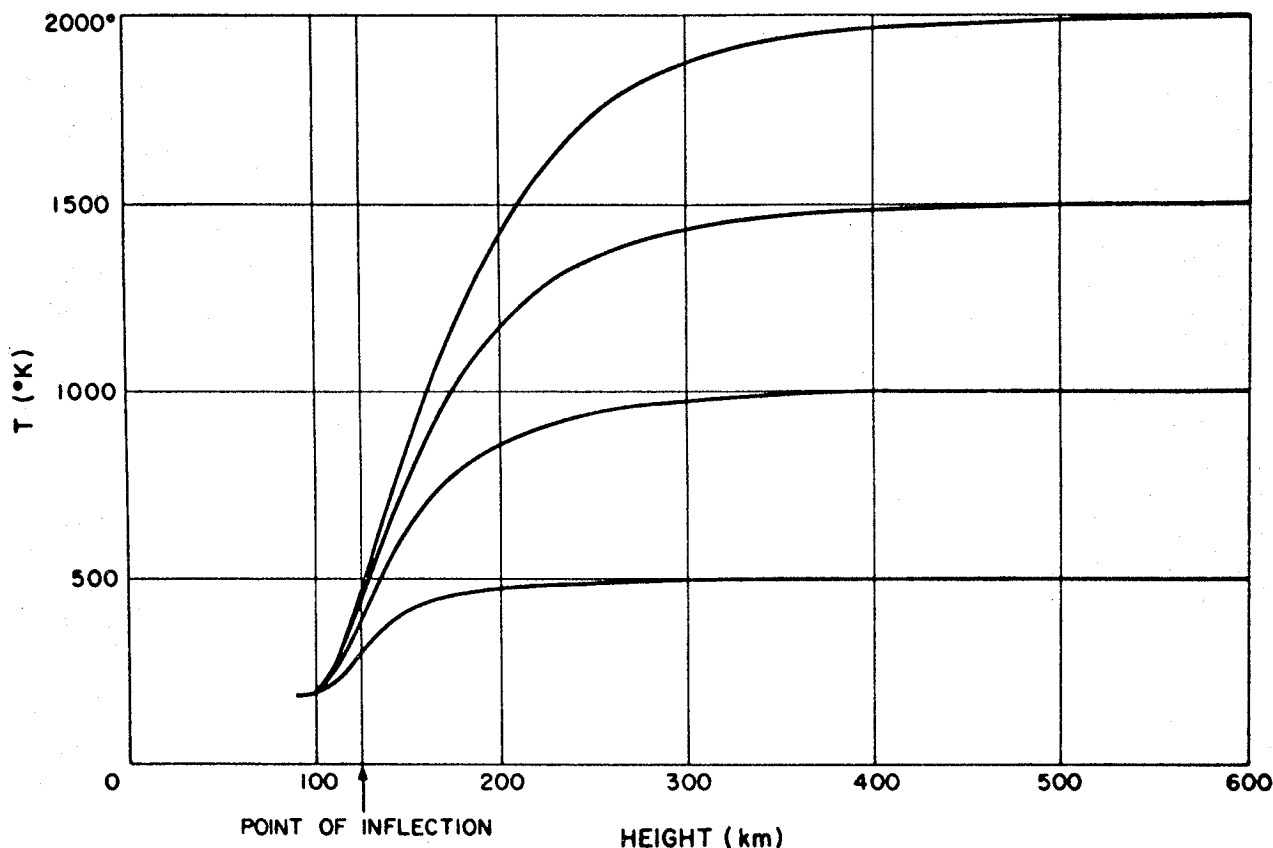


Figure B-1. Four temperature profiles from the present models [B-1].

#### B.1.1 Variations with Solar Activity

The ultraviolet solar radiation that heats and causes compositional changes (Fig. B-2) [B-1] in the earth's upper atmosphere consists of two components, one related to active regions on the solar disc and the other to the disc itself. The active-region component varies from day to day while the disc component varies more slowly, presumably with the longer periodicities in the solar activity; i.e., the ~11-year solar cycle. The atmosphere has been observed to react in a different manner to each of these two components. Jacchia and Slowey have found that the disc component of the solar radiation is, for all practical purposes, linearly related to the 10.7-cm solar flux smoothed over three solar rotations (81 days).

The effect of solar activity on atmospheric density is shown in Figures B-3 and B-4 after Jacchia [B-1]. When the short-period oscillations which are caused by the diurnal variation are removed, there is essentially an 11-year variation that parallels the smoothed 10.7-cm solar flux data.



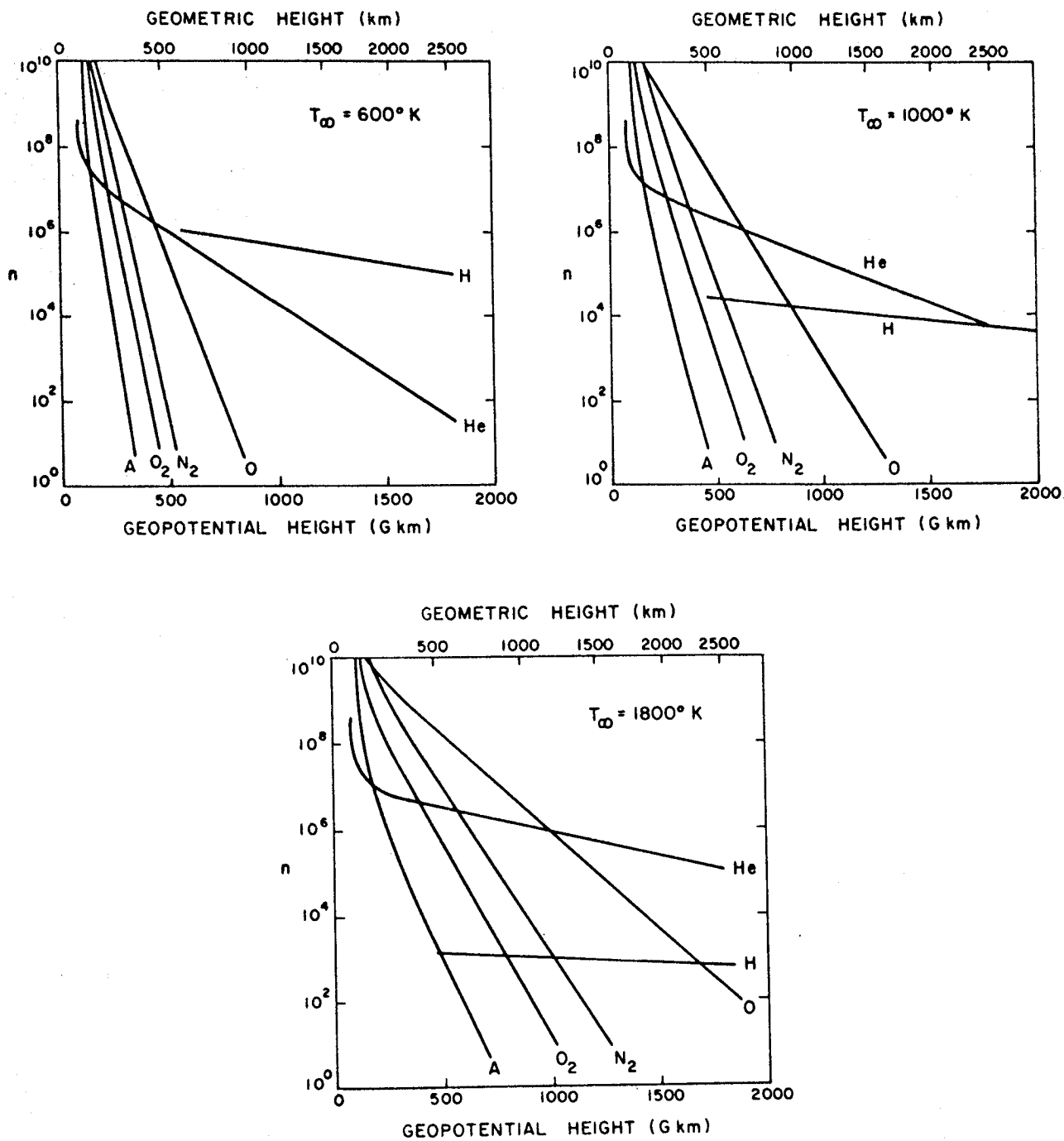


Figure B-2. Atmospheric composition for three values of the exospheric temperature [B-1]. (Number densities ( $n$ ) are plotted against geopotential height. The corresponding geometric heights are marked at the top of the diagrams.)

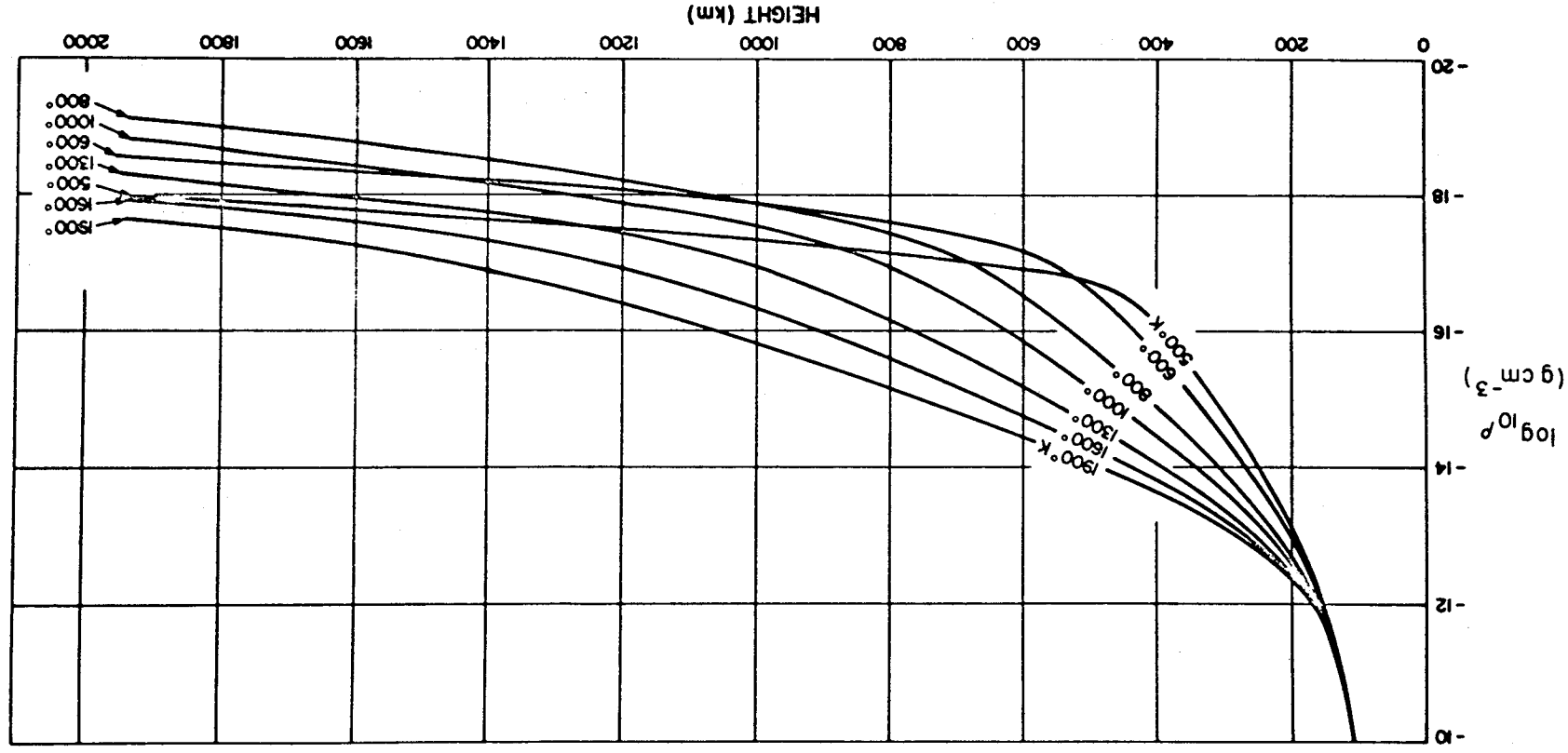


Figure B-3. Density profiles for seven values of the exospheric temperature [B-1].

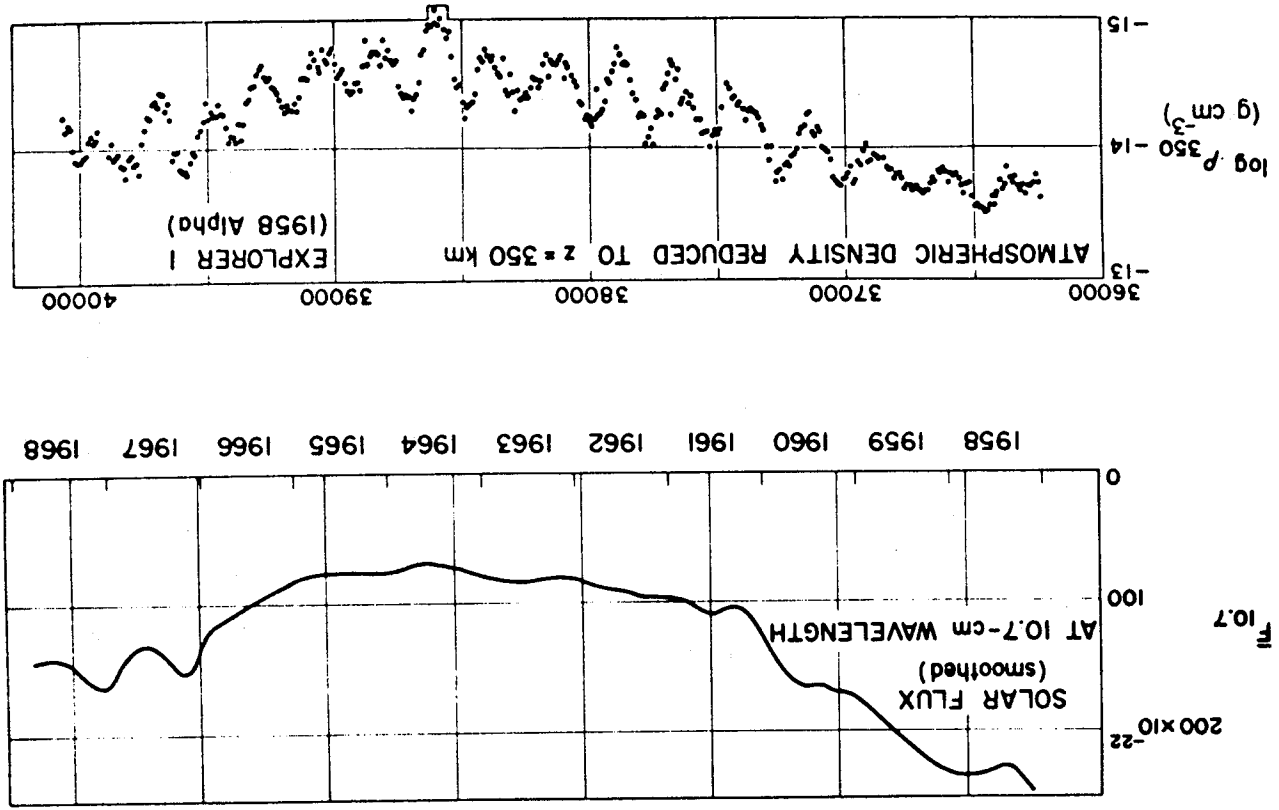


Figure B-4. Ten-day means of the densities obtained from the drag of the Explorer I satellite compared with variations in the 10.7-cm solar flux [B-1]. [M.J.D. is the Modified Julian Day (J.D. minus 2 400 000.5).]

Figure B-5, after Jacchia [B-1], shows some of the variations in greater detail. The variations with a 27-day period are caused by the sun's rotation — the active-region component. The semiannual variation can also be seen.

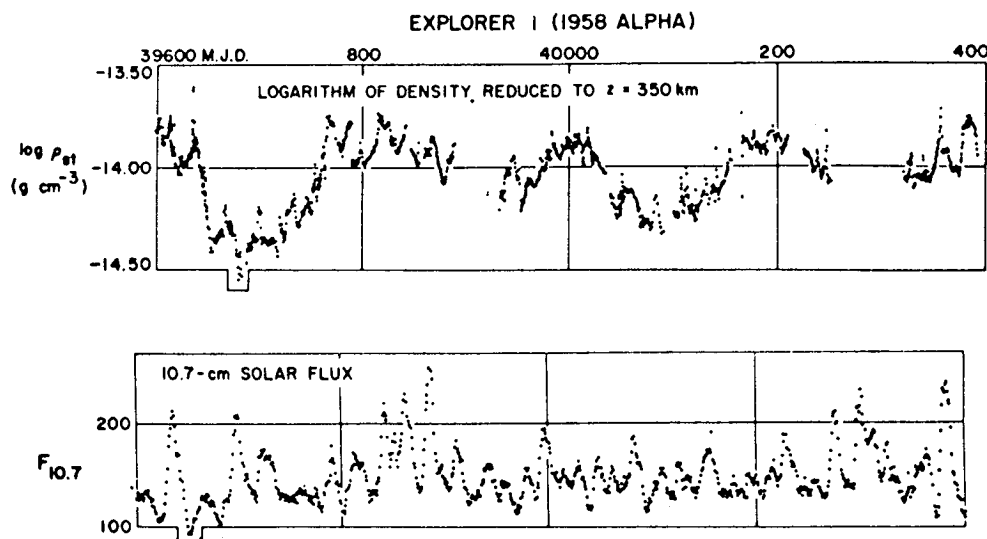
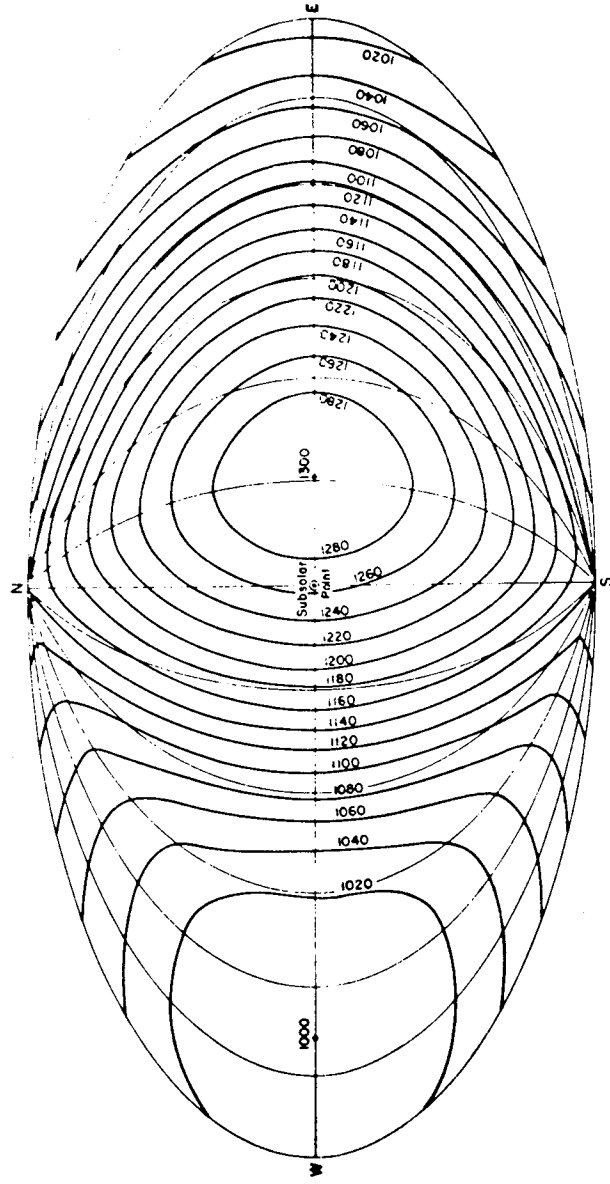


Figure B-5. Densities obtained from the drag of the Explorer 1 satellite compared with variations in the 10.7-cm solar flux.

### B. 1. 2 The Diurnal Variation

Analyses of satellite orbital decay histories have shown that upper atmospheric densities reach a maximum around 2 p.m. local solar time at a latitude approximately equal to that of the subsolar point while the minimum occurs between 3 and 4 a.m. at about the same latitude in the opposite hemisphere. Consistency between temperature and density cannot be achieved on a diurnal basis in a static model; therefore, the temperature profile has been used as a parameter so that observed density values can be reproduced by the models. The temperature distribution needed to achieve this required reproduction of the observed density values is depicted on a global scale in Figure B-6 [B-1]. Even though the global temperature distribution is an artifact developed solely for use in the density and composition models, some experimental results are in good agreement [B-2, B-3, B-4, B-5]. Thomson-scatter temperature measurements [B-6, B-7, B-8], as shown in Figure B-7 [B-1], generally show that the temperature maximum occurs between 3 and 5 p.m. rather than near 2 p.m. This controversy has not been resolved at this time; however, it appears as if there is a phase lag between the density maximum and the temperature maximum which cannot be included in the current atmospheric models.

# EXOSPHERIC TEMPERATURE DISTRIBUTION AT THE EQUINOXES



# EXOSPHERIC TEMPERATURE DISTRIBUTION AT NORTHERN SUMMER SOLSTICE

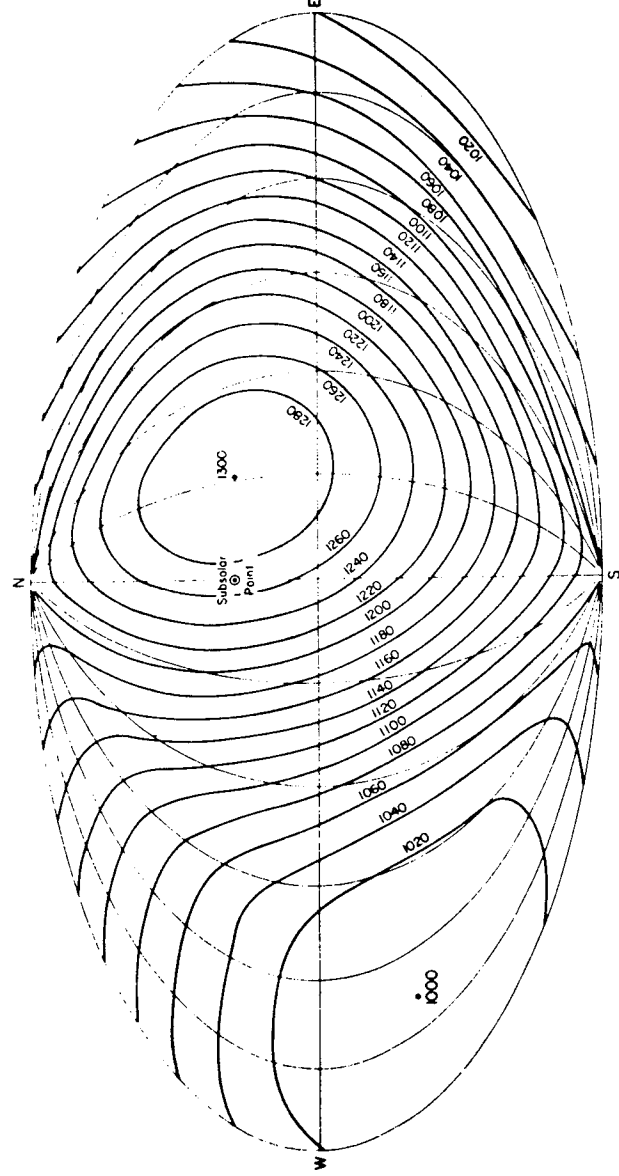


Figure B-6. Exospheric isotherms ( $^{\circ}$  K) above the globe, for the case when the minimum temperature is  $1000^{\circ}$  K [B-1]. (Top, equinoxes; bottom, northern summer solstice.)

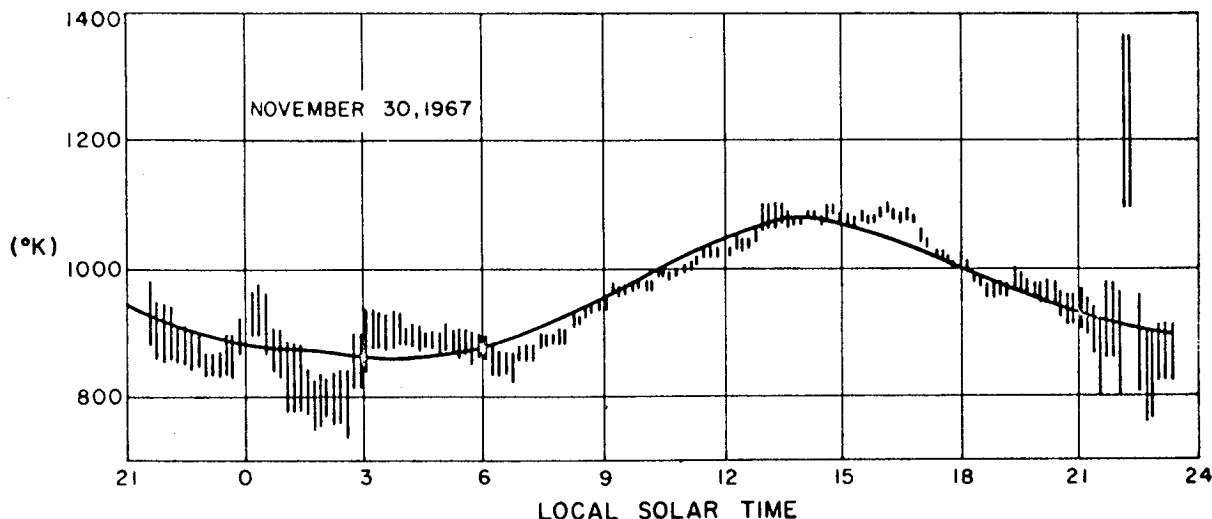


Figure B-7. Atmospheric temperatures obtained on November 30, 1967, by Carru and Waldteufel [B-7] by use of Thomson-scatter techniques, compared with temperatures predicted by the present models for a height of 300 km (solid line).

#### B. 1.3 The Semiannual Variation

No satisfactory explanation has been found for this variation. It was initially assumed that this density variation could be linked with a temperature variation; however, data from analyses of more recently orbited satellites showed that the original assumption was in error. The amplitude of this density variation is strongly height-dependent and variable from year to year, with a primary minimum in July and principal maximum in October; however, it does not appear to be related to solar activity. Figure B-8 [B-1] shows the semiannual variation as derived from the orbital decay analysis of Explorer 32.

#### B. 1.4 Variations with Geomagnetic Activity

Analyses of orbital decay histories can give only a blurred picture of the complex reaction of the upper atmosphere to geomagnetic disturbances (Fig. B-9) [B-1]. Blamont and Luton [B-9] and DeVries [B-10] have shown that the upper atmosphere first reacts in the auroral zones with the energy subsequently propagating equatorward apparently in the form of wave-like perturbations. It appears as if the atmosphere reacts with a zero time delay in the auroral zones with the geomagnetic storm effects showing up in the

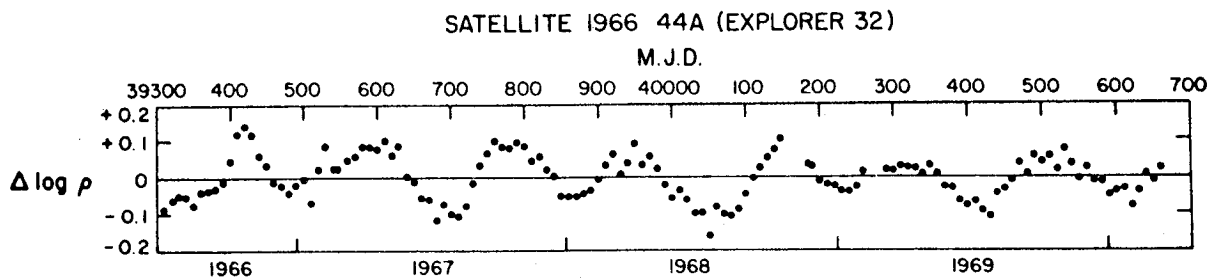


Figure B-8. The semiannual density variation as derived from drag analysis on Satellite 1966 44 A (Explorer 32). [All other variations have been suppressed by using the appropriate equations. M.J.D. is the Modified Julian Day (J.D. minus 2 400 000.5).]

equatorial zone about 6 to 9 hours later. It is very difficult to adequately include this effect in a static model. The current models calculate the density variations on the basis of a global increase in exospheric temperature. Observations [B-9, B-10] have shown that this is not the case; however, for satellite lifetime prediction calculations, an assumed global temperature increase is acceptable. For some calculations, such as control dynamics analyses, control moment gyro analyses and aerodynamic torques, instantaneous temperature (and therefore density), increases for short time periods and specific locations may be required. These studies may require special applications of the models.

#### B.1.5 Seasonal-Latitudinal Variations of the Lower Thermosphere

Presently accepted models assume constant temperature and density values at 90 km to prevent the models from becoming too complex even though large temperature and somewhat smaller density variations are known to exist. Current models therefore are constructed with a seasonal-latitudinal density variation which varies in the vertical from 0 at 90 km to a maximum at 110 and back to zero at 170 km. In the horizontal, the maximum occurs on December 27 at the North Pole and on June 25 at the South Pole. These variations are included as additions to the mass densities calculated as a function of the exospheric temperature used in the model. These variations are small and because they occur solely below 170 km altitude they will have little effect on orbital lifetime prediction calculations.

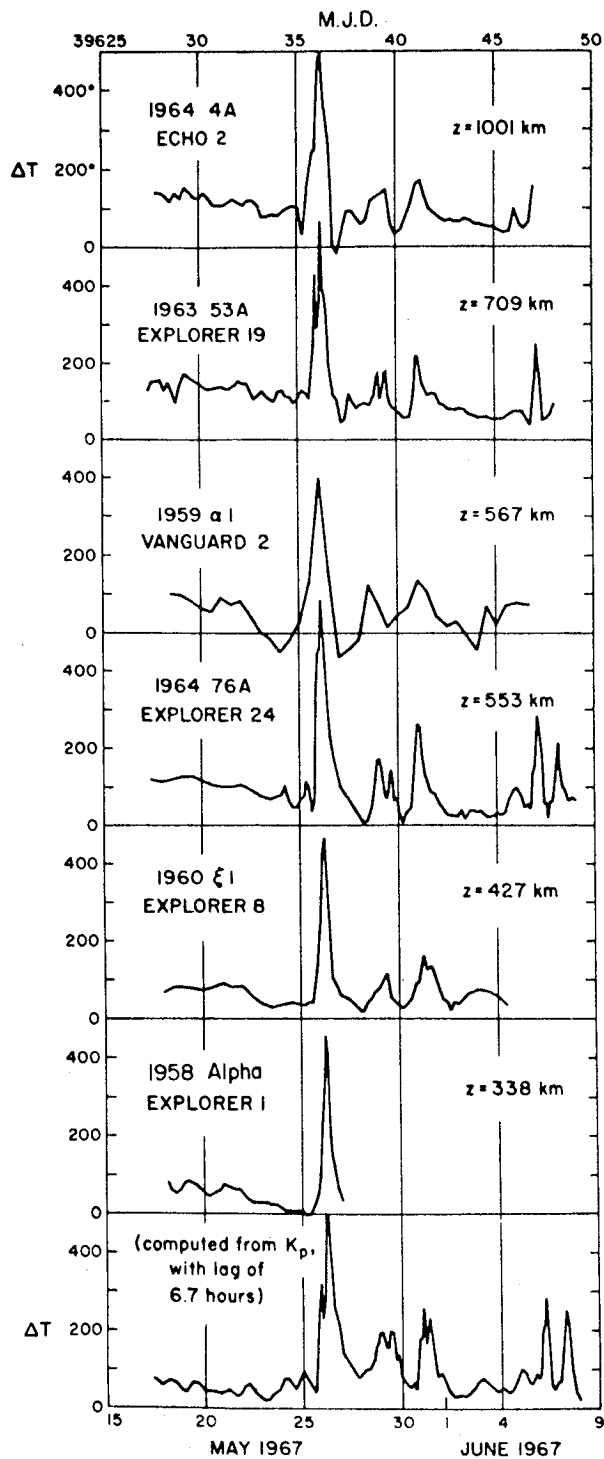


Figure B-9. The geomagnetic effect as derived from the drag of six satellites in May and June 1967. [The plotted  $\Delta T$ s are temperature residuals from the models when all variations except the geomagnetic effect have been taken into account. M.J.D. is the Modified Julian Day (J.D. minus 2 400 000.5).]



### B.1.6 Seasonal-Latitudinal Variations of Helium

Experimental results have shown a strong increase of helium above the winter pole. The mechanism for this migration is unclear; however, empirical equations which describe the phenomenon are included in the models. These variations influence the computed densities only at heights above approximately 600 km (Fig. B-10).

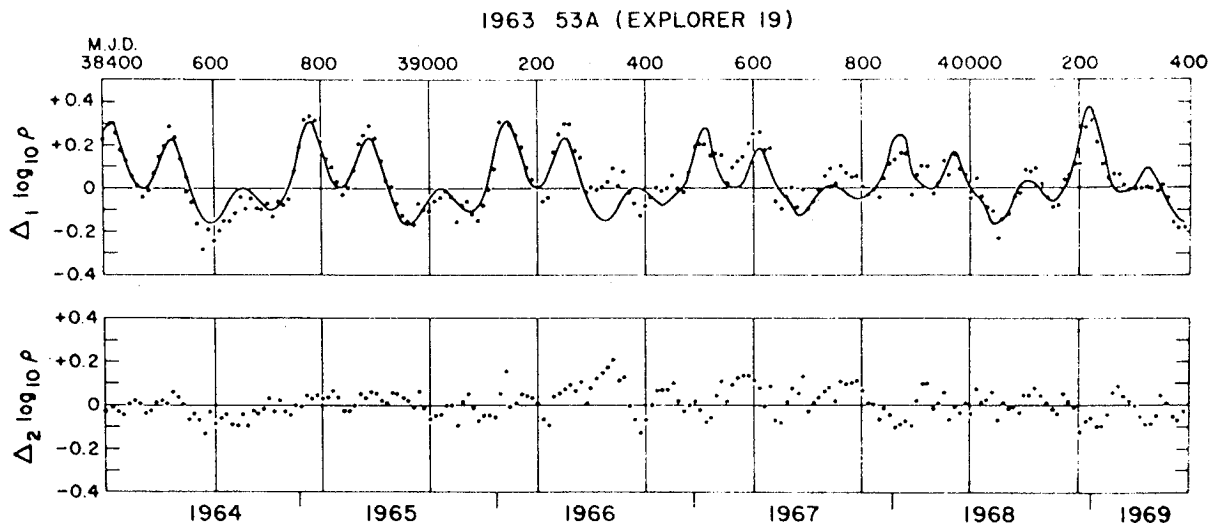


Figure B-10. Observed and computed density variations caused by the helium migration, as derived from the drag on Satellite 1963 53A (Explorer 19). [The data points in  $\Delta_1 \log \rho$  are density residuals from the model when all variations except the helium variation are suppressed.  $\Delta_2 \log \rho$  is the difference O-C in  $\Delta_1 \log \rho$ . M.J.D. is the Modified Julian Day (J.D. minus 2 400 000.5).]

### B.1.7 Density Waves

Ambient density waves have been detected throughout the upper atmosphere in the height range from 140 to at least 510 km [B-4, B-10]. In addition, traveling ionospheric disturbances (TIDs) have long been thought of as manifestations of internal gravity waves. The waves appear to be more prevalent at the higher latitudes near the auroral zone; however, TIDs have been observed at all latitudes. Their vertical wavelengths apparently increase with altitude. Density increases on the order of 100 percent have been observed

to occur over short distances [B-10]. The waves apparently propagate from either south to north or north to south with maximum horizontal wavelengths on the order of 500 to 700 km. Although current models do not include variations associated with internally propagating waves, users should be cautioned that they have been observed.

## B.2 Applications

Requirements exist for models of the earth's neutral upper atmosphere which will:

- a. When used in lifetime prediction calculations, make predictions of lifetimes for satellites with orbital altitudes between  $\sim 180$  and 2500 km within reasonable limits.
- b. Contain the short period fluctuations observed in upper atmospheric density which may influence the design and operation of reaction control systems (RCS), thrust augmented control systems (TACS), control moment gyroscopes (CMG), rendezvous and docking systems, etc.
- c. Provide continuous values of atmospheric parameters from orbital altitudes down to about 25 km altitude for use in evaluating thermal protection systems (TPS), control and guidance systems, etc., during reentry of space vehicle (e.g., the Shuttle), and in accomplishing orbital debris analyses.
- d. Provide data on the composition and thermal structure of the upper atmosphere and its temporal and spatial variability for use in interpreting and analyzing results of scientific and technical investigations; e.g., contamination surrounding the Skylab.
- e. Provide data on the variability of the neutral atmosphere at mesopause heights for use in aerobraking maneuver studies.

## B.3 Criteria

No single model currently available meets all of the requirements applications listed above; therefore, the following models should be used for the areas specified:

a. The Jacchia 1970 [B-11] atmosphere model will be used in conjunction with the MSFC Lifetime Prediction Computer Routine for calculating orbital lifetime. Data from the monthly Solar Activity memorandum prepared and distributed by the Aerospace Environment Division will be used as inputs to the model. A computerized simplified version of the Jacchia 1970 atmosphere model is available upon request from the Aerospace Environment Division.

b. MSFC Model Atmosphere 1971 will be used for all other applications with the exception of Paragraph e. above. This model is a combination of models in which the Groves [B-12] model of the lower atmosphere provides 90-km temperature and density values for inputs to the computational technique developed by Jacchia [B-1]. This procedure changes the model structure above 90 km completely; however, it provides continuous density, temperature, and composition data from 25 to 2500 km for analyses requiring these data; i.e., re-entry, aeromaneuvering, etc. Copies of the computer program for this model are available upon request to the Aerospace Environment Division, MSFC.

c. Personnel performing analyses requiring knowledge of any small scale, short time period fluctuations in atmospheric parameters such as those perturbations associated with internally propagating waves should contact the Aerospace Environment Division, MSFC, for model data to be used in each specific analysis.

## REFERENCES

- B-1. Jacchia, L. G.: Revised Static Models of the Thermosphere and Exosphere with Empirical Temperature Profiles. Smithsonian Astrophysical Obs., Special Report 332, May 5, 1972.
- B-2. Taeusch, D. R., Niemann, H. B., Carignan, G. R., Smith, R. E., and Ballance, J. O.: Space Research 8. A. P. Mitra, L. G. Jacchia, and W. S. Newman, eds., North Holland Publishing Co., Amsterdam, 1968, pp. 930-939.
- B-3. Reber, C. A., and Nicolet, M.: Planet Space Science. 13, 1965, pp. 617-646.
- B-4. Newton, G. P.: Journal of Geophysical Research. 74, 1969, pp. 6409-6414.
- B-5. Hall, L. A., Chagnon, G. W., and Hinteregger, H. E.: Journal of Geophysical Research. 72, 1967, pp. 3425-3427.
- B-6. Carru, H., Petit, M., and Waldteufel, P.: Planet Space Science. 15, 1967, pp. 944-945.
- B-7. Carru, H., and Waldteufel, P.: Ann de Geophys. 25, 1969, pp. 485-494.
- B-8. McClure, J. P.: Journal of Geophysical Research. 74, 1969, pp. 279-291.
- B-9. Blamont, J. E., and Luton, J. M.: Space Research 11. Akademie-Verlag, Berlin, 1971.
- B-10. DeVries, L. L.: Experimental Evidence in Support of Joule Heating Associated with Geomagnetic Activity. NASA TM X-64568, MSFC, February 10, 1971.
- B-11. Jacchia, L. G.: Smithsonian Astrophysical Observatory Special Report No. 313. 1970, pp. 87.
- B-12. Groves, G. V.: Environmental Research Papers, No. 368, AFCRL-71-0410, Bedford, Mass., 1971.

# APPENDIX C. A PRELIMINARY SUMMARY OF THE MSFC PLANETARY ATMOSPHERE COMPUTER PROGRAM

## Summary

The MSFC Planetary Atmosphere Computer Program contains the exact equations and most refined techniques necessary to the development of models of planetary atmospheres. All of the atmospheric parameters that are essential to spacecraft design studies and aerospace operations are output in tabular form for levels of geopotential height and geometric altitude from the surface to the altitude where the planetary atmosphere is the same as interplanetary space.

## I. Purpose

This appendix briefly outlines the computation procedure used in the Planetary Atmosphere Computer Program recently developed by the MSFC Computation Laboratory for the B5500 computer.

## II. Basic Data

In developing a model atmosphere, it is necessary to establish certain basic data so that various parameters that define the model may be computed. It has been found that the most refined models may be developed if these basic data consist of kinetic temperature and molecular weight versus geopotential height profiles and a surface pressure.

## III. Computational Procedure

### A. Input Data

1. Kinetic temperature at geopotential height levels.
2. Molecular weight at geopotential height levels.
3. Surface pressure.
4. Surface kinetic temperature.

5. Surface molecular weight.
6. Surface gravity.
7. Planet radius.
8. Universal gas constant.
9. Sutherland's constant.
10. Boltzman's constant.
11. Avogadro's number.
12. Effective collision diameter of mean air particle.
13. Ratio of specific heats.

B. Computations at Geopotential Height Levels

1. Kinetic temperature lapse rates

$$L_K = \frac{dT_K}{dH} = \frac{(T_K)_n - (T_K)_{n+1}}{H_{n+1} - H_n} \quad (C-1)$$

where  $n$  is the input levels in geopotential kilometers.

2. Molecular weight lapse rates

$$J = \frac{dM}{dH} = \frac{M_n - M_{n+1}}{H_{n+1} - H_n} \quad (C-2)$$

where  $n$  is the input levels in geopotential kilometers.

3. Kinetic temperatures

Kinetic temperatures are computed for each km from 1 to 1000 km geopotential height from the surface temperature  $(T_0)$  and the computed lapse rate  $(L_K)$ .

#### 4. Molecular weight

Molecular weight values are computed for each km from 1 to 1000 km geopotential height from the surface molecular weight ( $M_o$ ) and computed molecular weight lapse rate ( $J$ ) .

#### 5. Molecular temperatures

Molecular temperatures are computed for each km from 0 to 1000 km geopotential height.

$$(T_M)_j = \frac{(T_K)_j M_o}{M_j} \quad (C-3)$$

#### 6. Molecular temperature lapse rate

$$(L_M)_{j-1 \text{ to } j} = \frac{(T_M)_{j-1} - (T_M)_j}{H_j - H_{j-1}} \quad (C-4)$$

$j = 1, 2, 3, \dots, 999, 1000 - (T_M)_{j-1} = (T_M)_o$  for first computation.

#### 7. Atmospheric pressure (discussed later in this appendix)

a. If  $L_M \neq 0$  ,

$$P_j = P_{j-1} \left[ \frac{(T_M)_{j-1}}{(T_M)_j} \right]^{\frac{M_o G_o}{R^* (L_M)_{j-1 \text{ to } j}}} \quad (C-5)$$

where  $P_{j-1} = P_o$  for first computation.

b. If  $L_M = 0$  ,

$$P_j = P_{j-1} \exp \left[ \frac{M_o G_o (H_j - H_{j-1})}{R^* (T_M)_j} \right] \quad (C-6)$$

C. Computations for Each km from 0 to 1000 km Geometric Altitude

1. Geometric altitude

$$Z_i = \frac{RH_i}{R - H_i} \quad . \quad (C-7)$$

2. Atmospheric pressure

Using pressure values  $(P)_j$  computed at geopotential height levels by equations (C-5) and (C-6), atmospheric pressures are interpolated logarithmically for each kilometer of geometric altitude and denoted as  $(P)_i$ .

3. Kinetic temperature

Using kinetic temperatures  $(T_K)_j$  computed at geopotential height levels, kinetic temperatures are interpolated for each km of geometric altitude and denoted as  $(T_K)_i$ .

4. Molecular weight

Molecular weight values are similarly interpolated for each kilometer of geometric altitude and denoted by  $M_i$ .

5. Molecular temperature

$$(T_M)_i = \frac{(T_K)_i M_o}{M_i} \quad . \quad (C-8)$$

6. Atmospheric density

$$\rho_i = \frac{M_o P_i}{R^* (T_M)_i} \quad . \quad (C-9)$$



7. Gravity

$$G_i = G_o \left[ \frac{R}{R + (Z)_i} \right]^2 \quad (C-10)$$

8. Pressure scale height

$$SH_P = \frac{R^* (T_M)_i}{M_o G_i} \quad (C-11)$$

9. Density scale height

$$SH_d = \frac{(SH_P)_i}{1 + \frac{R^*}{M_o G_i} (dT_M/dZ)_i} \quad (C-12)$$

where

$$(dT_M/dZ)_i = \frac{(T_M)_{i-1} - (T_M)_{i+1}}{Z_{i+1} - Z_{i-1}} \quad (C-13)$$

10. Number density

$$(ND)_i = \frac{M_o NP_i}{R^* M_i (T_M)_i} \quad (C-14)$$

11. Most probable air-particle speed

$$PS_P = \left[ 2 \frac{R^*}{M_o} (T_M)_i \right]^{1/2} \quad (C-15)$$

12. Mean air-particle speed

$$PS_M = \left[ \frac{8}{\pi} \frac{R^*}{M_o} (T_M)_i \right]^{1/2} \quad (C-16)$$

13. Atmospheric mean free path

$$(MFP)_i = \frac{R^*(M)_i T_{M_i}}{\sqrt{2} \pi N \sigma^2 M_o (P)_i} \quad (C-17)$$

14. Collision frequency

$$(CF)_i = \frac{(PS_M)_i}{(MFP)_i} \quad (C-18)$$

15. Speed of sound

$$(C_s)_i = \left[ \gamma \frac{R^*}{M_o} T_{M_i} \right]^{1/2} \quad (C-19)$$

16. Coefficient of viscosity

$$(CV)_i = \frac{(T_K)_i^{3/2}}{(T_K)_i + S} \quad (C-20)$$

#### D. Output

The various computer parameters are printed in tabular form for kilometer increments of both geopotential height and geometric altitude. The program is designed so that the printing interval may be varied at the discretion of the operator. For example, parameters may be printed for each kilometer in the lower atmosphere, then for each 10 km over a defined altitude region, and then for each 100 km in the upper atmosphere.

### IV. Computer Program Accuracy and Versatility

Accuracy and versatility have been emphasized in the development of this computer program. Atmospheric pressures are computed from the exact hydrostatic equation without constant molecular weight or isothermal temperature assumptions. This pressure computation technique has been found to be more accurate than those approximation techniques which assume that the

molecular weight is constant and that the temperature is isothermal over the computation interval. The computation interval is considered as 1 km in this report, but the computer program is designed so that the size of this interval is input and may be varied. It should be noted, however, that the size of the computation interval does not influence the accuracy when the exact pressure equation is used.

To maintain a high degree of versatility in the application of this computer program, all constants that are descriptive of an individual planet are input. The program may be used in the development of the atmosphere of any planet including the earth. The program is designed to allow computations from the planet's surface to interplanetary space altitude levels, which generally occurs between 10 000 and 20 000 km.

APPROVAL

NASA TM X-64627

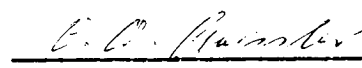
SPACE AND PLANETARY ENVIRONMENT CRITERIA GUIDELINES  
FOR USE IN SPACE VEHICLE DEVELOPMENT  
(1971 REVISION)

Edited by Robert E. Smith

The information in this report has been reviewed for security classification. Review of any information concerning Department of Defense or Atomic Energy Commission programs has been made by the MSFC Security Classification Officer. This report, in its entirety, has been determined to be unclassified.

This document has also been reviewed and approved for technical accuracy.

  
\_\_\_\_\_  
W. W. VAUGHAN  
Chief, Aerospace Environment Division

  
\_\_\_\_\_  
E. D. GEISLER  
Director, Aero-Astrodynamics Laboratory